

UCSF

UC San Francisco Electronic Theses and Dissertations

Title

Visualization and Analysis of Human Parafoveal Capillaries Using Motion Contrast Enhancement on Adaptive Optics Scanning Laser Ophthalmoscopy Videos

Permalink

<https://escholarship.org/uc/item/52d1j37k>

Author

Tam, Johnny

Publication Date

2011

Peer reviewed|Thesis/dissertation

Visualization and Analysis of Human Parafoveal Capillaries Using Motion
Contrast Enhancement on Adaptive Optics Scanning Laser Ophthalmoscopy
Videos

by

Johnny Tam

DISSERTATION

Submitted in partial satisfaction of the requirements for the degree of

DOCTOR OF PHILOSOPHY

in

BIOENGINEERING

in the

GRADUATE DIVISION

of the

UNIVERSITY OF CALIFORNIA, SAN FRANCISCO

AND

UNIVERSITY OF CALIFORNIA, BERKELEY

Copyright 2011

by

Johnny Tam

ACKNOWLEDGMENTS

First and foremost I would like to thank Austin Roorda, for being a fantastic mentor, and chair of my dissertation committee. I have been extremely fortunate to have such a supportive advisor, who has allowed me to develop my interests in research, teaching, and a handful of extracurricular activities. With Austin's encouragement and support, I was able to pursue a number of very meaningful opportunities, which included visiting the Maui Community College as a guest instructor, participating in the Fundamental Issues of Vision Research (FIVR) summer course at the Marine Biology Lab in Woods Hole, MA, and traveling to Rotterdam, Netherlands to present a paper at the International Symposium on Biomedical Imaging. These and many other opportunities have been truly eye-opening.

I am also deeply appreciative of my dissertation committee members, who have encouraged me at every step of the process. Some highlights: Dorian Liepmann, for encouraging me to present and attend the Diabetes Technology Meeting; Jonathan Horton, for his dedicated and engaging questions and comments; Ruzena Bajcsy, for being a true inspiration, kindly helping me to understand and appreciate the field of medical image analysis; and Jitendra Malik, for introducing me to the field of computer vision, and seeding the start of the vessel mapping and hemodynamics project that would ultimately become the theme of this dissertation.

I would like to thank the remaining members of my qualifying exam committee: David Saloner, for being a fantastic chair and for supporting me throughout the entire process of preparing for and completing the exam; David Copenhagen, for his insightful

feedback and for pushing me to learn more about the day to day life of patients with diabetes; and Anthony Adams, for his kind support and encouragement over the past few years, and for trusting me to recruit patients from his own ongoing Diabetes Study.

I would like to acknowledge my collaborators: most importantly, Anthony Adams and Marcus Bearse for their inspiration and support in setting up a collaborative diabetes study, and for graciously granting access to all the necessary data, equipment, supplies, and protocols needed to carry out the study; Pavan Tiruveedhula, for his tireless assistance with imaging sessions, effective troubleshooting capability, and willingness to implement numerous hardware and software modifications for the AOSLO; Kavita Dhamdhere, for accelerating the progress of the AOSLO Diabetes Study by enthusiastically assisting with patient recruitment, patient handling, data acquisition, and data analysis; Silvestre Manzanera, for successfully motivating Spanish-speaking patients to participate in the study and to carry out various tasks during imaging sessions; Brandon Lujan, for his encouragement and insightful perspectives regarding capillaries and diabetic retinopathy, and for introducing me to the world of ophthalmology; David Merino, for his help troubleshooting, fixing, and improving the AOSLO optics on several urgent occasions; Mark Campanelli, for developing the original implementation of the virtual AOSLO; Vincent Liu, for assisting with data processing; Brian Wolff, Maria Cardenas, Wendy Harrison, Glen Ozawa, and Michal Laron for assisting with patient recruitment and with countless logistical issues related to the AOSLO Diabetes study; and finally, past and present

members of the Roorda and Duncan labs, for day-to-day inspiration, support, and encouragement.

I am thankful for my family and friends who have supported me over the years and inspired me to reach my dreams.

I would like to acknowledge my primary sources of funding: National Institute of Health (NIH) Training Grant 5 T32 GM008155-23; National Defense Science and Engineering Graduate (NDSEG) Fellowship, awarded by the Department of Defense (DoD), Air Force Office of Scientific Research, 32 CFR 168a; and National Science Foundation (NSF) Graduate Research Fellowship Grant DGE-0648991. Additional support was received from: Graduate Scholarship, awarded by Phi Beta Kappa (PBK) of Northern California; Graduate Dean's Health Science Fellowship, awarded by the UCSF Graduate Division; and an Educational Scholarship in Optical Science and Engineering, awarded by the International Optics and Photonics Society (SPIE). Travel support was provided by the National Institute of Health (NIH), National Eye Institute (NEI), Juvenile Diabetes Research Foundation (JDRF) in conjunction with the Diabetes Technology Society, Institute for Astronomy (IfA) through the Akamai Workforce Initiative Program, and the UCSF-UCB Joint Graduate Group in Bioengineering.

The material in the dissertation is based on the following a series of publications and conference presentations. The dissertation author is the primary investigator and thanks co-authors for their contributions, described in more detail at the end of each chapter. The publications and presentations are listed below, listed alongside the most relevant chapter of the dissertation.

Refereed Journal Publications

- CH 3** **Johnny Tam**, Kavita P. Dhamdhere, Pavan Tiruveedhula, Silvestre Manzanera, Shirin Barez, Marcus A. Bearse, Jr., Anthony J. Adams, and Austin Roorda, “Disruption of the Retinal Parafoveal Capillary Network in Type 2 Diabetes Prior to the Onset of Diabetic Retinopathy,” *Investigative Ophthalmology and Visual Science* 52(12):9257-9266, 2011.
- CH 2** **Johnny Tam**, Pavan Tiruveedhula, and Austin Roorda, “Characterization of single-file flow through human retinal parafoveal capillaries using an adaptive optics scanning laser ophthalmoscope,” *Biomedical Optics Express* 2(4):781-793, 2011 (**Featured in the Optical Society of America’s “Spotlight on Optics”**).
- CH 2** **Johnny Tam** and Austin Roorda, “Speed quantification and tracking of moving objects in adaptive optics scanning laser ophthalmoscopy,” *Journal of Biomedical Optics* 16(3):036002, 2011.
- CH 1** **Johnny Tam**, Joy A. Martin, and Austin Roorda, “Non-invasive visualization and analysis of parafoveal capillaries in humans,” *Investigative Ophthalmology and Visual Science* 51(3):1691-1698, 2010.

Refereed Conference Papers

- CH 4** **Johnny Tam** and Austin Roorda, “Enhanced detection of cell paths in spatiotemporal plots for noninvasive microscopy of the human retina,” *Proceedings of the IEEE International Symposium on Biomedical Imaging (ISBI)*, pp. 584-587, 14-17 April 2010 (Acceptance rate for oral presentation: 15%).

Conference Abstracts and Presentations

- CH 3** **Johnny Tam**, Kavita P. Dhamdhere, Pavan Tiruveedhula, Silvestre Manzanera, Shirin Barez, Marcus A. Bearse, Jr., Anthony J. Adams, and Austin Roorda, “Noninvasive assessment of parafoveal capillaries in Type 2 diabetes prior to onset of diabetic retinopathy,” *Association for Research in Vision and Ophthalmology (ARVO)*, Fort Lauderdale, FL, May 2011, *oral presentation*
- CH 3** **Johnny Tam**, Kavita Dhamdhere, Brandon Lujan, Pavan Tiruveedhula, Robert N. Johnson, Wendy W. Harrison, Glen Y. Ozawa, Anthony J. Adams, Austin Roorda, “Noninvasive Assessment of Photoreceptors, Capillaries, and Leukocytes for Early Stages of Diabetic Retinopathy,” *Diabetes Technology Meeting*, Bethesda, MD, Nov 2010 (**Juvenile Diabetes Research Foundation Bronze Award**), *poster presentation*

-
- CH 2** **Johnny Tam**, Pavan Tiruveedhula, Austin Roorda, “Leukocyte dynamics in parafoveal capillaries using AOSLO,” ARVO, Fort Lauderdale, FL, May 2010, *poster presentation*
- CH 1** **Johnny Tam** and Austin Roorda, “Visualization and analysis of perfused vessels using AOSLO,” Oral Presentation, ARVO, Fort Lauderdale, FL, May 2009 (**National Eye Institute Travel Grant**), *oral presentation*

ABSTRACT OF THE DISSERTATION

VISUALIZATION AND ANALYSIS OF HUMAN PARAFOVEAL CAPILLARIES
USING MOTION CONTRAST ENHANCEMENT ON ADAPTIVE OPTICS
SCANNING LASER OPHTHALMOSCOPY VIDEOS

by

Johnny Tam

Doctor of Philosophy in Bioengineering

University of California, San Francisco and University of California, Berkeley, 2011

Professor Austin Roorda, Chair

The eye provides a window through which a complete vascular system of arteries, capillaries, and veins can be directly observed. An adaptive optics scanning laser ophthalmoscope (AOSLO), a custom-built optical microscope for the living human eye, can be used to directly acquire videos of blood flow through the smallest capillaries in the eye. However, in the absence of invasive contrast agents, the contrast of blood cells and capillaries is very low. Moreover, it is difficult to determine the locations of all capillaries, and therefore tracking and speed quantification of blood cells is hindered. In human eyes, contrast agents such as fluorescein are routinely used only in the later stages of certain diseases; as with any invasive procedure, there is also a risk for adverse

side effects. Instead of injected contrast agents, we used intrinsic signals from moving blood cells to create contrast. By applying custom motion contrast enhancement methods to AOSLO videos, we were able to noninvasively visualize complete capillary networks as well as characterize hemodynamics through the capillaries in the eye. We investigate capillaries in healthy and diseased eyes, and show that the flow dynamics of leukocytes and plasma gaps are heterogeneously distributed, with certain capillaries accounting for a clear majority of leukocyte traffic, and other capillaries primarily featuring plasma gap flow. Such capillaries may serve specific functional roles, such as to prevent inactivated leukocytes from entering exchange capillaries, or to serve as relief valves to minimize flow disruption due to the presence of a leukocyte in a neighboring capillary. In diabetes, we found evidence of capillary remodeling even before conventional clinical methods detected any changes. We establish that motion signals can be used to generate intrinsic contrast for visualization and analysis of capillaries and blood cells. These methods are important for evaluating diseases that affect the microcirculation, such as diabetes.

TABLE OF CONTENTS

Acknowledgments	iii
Abstract	viii
Table of Contents	x
List of Tables	xii
List of Figures.....	xiii
Chapter 1: Vessel Perfusion Mapping	1
1.1 Abstract	1
1.2 Introduction	2
1.3 Materials and Methods	10
1.4 Results	35
1.5 Discussion	44
1.6 Acknowledgments	50
Chapter 2: Hemodynamics.....	51
2.1 Abstract	51
2.2 Introduction	52
2.3 Materials and Methods	58

2.4 Results	86
2.5 Discussion	114
2.6 Acknowledgments	123
Chapter 3: Capillaries in Early-Stage Diabetic Retinopathy	124
3.1 Abstract	124
3.2 Introduction	125
3.3 Materials and Methods	131
3.4 Results	148
3.5 Discussion	173
3.6 Acknowledgments	186
Chapter 4: Conclusions	188
4.1 Summary of Findings	188
4.2 Future Directions	190
4.3 Acknowledgments	246
References	247

LIST OF TABLES

Table 1.1: Comparison of FAZ sizes to other studies.....	38
Table 2.1: Imaging Parameters	60
Table 2.2: Virtual AOSLO Parameters.....	78
Table 2.3: Parameters for simulated videos.....	80
Table 2.4: Evaluation of speed quantification	92
Table 2.5: Summary of cell speeds.....	100
Table 3.1: Longitudinal study visit information	133
Table 3.2: Subject characteristics	141
Table 4.1: Evaluation of study metrics in NPDR	202

LIST OF FIGURES

Figure 1.1: AOSLO images without contrast enhancement	9
Figure 1.2: Desinusoiding artifact.....	13
Figure 1.3: Vessel perfusion mapping steps	16
Figure 1.4: Arithmetic vs. Geometric SD	17
Figure 1.5: Effect of the number of frames.....	20
Figure 1.6: Effect of filter size.....	21
Figure 1.7: Focus and vessel appearance.....	24
Figure 1.8: Effect of defocus on apparent vessel diameter	25
Figure 1.9: Semi-automated vessel extraction procedure	27
Figure 1.10: Example of FAZ extraction.....	28
Figure 1.11: Automated algorithm for ROI extraction	32
Figure 1.12: Extraction of capillaries in the ROI.....	33
Figure 1.13: Montage of parafoveal capillaries	36
Figure 1.14: Montage of the capillary network	37
Figure 1.15: Extracted capillaries	39
Figure 1.16: Capillary density in four directions.....	40
Figure 1.17: Comparison to FA	41
Figure 1.18: Comparison to FA and RFI	42
Figure 1.19: Repeatability of montages.....	43
Figure 1.20: Motion contrast enhancement simulation.....	47
Figure 1.21: Sources of artifacts	48
Figure 2.1: Raster scan problem formulation	57
Figure 2.2: AOSLO video frames before contrast enhancement.....	61

Figure 2.3: Visualization of vessels and moving objects.....	64
Figure 2.4: Conversion of Xyt coordinate system into st coordinate system	68
Figure 2.5: Single trace before and after motion contrast enhancement.....	70
Figure 2.6: Generation of motion-contrast enhanced ST plots	71
Figure 2.7: Overview of virtual AOSLO	77
Figure 2.8: Pulse blips and spatiotemporal plots	85
Figure 2.9: Expected raster scan error	89
Figure 2.10: Tracking and speed quantification on V1_EM.....	91
Figure 2.11: Effect of correction on extracted traces.....	97
Figure 2.12: Tracked objects.....	100
Figure 2.13: Montage of parafoveal capillary network	102
Figure 2.14: Comparison of AOSLO with red free fundus photography	103
Figure 2.15: Interpretation of traces on ST plots	108
Figure 2.16: Identification of LPPs and PGCs.....	109
Figure 2.17: Spatial distribution of LPPs and PGCs.....	110
Figure 2.18: Examples of velocity waveforms	113
Figure 2.19: Defocus and ST Plots	120
Figure 3.1: AOSLO images from a single video	130
Figure 3.2: Example of AOSLO imaging.....	138
Figure 3.3: Identification of AV channels	143
Figure 3.4: Comparison of AOSLO imaging to color fundus photography	150
Figure 3.5: Comparison of AOSLO imaging to fluorescein angiography.....	151
Figure 3.6: Capillary dropout at the edge of the FAZ.....	154
Figure 3.7: Extracted FAZs for size quantification	155

Figure 3.8: Microaneurysms and intraretinal microvascular abnormalities	156
Figure 3.9: Capillary bends.....	157
Figure 3.10: Subclinical capillary dropout.....	159
Figure 3.11: Longitudinal tracking of LPPs	161
Figure 3.12: Measurements of leukocyte speed in LPPs	162
Figure 3.13: Assessment of cone photoreceptors	164
Figure 3.14: Examples of parafoveal montages.....	167
Figure 3.15: Capillary abnormalities	168
Figure 3.16: AV channels	169
Figure 3.17: Extracted FAZs.....	170
Figure 3.18: Extracted capillaries	171
Figure 3.19: Boxplots of study metrics.....	172
Figure 3.20: Cross-sectional study hypothesis	179
Figure 4.1: Variation in leukocyte speed along a vessel.....	194
Figure 4.2: AOSLO video locations and the mfERG grid.....	196
Figure 4.3: Comparison of neural and vascular abnormalities	198
Figure 4.4: AV channels in NPDR	201
Figure 4.5: Two vessel planes in MacTel	204
Figure 4.6: MacTel example	205
Figure 4.7: Retinal Vein Occlusion	207
Figure 4.8: Age-related Macular Degeneration	209
Figure 4.9: Vessel crossings	212
Figure 4.10: Special case of two leukocytes.....	214
Figure 4.11: Capillary flow regimes	222

Figure 4.12: Selection of a capillary for microhemodynamics.....	227
Figure 4.13: Example of capillary segment	228
Figure 4.14: Automated cell path extraction.....	234
Figure 4.15: Errors of automated extraction.....	235
Figure 4.16: Automated extraction results on alternate data set.....	236
Figure 4.17: Weaving process to generate 60 Hz videos.....	238
Figure 4.18: Video cropping strategy	240
Figure 4.19: Twitching.....	244

CHAPTER 1

VESSEL PERFUSION MAPPING

1.1 Abstract

The retina is one of the most metabolically active tissues in the human body, and as such, is coupled with a unique system of blood vessels. These blood vessels are an important marker of retinal health. Although there are many imaging methods to visualize and assess the larger arterioles and venules in live human subjects, few methods address visualization and assessment of the capillary network. This is largely because capillaries have very low contrast under most imaging conditions, particularly when no contrast agents are administered. In this chapter, we demonstrate a noninvasive method to visualize and analyze the parafoveal capillary network in humans, using an adaptive optics scanning laser ophthalmoscope, a custom-built confocal microscope designed for the living human eye. We optimized imaging parameters for vascular imaging and developed custom video and image processing tools to enhance motion contrast. Motion contrast methods were applied to visualize capillaries from 10 subjects with clear ocular media and no history of prior ocular or systemic disease. The resulting images compared well to fluorescein angiography, the gold standard for visualizing human retinal capillaries. The average area of the foveal avascular zone was 0.323 mm^2 , corresponding to an average effective diameter of $633 \text{ }\mu\text{m}$. There was no variation in capillary density in the region immediately outside of the foveal avascular zone, when considering superior, inferior, temporal, and nasal directions. These results show that

motion contrast enhancement combined with adaptive optics scanning laser ophthalmoscopy can be used to unambiguously visualize and analyze the parafoveal capillary network, without the need for injection of invasive contrast dyes.

1.2 Introduction

The retina is one of the most metabolically active tissues in the human body, and as such, is coupled with a unique system of blood vessels. One of the most striking features of the inner retinal blood vessels is the presence of a large avascular zone, called the foveal avascular zone (FAZ). Specialized photoreceptors called foveal cones reside inside the FAZ. These cones are responsible for central vision, and are necessary for fine visual tasks such as reading. It is believed that the FAZ exists in order to provide these foveal cones with an unobstructed view of the exterior world. In regions of the retina outside of the FAZ, retinal vessels sit in front of the photoreceptors. Such vessels can absorb or scatter incoming light, diminishing the final number of photons which reach the photoreceptors. Thus, the FAZ serves as a vascular window through which the foveal cones can gather incoming light.

Since the inner retinal vessels reside in front of the photoreceptors, it is sometimes possible to observe in one's own vision several interesting phenomena. First, it is possible to see shadows of retinal vessels in a phenomenon known as "Purkinje's figures," first described without explanation by Johannes Purkinje (1787-1869), and subsequently interpreted by Heinrich Müller (1820-1864) (Polyak 1957). One can observe this phenomenon in a dark room by shining a light towards the retina, and then slowly moving

the head or the eye in a constant speed, thereby generating an image of the shadows of the vasculature on the retina. Second, it is possible to observe a rapid but transient movement of tiny bright objects through the retinal circulation in a phenomenon known as the “blue field entoptic phenomenon,” described as early as 1860 by Karl von Vierordt (Riva and Petrig 1980; Sinclair, Azar-Cavanagh et al. 1989). The accepted explanation for this phenomenon is that moving objects correspond to leukocytes in small retinal capillaries (Sinclair, Azar-Cavanagh et al. 1989). With practice, one can observe this phenomenon by staring at any bright uniform background, such as the sky. A third phenomenon allows one to visualize his or her own FAZ by looking through a pinhole at a bright background, and wiggling the pinhole around. All three phenomena are based on the movement of some object relative to the photoreceptors, since any object that casts a perfectly static image on the underlying photoreceptors will disappear (this is the reason why blood vessels are invisible under normal viewing conditions, despite the fact that the vessels sit in front of the photoreceptors) (Ditchburn 1987). In the first case, the movement of a high contrast shadow of the blood vessels relative to the photoreceptors enables one to observe the vasculature; in the second case, the movement of low contrast leukocytes through capillaries enables one to observe patterns of flow. Interestingly, with specialized instrumentation and proper training, one might even be able to use the entoptic phenomenon to observe one’s own lesions, such as microaneurysms due to diabetic retinopathy (Applegate, Bradley et al. 1997); however, direct and objective measurements are not possible. Until recently, the only noninvasive methods to identify and investigate the FAZ were based on these phenomena.

The FAZ is an important indicator of foveal health in a number of different diseases, including diabetic retinopathy (Mansour, Schachat et al. 1993; Sander, Larsen et al. 1994; Conrath, Giorgi et al. 2005), sickle-cell disease (Sanders, Brown et al. 1991), branch retinal vein occlusion (Parodi, Visintin et al. 1995), and retinopathy-of-prematurity (Mintz-Hittner, Knight-Nanan et al. 1999). Functionally, the capillaries at the edge of the FAZ supply a transition zone in the retina where the retina begins to become too thick to be supplied by the underlying choroidal blood supply. The choroid is a system of blood vessels residing behind the photoreceptors, extending over the entire area of the retina. The central fovea is the only portion of the retina that is thin enough (about 0.2 mm) to be nourished by only the choroid; in all other portions of the retina, the retina is thicker (about 0.5 mm), and inner retinal vessels are needed to supply the inner portions of the retina. The limit of 0.2 mm corresponds approximately to the maximum tissue thickness through which nutrients from the choroid can effectively nourish the retina (Buttery, Hinrichsen et al. 1991), especially when considering that the eye is normally under pressure, which limits the effective distance over which nutrients from the choroid are able to freely diffuse. While the photoreceptors receive their nutrients primarily from the choroid, it appears that the inner retinal capillaries near the FAZ primarily nourish the beginnings of the ganglion cell layer (Iwasaki and Inomata 1986). Therefore, although there are two systems of blood vessels that supply the retina, the two systems are not redundant, since different layers are nourished by different systems of blood vessels. This makes the retina doubly vulnerable to any disease that affects the vasculature. More importantly, disruption of the FAZ could indicate damage to the foveal region. Although the foveal region comprises less than 4% of the total retinal area in humans, it is a highly

specialized area that accounts for an estimated 25% of the total ganglion cell output to the brain (Provis, Penfold et al. 2005). Therefore, it is vital that all of the vasculature which surrounds the fovea remain healthy.

In order to appreciate the pathological changes that manifest in the FAZ during disease, it is important to consider the development of the FAZ. Until recently, there has been very little data about the development of the FAZ in humans. A common assumption was that the fovea was fully vascularized prior to birth, with subsequent apoptotic pruning resulting in the formation of a FAZ. This hypothesis was based on observations of a condition known as retinopathy of prematurity, in which the FAZ appears to be small or entirely absent in babies born prematurely (Mintz-Hittner, Knight-Nanan et al. 1999). Although a subsequent histological study based on monkeys and cats seemed to confirm that this was the case (Henkind, Bellhorn et al. 1975), more recently, evidence has been presented that suggests that the foveal zone is avascular throughout the developmental cycle (Provis and Hendrickson 2008). Knowledge of this controversy is important in evaluating strategies for treatment of diseases affecting the FAZ, since there are often parallel processes that occur in development and aging.

Histological studies, which are restricted to evaluation of animals and post-mortem humans, provide a limited picture of the role of the parafoveal capillaries in disease. With this limitation in mind, there have been two impressive histological studies, which have defined the structure and topology of the “normal” primate and human parafoveal capillaries. Using excised monkey retinas, the inner retinal microvasculature that surrounds the FAZ has been mapped out in detail (Snodderly, Weinhaus et al. 1992). Far from the fovea, the capillary network is multi-layered; closer to the fovea, the network

thins down, first to two layers of capillaries in the peri- to parafoveal region, and then to one layer in the parafoveal region closest to the foveal center. As the capillary layers thin down, the deep layers are the first to disappear. Thus, in the fovea, where there are no vessels, the FAZ is formed by what would have been the most superficial layer of the capillary network. These observations have been confirmed in humans (Yu, Balaratnasingam et al. 2010). Although these studies are highly detailed, it is important to remember that the idea of a normal FAZ is an idealized concept, because in fact there is considerable individual variation in the size and appearance of the FAZ (Bird and Weale 1974; Laatikainen and Larinkari 1977). Normal variation in the parafoveal capillaries could easily be misinterpreted as pathological signs.

There are clear advantages to developing in vivo methods to directly visualize and assess the human FAZ and parafoveal capillaries. First, the human vasculature is unique. The presence of a dual blood supply and an FAZ is a unique feature of primates, which makes it difficult to develop disease models for macular diseases; even when comparing rhesus monkeys to humans, the natural progression of diabetic retinopathy has subtle differences (Kim, Johnson et al. 2004). Second, methods to assess the FAZ may lead to new insights about the progression of diseases such as diabetic retinopathy (Arend, Wolf et al. 1991). To this end, fluorescein angiography (FA), the gold standard for in vivo visualization of human retinal capillaries, is useful for evaluating the later stages of certain diseases. However, even FA has its limitations, which include the observation that it is difficult to assess the deeper capillaries using FA (Weinhaus, Burke et al. 1995). This deep layer of capillaries is sparser than the superficial layer (Yu, Balaratnasingam et al. 2010), but both layers can contribute to disease. This suggests that the modern clinical

understanding of retinal capillaries is largely an understanding of the superficial capillary layer, with little knowledge about the deeper layers of capillaries. Moreover, as with any invasive procedure, FA is associated with a small risk for adverse side effects (Kwan 2006), making it an undesirable method to perform unless there is a clear clinical benefit to be reaped. To further elucidate fine vascular structures in disease, a better noninvasive method for imaging live human parafoveal capillaries is needed.

In the past few decades, there have been many different technologies that have been introduced for noninvasive imaging of the parafoveal capillaries. Excluding methods based on adaptive optics, the two most promising methods are based on optical coherence tomography (OCT) and fundus photography. Using high-speed OCT combined with a phase variance technique, a 3D image of the human retinal parafoveal capillaries can be generated (Kim, Fingler et al. 2011). The key advantages of this technique are the speed of data acquisition (3.6 seconds for a 3x3 square millimeter field of view), and the ability to generate 3D data; key limitations are low signal to noise ratios when considering the smallest capillaries in the retina. The retinal function imager (RFI) is a method based on rapidly capturing 8 consecutive fundus photographs of the human eye (Nelson, Krupsky et al. 2005). The key advantages are the speed of data acquisition (140 milliseconds) and the ability to generate large field-of-view images of the vasculature; key limitations are patient comfort (very bright flashes of green light) and difficulty in capturing the smallest capillaries. Thus far, there have been no in vivo approaches which have replicated the histological detail with which capillaries can be visualized. Furthermore, excluding methods based on adaptive optics, current systems for noninvasive imaging of retinal capillaries are all limited by ocular aberrations and low image contrast of capillaries.

There are two key challenges that must be addressed to successfully image the retinal microcirculation: aberrations in the eye, and low capillary contrast. Aberrations in the eye may hinder the resolution of the smallest capillaries (i.e. those with diameter $\sim 5 \mu\text{m}$), for any imaging system employing conventional optics, such as conventional FA, as well as any system based on conventional fundus photography. Aberrations can be corrected using Adaptive Optics (Liang 1997). Recently, an Adaptive Optics Scanning Laser Ophthalmoscope (AOSLO) was used to quantify leukocyte speeds through parafoveal capillaries (Roorda, Romero-Borja et al. 2002; Martin 2005). These methods were based on human identification of leukocytes and capillaries, which is a difficult task due to low contrast (**Figure 1.1**). Contrast is typically improved using a contrast agent, such as in FA. However, contrast agents cannot be used if one wants to design a noninvasive imaging system. An alternate method to improve capillary contrast is to use video processing tools based on flow visualization (Japee, Ellis et al. 2004). These tools included mean, variance, min, max, range, and transition images. The variance image has been previously applied as a method for increasing vessel contrast in microvessels prior to applying leukocyte tracking algorithms (Sato 1997). However, when AOSLO videos are processed using these flow visualization tools, the contrast of the vessels actually decreases. Moreover, all these methods assume access to the retinal capillaries, without consideration of optical aberrations.

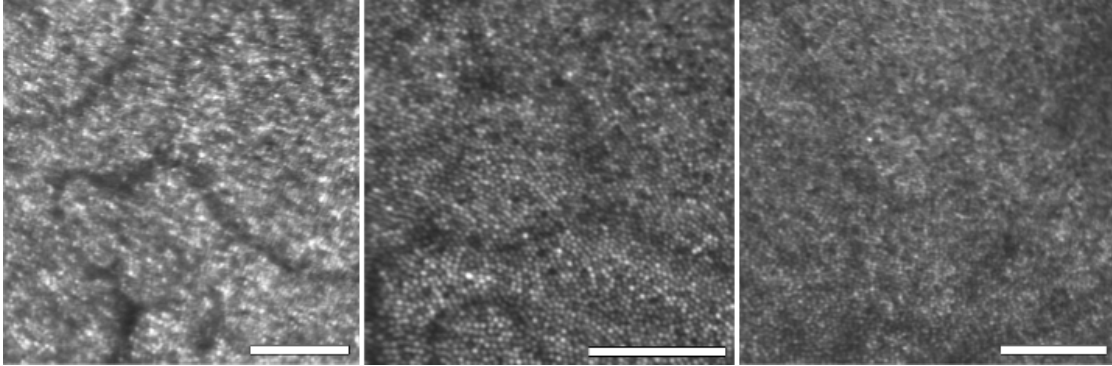


Figure 1.1: Examples of unprocessed AOSLO images of retinal capillaries, acquired on three different human subjects using light sources with 532 nm wavelengths (left) and 840 nm wavelengths (middle and right). Dark, fuzzy lines usually correspond to capillaries. However, while some capillaries can be seen, it is very difficult to precisely locate all capillary paths. Scale bars, 100 μm .

In this chapter, we will describe novel video and image processing tools for AOSLO imaging to demonstrate an improved method that can detect even the smallest capillaries in the parafoveal region without the use of injected dyes. We use these methods to generate highly detailed, noninvasive images of the FAZ and surrounding capillaries in live human subjects. The methods developed in this chapter form the foundation for studies of hemodynamics and diabetic retinopathy in the remainder of the dissertation.

1.3 Materials and Methods

Image acquisition

All procedures performed in this study adhered to the tenets of the Declaration of Helsinki. After a detailed explanation of the procedures, written informed consent was obtained from all participants. The research protocol was approved by the University of California, Berkeley Committee for Protection of Human Subjects. Videos were acquired on human subjects as described previously (Martin 2005), using a variety of imaging parameters. Briefly, videos were acquired at 512×512 pixels², 30 or 60 fps, for 5 to 40 seconds in overlapping windows in the parafoveal region. The field of view ranged from 1.2 to 2.5 deg. The imaging wavelength was either 532 nm or 840 nm.

Ten subjects with clear ocular media and no history of prior ocular or systemic disease were used. For each subject, a total of 20 to 78 videos were collected. The average age of the subjects was 27 with a standard deviation of 6.4.

Video Preprocessing

Raw videos were preprocessed to correct for distortions due to raster scanning and eye motion. Preprocessing involves desinusoiding, cropping, and frame deletion.

Desinusoiding and stabilization

To achieve high line density and high frame rates, the AOSLO employs a resonant scanner combined with a sensor that reads in data at a constant rate. The velocity of the scanner varies sinusoidally across each scan line, which results in a horizontal distortion in the raw videos. Desinusoiding corrects this distortion, which is characterized from videos of calibration grids. The velocity of the scanner is slowest at the left and right edges of the frame, and fastest in the middle; thus, there are more pixels per retinal area towards the edges compared to the center. The redistribution of pixels can result in a desinusoiding artifact due to a change in the distribution of noise (**Figure 1.2**). We minimized this artifact using median and Gaussian filtering.

Stabilization is the process that corrects for the distortions due to eye motion that occur during acquisition of each raster-scanned frame. Detailed procedures for desinusoiding and stabilization can be found elsewhere (Vogel 2006; Arathorn, Yang et al. 2007). Briefly, the task involves splitting each frame in a video into a set of horizontal strips, each of which is registered using affine transformations to a desinusoided reference frame and reassembled using linear interpolation. The result is a desinusoided and stabilized video.

Cropping the video

Due to eye motion, there are regions of the retina that are not present in all video frames, particularly at the edges of each frame. To account for this, the desinusoiding and stabilization process introduces borders around each frame so that each registered frame will be of the same size. The thickness of each border changes according to the eye motion. We cropped the videos such that each frame contains only the portion of the video that was visible in the majority of all frames, thereby eliminating the black borders.

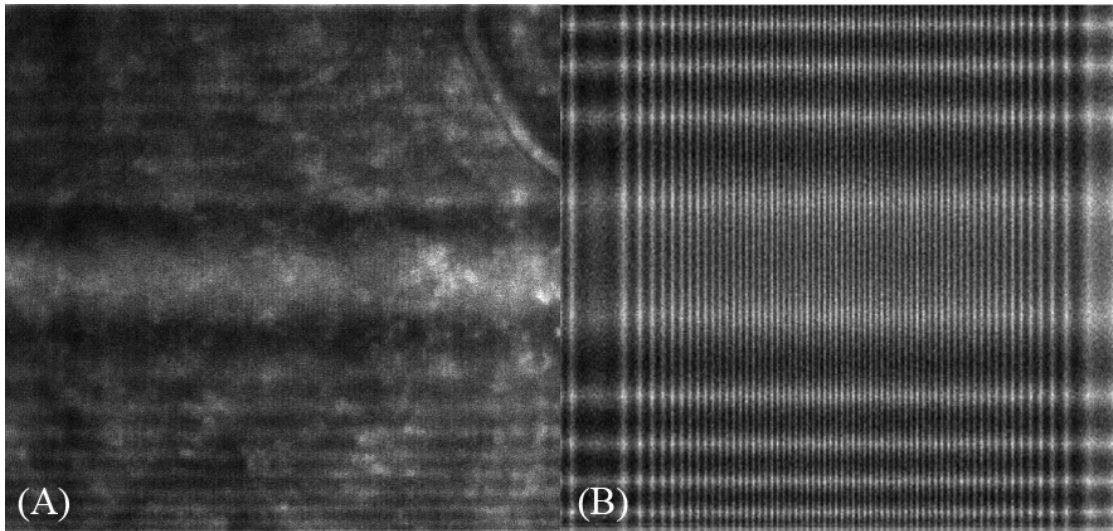


Figure 1.2: Desinusoiding artifact that is commonly observed in raster scanning systems when the SNR is low. (A) An AOSLO video with a very low signal-to-noise ratio (SNR) acquired using a 532 nm wavelength laser. When the variance image of the video is calculated to determine regions of high intensity fluctuations, the resulting artifact that appears is shown. (B) The source of the artifact is due to a redistribution of SNR, as demonstrated using a model video. A model video of uniform Gaussian noise was desinusoided, and then the standard deviation of the desinusoided video was calculated, resulting in the image shown. Uniform noise is redistributed by the desinusoiding process, resulting in bright bands of higher noise. It is important to apply proper filtering to the videos in order to eliminate this artifact.

Frame deletion

In the processed videos, there were four types of improper frames that were identified for deletion. First, insufficient overlap between the image and the reference frame resulted in poor stabilization. This occurred when the eye wandered too far away from its fixation target. Second, blinks resulted in the image intensity dropping to zero throughout the blink. Third, large saccades, involuntary fast eye movements, caused intraframe shearing and distortion on single frames and prevented proper image stabilization. Fourth, frames where image quality was poor, due to uncorrected high frequency tear film induced aberrations, were also deleted.

Motion Contrast Enhancement

When viewing individual AOSLO video frames, one can see that vessel contrast disappears in the presence of leukocytes (**Figure 1.3**). The intensity variations of pixels in vessel regions are similar in magnitude to intensity variations of pixels near photoreceptor boundaries. Our strategy is first, to enhance the contrast of individual fluid parcels, and second, to apply flow visualization tools to the locally enhanced videos.

It is possible to see individual flow parcels traveling through capillaries (**Figure 1.3**). We introduce the concept of multi-frame division videos. Division videos are similar in concept to difference videos, except that instead of subtracting, individual pixels are divided by each other. A division image, $D(x,y)$, is calculated from each pair of consecutive frames as $D_j(x,y) = I_j(x,y) / I_{j+1}(x,y)$, where $I_j(x,y)$ represents the intensities of frame j . Division images are used instead of difference images to enable arithmetic averaging of multiple frames, which improves the signal to noise ratio, as

opposed to using the arithmetic average of two consecutive difference images, which yields no improvement in signal to noise (Tam and Roorda 2010). Consecutive division images are averaged together to create a multi-frame division image, $M_j(x,y) = [D_j(x,y) + D_{j+1}(x,y)] / 2$, with high contrast ratios between the fluid parcels and the background tissue. M_j gives the j th frame of the multi-frame division video.

Finally, the capillaries are visualized by collapsing the multi-frame division video down to a single image (subsequently referred to as the vessel perfusion image). This is done by calculating the standard deviation image of the multi-frame division video. The standard deviation image $S(x,y)$ can be calculated using either arithmetic or geometric definitions. The arithmetic definitions are given by:

$$S(x,y) = \sqrt{\frac{1}{n-1} \sum_{j=1}^n (M_j(x,y) - \overline{M}(x,y))^2};$$

$$\overline{M}(x,y) = \frac{1}{n} \sum_{j=1}^n M_j(x,y) \tag{1}$$

The geometric definitions are given by:

$$S(x,y) = \exp\left(\sqrt{\frac{\sum_{j=1}^n [\ln M_j(x,y) - \ln \overline{M}(x,y)]^2}{n-1}}\right);$$

$$\overline{M}(x,y) = \sqrt[n]{\prod_{j=1}^n M_j} \tag{2}$$

In both cases n is the total number of frames.

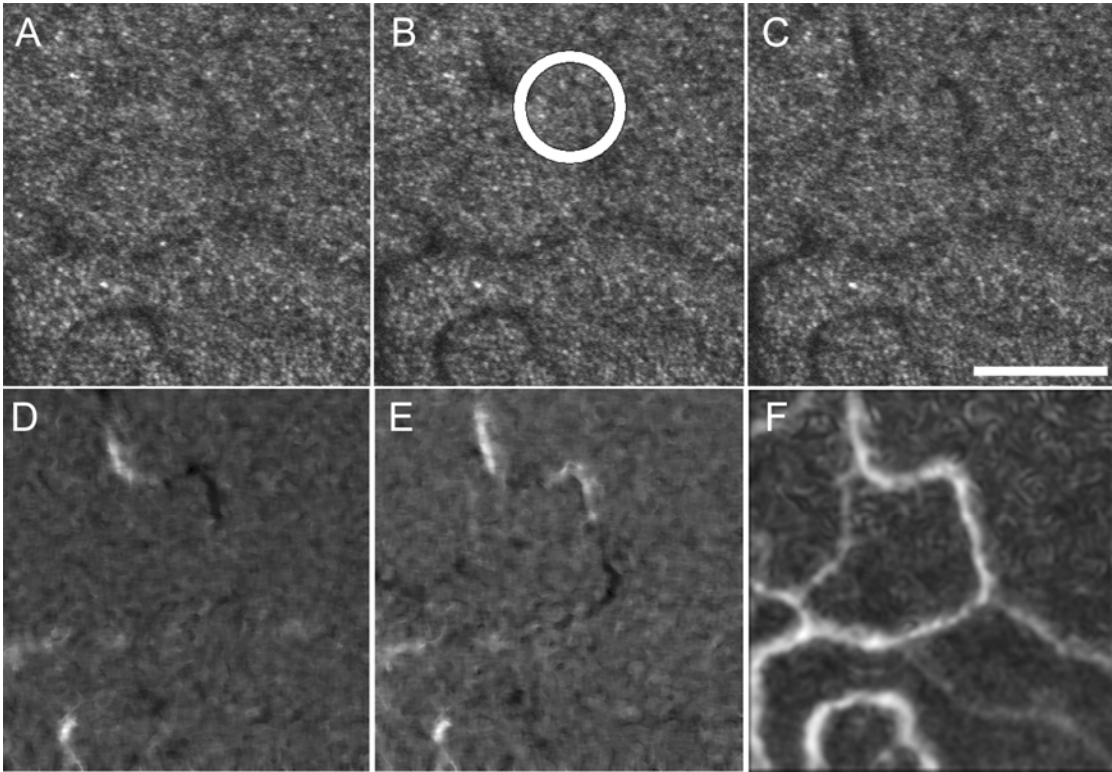


Figure 1.3: High resolution images of the human retina, acquired noninvasively using an 840 nm laser. The video and image processing steps are illustrated. **(A, B, C)** Three consecutive frames from an unprocessed video. Individual photoreceptors can be seen as small dots. However, it is difficult to distinguish the locations of vessels and of individual leukocytes (one leukocyte is shown inside the circle). Scale bar, 100 μm . **(D)** The first step in motion contrast enhancement is the division image, $D_j(x,y)$; **(E)** An averaged division image, $M_j(x,y)$; **(F)** The highlighted image, $S(x,y)$, showing perfused vessels.

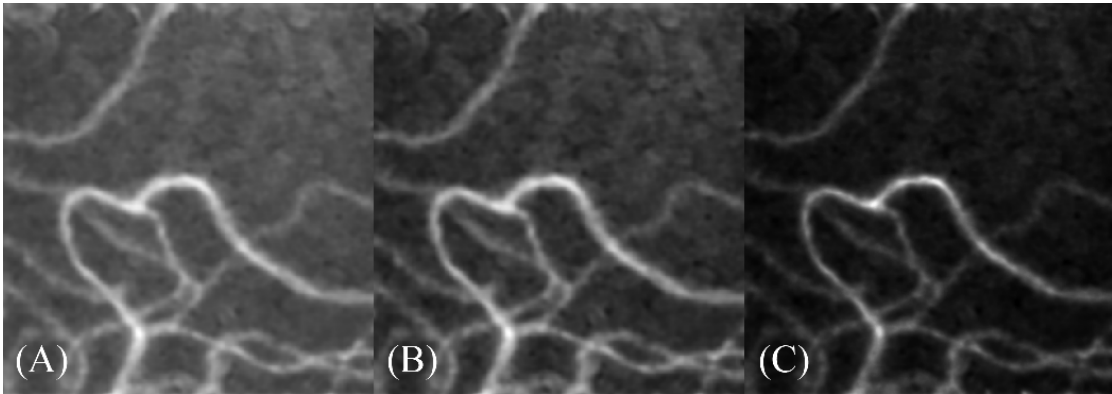


Figure 1.4: Successive improvements in image quality, demonstrated using a video acquired using a 532 nm wavelength laser, from the same video as shown in **Figure 1.1A** (A) Vessel perfusion image before frame deletion, using the arithmetic definition of standard deviation. (B) Vessel perfusion image after frame deletion, using the arithmetic definition of standard deviation. (C) Vessel perfusion image after frame deletion, using the geometric definition of standard deviation. This demonstrates that frame deletion and use of the geometric definition of standard deviation can result in improved image quality.

We used both arithmetic and geometric definitions. The arithmetic definitions were more robust against noise as well as errors in stabilization, and could be used for general cases, while the geometric definitions gave higher quality results, but required excellent stabilization. The subtle improvement in the quality of the vessel perfusion image is shown in **Figure 1.4**.

There is also an advantage to using multiple frames in the calculation of the division video. Multi-frame division videos improve the signal-to-noise ratio (SNR) through signal averaging. Consider three frames from a video with noise, I_j , I_{j+1} , and I_{j+2} . A conventional difference image is given by $I_j - I_{j+1}$. The average of consecutive difference images, $(I_j - I_{j+1} + I_{j+1} - I_{j+2}) / 2$ yields the expression $I_j - I_{j+2}$, which is not an improvement over the single frame difference image. However, using division images, defined as $D_j = I_j / I_{j+1}$, we can define a multi-frame division image as $M_j = (D_j + D_{j+1}) / 2$. Assuming that there is a constant background in the images (consisting of all static features), the background can be defined as $B_j = \{(x,y) \mid D_j(x,y) = D_{j+1}(x,y) = I + \varepsilon\}$, where ε can be adjusted depending on the level of the noise. Suppose each image I_j has a noise component proportional to the signal intensity, $\eta_j I_j$, such that $I_j = I_j' + \eta_j I_j'$, where I_j' denotes the noise-free component of image intensities. Let $D_j' = I_j' / I_{j+1}'$ and $M_j' = (D_j' + D_{j+1}') / 2$, which are the ideal responses of the single and multi-frame division images in the absence of noise. For $(x,y) \in B_j$, let $N_j = D_j - D_j'$, which is the deviation from the ideal response, and the noise component of the single-frame division image. For the multi-frame division images, $M_j - M_j' = (N_j + N_{j+1}) / 2$. This shows that the noise is averaged in the background.

The number of high quality frames needed to generate a good quality image is about 300, corresponding to 10 high quality seconds of video at 30 Hz, or 5 high quality seconds of video at 60 Hz (**Figure 1.5**). While the use of additional frames does result in improved image quality, the improvement in image quality diminishes after about 600 frames.

Filter size is another important consideration. As it is important to apply filtering to minimize the desinusoidal artifact (**Figure 1.2**), and both Gaussian and median filtering were selected, the next parameter to adjust is the size of the filter window. Typically, filter windows are selected based on the size of the object of interest. The size of a photoreceptor is on the order of 2-5 μm in the parafovea; for a 1.5 degree field of view AOSLO video, this corresponds to approximately 2 to 6 pixels. Capillary diameters are on the order of 4 to 10 μm , corresponding to approximately 5 to 11 pixels. Therefore, to minimize the effect of intensity fluctuations due to photoreceptors, one should select a filter window of at least 5 pixels, but less than 11 pixels. We selected a window size of 10 pixels, which appeared to be the optimal size for motion contrast enhancement (**Figure 1.6**).

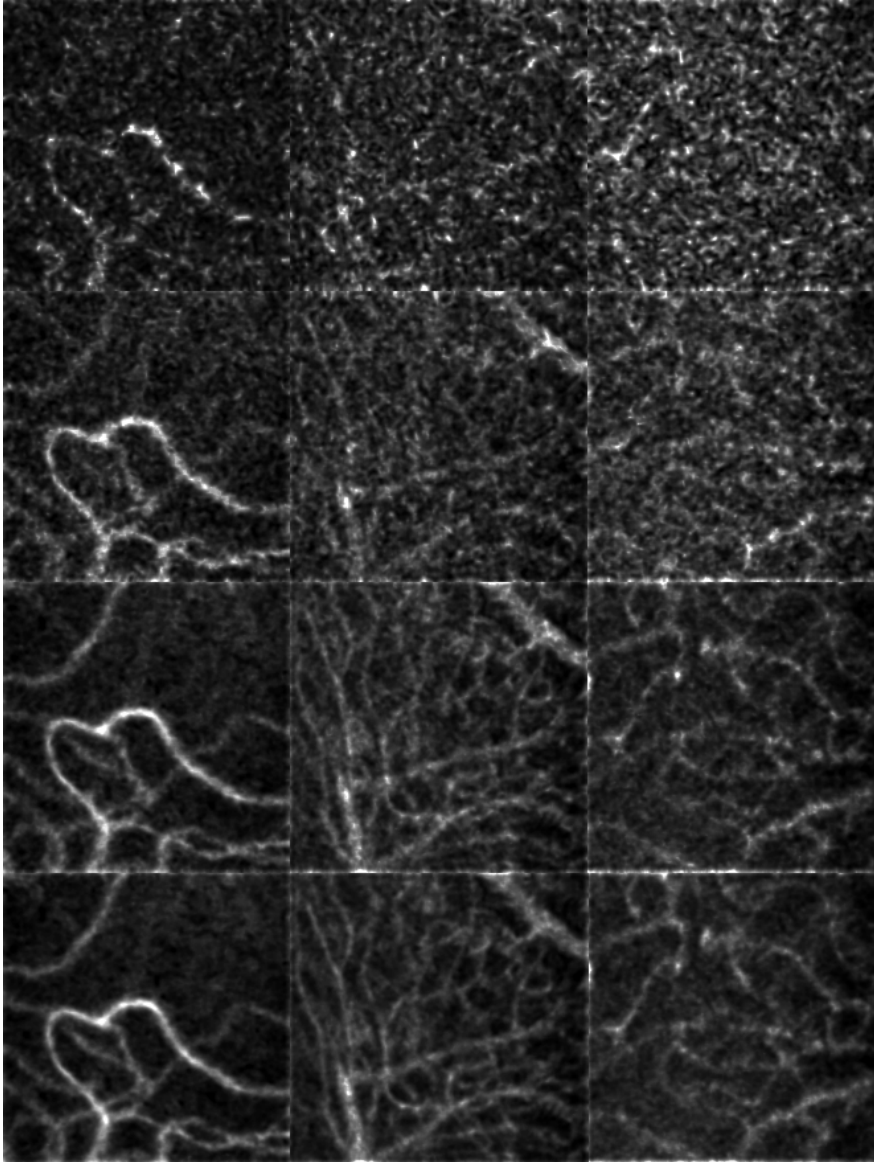


Figure 1.5: Effect of the number of frames on motion contrast images. Columns: one video acquired using a 532 nm laser (left column), and two videos acquired using an 840 nm laser (middle and right columns). Rows, from top to bottom: resulting motion contrast image using 15 frames, 75 frames, 300 frames, and 600 frames. A good quality image can be obtained using about 300 frames.

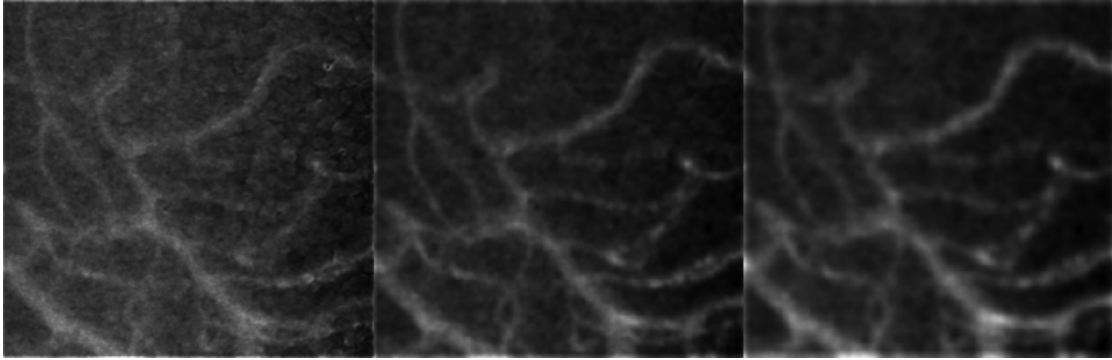


Figure 1.6: Effect of filter size on appearance of motion contrast enhancement, for an AOSLO video acquired using an 840 nm light source. From left to right, images with filter window sizes of 5, 10, and 15 pixels are shown. At 5 pixels, there is a spotty appearance due to the presence of photoreceptors. These spots are eliminated when using a window size of 10 pixels. At 15 pixels, some of the fine details of capillary features are lost. Thus, the optimal window size for a typical AOSLO video is 10 pixels.

Finally, it is important to select an appropriate plane of focus. Retinal capillaries reside anterior to the plane of focus of the photoreceptors. Although the capillary network is single-layered immediately outside of the FAZ, it is still possible for different capillaries to reside in different planes of focus. The appearance of capillaries is very different depending on the plane of focus (**Figure 1.7**). When the plane of focus is set to the capillary level, a bright vessel reflex appears along the centerline of the vessel, and a high density of particles can be seen traveling through the reflex region. The particles have brighter intensities than the background. When the plane of focus is set to the photoreceptor layer, capillaries are either equal in intensity or darker in intensity than the background tissue. This is likely due to small differences in the location of the capillary with respect to the plane of focus: capillaries on the anterior to the plane of focus would appear darker than capillaries closer to the plane of focus, as long as capillaries are not too far from the plane of focus to be imaged. However, although the spatial appearance of capillaries may change with different focal planes, the fact that there is visible motion through the capillaries does not change.

The diameter of the vessel also appears larger when out of focus, potentially complicating any attempts to measure vessel diameter (**Figure 1.8**). Specifically, diameter measurements may not be reliable unless the position of the vessel relative to the plane of focus is known or can be estimated. When the plane of focus is set near the photoreceptors, a high density of particles can no longer be seen in the capillaries. Instead, individual particles can occasionally be seen traveling through some, but not all of the capillaries. These particles have a very similar intensity compared to the background

tissue of photoreceptors. In AOSLO imaging, the plane of focus is controlled using a defocus parameter. Despite small variations in the appearance of capillaries in any given video, it is possible for motion contrast enhancement to identify aspects of capillaries which are in multiple planes of focus.

FAZ Quantification

Overlapping videos of the parafoveal region were used to generate a montage of the capillary network. To create montages, each video was analyzed separately, and then maps of highlighted images were pieced together using Adobe Photoshop (Adobe Systems, Inc.). Intensities were normalized by manually adjusting histogram levels as well as brightness and contrast. The vessel perfusion images were linked to their corresponding images of photoreceptors; this enabled accurate registration of vessel perfusion images, down to the level of individual photoreceptor cells. Finally, a Gaussian eraser was used to minimize the appearance of hard edges at regions of overlap. The effect of the Gaussian eraser can be seen by comparing **Figure 1.12** and **Figure 1.14**.

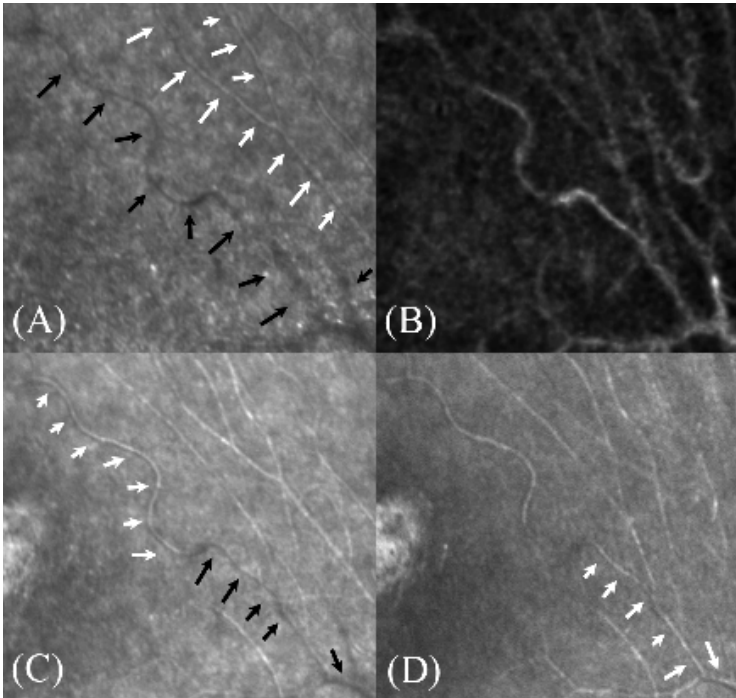


Figure 1.7: Plane of focus determines vessel appearance. (A,B) AOSLO image before and after motion contrast enhancement at a defocus of 0.1, on a 5.5 μm maximum stroke MEMs deformable mirror (Boston Micromachines, Cambridge, MA). This focal plane is posterior to one vessel and near a second vessel. Note that when the focal plane is posterior to the vessel, a dark shadow is seen (dark arrows), compared to a bright vessel reflex when focused at or near the vessel (bright arrows). Both planes of vessels are present in (B), albeit to different amounts. (C) Image taken with a defocus of 0.175, anterior to the plane of (A). One of the vessels resides in two different planes (bright and dark arrows). (D) Image taken at a defocus of 0.2, anterior to the plane of (C). The capillary segment from (C) is now in focus (bright arrows). If a capillary segment is too far from the plane of focus, then it will be completely absent from the image, unless there is some motion that can be seen.

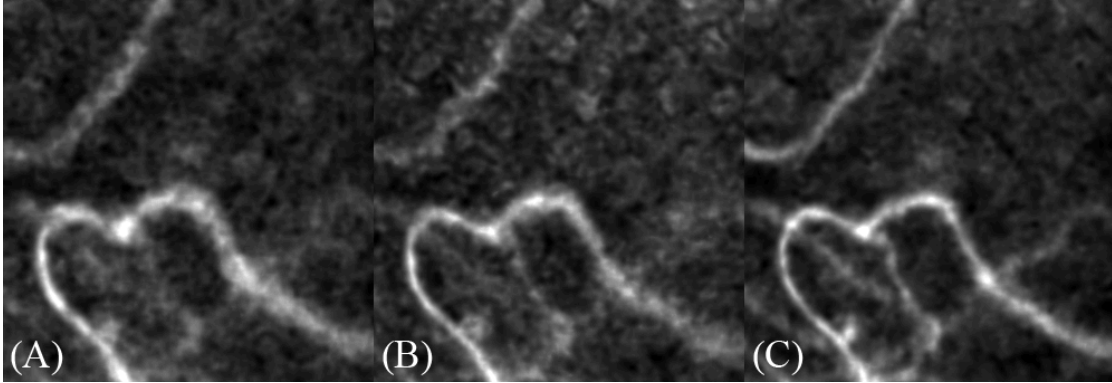


Figure 1.8: Effect of defocus on apparent vessel diameter. The same vessel, imaged at different focal planes. A defocus of (A) $-0.025D$, (B) $0D$, and (C) $+0.025D$ was applied using a $3\ \mu\text{m}$ maximum stroke MEMS deformable mirror (Boston Micromachines, Cambridge, MA). If a capillary is too far away from the plane of focus, it generates a very faint signal that could be misinterpreted as an artifact by the untrained observer. The focus level also changes the apparent diameter of the vessel. It is important to optimize the plane of focus during imaging to achieve the highest quality vessel perfusion image.

We applied custom image analysis tools to the montage of vessel perfusion images to analyze the FAZ. The FAZ boundary was defined as the centerline of the bordering vessels. To extract vessel centerlines, we used a semi-automated method based on the Frangi vesselness measure (Frangi, Niessen et al. 1998) (**Figure 1.9**), in the following manner. A closed contour, $C(t)$, was used to mathematically represent the FAZ boundary. First, through a graphical user interface, seed points, $p_i(x,y)$, were selected by the user at points near the boundary of the FAZ. Next, $p_i(x,y)$ were displaced toward the centerline of the nearest vessel in order to reduce variations due to user input. To identify vessel centerlines, we calculated the Frangi vesselness measure (Frangi, Niessen et al. 1998). A neighborhood, N_i , was generated around each $p_i(x,y)$. The vesselness values in N_i , denoted as V_i , were used to determine the location of the new point, $q_i(x,y)$, as $q_i(x,y) = \max(V_i)$. The amount of displacement from the seed point toward the centerline point was restricted by the size of the neighborhood around which to search. Finally, $C(t)$ was generated using piecewise Cardinal splines between neighboring pairs of $q_i(x,y)$, with the restriction that interpolation points needed to fall into the pixel space of the montage image. $C(t)$ was used to generate a mask of the FAZ for the area calculation (**Figure 1.10**).

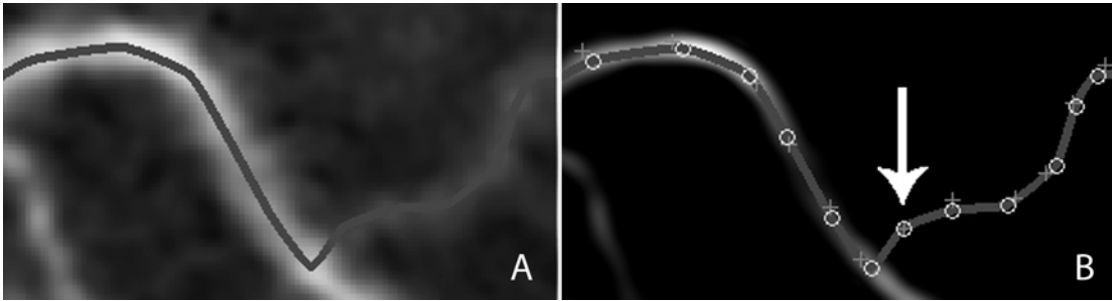


Figure 1.9: Vessels were extracted using a semi-automated procedure. **(A)** A piece of a highlighted image at the edge of the FAZ, showing a faint vessel segment connected to a bright vessel segment, with the extracted vessel overlaid as a thick gray line. **(B)** The Frangi vesselness measure is used to guide the vessel extraction, with seed points, $p_i(x,y)$, depicted as crosses, and displaced points, $q_i(x,y)$, depicted as circles. In areas where there is no information from the vesselness measure (arrow), no correction is applied.

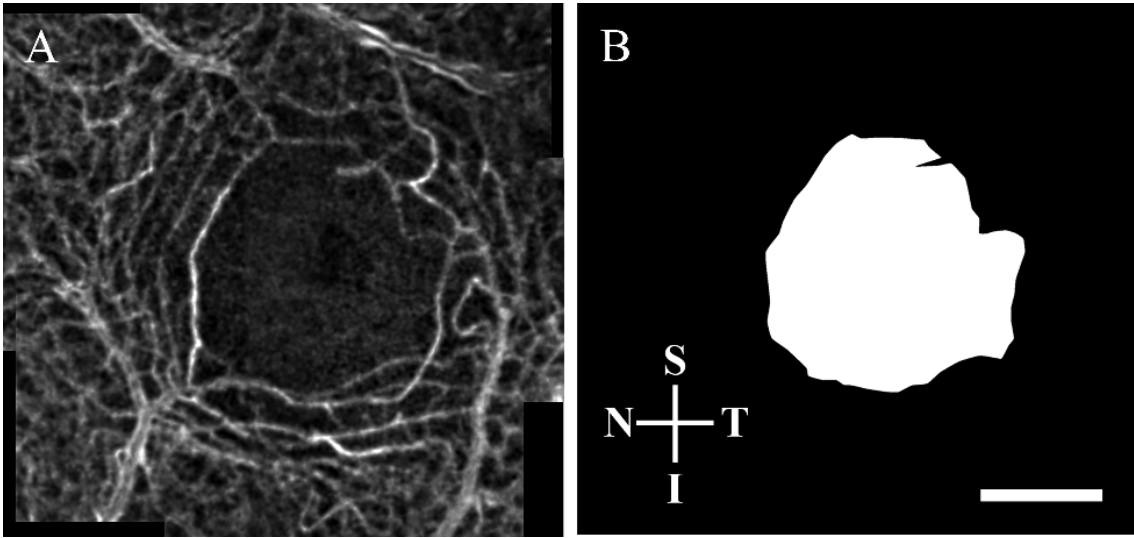


Figure 1.10: An example of FAZ extraction, from 532 nm videos. (A) Nine overlapping videos were separately processed and then compiled into a montage, showing parafoveal capillaries. (B) The FAZ was extracted and used for area quantification. Superior, Inferior, Nasal, and Temporal directions are labeled (S, I, N, T). Scale bar, 300 μm .

Area was calculated from the mask of the FAZ in square pixels and then converted to mm^2 using a model eye parameterized by axial length, anterior chamber depth (ACD), and corneal curvature (CC). Axial length was measured on all subjects. We used ACD and CC values from Bennett's model eye (Bennett 1990), except in the case of four subjects, where we were able to measure ACD and CC directly, using an IOL Master (Carl Zeiss Meditec AG, Germany). The use of additional biometry measurements, such as ACD and CC, improves the conversion from angle to distance; however, the amount of improvement is small (Li, Tiruveedhula et al. 2010). Using ray tracing, the posterior nodal point (PNP) of the eye was estimated from these parameters. Finally, we calculated $\text{mm/deg} = d * \tan(1 \text{ deg})$, where d was the distance from the PNP to the retina.

A two step process was used to calculate the number of pixels per degree. First, an image of a calibration grid was acquired. The calibration grid consisted of an array of 0.1 degree x 0.1 degree squares. The number of pixels per degree were measured in both the horizontal and vertical directions to derive a preliminary conversion factor from pixels to degrees. Second, the spectacle correction was taken into consideration. Since the AOSLO is designed to correct for higher-order aberrations, the lower-order aberrations (i.e. sphere and cylinder) need to be corrected using spectacle lenses. A scaling factor, M , was calculated as $M = 1/(1-0.14*S)$, where S was the spherical equivalent of the two lenses. The pixels per degree was then calculated by multiplying the scaling factor M by the preliminary conversion factor from pixels to degrees.

The effective diameter, d_{eff} , was calculated as the diameter of a circle with equal area:

$$d_{eff} = 2\sqrt{\frac{Area}{\pi}} \quad (3)$$

Capillary density measurements

Vessels were mapped out and extracted with the same approach used in the FAZ analysis (**Figure 1.9**). Since the microvessels are similarly-sized near the FAZ, we defined capillary density as L_{Tot}/A , where L_{Tot} was the combined length of all capillary segments in a region of interest (ROI), and A the area of the ROI, as described previously (Zheng, LaMantia et al. 1991). We selected a special ROI to represent the zone at which there was only a single layer of capillaries, with no major retinal vessels (arteries and veins). In our datasets, this was the zone that was 0.15 degrees from the edge of the irregularly-shaped FAZ.

The ROI was generated automatically from $C(t)$ (**Figure 1.11**) in the following manner. The distance transform (Blum 1967) was used to calculate the distance of all pixels outside of the FAZ, as defined by $C(t)$. We discarded all pixels that were outside of 0.15 degrees from the edge of the FAZ, as well as pixels that were in the interior of $C(t)$.

To investigate whether there was a variation in capillary density in different directions (e.g. superior vs. inferior), we divided the ROI into four quadrants (**Figure 1.12**). These were defined by calculating equiangular line segments radiating outwards from the centroid of the FAZ. We used quadrants in order to (i) maximize the amount of

data used to calculate capillary density, and (ii) minimize effects due to the proximity to feeding arterioles, since there is a capillary free zone (Michaelson 1954) that surrounds arterioles, which would alter measurements of capillary density. To generate the L_{Tot}/A measure, we took the sum of capillary lengths in each of the quadrants and divided by the area of the ROI contained within the quadrant. To determine statistically whether there was a difference in capillary density in different directions, we used the Kruskal-Wallis One-Way ANOVA (Glantz 2002).

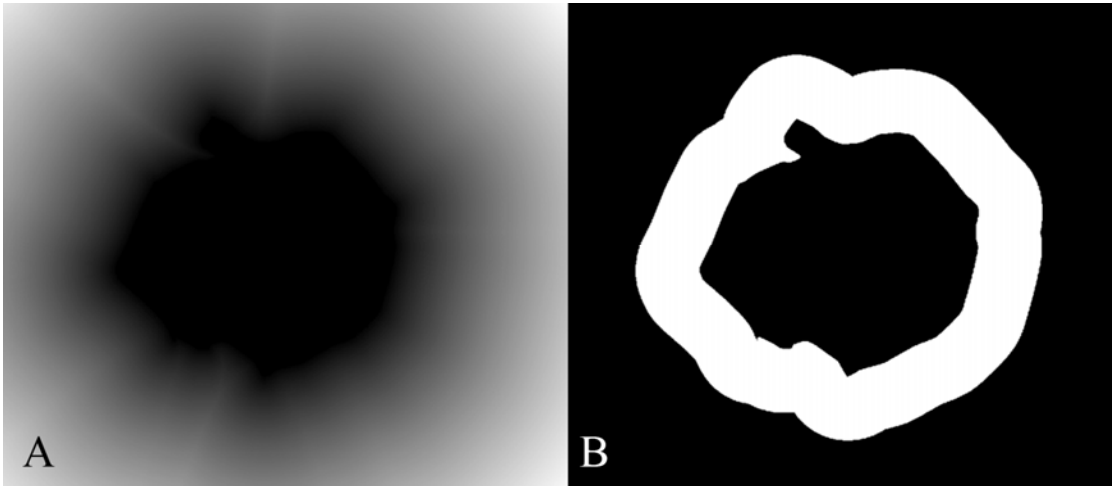


Figure 1.11: Illustration of the automated algorithm for ROI extraction. (A) Visual representation of the distance map, showing the distance to the nearest point in the FAZ. Inside the FAZ, the distance is 0, represented as black; as one moves farther away from the FAZ, the distance increases towards the maximum distance, represented as white. (B) The resulting ROI.

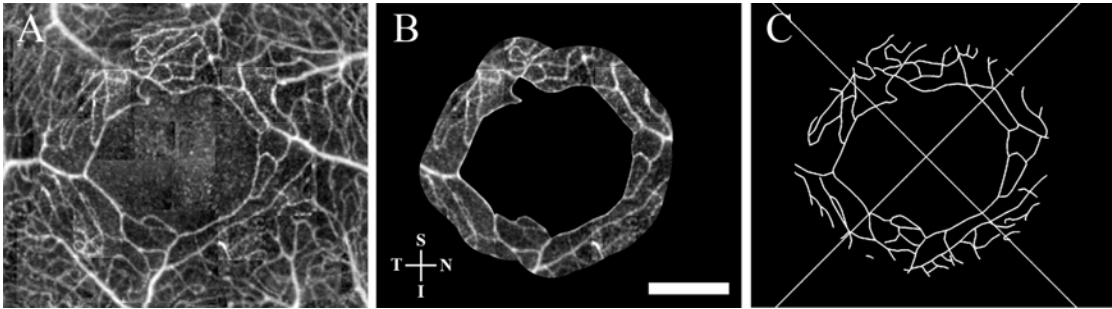


Figure 1.12: Capillary extraction in the ROI, from 840 nm videos. (A) Montage of processed frames showing parafoveal capillaries (frame edges are visible in the image; the corresponding image after removal of frame edges, as described in the text, is shown in **Figure 1.14**). (B) Portion of the processed montage corresponding to the ROI. S, I, N, and T directions are labeled. The scale bar is 300 μm . (C) Extracted capillaries, divided into four quadrants originating from the centroid of the FAZ.

Comparisons

Since FA's are considered the gold standard for studying the retinal vessels, we performed a comparison between the vessels identified using our method and using a standard FA, for one normal subject. Although FAs are not performed on normal subjects, we had access to two FAs due to a special case for one subject where the FA was performed for a different reason. In the first case, the FA was acquired using a digital fundus camera with a 30 degree field (Topcon 50 EX, Topcon, Livermore, CA). 2.5 mL of sodium fluorescein 25% in sterile water (Hub Pharmaceuticals, Rancho Cucamonga, CA) was injected into an antecubital vein using a 25 gauge needle, followed by 5 mL of normal saline. Photos were acquired at the time of injection and through the early transit phase in the left eye, followed by photos in the each eye in the mid transit and late phases. In the second case, the FA was acquired using a Spectralis HRA (Heidelberg Engineering, Carlsbad, CA). The goal of this comparison was to see that vessels were being properly identified.

We also compared vessels identified using the AOSLO to a retinal functional imager (RFI) for one subject. The RFI provides an alternate method to noninvasively visualize retinal vessels and is based on fundus photography (Nelson, Krupsky et al. 2005).

Finally, we compared images acquired using two different laser wavelengths (532 and 840 nm), acquired at different time points, in order to demonstrate that we could achieve similar results (i) with different imaging sessions, and (ii) using different imaging parameters.

1.4 Results

Video and image processing algorithms were implemented using MATLAB (The MathWorks, Inc). The approximate time to construct and analyze a high-quality, 8-video montage of the FAZ using 40 second videos was 2.5 hours, including time for preprocessing and deletion of bad frames. Vessels were mapped for 10 subjects. An example of vessel perfusion mapping is shown for one subject (**Figure 1.13**). A larger montage showing the parafoveal capillary network with arterioles and venules is also shown (**Figure 1.14**).

For all 10 subjects, FAZs were quantified. The area of the FAZs was $0.323 \text{ mm}^2 \pm 0.107 \text{ mm}^2$, and the effective diameter was $633 \pm 103 \text{ }\mu\text{m}$ (mean \pm standard deviation), similar to results from other studies (**Table 1**).

Since we used some video sets that were acquired for the purpose of other studies, there were some montages that were missing data near the FAZ; thus we were only able to extract and analyze capillaries on 7 out of the 10 subjects (**Figure 1.15**). The average capillary densities were 34.0, 31.5, 30.3, and 30.7 mm^{-1} in the S, I, N, and T directions (**Figure 1.16**), similar in magnitude to capillaries in the brain (Zheng, LaMantia et al. 1991).

For two subjects, the parafoveal region of the FA was extracted and compared to the vessels extracted using our method (**Figures 1.17, 1.18**). For the second subject, images were also compared to a fundus photograph and an image generated using an RFI. The same eye was imaged twice at different times using different parameters (**Figure 1.19**).

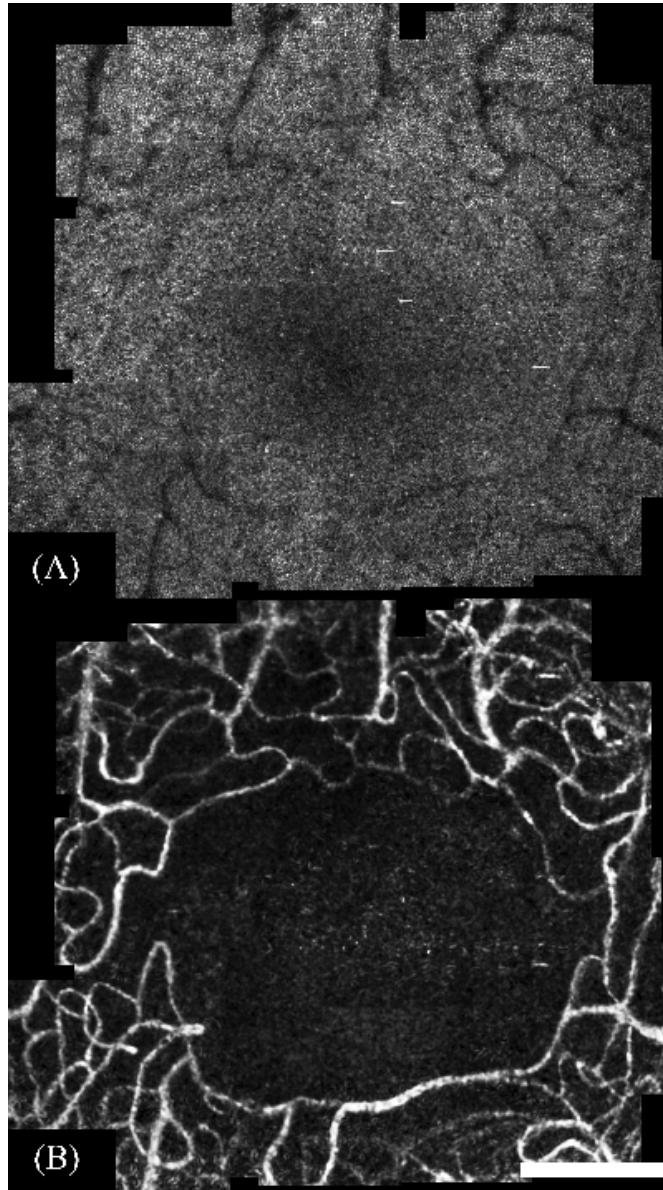


Figure 1.13: Example of capillary mapping in the parafoveal region, using 60 overlapping videos acquired using an 840 nm laser. (A) The montage from unprocessed videos, showing photoreceptors. (B) The montage from processed videos, showing perfused vessels. Scale bar, 300 μm .

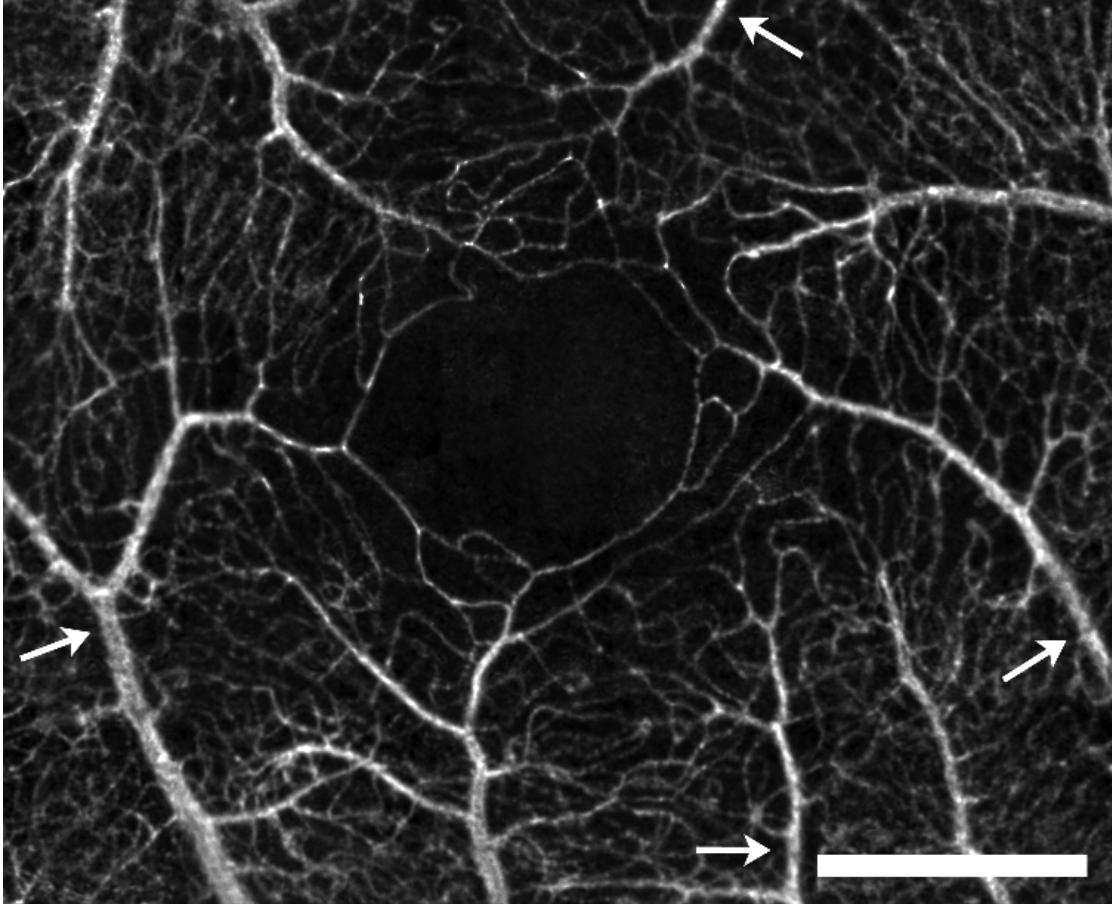


Figure 1.14: Montage showing parafoveal capillaries generated by applying motion contrast enhancement to 76 overlapping AOSLO videos acquired noninvasively without contrast agent. Arrows denote arterioles. Scale bar, 500 μm .

Table 1.1 Comparison of FAZ sizes to other studies

Method	Mean area (mm²)	Mean diameter (µm)	Subject criterion
AOSLO ¹	0.323	633	No ocular disease
SLO + FA ²	0.231	542 ⁵	Non diabetics
FA ³	0.350	730	Non diabetics
FA ⁴	0.221 ⁶	530	10 < Age < 39
	0.292 ⁶	610	Age > 40

¹ Our method.

² (Arend, Wolf et al. 1991)

³ (Bresnick, Condit et al. 1984)

⁴ (Laatikainen and Larinkari 1977)

⁵ Effective diameter calculated from the area.

⁶ Area estimated from diameter measurement.

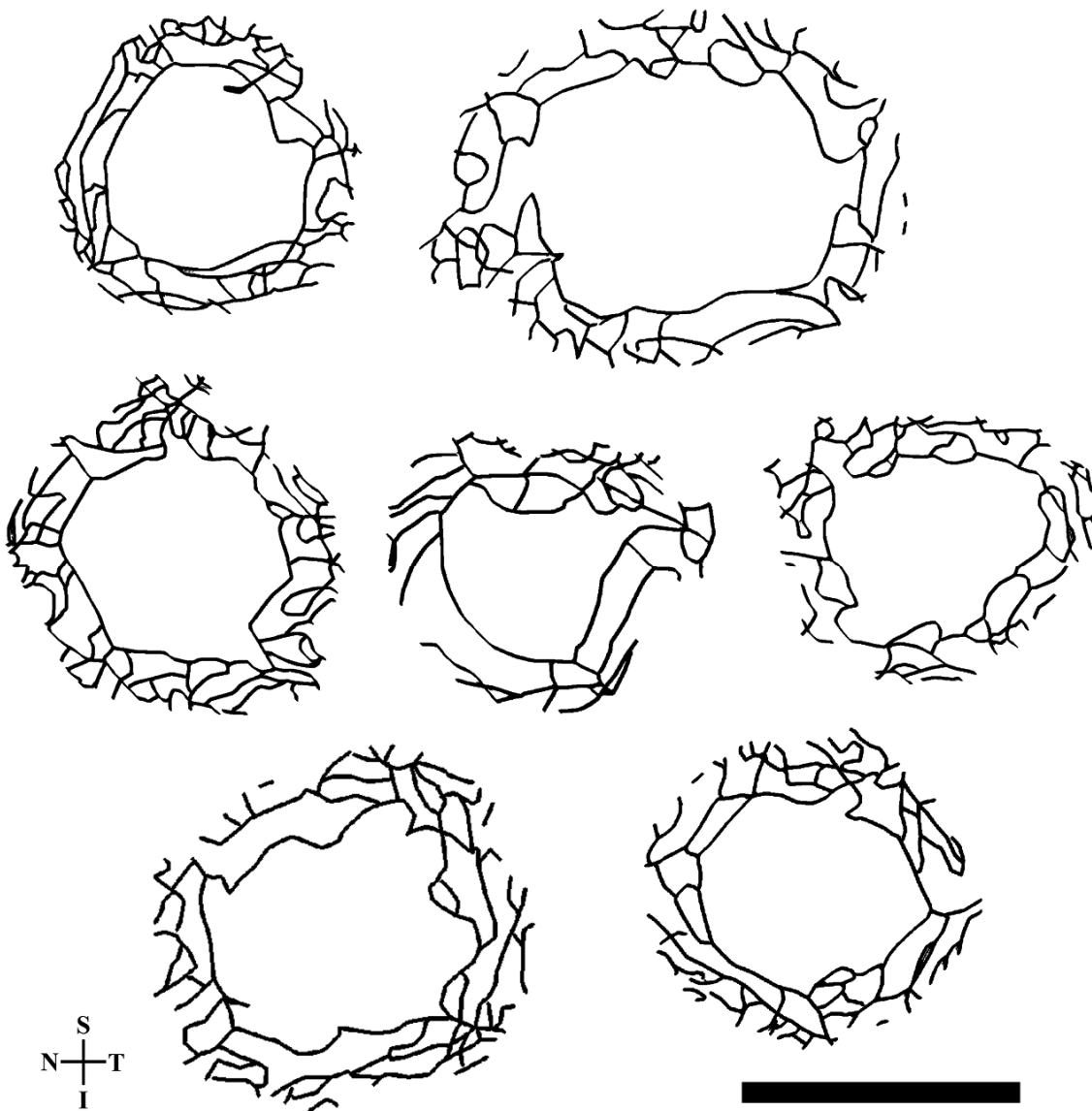


Figure 1.15: Extracted capillaries in the ROI for all the subjects that were analyzed. OD images were flipped horizontally to match OS images, in order to label the four directions (S, I, N, T). The scale bar is 900 μm .

Capillary density

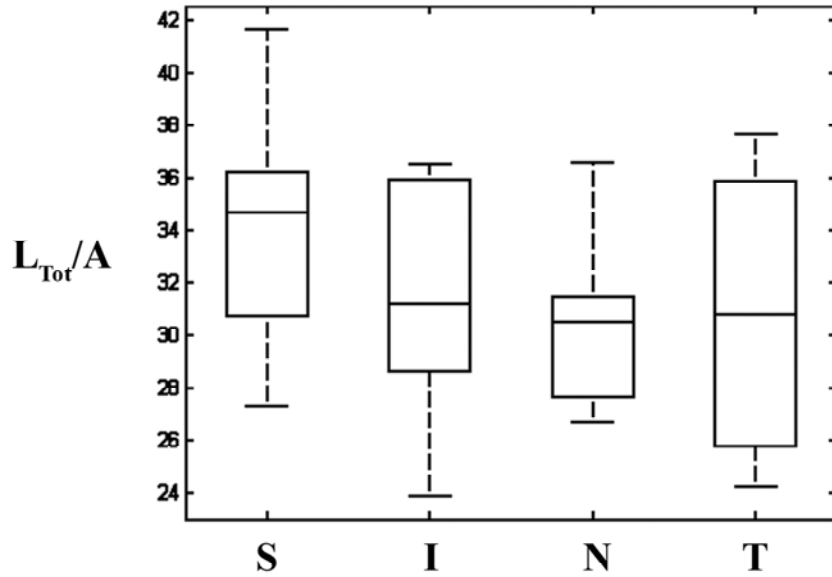


Figure 1.16: Capillary density in four directions (S, I, N, T), where density is defined as L_{Tot}/A , the total length of capillary segments divided by the area of the analysis region. There was no significant difference in densities in four directions ($p = 0.31$).

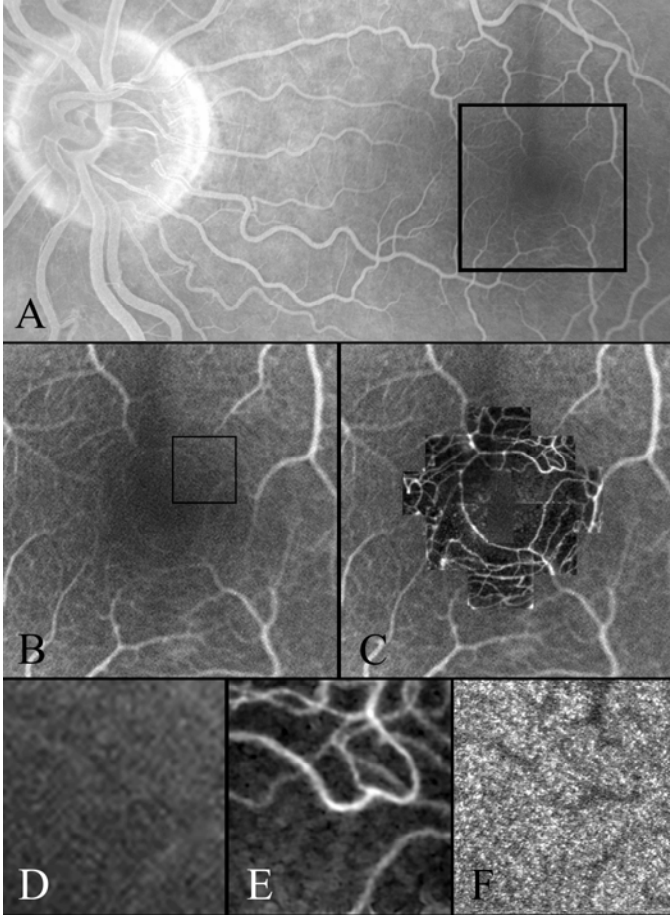


Figure 1.17: Comparison of FA to our method, for one subject imaged using a 532 nm laser. (A) The posterior pole region from a FA. The box shows the location of the fovea and parafoveal capillaries. (B) Contrast-enhanced FA in the parafoveal region (box from A). The location of a single video location is shown in the small box. (C) Contrast-enhanced FA, with the montage from processed images overlaid. (D) Contrast-enhanced FA at the edge of the FAZ (box from B). (E) Image from a single processed video showing perfused capillaries (at box from B). (F) Single frame from the unprocessed video showing photoreceptors (at box from B).

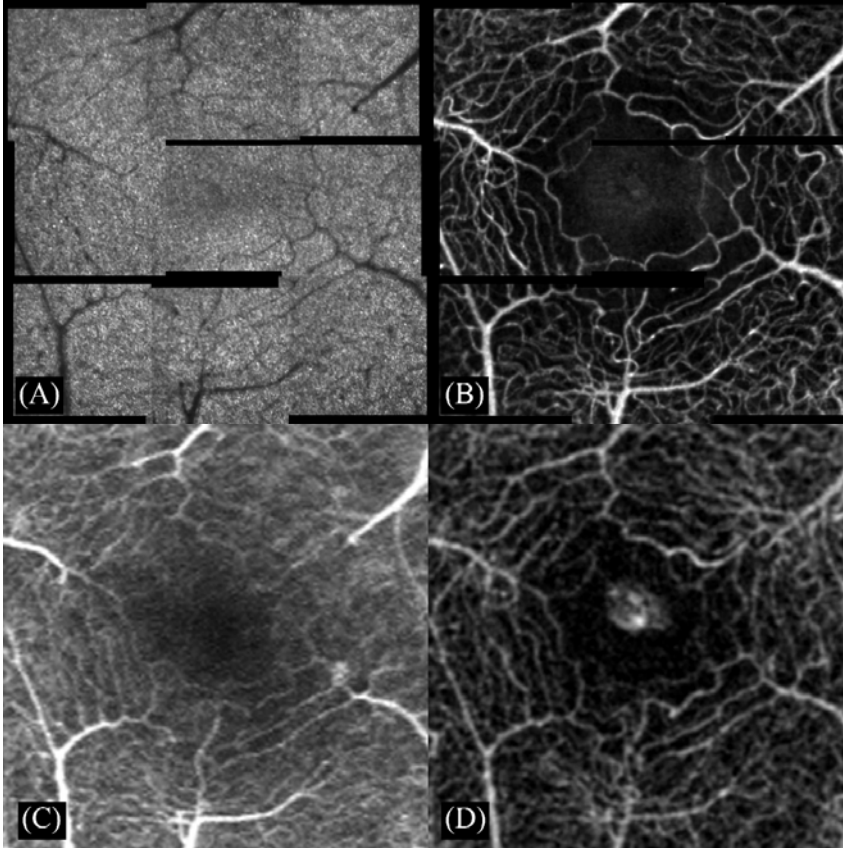


Figure 1.18: Comparison of AOSLO images to alternate imaging modalities, for one subject imaged using an 840 nm light source. (A) AOSLO image of photoreceptors. Although some larger capillaries can be seen, many are not visible. Black regions correspond to areas that were not imaged by the AOSLO. (B) Motion contrast enhanced AOSLO image of capillaries. (C) FA acquired using a Spectralis HRA (Heidelberg Engineering). (D) Image of vessels acquired using a Retinal Function Imager (Optical Imaging, Ltd).

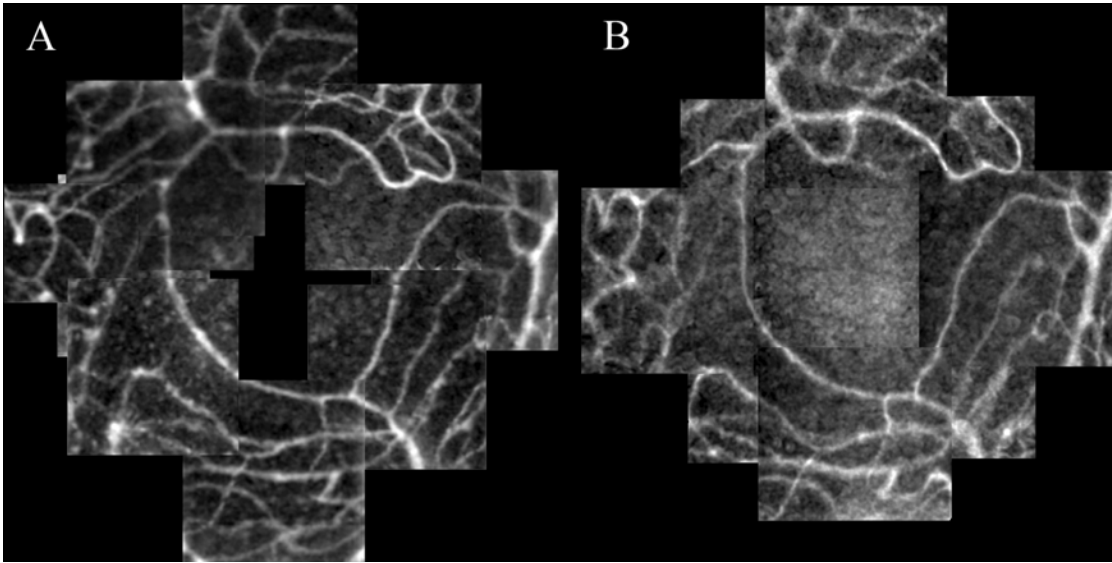


Figure 1.19: Montages of processed videos showing vessels from two separate imaging sessions. The parafoveal region of the same eye was imaged twice: (A) using a 532 nm wavelength laser, and (B) using an 840 nm wavelength laser, 53 months later.

1.5 Discussion

This chapter presents a method to visualize and analyze the FAZ and parafoveal capillary network noninvasively. The approach is based on the idea of using motion as intrinsic contrast. The key assumption is that blood cells move relative to their surrounding photoreceptors – thus, by extracting motion from videos of the eye, one can visualize perfused vessels. Motion is extracted using multi-frame division videos: using division images enables multiple division images to be averaged together arithmetically. This averaging enhances the final SNR. In general, non-invasive videos of the microcirculation from many imaging modalities suffer from low contrast, a common challenge for many vessel analysis algorithms. Our technique for motion contrast enhancement is general, and can be applied as an enabling step for more advanced analyses, such as quantification of the FAZ and parafoveal capillary density.

There are several advantages to using this approach. Most importantly, it is non-invasive, and can potentially be applied with low risk for subjects ranging from normal to pre-disease to disease states. The comparison of the vessel montage to FA shows that the method is able to detect retinal capillaries and generate a complete parafoveal map. FAs were not performed on all subjects to avoid unnecessary risks associated for eyes with no ocular conditions. Another advantage of this technique is the availability of other retinal measurements from the same dataset. For example, the structural integrity of the photoreceptor mosaic can be analyzed from the same videos (**Figures 1.13 and 1.18**). Also, it is possible to investigate the speed and pulsatility of individual

leukocytes as they move through capillaries, using offline analysis (Martin 2005; Martin 2009). Finally, one can extend the analysis to compute statistics such as vessel density, as illustrated in this chapter.

The main limitations to the method are (i) it may be too time consuming for immediate clinical use, (ii) subjects must have clear ocular media, and (iii) good subject compliance is necessary. First, our technical methods for visualization of the parafoveal capillaries were developed to demonstrate a new concept, and not for immediate clinical implementation. Also, the time to acquire overlapping videos may influence which subjects might be good candidates. Second, there are many potential subjects that have clear ocular media, particularly subjects in normal and pre-diseased states, as well as some subjects with certain diseases; these subjects are usually precluded from invasive procedures such as FA. Finally, good subject compliance is needed during imaging session, which may limit the pool of potential patients; however, the subject tasks are relatively straightforward, involving fixation on targets presented at various locations, and it is possible to successfully perform AOSLO assessment on cooperative patients (Duncan, Zhang et al. 2007).

There are tradeoffs when imaging with two different laser wavelengths. A prior study showed that green laser wavelengths were optimal for vessel contrast in scanning laser ophthalmoscopy (SLO) systems (Reinholz, Ashman et al. 1999). While we found that the contrast of vessels and flow through vessels was higher for the 532 nm laser compared to the 840 nm laser (**Figure 1.19**), we did not observe any differences in the vessels that could be identified for analysis. However, there are major advantages to using the 840 nm laser. The SNR of the photoreceptors is much higher for videos

acquired at 840 nm, an important consideration when evaluating photoreceptor health; this was because we imposed conservative light exposure limits. To insure safe light levels, the power that reached the subjects' retinas was maintained at a level that was at 10x below the Maximum Permissible Exposure limit defined by ANSI (2007). Since the SNR improves as the power of light increases, and since we imposed our conservative light exposure limits, the videos acquired at 532 nm had considerably lower SNRs. Finally, the lower brightness 840 nm light source (~ 50 trolands) was better for subject comfort.

For one subject, we performed an extended imaging session using the 840 nm light source (**Figure 1.14**). It appears that the methods presented in this chapter work best for the parafoveal capillaries closest to the FAZ, due to the lower capillary density (there is a single layer of capillaries immediately outside of the FAZ). Further from the FAZ, capillaries are still identifiable, but the higher capillary density makes it difficult to delineate specific capillary paths, a consideration for future work relating to the quantification of capillary hemodynamics.

Motion contrast enhancement is based on the assumption that fluctuations in intensity are due to motion. These fluctuations in intensity are inherently weak signals; considering an idealized model of the situation, application of flow visualization tools can lead to either decreases or increases in vessel contrast (**Figure 1.20**). It is possible for artifacts to arise in the presence of any signals stronger than the motion signal. Specifically, any fluctuation in intensity not due to motion of blood cells will lead to an artifact. Two common sources of artifacts include dust and failed stabilization (**Figure 1.21**).

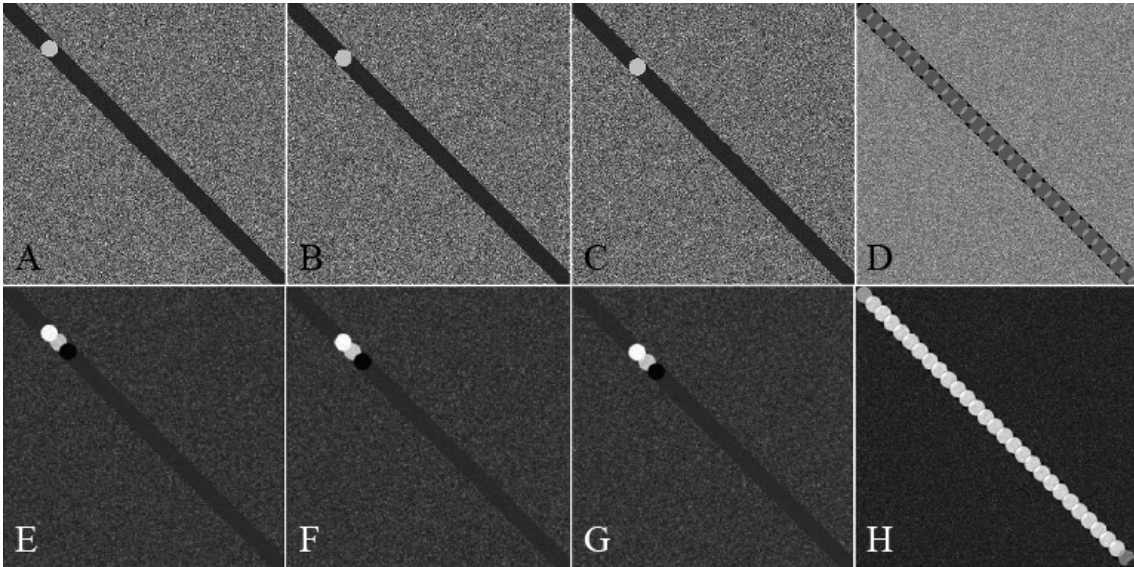


Figure 1.20: Motion contrast enhancement demonstration on a simulated video. (A,B,C) Three consecutive frames from a simulated video showing a diagonal dark vessel with a single bright leukocyte traveling downwards, with Gaussian noise in the background. (D) The standard deviation image from a longer video sequence, which shows that vessel detection methods based on image statistics can actually *decrease* the contrast of the vessel. (E,F,G) The corresponding consecutive frames after motion contrast enhancement methods were applied. (H) The standard deviation image of the division video, which shows that the variation in the image intensities in the vessel region has increased when compared to the original video.

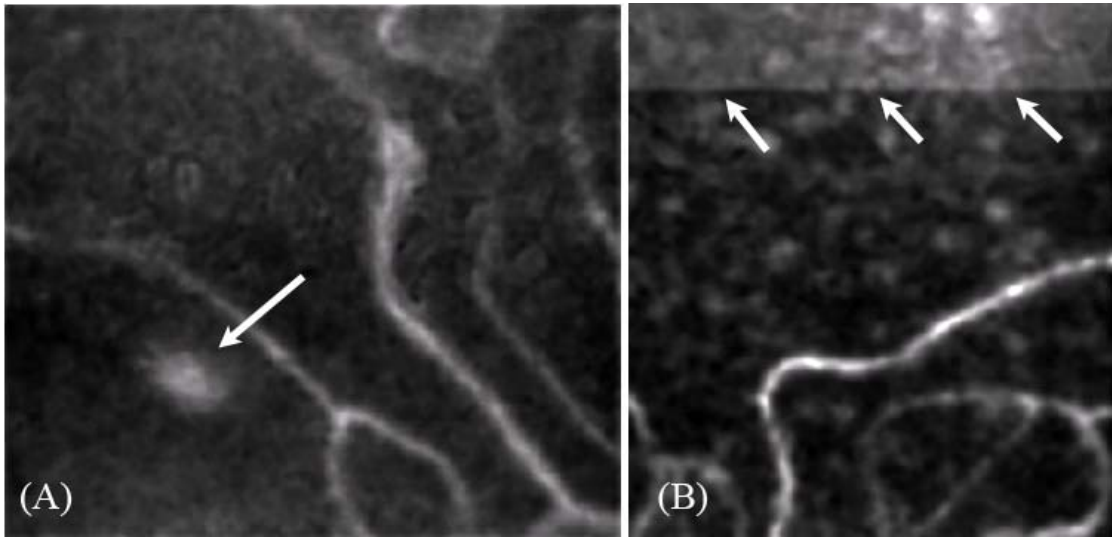


Figure 1.21: Sources of artifacts. (A) A piece of dust was present during video acquisition. The piece of dust remained stationary in the video while the eye moved around. After video stabilization (e.g. correction for eye motion), the piece of dust appeared to move around, leading to fluctuations in intensity and manifesting as the spot on the vessel perfusion image (arrow). (B) Failure to stabilize all portions of the video frame resulting in a subset of frames with bright intensity below the line and dark intensity above the line (arrow); since these failed frames were interspersed throughout the video, they appear as a source of intensity fluctuation. This artifact can be removed by deleting all failed frames prior to the motion contrast enhancement process.

Despite variations in imaging parameters, we were able to achieve good results overall with our algorithms. Such variation would potentially require variations in video and image processing parameters; however, we were able to apply the same general method to all videos. We describe a set of optimized parameters for visualization of retinal capillaries using motion contrast enhancement. We also showed that we could achieve similar results using videos from different imaging sessions (**Figure 1.19**). Due to the unique nature of this approach, there are no direct methods to validate the approach other than comparison to FA. Even when contrast agents are combined with SLO (Arend, Wolf et al. 1991; Paques, Boval et al. 2000), the level of detail that we achieved was not observed. Previously, the only established method for non-invasive visualization of the FAZ and parafoveal capillary network was based on the entoptic blue field phenomenon (Bradley, Zhang et al. 1998).

There are many areas for future work. Since detection of parafoveal capillaries was the goal of this chapter, there remains much work in image analysis for automation, enhanced segmentation, classification, and registration of vessels from motion contrast enhanced images. There are also important applications in clinical medicine based on FAZ quantification and capillary density, including the development of potential biomarkers for disease, measures of retinal health in disease progression, or endpoint measures for clinical trials.

1.6 Acknowledgments

Portions of this chapter are published in *Investigative Ophthalmology and Visual Science*, *Journal of Biomedical Optics*, and *IEEE Proceedings of the International Symposium for Biomedical Imaging (ISBI) 2010*. The dissertation author is the primary investigator and thanks co-authors, Drs. Joy Martin and Austin Roorda for their contributions. The authors thank Pavan Tiruveedhula for his technical support in implementing software modifications for the AOSLO, and Kaccie Li for implementing the ray tracing algorithm used to estimate the mm/deg conversion. This work was supported by grants from NSF Center for Adaptive Optics AST-9876783 and the NIH Bioengineering Research Partnership EY014375, and in part by the NSF Graduate Research Fellowship and the National Defense Science and Engineering Graduate Fellowship.

CHAPTER 2

HEMODYNAMICS

2.1 Abstract

Adaptive Optics Scanning Laser Ophthalmoscopy (AOSLO) can be used to noninvasively investigate single-file flow through live human retinal parafoveal capillaries. We developed a system of video and image analysis to enable accurate quantification of object speeds, and used the system to characterize, in detail, single-file flow dynamics through the parafoveal capillary network of one subject. There are two key components to the system: motion contrast enhanced spatiotemporal plots, and a slope modification procedure to accurately calculate speed of moving objects. Spatiotemporal plots, which are used to visualize and track moving objects, are difficult to implement in AOSLO videos due to the low contrast of blood cells and capillaries. However, we were able to implement spatiotemporal plots using motion contrast enhancement. The second component is a method to quantify object speed. Speed quantification is confounded by several simultaneous motions. During video acquisition, the objects of interest are in constant motion relative to the background tissue (object motion). The background tissue is in constant motion relative to the AOSLO, due to continuous eye motion during video recordings (eye motion). The location at which AOSLO acquires data is also in continuous motion, since the imaging source is swept in a raster scan across the retina (raster scanning). Object motion, eye motion, and raster scanning must all be taken into consideration for accurate quantification of object speeds. We validated these methods on both experimental

AOSLO videos as well as synthetic videos generated by a virtual AOSLO. Finally, we characterized in detail the flow of plasma gaps and leukocytes through the parafoveal capillary network of one subject. We found that both the capillary topology and the flow dynamics were heterogeneous. Certain capillaries accounted for a clear majority of leukocyte traffic (Leukocyte-Preferred-Paths, LPPs), while other capillaries primarily featured plasma gap flow (Plasma-Gap-Capillaries, PGCs). LPPs may serve as a protective mechanism to prevent inactivated leukocytes from entering exchange capillaries, and PGCs may serve as relief valves to minimize flow disruption due to the presence of a leukocyte in a neighboring LPP. The methods developed in this chapter enable noninvasive and accurate investigations of flow dynamics through a live human capillary network.

2.2 Introduction

The flow of individual cells through capillary networks is dependent on a number of interacting factors, including metabolic demand and organ-specific factors (Zweifach 1961; Hogg and Doerschuk 1995), network topology (Schmid-Schonbein, Skalak et al. 1980), heart rate (Zweifach 1974; Zweifach 1974; Martin 2009), and the presence and distribution of erythrocytes and leukocytes (Lipowsky 2005; Popel and Johnson 2005). Although erythrocytes outnumber leukocytes by a ratio of about 1000:1, the role of leukocytes in the microcirculation is particularly important, because leukocytes are larger and less deformable than erythrocytes (Schmid-Schonbein 1980), and thus travel significantly slower through the microcirculation (Kuebler, Kuhnle et al. 1994; Ben-nun

1996). The transit of leukocytes through narrow capillaries compresses the glycocalyx (Damiano and Stace 2005) and upsets the normally faster-moving erythrocytes (Ben-nun 1996), creating a plasma zone immediately upstream of the leukocyte (Fitz-Gerald 1972) with a corresponding erythrocyte train immediately downstream (Schmid-Schonbein, Usami et al. 1980; Pries, Secomb et al. 1990). Further upstream, at the prior branch point, the channel of higher flow (Schmid-Schonbein, Skalak et al. 1980) may shift from one branch to the other as the flow resistance is temporarily increased in the branch containing the leukocyte (Sutton and Schmid-Schonbein 1992). Thus, there is a dynamic interaction between leukocytes and erythrocytes in capillary networks, particularly at the level of single-file flow. It is important to characterize the nature of single-file flow to better understand diseases that affect the microcirculation, such as diabetic retinopathy.

The human parafoveal capillary network, a highly organized system residing in the inner layers of the retina, can be observed noninvasively and in situ using an Adaptive Optics Scanning Laser Ophthalmoscope (AOSLO) (Roorda, Romero-Borja et al. 2002; Martin 2005; Zhang, Poonja et al. 2006; Tam, Martin et al. 2010). Of particular interest is the terminal capillary network near the fovea, marked by the foveal avascular zone (FAZ), a zone approximately 500-600 μm in diameter that is free of vascularization in the inner retina (Laatikainen and Larinkari 1977). Immediately outside the FAZ, the parafoveal capillaries are single-layered and planar (Snodderly, Weinhaus et al. 1992). Flow is necessarily single-file. Erythrocytes, which have a mean major diameter of 7.82 μm (Evans and Fung 1972), lymphocytes, with diameters of 5.75 μm , and neutrophils, monocytes, and eosinophils, with diameters of 7.25 μm

(Schmid-Schonbein 1980), must squeeze through narrow parafoveal capillaries with lumen diameters of 3.5-6 μm (Lutty, Cao et al. 1997). This network is fed by interdigitating arterioles and venules oriented in directions normal to the FAZ contour; in contrast, the capillaries are preferentially oriented in directions tangential to the FAZ contour (Snodderly, Weinhaus et al. 1992; Yu, Balaratnasingam et al. 2010). Immediately exterior to each arteriole, there is a zone of reduced capillary density; farther from the arteriole, the capillary density gradually increases, reaching a maximum at the location of each venule (Michaelson 1954). These observations show that at the cellular level, the parafoveal capillary network is locally heterogeneous.

The distribution of individual blood cells in capillary networks is also heterogeneous, both spatially across different capillaries (Schmid-Schonbein, Skalak et al. 1980), and temporally within the same capillary (Kleinfeld, Mitra et al. 1998). At a bifurcation spawning two daughter vessels of unequal flow, the distribution function of erythrocytes is highly nonlinear (Schmid-Schonbein, Skalak et al. 1980). Thoroughfare channels, which connect terminal arterioles to collecting venules, contain high volumes of blood flow relative to neighboring capillaries (Zweifach and Metz 1955; Hudetz 1997). The remaining capillaries have been termed exchange, or true capillaries, through which a normal ebb and flow of cells can sometimes be observed (Hudetz 1997). In many capillary networks, flow is regulated by precapillary sphincters; however, this does not appear to be the case in the cat retina (Friedman, Smith et al. 1964). Erythrocytes have been observed to fluctuate in both concentration and flow direction in the cat retina (Friedman, Smith et al. 1964), and spontaneously pause during flow through monkey retinal capillaries (Flower, Peiretti et al. 2008); however, a

separate study using invasive endoscopy found variations in erythrocyte speed in cat retinal capillaries, but no evidence of plasma skimming, stasis, or intermittent flow (Jensen and Glucksberg 1997). Leukocytes have also been observed to preferentially flow through specific channels in the retina (Nishiwaki, Ogura et al. 1996). These peculiarities can be lost with ex-vivo approaches. To our knowledge, the distribution of blood constituents in thoroughfare and exchange capillaries in humans has not yet been characterized in vitro.

It is important to utilize a noninvasive, in situ method to investigate the behavior of single cells in parafoveal capillaries, since any invasive method can potentially change the nature of flow, particularly at the level of single-file flow. Currently, most imaging methods for investigating the microcirculation are (i) invasive, (ii) require administration of a contrast agent, or (iii) cannot be performed in humans. A notable exception is the Retinal Function Imager (Nelson, Krupsky et al. 2005), which can investigate blood flow noninvasively in humans using intrinsic motion signals; however, there are two considerations. First, this method is limited to an imaging sequence consisting of 6 snapshots spaced 17 milliseconds apart, for a total observation time of about 100 milliseconds; and second, it is uncertain whether there is sufficient detail to examine the dynamic activity in the smallest capillaries. Another example, which is minimally invasive, uses fluorescein labeled autologous leukocytes to study flow dynamics in humans; however, the authors find evidence of leukocyte activation (Paques, Boval et al. 2000). The process of removing, labeling, and reinserting leukocytes increases the spontaneous activation of leukocytes (Becker, Chen et al. 2004), which alters their mechanical properties (Schmid-Schonbein, Sung et al. 1981),

thereby changing the characteristics of the flow. We have recently described a method to noninvasively visualize human parafoveal capillaries using AOSLO videos acquired without administration of contrast agents (Tam, Martin et al. 2010).

There are key issues that must be addressed to make AOSLO an effective system for the study of hemodynamics. Methods to quantify object speeds in AOSLO videos are important for hemodynamics, but are confounded by raster scanning, eye motion, and object motion. Since videos are acquired using a raster scanning system, different pixels within a video frame are acquired at different points in time. This affects the appearance of moving objects – the apparent object speed is dependent on the speed of the raster scan (**Figure 2.1**). The magnitude of the error in measured speed due to raster scanning depends on the configuration of AOSLO imaging parameters, but can be as large as 37.8% (as derived in this chapter). There is also constant eye motion that occurs during acquisition of video frames (Martinez-Conde, Macknik et al. 2004; Stevenson, Roorda et al. 2010). Since the raster scan continuously scans in a fixed pattern, this results in unique distortions in each video frame (Vogel 2006; Yang, Arathorn et al. 2007). Finally, the object itself is also in constant motion, simultaneous to raster scanning and eye motion. The motions of the object, eye, and raster scan must be considered simultaneously for accurate quantification of object speeds in an AOSLO system.

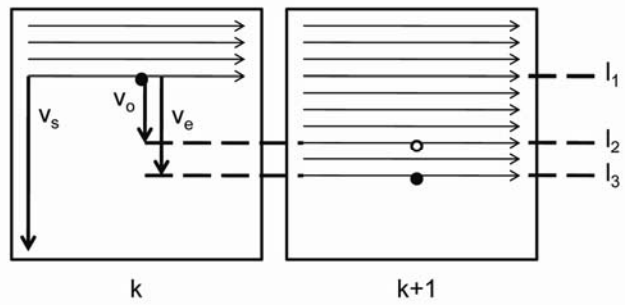


Figure 2.1: Raster scan problem formulation showing speed overestimation for a downward moving object from frame k to $k+1$. The vertical speed of the scanner is v_s . In frame k , the object (solid black circle) is at line l_1 . After exactly one frame, when the scanner has reached line l_1 on frame $k+1$, the object is at line l_2 . However, the scanner catches the object at line l_3 . The object speed, v_o , is overestimated as v_e .

In this chapter, we describe methods for tracking and accurate speed quantification of moving objects in AOSLO videos. We use spatiotemporal (ST) plot analysis and motion contrast enhancement to track moving objects and measure apparent object speeds. Apparent object speeds are then corrected using a slope modification method to correct for errors introduced by eye motion and raster scanning. The accuracy of the proposed methods is validated using synthetic data sets generated by a virtual AOSLO. Finally, we apply these methods to characterize single-file flow through capillaries in a living human eye.

2.3 Materials and Methods

The experiments described in this study were approved by the University of California, Berkeley Committee for Protection of Human Subjects. After detailed explanation of the procedures, written informed consent was obtained. For the first two subjects, a 37-year-old male and a 26-year-old female, we used previously acquired videos. For the third subject, we recruited one 24-year-old female subject. All three subjects had no history of ocular or systemic disease at the time of imaging.

Biometry Measurements

Axial length was directly measured after maximal dilation was achieved (IOL Master, Carl Zeiss Meditec Inc., Dublin, CA, USA). For the first and third subjects, anterior chamber depth and corneal curvature were also measured, using the same instrument. For the second subject, these two parameters were estimated using a model eye (Bennett

1990). These measurements were used to make accurate conversions from visual angle to retinal distance (Li, Tiruveedhula et al. 2010; Tam, Martin et al. 2010), which were the units used in the spatiotemporal plot analysis.

Fundus Photography

For the third subject, in order to identify arterioles and venules for the extended characterization of flow dynamics, a digital fundus camera was used to acquire a red-free photograph of the posterior pole of the right eye at a 30° field size (Zeiss Visucam NM/FA, Carl Zeiss Meditec Inc., Dublin, CA, USA). Red-free fundus photography is the gold standard for noninvasively imaging retinal vessels, in the absence of contrast agents.

AOSLO Imaging

AOSLO videos were acquired as described previously (Martin 2005; Tam, Martin et al. 2010). One randomly selected eye from each subject was dilated (2.5% Phenylephrine Hydrochloride, 1% Tropicamide).

AOSLO videos can be acquired using different imaging configurations, depending on the application. We consider three different configurations of imaging parameters (Type 1, 2, and 3), as described in **Table 2.1**.

Table 2.1. Imaging Parameters

<i>Specification</i>	<i>Type 1</i>	<i>Type 2</i>	<i>Type 3</i>
Imaging wavelength [nm]	532	840	840
Frame rate [Hz]	30	30	60
Raw video frame size [pixels²]	525x512	512x512	512x525
Field of view (approx.) [deg²]	1.5 x 1.5	1.2 x 1.2	1.5 x 1.5
X scale factor [pixels / deg]	342	414	328
Y scale factor [pixels / deg]	342	409	330
Length of video [seconds]	40	2-10	40
Retinal scale factor [mm/deg]	0.28008	0.28697	0.28889
Subject age	37	26	24
Refractive error, sphere [D]	+1.0	-1.0	+0.5
Refractive error, cylinder [D]	-0.25	0.0	0.0

Imaging parameters and subject data for various types of AOSLO videos. Three representative configurations of imaging parameters used for AOSLO imaging, for three different subjects. Representative values are given for the scale factors, which vary by small amounts across different imaging sessions due to small variations in hardware alignment and eye morphology.

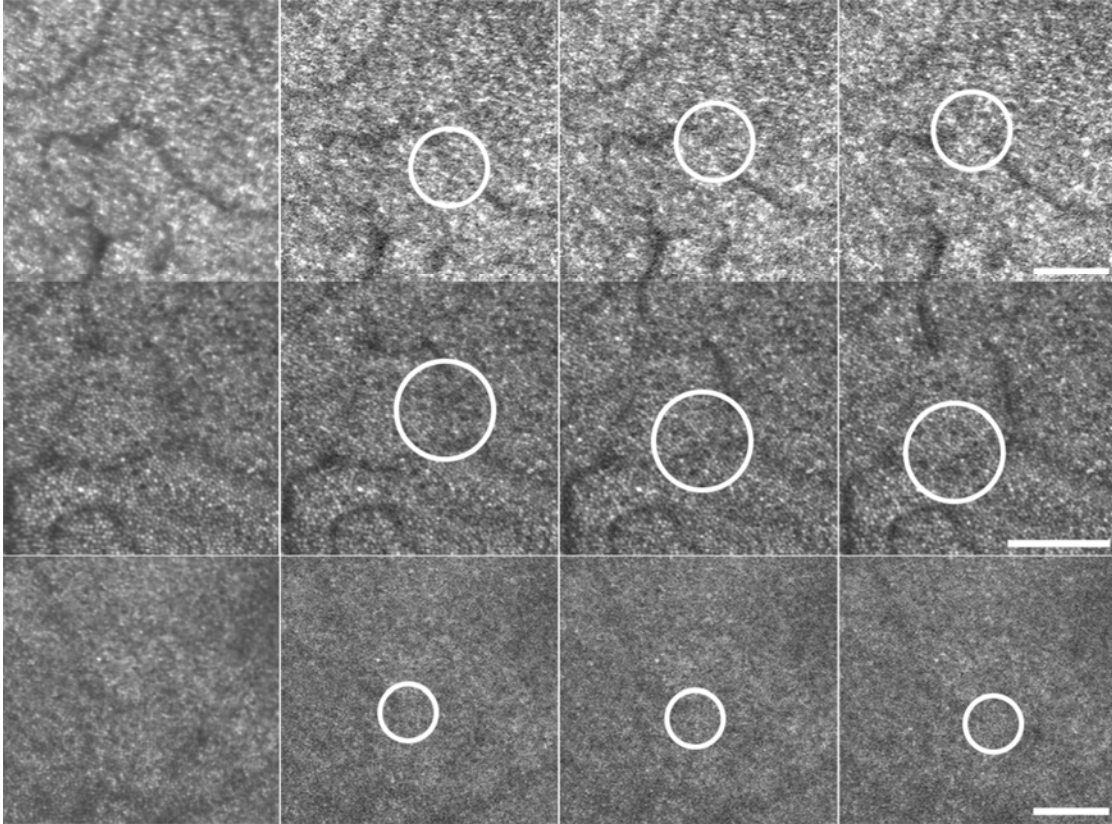


Figure 2.2: Examples of retinal images acquired noninvasively in human subjects using an AOSLO, for a Type 1 (*top row*), Type 2 (*middle row*), and Type 3 (*bottom row*) video. The first column shows the averaged image of all frames for each video. The remaining three columns are three consecutive frames, showing a leukocyte (circled) traveling through a parafoveal retinal capillary. The frames in these videos have been preprocessed. The foveal center is near the top right corner for all three videos. Circular dots are photoreceptors, and dark, fuzzy lines usually correspond to capillaries. However, the locations of all capillaries are not obvious. Scale bar, 100 μm .

The three video types correspond to the three subjects that were used in this study. Type 1 videos were acquired for the purpose of analyzing blood flow, Type 2 for analyzing photoreceptors, and Type 3 for analyzing both blood flow and photoreceptors. Type 1 videos were acquired using a green wavelength laser, which has been reported to be the optimal wavelength for obtaining good contrast in blood flow imaging (Reinholz, Ashman et al. 1999). Type 2 and 3 videos were acquired using a near-IR laser – a more desirable wavelength in terms of (i) risks due to laser damage on the retina, (ii) compatibility with the AOSLO hardware, and (iii) overall subject comfort. Type 1 and 3 videos were acquired for longer durations in order to increase the number of leukocytes that could be counted. Examples of frames from Type 1, 2, and 3 videos are shown in **Figure 2.2**.

An extended session of AOSLO imaging was performed for the third subject, using parameters that were optimized for blood flow imaging (Tam, Martin et al. 2010). As described in Chapter 1, it is important to select an appropriate plane of focus. It is advantageous to acquire images near the photoreceptor layer, since this layer contains high contrast spatial features that are useful for stabilizing videos to correct for eye motion. However, since the inner capillary layers reside anterior to the photoreceptors, it is also advantageous to acquire images near the capillary layers, to maximize both the sharpness of the resulting vascular images and also the motion contrast of the individual cells. Thus, we selected a plane of focus that was slightly anterior to the photoreceptor layer. A total of 76 overlapping videos were acquired in one 2 hour session, with 9 videos acquired near the FAZ (40 second videos with 1.5° field sizes), and 68 videos

farther from the FAZ (15 second videos with 1.8° field sizes), for a combined field of approximately $6.5^\circ \times 9.5^\circ$ (height and width).

For the third subject, videos were acquired at 60 frames per second (fps), using an 840 nm super luminescent diode. The AOSLO normally acquires images at 30 fps, using the forward sweep of a fast resonant scanner that operates at 16 kHz; to achieve 60 fps, we incorporated both the forward and return sweeps of the scanner. Instead of recording 512 lines of the forward sweep at 30 fps, we recorded 256 lines of the forward sweep and 256 lines of the return sweep at twice the line spacing as normal, in order to achieve 60 fps imaging without compromising the pixel density within each frame. To insure safe light levels, we maintained an exposure level that was more than 10x below the Maximum Permissible Exposure limit defined by the American National Standards Institute (ANSI 2007). There was no injection of a contrast agent.

Raw videos were preprocessed to correct for distortions due to raster scanning and eye motion, without considering object motion. As described in Chapter 1, preprocessing involves desinusoiding, stabilization, cropping, and frame deletion. The process of desinusoiding and stabilization generates a high-frequency eye motion trace, which is stored in a data file and used in the calculation of the distance that a moving object has traveled. The number of lines at the top edge that were removed due to cropping was also stored in a lookup table, and used in the calculation of object speeds. Note that deletion of frames is important for generation of high quality images of photoreceptors and vessels; however, we did not delete any frames for the speed analysis since deletion of frames would increase the apparent speed of a moving object.

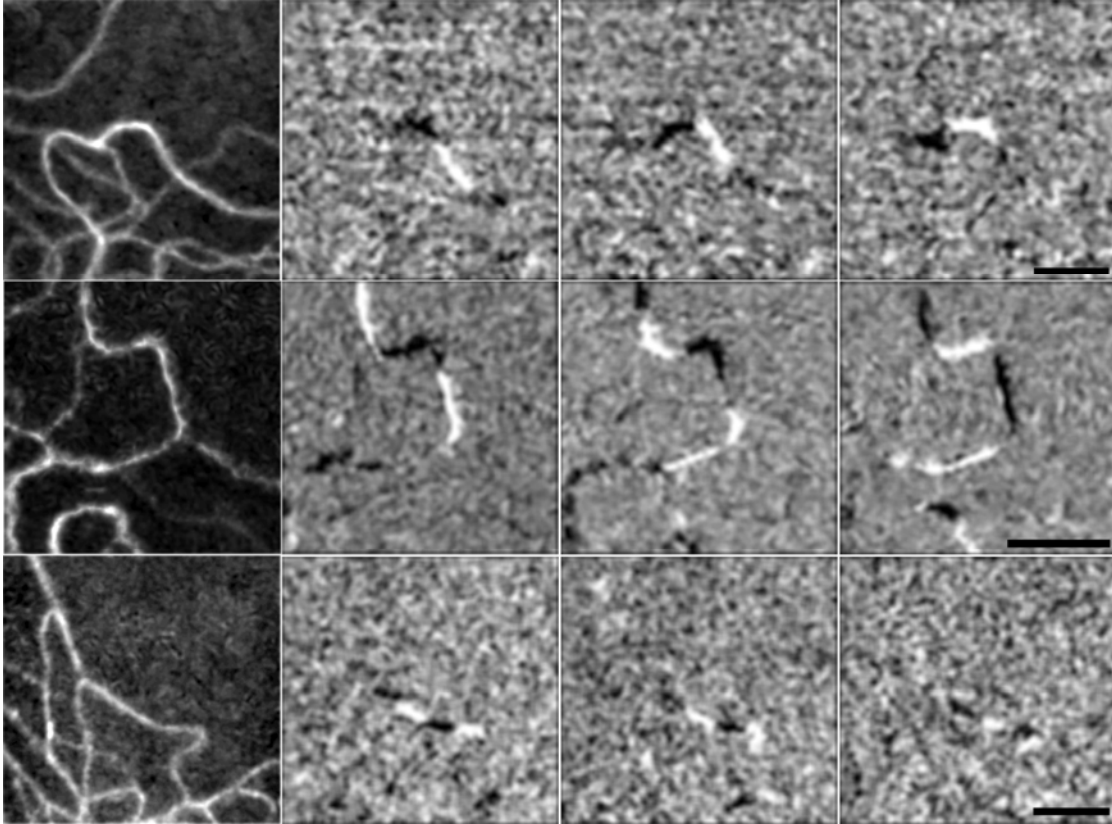


Figure 2.3: Visualization of vessels and moving objects by applying motion contrast enhancement to the Type 1 (*top row*), Type 2 (*middle row*), and Type 3 (*bottom row*) AOSLO videos shown in **Figure 2.2**. The first column shows the standard deviation image, which enhances the contrast of vessels. The next three columns show three consecutive frames of the multi-frame division video, which enhances the contrast of moving objects. Scale bars, 100 μm .

Motion Contrast Enhancement

Since spatial contrast is low, motion contrast enhancement is used to visualize moving objects and vessels (**Figure 2.3**). Methods for motion contrast enhancement have been described previously (Sato 1997; Japee, Ellis et al. 2004; Nelson, Krupsky et al. 2005; Tam, Martin et al. 2010). We implement a method that works well with AOSLO videos (Tam, Martin et al. 2010), using a multi-frame division video and a standard deviation image. The multi-frame division videos were used to visualize moving objects, and the standard deviation image was used to visualize vessels. Median and Gaussian filtering were applied before and after calculation of the multi-frame division video, respectively.

A preprocessed video has moving blood cells in front of a stationary background tissue, consisting of photoreceptors and vessels. Given two frames, $I_j(x,y)$ and $I_{j+1}(x,y)$,

the division image $D_j(x,y) = \frac{I_j(x,y)}{I_{j+1}(x,y)}$ emphasizes the objects in motion as long as the

intensity of background tissue remains relatively constant. Here, $I_j(x,y)$ represents the intensities of frame j at position (x,y) . We defined a multi-frame division video as

$M_j(x,y) = \frac{D_j(x,y) + D_{j+1}(x,y)}{2}$. To visualize the perfused vessels, an image was

calculated from the multi-frame division video, using the geometric standard deviation.

For a video with n frames, the geometric standard deviation image, $S(x,y)$, is defined in

Equations 1 and 2.

$$S(x, y) = \exp \left(\sqrt{\frac{\sum_{j=1}^n [\ln M_j(x, y) - \ln \bar{M}(x, y)]^2}{n-1}} \right) \quad (1)$$

$$\bar{M}(x, y) = \sqrt[n]{\prod_{j=1}^n M_j} \quad (2)$$

Spatiotemporal Plots

Spatiotemporal (ST) plots (also known as kymograms) are used to visualize motion in many custom video microscopy systems. Some examples include visualization of intracellular structures, such as vesicles (Racine, Saschse et al. 2007) and microtubules (Smal, Grigoriev et al. 2009), as well as blood cells within small vessels, in the hamster muscle (Ellis, Ellsworth et al. 1992), rat mesentery (Sato 1997), rat neocortex (Kleinfeld, Mitra et al. 1998), and cat retina (Jensen and Glucksberg 1997). We use ST plots to visualize hemodynamics. There are two major advantages. First, the ST plot representation is more compact, which assists in pattern identification. Variables such as density, frequency, and variations in speed both spatially and temporally can easily be observed on ST plots, but not from direct examination of the original video. Second, the dimensional complexity of the problem is reduced from a 4-dimensional (3D+1T) problem to a 3-dimensional (2D+T) problem, which minimizes the computation cost. In the case of single-file flow, there is no loss of speed information when switching from the X - Y - T representation to the s - T representation. This is because (i) the size of the vessels is small enough to feature single-file flow of cells, and (ii) the spatial location of

the vessel can be determined using motion contrast enhancement. These plots have also been used in AOSLO systems (Zhong, Petrig et al. 2008; Tam and Roorda 2010).

ST plots were generated by converting an X - Y - T coordinate system into an s - T coordinate system (**Figure 2.4**). Consider an arbitrary vessel in a sequence of frames, with an object that moves along the trajectory of the vessel, given by $f(x,y)$. By plotting intensity values along the vessel, and discarding all other pixel values, a two-dimensional plot can be generated that shows the movement of individual objects traveling through a one-dimensional line, given by $f(s)$, where the mapping $f(x,y) \leftrightarrow f(s)$ is defined naturally, with the first coordinate of $f(x,y)$ mapping to the first element of $f(s)$, the second coordinate to the second element, and likewise for the remaining elements. Since we are exactly specifying the mapping from each pixel in X - Y - T space to s - T space, the mapping is invertible.

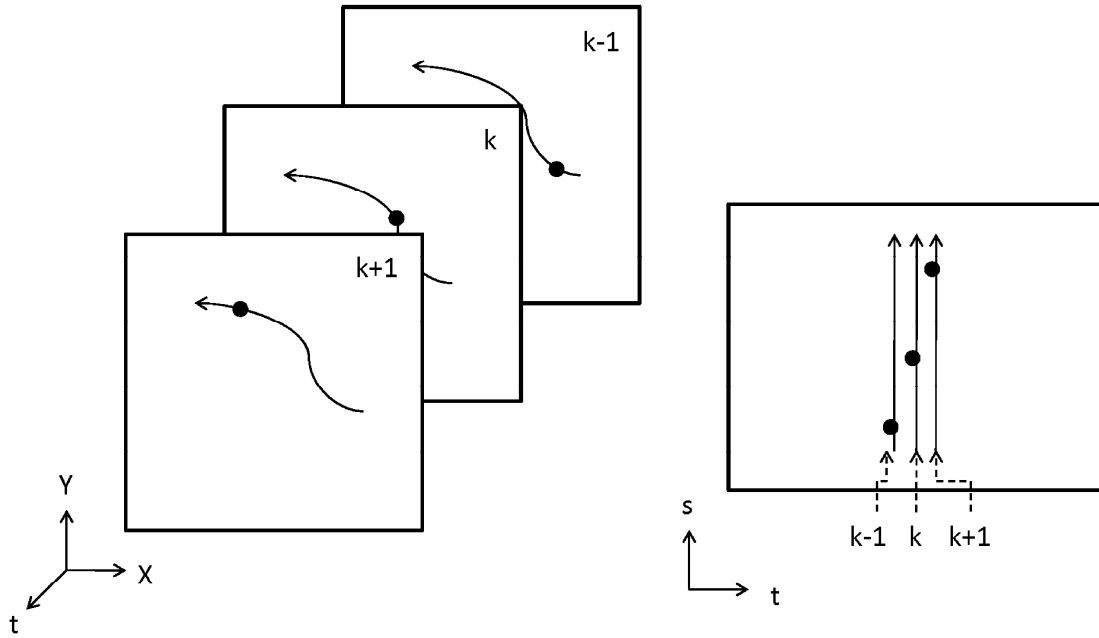


Figure 2.4: Conversion of X - Y - t coordinate system (left) into s - t coordinate system (right). Three consecutive frames, $(k-1, k, k+1)$, are shown with a dark circle representing a single leukocyte traveling along a vessel centerline.

Motion contrast enhancement improves ST plot implementation by increasing the accuracy of vessel centerline extraction, and by increasing the contrast of cell paths (Tam and Roorda 2010) (**Figure 2.5**). Using motion contrast enhanced ST plots, we manually extracted cell traces for the tracking and speed quantification. To identify traces, the user was presented with a graphical user interface (GUI) showing a portion of a ST plot. The user identified traces by selecting points along that trace. For consistency, points were selected at the border between the dark and bright regions of the trace, on the leading edge (**Figure 2.6**). After points were selected, interpolation was performed using piecewise splines constrained to the pixel resolution.

ST plots can also be used to label cells on the unprocessed AOSLO video (i.e. cell tracking). To do cell tracking, the coordinates of each extracted trace were used to register the location of the blood cells in the video. ST coordinates (s, t) were converted back to video coordinates (x, y, t) using the invertible mapping defined during generation of ST plots. Video coordinates were compiled into a list and then used to mark object locations to visualize the tracking results, and to verify that objects were being identified correctly.

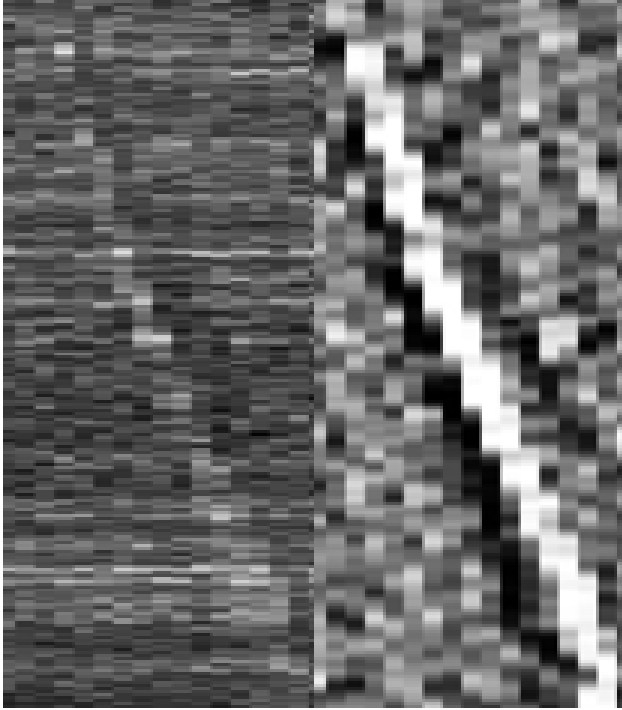


Figure 2.5: Single trace before and after motion contrast enhancement. The vessel centerline was identified with motion contrast enhancement, and the same centerline was used to generate the spatiotemporal plot of a single trace in both cases. Motion contrast enhancement incorporates information in both the spatial and temporal directions. The process of motion contrast enhancement thickens traces and enhances the contrast.

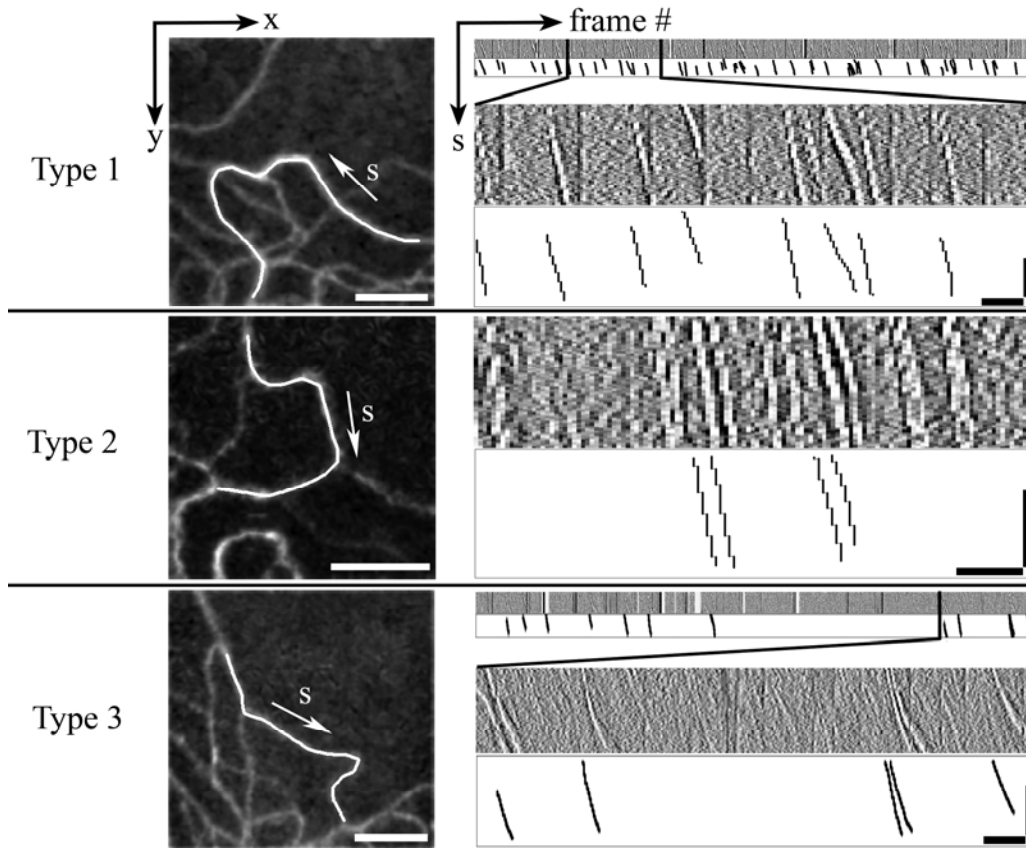


Figure 2.6: Generation of motion contrast enhanced ST plots from AOSLO videos using the same videos shown in **Figure 2.2**. The first column shows the vessel centerline that was selected for analysis. The second column shows ST plot analysis. On the ST plots, diagonal streaks represent moving objects, while vertical streaks represent blinks or saccades, where the video intensity drops for 1-3 frames. Extracted traces are shown directly beneath the corresponding ST plot. (top) Type 1 video, all frames (1 to 1200), and frames 201 to 400 magnified from entire strip. (middle) Type 2 video, all frames (1 to 126). (bottom) Type 3 video, all frames (1 to 2387), and frames 1987 to 2387 magnified from entire strip. Vessel image scale bars, 100 μm ; ST plot horizontal scale bars, 0.5 seconds, vertical scale bars, 0.25 mm.

Quantification of object speeds

In the absence of eye motion, the speed of an object in a raster scanning system can be explicitly computed using line information from pairs of frames (Xu, Manivannan et al. 2002). The correction is based on computing the actual time at which a given line was acquired, as opposed to assuming that the entire frame was acquired at the same time.

The true time, t , can be computed as

$$t = T_f \left(1 + \frac{l_2 - l_1}{N_l} \right), \quad (3)$$

where T_f is the time per field, l_1 and l_2 the scan lines of the object center in the first and second frames, and N_l the number of scan lines per frame. However, this approach (**Equation 3**) must be modified for AOSLO videos since the effect of the raster scan is confounded with eye motion and desinusoiding.

In a non-raster scanning system without eye motion, the speed of an object can be computed by simply computing the slope of the extracted trace from an ST plot. However, in the AOSLO, the slope of the trace gives speeds in time units of frames. We present a slope modification procedure to correct speeds, based on computing the acquisition time the coordinates in the extracted traces. In order to perform the correction, line numbers on preprocessed videos need to be transformed back to line numbers on the raw videos (not preprocessed). This is important because the correction for intraframe eye motion results in local stretching or compression of pixels, thereby altering line numbers.

The AOSLO uses a fast horizontal scan and a slower vertical scan, from left to right and top to bottom directions, respectively. The main component of the error is due

to the slower vertical scan; the error due to the horizontal scan is small and does not need to be corrected (discussed in more detail in subsequent sections). As an example, in the absence of eye motion, a downward moving object will have a larger observed displacement compared to the actual displacement, since the scan is chasing a moving target. More generally, any object that is moving in a non-horizontal trajectory has a vertical component of velocity that needs to be corrected. If there is eye motion, then the actual displacement is also dependent on the amount that the eye has moved.

Consider coordinates from the extracted traces, given as $(frame\ number, s)$. The acquisition time for each line (in units of partial frames) can be computed as:

$$acquisition\ time = frame\ number + \frac{L}{512} \quad (4)$$

L is the line number at which the data was taken on the raw video, and can be recovered in the following manner:

1. Recover the line number, L_{crop} , of the object on the cropped video by determining the y coordinate from the inverse transformation $s \rightarrow (x,y)$.
2. Correct the line number for cropping by adding back the number of lines at the top of the image that were removed during cropping, dL_{crop} , stored during preprocessing.
3. Correct for eye motion by applying the inverse transformation, S^{-l} , from raw to stabilized videos. S^{-l} was stored during preprocessing in the eye motion trace.

Compute $L = S^1(L_{crop} + dL_{crop})$. The extracted traces are then plotted as (*acquisition time, s*).

For each corrected trace, a linear regression was applied and the slope of the line, with units of *pixels/frame*, was used to compute the speed of the leukocyte (in units of *mm/s*) through the selected vessel segment in the following manner:

$$slope * \left(\frac{2 * frame\ rate * \frac{mm}{deg}}{X\ scale\ factor + Y\ scale\ factor} \right) = speed\ in\ \frac{mm}{s} \quad (5)$$

Sample conversion parameters for Type 1, 2, and 3 videos are summarized in **Table 2.1**.

The mm/deg conversion factor on the retina was estimated as described previously (Li, Tiruveedhula et al. 2010; Tam, Martin et al. 2010).

Virtual AOSLO

The AOSLO is a custom-built, unique instrument with ~5x the resolution of a commercial Scanning Laser Ophthalmoscope. Typically, ground truth for new systems is generated using manual analysis performed by subject experts. However, due to the low contrast of the moving objects, it is difficult and unreliable to analyze videos by naked eye. Therefore, we used a virtual AOSLO to simulate realistic videos to create a synthetic dataset for use as ground truth in order to validate our methods.

Virtual AOSLO Parameters

A virtual AOSLO has previously been used to characterize scanning distortions due to raster scanning and eye motion for static images (Campanelli, Vogel et al. 2003). We

modified this virtual AOSLO to simulate the acquisition of a video in the presence of an object that is moving at the same time as the scanner. For the virtual AOSLO, we selected scanning parameters for a Type 1 video, which is the data set on which the proposed methods were developed. Since we were able to specify exactly the speed and position of the moving object, we considered the simulated videos to be ground truth. Due to the complexity of the AOSLO, the following assumptions were used for the virtual AOSLO:

1. The imaging laser is a perfect, dimensionless dot that samples with true fidelity one pixel of the input image at one time.
2. The retina is rigid and planar across the field of view.
3. Eye motion is strictly translational, with no torsional component.
4. Imaging parameters are constant.

The first assumption bypasses sampling and resolution issues introduced by the optics of a human eye. This means that the quality and appearance of the simulated video depends primarily on the input image. Second, for the field of view of the simulation (1.5 degrees in each direction), it is reasonable to assume that this region is both rigid and planar. Third, as described previously, the primary components of eye motion are translational (Martinez-Conde, Macknik et al. 2004). While we have observed torsional motions, they are typically small (unpublished experimental observations). The final assumption is that imaging parameters are constant – in actual practice, due to additional complexities such as calibration and temperature-dependent drift of

electronic components, different imaging sessions have minor variations in imaging parameters (these variations are addressed using calibration steps prior to each imaging session).

An overview of the virtual AOSLO is shown in **Figure 2.7**, and a summary of the parameters selected for the simulation are shown in **Table 2.2**. The input image was generated using individual frames from overlapping AOSLO videos near the fovea, which were scaled to the appropriate size (circle diameter = 3.75 degrees). The spatial resolution of the input image was selected to be twice that of the output video, and sampled by the virtual AOSLO using nearest neighbor interpolation. Thus, the simulated videos are similar to actual AOSLO videos, which allow us to apply the same correction steps that we would have applied to actual AOSLO videos.

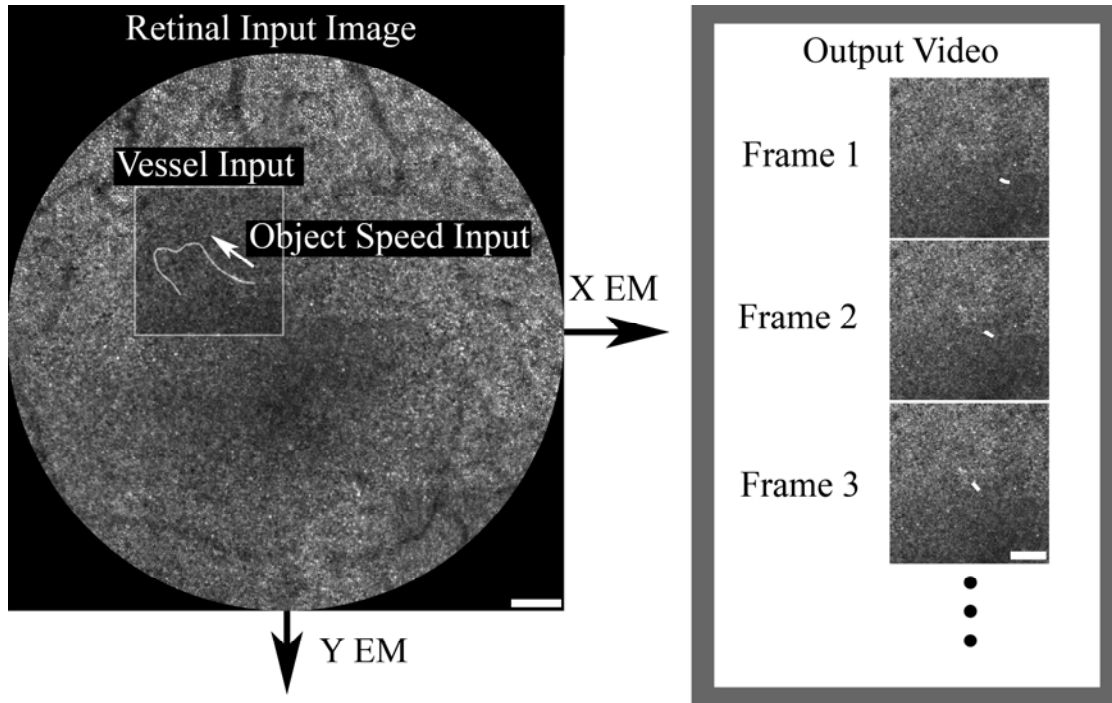


Figure 2.7: Overview of virtual AOSLO used to simulate videos of a moving object in the presence of raster scanning and eye motion. An arbitrary vessel and flow direction was inserted into a retinal input image, and an object speed was specified. The rigid input image, vessel, and object were translated according to specified X and Y eye motion (EM) inputs. The frames in the output video were generated using the scan parameters and configuration described in **Table 2.2**. Scale bars, 100 μm .

Table 2.2. Virtual AOSLO Parameters

<i>Parameter</i>	<i>Value</i>
Horizontal raster frequency	15.36 kHz
Vertical raster frequency	30 Hz
Video frame size	512 x 512 pixels
Video acquisition rate	30 fps
Sampling band	Central 80% of forward sweep
Retinal scale factor	0.296 mm/deg
X and Y scale factors	341.33 pixels/deg
Vessel diameter	5 μm
Leukocyte length	15 μm in the direction of travel
Leukocyte speeds	1.00 to 3.00 mm/s

Simulated videos were generated pixel by pixel. The basic steps were to (i) calculate the pixel timing given the raster parameters, (ii) convert timings to spatial coordinates on the input image, and (iii) sample the input image at the specified spatial coordinates. The time that each pixel is sampled can be computed directly using the raster scan parameters. To convert times to spatial coordinates, two calculations were done. First, the spatial coordinates were calculated assuming a static image. Second, the spatial coordinates were translated horizontal and vertically as specified by the X and Y components of eye motion, corresponding to the timing at each pixel location. Finally, sampling was performed after insertion of a moving object into the input image. For the moving object, we specified the trajectory and speed and used a high contrast, elongated object oriented along the direction of travel. The time-dependent input image was then sampled at the corresponding spatial coordinate for each pixel to generate a simulated AOSLO video.

Experiments using the virtual AOSLO

The virtual AOSLO was used to generate a synthetic data set for validation. The synthetic data set consisted of simulated videos with different configurations, varying in object speed, vessel geometry and orientation, eye motion, and noise (**Table 2.3**). A single moving object was used for each of the videos.

Table 2.3. Parameters for simulated videos

<i>Video code</i>	<i>Vessel orientation</i>	<i>Object speed</i>	<i>Eye motion</i>
H3	Horizontal	3 mm/s	No
V1	Vertical	1 mm/s	No
V3	Vertical	3 mm/s	No
V1_EM	Vertical	1 mm/s	Yes
A2	Arbitrary	2 mm/s	No
A2_EM	Arbitrary	2 mm/s	Yes

The goals of these experiments were to (i) verify that the error in measured speed was negligible in the horizontal direction, (ii) verify that the theoretical errors in measured speeds were consistent in the vertical direction, and (iii) examine the expected effects on calculated speeds due to experimental conditions. H3 was used to quantify the error due to raster scanning in the horizontal case, for an object moving at 3 mm/s – the faster the object moves, the greater the error expected. Most objects traveled at speeds between 1 and 3 mm/s. V1 and V3 were used to quantify the error due to raster scanning alone for an object traveling in the vertical direction. For the experimental conditions, the two factors that contribute most to changes in measured speeds were considered: vessel trajectory and eye motion. For the vessel trajectory videos (A2, A2_EM), we used the vessel centerline extracted from the Type 1 video as the vessel input. For the eye motion, we used the extracted eye motion trace from the first 1.3 seconds of the Type 1 video. We considered these two factors both separately (V1_EM, A2), and simultaneously (A2_EM).

Measurements of flow dynamics across the capillary network

For the third subject, we acquired a more extensive set of AOSLO videos, and used these videos to measure various aspects of flow dynamics. Specifically, every capillary segment near the FAZ was individually analyzed using ST plots. For each ST plot, sloped traces were manually extracted to derive the following information about flow dynamics: frequency, flow direction, speed, and pulsatility. Frequency information could be computed by simply counting the number of extracted traces, and dividing by the length of the video. To compute flow direction of each trace, a linear regression was

applied, and the sign (positive or negative) of the slope was used to determine the flow direction. The speed was quantified using the procedure described above that corrects for measurement errors due to raster scanning and eye motion.

To measure pulsatility, a photoplethysmograph (MED Associates Inc., St. Albans, VT, USA) was attached to the subject's thumb, and the output was continuously recorded in a data file during video recordings, using a data acquisition (DAQ) device (USB-6008, National Instruments, Austin, TX). The output was simultaneously analyzed in real-time to detect the location of the largest peak of the pulse waveform, and then encoded onto the video by marking the frame at which the detection occurred with a small white square (referred to as a "pulse blip" in the remainder of the manuscript). Typically, the pulse waveform consists of two peaks. The absolute and relative amplitudes of the two peaks varied depending on the individual. Although a pulse detection algorithm had already been previously implemented (Martin 2009), we found that the previous algorithm occasionally identified false blips in situations when the subjects' secondary waveform peak was very prominent. Thus, we developed a new algorithm. The real-time algorithm that was implemented in order to detect the location of the largest peak of each waveform is described in pseudocode below. This algorithm is based on finding the first peak of the approximated first derivative of each pulse waveform. After the imaging session, the encoded blips were checked against the recorded data files to verify proper detection and proper encoding into videos.

Pulse waveform peak detection algorithm

```
% Continuously calculate pairwise differences
current_pairwise_difference_value = current_waveform_value-
previous_waveform_value;
[continuously record these values in the pulse data file]

-----

% Initialization (run once after stable waveform achieved)

% Calculate the RMS average of at least 3 complete waveforms
RMS_avg; % Store result in RMS_avg
% set threshold to twice the RMS_avg
threshold = RMS_avg*2;

-----

% Detection code (run continuously during video acquisition)

% Look for a peak if the threshold is breached
if(current_pairwise_difference_value > threshold)
    % keep going until first peak; then stop
    while(current_pairwise_difference > currentmax)
        currentmax = current_pairwise_difference;
    end
    % When at the first peak, stop and record it.
    [Mark a blip on the current frame]
    [Mark the peak location in the pulse data file]

    % Reset current max to get ready for the next blip
    currentmax = 0;

    % Wait until the next waveform before continuing
    while(current_pairwise_difference_value > threshold)
        [Do nothing]
    end
end
end
```


To quantify a pulsatility index, a velocity waveform was generated using the encoded pulse blips. Since each pair of pulse blips corresponded to one pulse cycle, a velocity waveform could be generated by combining all pairs of pulse blips across a video. Speeds were plotted as a function of time relative to the pulse cycle, given by $(F_T - F_{B'}) / (F_{B''} - F_{B'})$, where F_T is the central frame of the extracted trace, and $F_{B'}$ and $F_{B''}$ are the frames of the pulse blips immediately preceding and following F_T (**Figure 2.8**). At the beginning of the video, when there is no preceding pulse blip, the timing is estimated by extrapolating from the next two pulse blips, given by $(F_T - F_{B''}) / (F_{B'''} - F_{B''})$, where $F_{B''}$ and $F_{B'''}$ are the frames of the next two pulse blips. A similar procedure is used at the end of the video, if there is no pulse blip after an extracted trace. This process normalizes measured speeds to the current heart rate, and is appropriate when the heart rate stays reasonably constant for the duration of the recording session. To compute an averaged velocity waveform, the pulse cycle was divided into five equal segments, and data within each segment was averaged, as described previously (Martin 2009). These segments were used to compute the pulsatility index, given by $V_{max} - V_{min} / V_{mean}$, where V_{max} and V_{min} are the maximum and minimum calculated speeds across the entire video for a given vessel, and V_{mean} is the average (Riva and Petrig 1980).

Artifacts due to blinks or failures to properly correct for eye motion are easily distinguished from actual signal due to blood flow, since they give rise to purely vertical lines on the spatiotemporal plots.

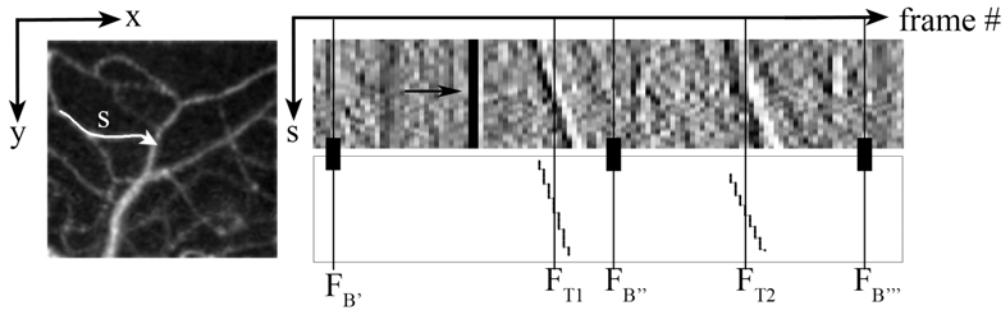


Figure 2.8: Generation and analysis of a spatiotemporal plot. An example is shown for one capillary segment from one video. A vessel centerline is identified on the image of perfused capillaries. Vessel coordinates are converted from (x,y) coordinates to (s) coordinates to reduce data by one spatial dimension. To generate the spatiotemporal plot, intensities along s are plotted for each frame of the division video. A 120-frame segment of the spatiotemporal plot for the selected vessel is shown. Sloped traces, which correspond to motion of fluid parcels, are manually extracted. Purely vertical traces are due to artifacts – one example, due to a blink, is shown (arrow). Two example traces that were extracted are shown. The extracted traces were analyzed to give information about flow direction, frequency, speed, and pulsatility as described in the text. F_{T1} and F_{T2} are the frames at which traces were extracted; $F_{B'}$, $F_{B''}$, and $F_{B'''}$ are the frames at which pulse blips occurred.

2.4 Results

Since the Type 1 videos had the highest spatial contrast for the moving blood cells, we developed our methods using only Type 1 videos, and used Type 2 and 3 videos as well as synthetic videos generated by a virtual AOSLO for verification. The proposed methods performed well on both the synthetic data set generated using the virtual AOSLO, and on experimental videos acquired on the AOSLO.

Expected error due to raster scanning

The raster scan error is significant for AOSLO videos. In this section, we develop a theoretical model to quantify the magnitude of the raster scan error. To understand the nature of the expected raster scan error, consider the case of a vertically oriented vessel with a downward-moving object that starts at the top of the image (**Figure 2.1**). Assuming that there is no eye motion, we derive the expected raster scan error in the vertical and horizontal cases for comparison to actual measured error rates, and show that it is significant in the vertical direction, but not the horizontal direction.

We introduce the dimensionless number,

$$RS = \frac{v_o}{v_s} \tag{6}$$

where v_o is the speed of the object, and v_s is the speed of the scanning line.

If $RS > 1$, then the system is unable to image the object and the error becomes infinite. When $RS = 0.5$, the error is exactly 100%. When $v_o \ll v_s$, $RS \rightarrow 0$, and the raster scan error is negligible. By convention, leukocyte speeds on the retina are reported in mm/s. For an object speed given in mm/s , $\overline{v_o}$, with scan speed, v_s , given in $pixels/frame$, with scale factor as defined in **Table 2.1**, RS can be calculated as

$$RS = \frac{\text{scale factor in scan direction}}{\text{frame rate} * \text{mm / deg on the retina}} * \frac{\overline{v_o}}{v_s} \quad (7)$$

When the object is moving in the same direction as the raster scan, the speed of the object as measured by the system, v_e , will be overestimated. The percent error due to raster scanning is given by

$$\text{percent error} = \frac{v_e - v_o}{v_o} \quad (8)$$

Assuming the object and scan have speeds of v_o and v_s , the relationship between object speed and measured speed is:

$$v_e = \frac{v_o}{1 - RS} \quad (9)$$

The percent error due to the raster scan is

$$\text{percent error} = 100\% * \frac{RS}{1 - RS} \quad (10)$$

For a model object moving downwards at 1 mm/s in the vertical direction, the overestimation is 8.1% for a Type 1 video, 10.1% for a Type 2 video, and 4.0% for a Type 3 video, assuming no eye motion. At 3 mm/s, the overestimation is 29.1% for a Type 1 video, 37.8% for a Type 2 video, and 13.0% for a Type 3 video (**Figure 2.9**).

Thus, the raster scan error increases when one or more of the following occur: v_s decreases, $\overline{v_o}$ increases, or the field of view decreases (the field of view varies inversely with the scale factor in the scan direction).

A similar analysis can be used to estimate the expected error in the horizontal scan direction. Since the scan speed is defined as the number of rows required to reach the edge of the frame, for the horizontal direction, $RS_{horizontal} = RS_{vertical} / 512$. The

$$\text{percent error in the horizontal direction} = 100\% * \frac{RS_{vertical}}{512 - RS_{vertical}}. \text{ Since}$$

$RS_{vertical} < 1$ for objects of interest, the percent error in the horizontal direction will always be less than 0.20%. When $RS_{vertical} = 0.5$, the percent error in the horizontal direction drops to 0.098%. Therefore, we do not need to apply the raster scan correction to the horizontal component of calculated speeds.

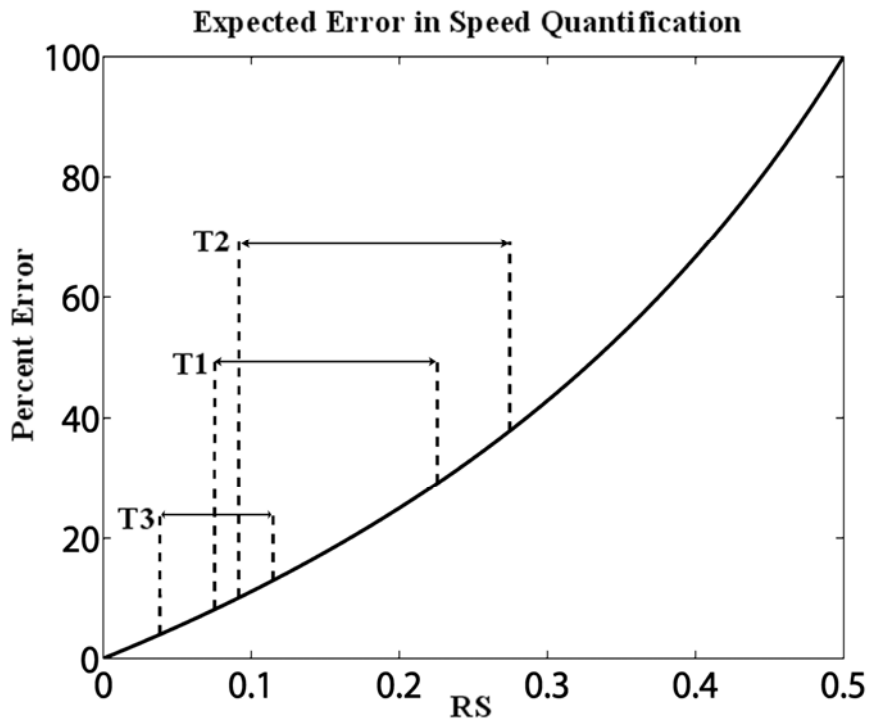


Figure 2.9: Expected raster scan error assuming no eye motion, for a vessel that is oriented in the same direction as the scanner. The range of errors for an object moving between 1 and 3 mm/s is shown for a Type 1 (T1), Type 2 (T2), and Type 3 (T3) AOSLO video. The portion of the plot corresponding to each video type is marked.

Evaluation of accuracy and validity using a virtual AOSLO

We applied the proposed methods for tracking and speed quantification (**Figure 2.10**). To measure speeds in the simulated videos, we repeated the analysis 5 times and took the average of computed speeds, in order to reduce the errors due to operator bias and differences in data precision. The data precision varied since there were 3 times as many data points that could be extracted to measure speeds at 1 mm/s vs. 3 mm/s. At 3 mm/s, due to large pixels/frame displacements, the traces on the ST plots were disconnected.

To validate that objects were being tracked correctly, we generated a tracked video and used frame-by-frame examination. As expected, for all videos, the extracted traces corresponded to the moving objects. However, the labeled lines would sometimes lead or lag the moving objects by small amounts. Since the amount of lag/lead was preserved for each moving object, the slope of the traces was accurate. The error was due to the estimation of frame number from the coordinates of the extracted traces, due to the low temporal resolution relative to the speed of the leukocytes. Taking this into consideration, there were no false positives and no false negatives.

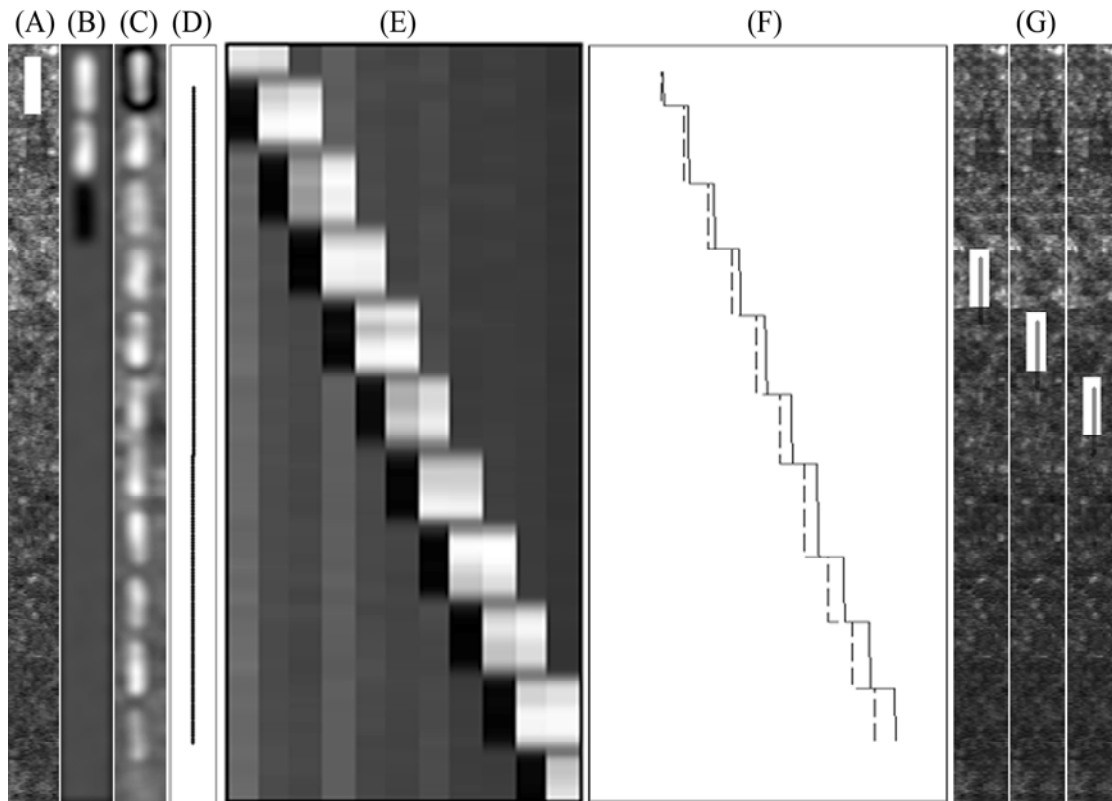


Figure 2.10: Tracking and speed quantification on V1_EM. (A) First frame in which the object appears from a preprocessed video. (B) Corresponding frame in the multi-frame division video. (C) Standard deviation image calculated from 15 frames. (D) Extracted vessel for offline generation of the ST plot. (E) ST plot for the selected vessel. (F) Extracted trace from the ST plot (dotted line on left), and the corrected trace taking into consideration both raster scanning and eye motion (solid line on right). Notice that the speed was overestimated prior to correction, as expected. (G) Three consecutive frames of the video showing tracking results.

Table 2.4. Evaluation of Speed Quantification

<i>Video code</i>	<i>H3</i>	<i>V1</i>	<i>V3</i>	<i>V1_EM</i>	<i>A2</i>	<i>A2_EM</i>
No RS [mm/s]	3.0082	1.1428	3.9370	1.1242	1.8956	2.0067
RS [mm/s]	3.0110	1.0552	3.0608	1.0361	1.9766	2.0283
No RS vs. RS %	-0.09%	8.31%	28.63%	8.50%	-4.10%	-1.07%
RS vs. Actual %	0.37%	5.52%	2.03%	3.61%	-1.17%	1.42%

Speeds are reported before (No RS) and after (RS) the proposed correction. Actual speeds are the object speeds corresponding to each video, as listed in **Table 2.3**.

We compared the corrected speeds to the actual speeds (**Table 2.4**). We define the residual error as the percent difference between corrected and actual speeds, and found that the residual error was on average 2% for moving objects traveling between 1 and 3 mm/s. The sources of error are most likely due to vessel and trace extraction, which are dependent on user interaction. For experimental data, these sources of error are likely to increase due to (i) lack of prior information about vessel trajectories and (ii) variations in trace slopes. For the synthetic data sets, extraction is more accurate due to prior knowledge about the shape of the vessel (since it was specified), and due to the fact that object speeds are uniform (so that there is no variation in trace slopes).

H3 confirms that the error in measured speed is negligible in the horizontal direction, since the calculated error was -0.09%. This is also in agreement with the theoretical model, which specifies an upper bound of 0.20% for the error. Therefore, it is a reasonable assumption to neglect the error due to horizontal scanning.

V1 and V3 confirm the theoretical errors due to the vertical component of raster scanning. We found errors of 8.3% and 28.6%, which are in agreement with the theoretical errors of 8.1% and 29.1%. Therefore, in the absence of eye motion, the computed errors are in agreement with the expected errors.

Eye motion can either increase or decrease the magnitude of the error. If eye motion is random and isotropic, then over time the average speed should not be affected by eye motion. However, if the eye favors motion along a preferred direction, then the computed speed is affected – the computed speed is maximally increased when the object, raster scan, and eye motion are in the same direction (i.e. all vertical and

downward). Initially, the vertical component of the eye motion trace input is in the same direction of the scan – as expected, the error for V1_EM is slightly larger than V1.

In practice, vessels are rarely horizontal or vertical, particularly when considering capillaries. First, the magnitude of the error in calculated speed depends on the trajectory of the vessel at the object location, since only the vertical component of speed is corrected. Therefore, deviations from a vertically-oriented vessel should result in diminishing error magnitudes. Second, the start and end points of the vessel ultimately determine whether speeds are over- or underestimated. The vessel in A2 and A2_EM has both upward and downward components, but since the endpoint is lower than the starting point, this means that we should expect speeds to be underestimated when comparing A2 to V2. Since the eye motion results in a slight overestimation (comparing V1_EM to V1 and using the same eye motion input), this explains why the error for A2_EM is less than the error for A2.

Evaluation on experimental AOSLO videos

We performed the proposed methods on 40 vessels from 10 AOSLO videos; first we report results across all videos, and then we show detailed results for one representative vessel for each video Type.

10 vessels were analyzed from 1 Type 1 video; 10 vessels from 3 Type 2 videos; and 20 vessels from 6 Type 3 videos. The average absolute error in measured speed was 2.59% for the Type 1 video, 3.39 % for the Type 2 video, and 2.04% for the Type 3 video, where absolute error was defined as the absolute value of the percent difference between corrected and non-corrected speeds for one trace, and the average absolute

error was defined as the average absolute error across all extracted traces for each video Type. For comparison, we estimated the error using the RS parameter defined at the beginning of this section, taking $\overline{v_o}$ to be the average object speed. In the absence of eye motion, for a vertically-oriented vessel, the theoretical error was 12.56% for the Type 1 video, 12.84% for the Type 2 video, and 5.27% for the Type 3 video. This suggests that either vessel orientations are horizontally biased, or that eye motion is not uniformly distributed across all orientations.

We selected three representative vessels from Type 1, Type 2, and Type 3 videos to further characterize the error in measured speeds. For each vessel, traces were extracted from ST plots and used for tracking on the original videos and speed quantification (**Figure 2.11**). Close examination of **Figure 2.11** shows that the orientation of the vessel has an effect on the slope modification as long as the effect due to eye motion is small (i.e. one can see whether the slope was over- or under- estimated corresponding to a downward- and upward-oriented vessel). We will discuss this effect in more detail considering the actual errors in average speeds that were calculated (**Table 2.5**). In experimental videos, there are complexities such as arbitrary vessel shapes and orientations, eye motion, and variations in cell speeds both temporally and spatially. There is also noise due to variations in the intensity of the background photoreceptor tissue, likely due to dynamic scattering changes over time (Pallikaris, Williams et al. 2003), and also coherence artifacts (Jonnal, Rha et al. 2007; Putnam, Hammer et al. 2010). These variations generate noise in the multi-frame division videos, and affect the appearance of the ST plots. Therefore, the actual error in

calculated speeds due to raster scanning and eye motion will be different. We compared our corrected speeds to uncorrected speeds, where uncorrected speeds were taken as simply the slope of the manually extracted trace, which assumes that the entire frame was acquired at the same moment in time.

The actual error in the average speeds is 2.51% for the Type 1 video, 9.25% for the Type 2 video, and 2.83% for the Type 3 video. As described previously, the magnitude and sign of the error is determined largely by the trajectory of the vessel. For all three Types, the vessels deviate from a purely vertical vessel, and so the magnitude of the error is diminished compared to the model. In addition, because the end point of each vessel is lower than the start point, we expect an overestimation of speed for all three Types. The Type 2 video has the largest error, as predicted by the theoretical model (**Figure 2.9**). Notice that there is a nonlinear shift that results due to the raster scan correction. Close examination of the Type 1 traces in **Figure 2.11** show that the slopes at the bottom of individual traces were decreased after application of the raster scan correction, while slopes at the top were increased. This suggests that the entrance side of the path segment underestimated speeds, while the exit side overestimated speeds, corresponding to a net upwards and net downwards vertical orientations, respectively. As can be seen from **Figure 2.6**, this was exactly the case.

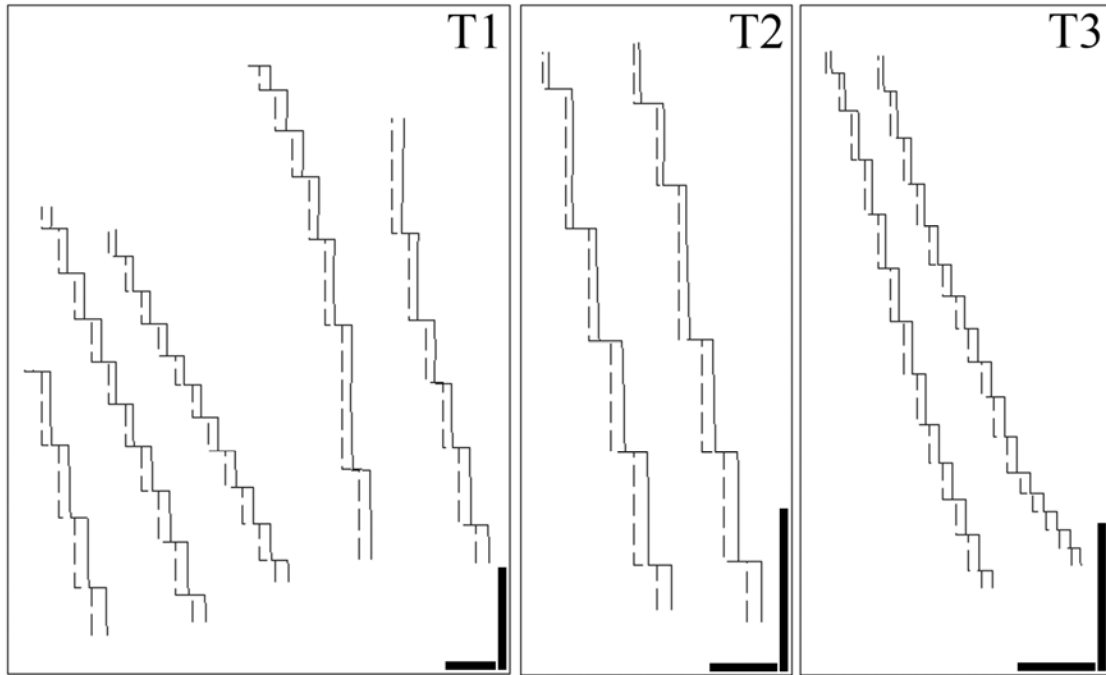


Figure 2.11: Effect of raster scan showing extracted traces (dotted lines on left) and raster scan corrected traces (solid lines on right), for Type 1 (T1, frames 800-830), Type 2 (T2, frames 48-60), and Type 3 (T3, frames 2278-2302) videos. The shifts are nonuniform due to the confounding effects of eye motion. Vertical scale bars, 0.1 mm; horizontal scale bars, 0.1 seconds.

Table 2.5. Summary of cell speeds

<i>Parameter</i>	<i>Type 1</i>	<i>Type 1</i>	<i>Type 2</i>	<i>Type 2</i>	<i>Type 3</i>	<i>Type 3</i>
RS	no	yes	no	yes	no	yes
N	50	50	4	4	12	12
Mean [mm/s]	2.04	1.99	1.89	1.73	2.18	2.12
SD [mm/s]	0.62	0.58	0.30	0.26	0.45	0.43
Min [mm/s]	0.93	0.94	1.62	1.50	1.56	1.53
Max [mm/s]	3.47	3.27	2.16	1.97	2.90	2.80

Summary of cell speeds in selected vessel segments with and without the raster scan correction.

As a final comparison, for the Type 1 video, the error was 2.51%, compared to -1.07% for the same vessel in A2_EM. The reason for this is due to a small difference in the starting and ending points of the vessel. Although we used the same trajectory, the end point of the vessel terminates slightly higher than the starting point for A2_EM, which explains the difference in the sign of the error.

To verify that each extracted trace corresponded to an object on the input video, extracted traces were registered (illustrated in **Figure 2.12**). We individually verified each extracted trace by examining the tracked video frame-by-frame. Overall, the labeled lines tracked the leukocytes well. There were no false positives; it was not possible to calculate a false negative rate.

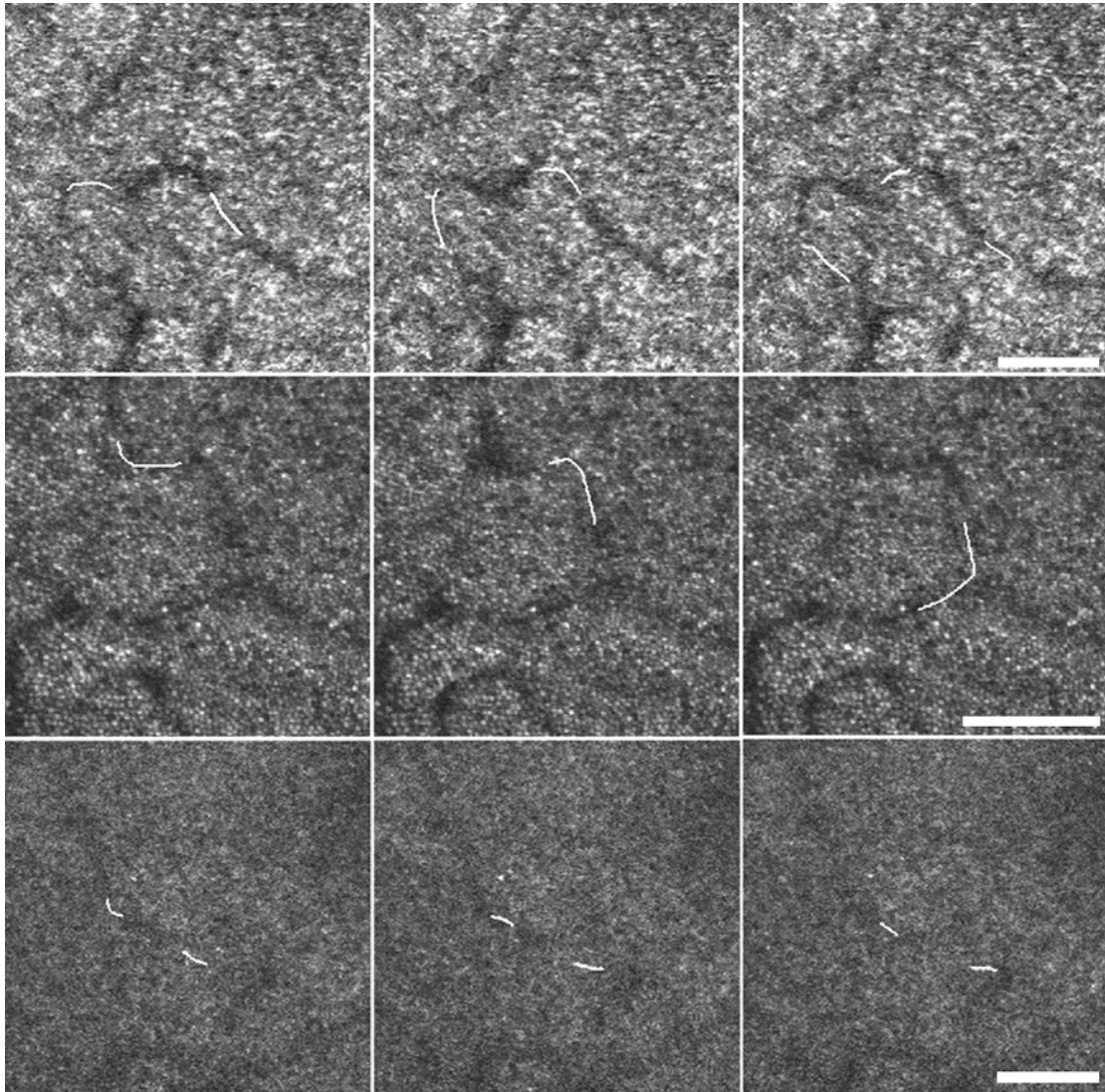


Figure 2.12: Moving objects labeled using white lines in the cropped video using extracted traces from ST plots, for a Type 1 (top), Type 2 (middle), and Type 3 (bottom) video. For visualization purposes, we thickened the line by 2 pixels. Scale bars, 100 μm .

Detailed characterization of single-file flow

For the third subject, a montage of parafoveal capillaries was generated by first applying motion contrast enhancement to each AOSLO video, and then combining overlapping images using image editing software (Adobe Photoshop; Adobe Systems, Inc., San Jose, CA, USA) (**Figure 2.13**). For display purposes, image intensities were normalized and image borders were deleted. This had no effect on the ST plot analysis, since we used non-edited images for the analysis of each video. Arterioles and venules were identified on a fundus photograph of the same eye by a retina specialist; identification of arterioles and venules on the AOSLO montage was then performed by overlaying the montage onto the fundus photograph (**Figure 2.14**). We confirmed many features of the parafoveal capillary network that have been previously described: an FAZ, surrounded by a single layer of capillaries in the zone immediately outside the FAZ; interdigitation of arterioles and venules; arterioles and venules oriented in directions normal to the contour of the FAZ, and capillaries oriented tangentially. Although some arterioles exhibited reduced capillary density compared to venules, this effect was less apparent near the macular region, as previously reported (Yu, Balaratnasingam et al. 2010).

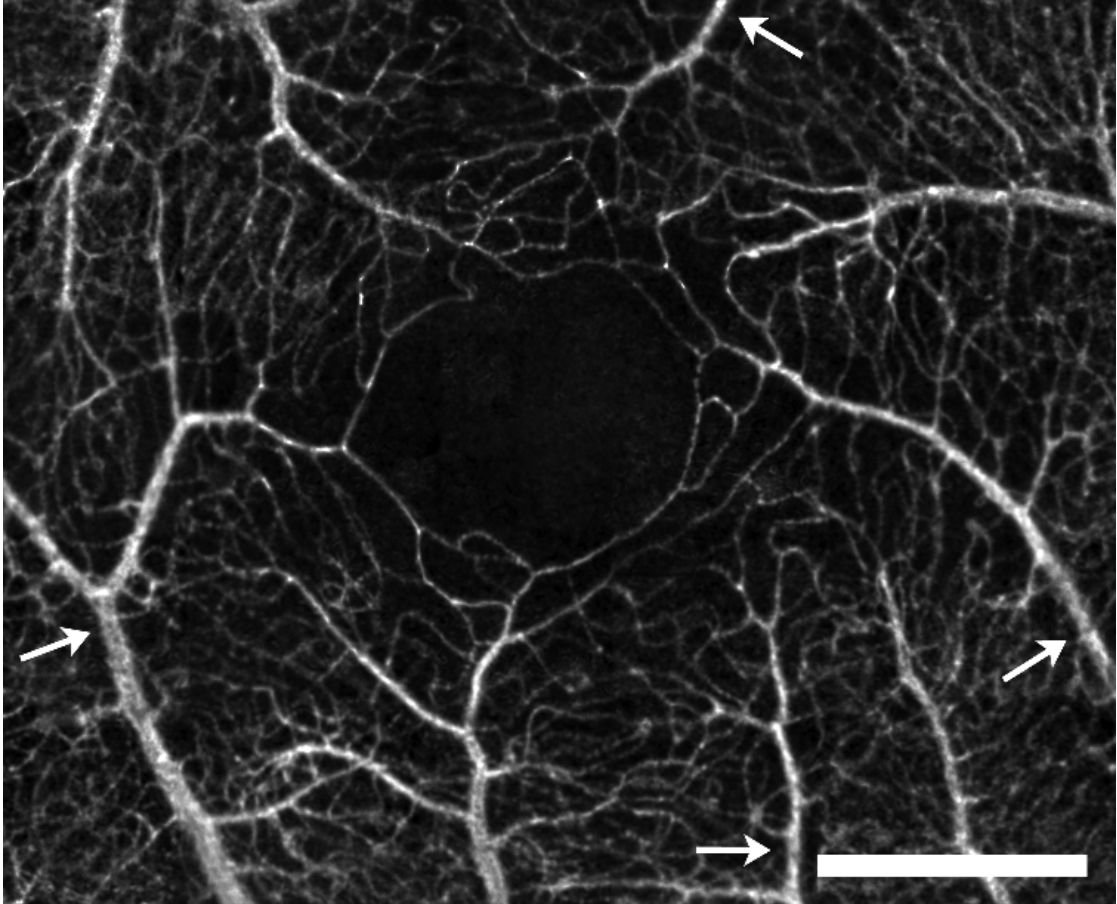


Figure 2.13: Montage showing parafoveal capillaries generated by applying motion contrast enhancement to 76 overlapping AOSLO videos acquired noninvasively without contrast agent. Arrows denote arterioles. Scale bar, 500 μm .

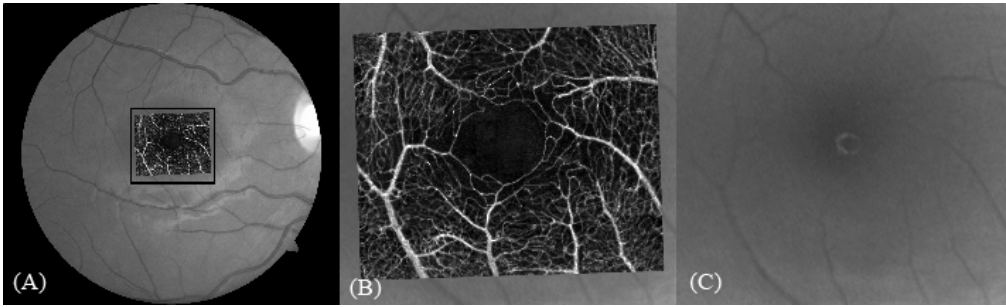


Figure 2.14: Comparison of AOSLO with red free fundus photography. (A) AOSLO overlay on fundus photograph. The black box is magnified in panels (B) and (C).

Comparison to red-free fundus photography

Vessels were overlaid onto the red-free fundus photography for comparison (**Figure 2.14**). Red-free fundus photography was the best option for visualization of vessels in the clinic for this subject, since fluorescein angiography, which involves injection of contrast agent, is not routinely performed for subjects with no systemic or ocular disease. All vessels that could be identified on the red-free were seen on the AOSLO image; the AOSLO image also showed additional capillaries that were not visible on the red-free fundus.

Interpretation and analysis of spatiotemporal plots

There was considerable variation in the appearance of spatiotemporal plots (**Figure 2.15**). In situations where contrast is generated invasively, interpretation of spatiotemporal plots is straightforward: traces on spatiotemporal plots correspond either to fluid gaps from injected dyes, or to individual cells from fluorescently-labeled cells. In the case of cell labeling, one can exactly verify the type of cell that is being analyzed. Since AOSLO images are acquired without contrast agents, direct verification is not possible. We present an interpretation of two unique patterns of the spatiotemporal plots, which we attribute to leukocytes and plasma gaps.

The first category of traces included those that were (i) thick, (ii) high contrast, (iii) sparse, and (iv) unidirectional. We classified these traces as leukocytes traces when all four criteria were met, for the following reasons. First, since leukocytes are larger than erythrocytes, they have a longer length in single-file flow; this corresponds to a thicker trace on the spatiotemporal plot. Second, as described earlier, the fluid

mechanics model of single-file leukocyte flow features an erythrocyte-free plasma zone immediately upstream of the leukocyte, followed by an erythrocyte-packed zone immediately downstream. The size of the plasma and erythrocyte-packed zones are large compared to the size of normal red cell spacings in the absence of leukocytes (Schmid-Schonbein, Usami et al. 1980). At the imaging wavelength (840 nm), erythrocytes are strongly absorbing relative to plasma (Meinke, Muller et al. 2007). We suspect that leukocytes have low absorbance at near infrared. Taken together, these assumptions would lead to high contrast leukocyte traces on the spatiotemporal plots for single-file capillaries. Third, leukocytes were sparse, appearing only in a minority of frames, and absent in the majority of frames; this corresponds to sparse traces on the spatiotemporal plots. Finally, examining the videos directly, leukocytes were always observed to flow in a single direction, with no pausing or dwelling; this corresponds to unidirectional traces. By direct comparison of videos to spatiotemporal plots (i.e. by labeling videos with the coordinates of extracted traces), we verified that when these four conditions were met, extracted traces corresponded to leukocytes on AOSLO videos.

The second category of traces included those that were (i) thin and (ii) dense. We classified these traces as plasma gap traces. These traces tended to have lower contrast than leukocyte traces, which is consistent with direct observations of AOSLO videos, where leukocyte-type objects exhibit higher spatial contrast compared to higher frequency fluctuations that are due to other elements of blood flow. First, a thinner trace corresponds to an object that is shorter; thin traces are unlikely to correspond to leukocytes. This suggests that thin traces are due to either individual erythrocytes or to

plasma gaps between erythrocytes. However, since the density of erythrocytes in capillary flow is high, we do not expect to have the spatial and temporal resolution to reliably visualize the motion of individual erythrocytes. Second, denser traces correspond to higher frequencies. Many of the thin traces occurred at frequencies that were too high to be generated by leukocytes. Some of these traces also exhibited some evidence of bidirectionality (i.e. reversal of flow direction).

Identification of Leukocyte-Preferred Paths and Plasma-Gap Capillaries

Spatiotemporal plots were generated for selected capillary segments near the FAZ, and analyzed for leukocytes and plasma gaps. A total of 114 traces due to leukocytes and 1711 traces due to plasma gaps were identified across 21 capillary segments. We confirmed that the distribution of leukocytes and plasma gaps across the parafoveal network was not uniform.

Leukocyte traffic was not observed through most capillaries. To investigate the distribution of leukocytes, we calculated the frequency of leukocyte flow for each capillary segment, and then generated a histogram showing the distribution of leukocyte frequencies across all capillary segments (**Figure 2.16**). Capillaries tended to either have very few leukocytes (non leukocyte-preferred-paths, non-LPPs), or have many leukocytes (leukocyte-preferred-paths, LPPs); we arbitrarily drew a line in the histogram to separate non-LPPs and LPPs. Next, we labeled non-LPPs and LPPs on a larger montage to show the spatial distribution of leukocyte flow, and found that LPPs were connected capillary segments that corresponded to a subset of thoroughfare

channels, which were the simplest and most direct paths connecting arterial to venous circulations (**Figure 2.17**).

Plasma gaps were observed in all capillaries, but the distribution was also nonuniform. First, we generated a histogram showing the frequency of plasma gaps across all capillary segments (**Figure 2.16**). There was a clear separation in the histogram showing two capillary segments that exhibited steady plasma-gap patterns across the entire spatiotemporal plots (plasma gap capillaries, PGCs), shown to the right of the line in the histogram. Next, we labeled PGCs on a larger montage and found that PGCs were short capillary segments that served as anastomoses between more direct paths (**Figure 2.17**).

To verify the computed flow directions, we also recorded the direction of flow for all the leukocytes, and found that they were in agreement with the direction of flow from arteries to veins as identified on the red-free fundus.

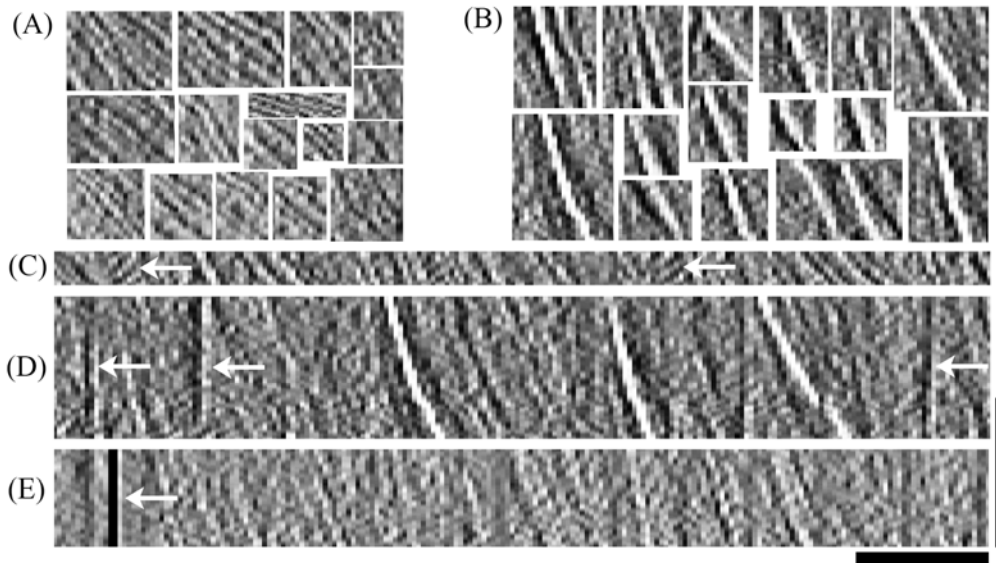


Figure 2.15: Interpretation of spatiotemporal plots, showing representative traces due to (A) plasma gaps and (B) leukocytes. These traces were isolated from full spatiotemporal plots to illustrate the two categories of traces that were identified for analysis. Plasma gap traces are thin and dense, while leukocyte traces are thick, high contrast, sparse, and unidirectional. 200-frame segments of spatiotemporal plots are shown from capillary segments that were identified as a (C) PGC, (D) LPP, and (E) neither a PGC nor a LPP. Note the areas of apparent bidirectionality in the PGC (arrow in C), and artifacts due to poor stabilization when correcting for eye motion (arrows in D) and a blink (arrow in E). Vertical scale bar, 0.5 mm; Horizontal scale bar, 0.5 seconds.

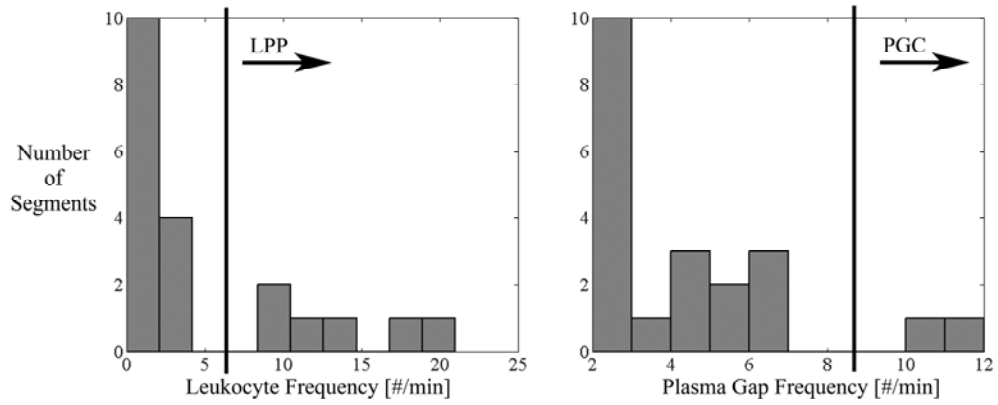


Figure 2.16: Identification of leukocyte-preferred paths (LPPs) and plasma gap capillaries (PGCs). The distribution of leukocyte and plasma gap frequencies [# /min] are shown across all analyzed capillary segments. Vertical lines are inserted at breaks in the histograms to define LPPs and PGCs.

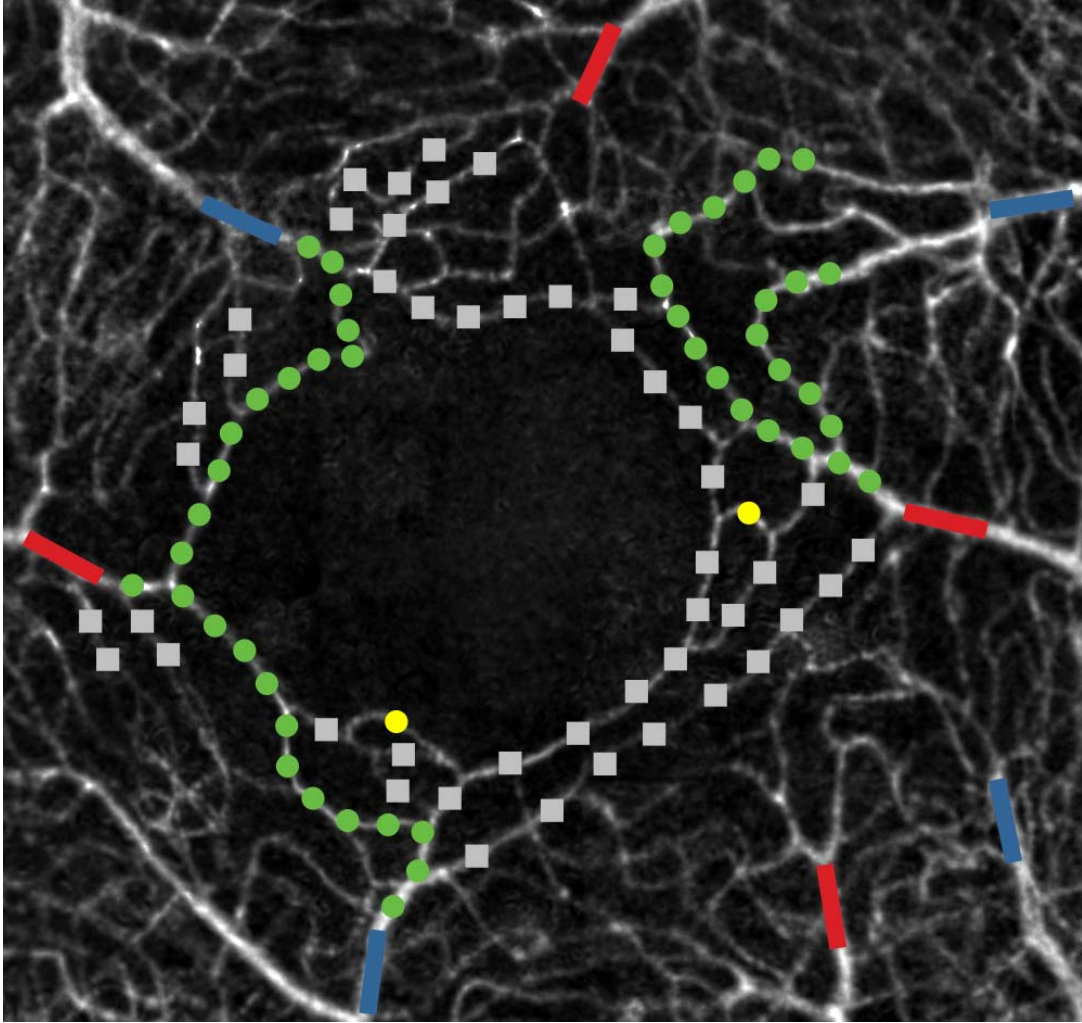


Figure 2.17: Spatial distribution of LPPs (green), PGCs (yellow), and all others capillaries that were selected for analysis (gray). Terminal arterioles (red) and collecting venules (blue) are shown for reference.

Speed and pulsatility of leukocytes and plasma gaps

The speed of leukocytes and plasma gaps were similar in LPPs, and the pulsatility of leukocytes and plasma gaps were similar when considering all capillary segments. To investigate speeds, we calculated the average speeds of leukocytes and plasma gaps. There was sufficient data to calculate plasma gap speeds across all vessels; however, for the leukocytes, only the six capillary segments corresponding to LPPs contained sufficient data for leukocyte speed quantification. All values are reported as mean \pm standard deviation. Leukocytes had a speed of 1.80 ± 0.22 mm/s ($n = 114$ leukocytes in 6 LPP segments), significantly higher than the speed of plasma gaps, which was 1.30 ± 0.55 mm/s ($n = 1711$ plasma gaps in 21 capillary segments) ($p < 0.05$). However, the speed of plasma gaps through the same 6 capillary segments selected for the leukocyte speed measurement was 1.73 ± 0.28 mm/s ($n = 311$ plasma gaps in 6 LPP segments), which was not statistically different compared to the leukocyte speeds ($p = 0.64$).

To investigate pulsatility, we generated averaged velocity waveforms as a function of time relative to the pulse cycle. The pulse cycle was divided into five equal segments to generate an averaged waveform for the calculation of the pulsatility index (**Figure 2.18**). We calculated pulsatility indices only when there was more than one speed measurement in each of the five segments. For the leukocytes, 2 out of 6 LPP segments satisfied these criteria; for the plasma gaps, there were 19 out of 21 capillary segments. There was no significant difference in the pulsatility indices for leukocytes, 0.54 ± 0.05 ($n = 45$ leukocytes in 2 LPP segments), and plasma gaps, 0.61 ± 0.14 ($n = 1652$ plasma gaps in 19 capillary segments) ($p = 0.50$). There was no apparent difference in pulsatility index across the capillary network.

The average heart rate across all videos was 64.8 +/- 5.0 bpm (n = 225 measurements).

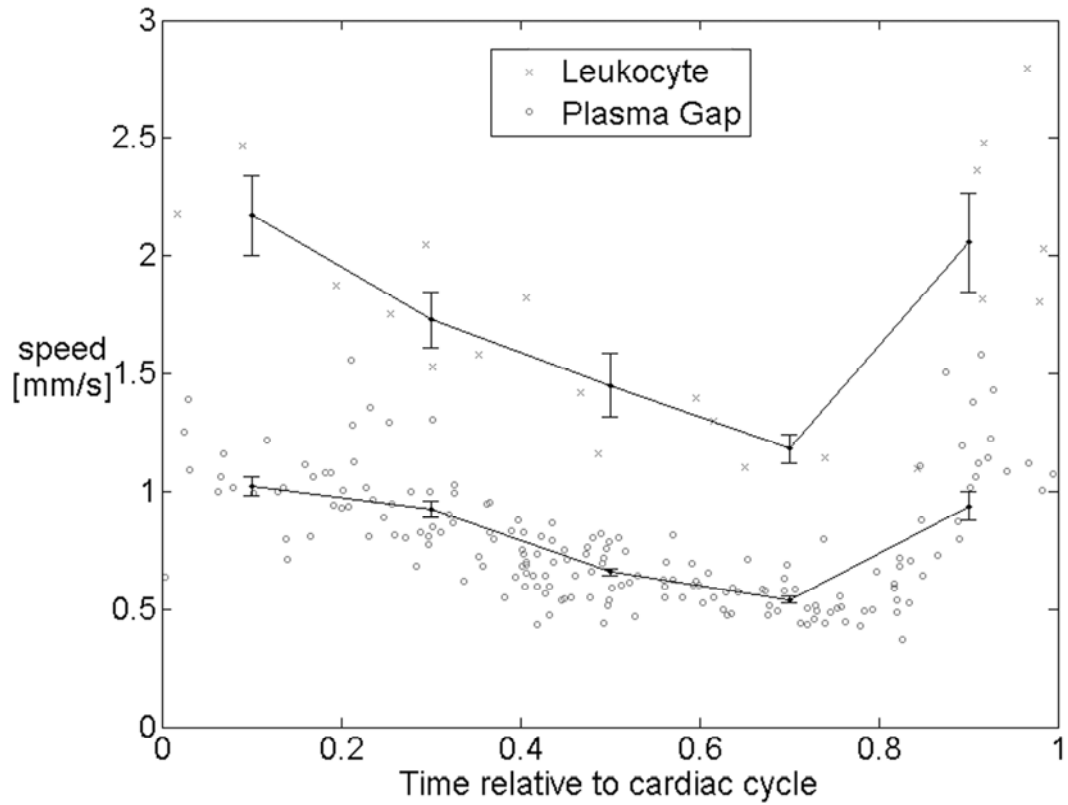


Figure 2.18: Examples of averaged velocity waveforms for leukocytes in a single representative LPP segment (top) and plasma gaps in a single representative PGC (bottom), demonstrating the existence of pulsatility in capillaries with single-file flow. Data from extracted leukocytes and plasma gaps are averaged for five equal segments of the cardiac cycle to generate an averaged waveform.

2.5 Discussion

Tracking and speed quantification of moving objects

This chapter demonstrates a method for quantifying object speeds in AOSLO videos. We demonstrated a multi-frame approach for motion contrast enhancement that improves the contrast of moving objects and vessels. Motion contrast enhanced ST plots were used to visualize hemodynamics, and individual traces were extracted for analysis. Extracted traces were used to track objects on the input videos and also for speed quantification. Speed quantification was done using a slope-modification technique that corrects for raster scanning in the presence of eye motion. We validated our results using a virtual AOSLO. The combination of selected techniques is significant in terms of putting together a complete system of video and image analysis for non-invasive vascular video imaging.

Our results are similar to other methods. A previously reported method using manual identification and analysis on the same vessel from the same Type 1 AOSLO video used in this chapter found a total of 35 objects with a speed of 1.82 ± 0.42 mm/s, without considering the error due to raster scanning or eye motion; our uncorrected speed was 2.04 ± 0.62 mm/s for 50 objects. While the numbers are similar, the discrepancies can be explained with the following considerations: The number of objects identified by the manual method was less than our method, probably due to difficulties in visualizing objects without motion contrast enhancement. It may have been more difficult to visualize objects that were traveling at faster speeds using

the manual method. Finally, the vessel trajectory may not have been as accurate in the manual method.

There are a few similar results from different imaging modalities. Using fluorescein-aided scanning laser ophthalmoscopy, blood flow velocity was measured to be 3.29 mm/s (SD 0.45) in the parafoveal capillaries of 21 healthy volunteers (Arend, Wolf et al. 1991). Our measured speeds are similar in magnitude to these results, but we can explain the discrepancies as follows. First, the location and size of the capillaries was different. Second, we measured leukocyte speeds, while they measured whole blood speeds using fluorescein. It is known that leukocytes travel slower through capillaries than erythrocytes (Ben-nun 1996), which constitute the majority of blood by volume. Thus, differences in spatial locations, small sample size, and differences in the element of blood that is being measured could account for differences in measured speeds. The blue field entoptic phenomenon is another method to examine capillary flow in the parafoveal region that can be used for estimating blood velocities (Arend, Harris et al. 1995). The blue field entoptic phenomenon refers to the movement of “flying corpuscles” that can be seen when looking at an illuminated blue background (Loebl and Riva 1978). It is thought that these “flying corpuscles” are in fact leukocytes. By having observers compare the speeds of these moving objects to those of simulated velocity fields, one can estimate speeds. One study found a speed of 0.89 +/- 0.2 mm/s (Arend, Harris et al. 1995), while another found speeds between approximately 0.5 and 1 mm/s (Riva and Petrig 1980). These speeds are similar in magnitude to those that we obtained, but one needs to be cautious since the blue field technique is subjective in nature.

The methods presented in this chapter can be potentially applied to other high-resolution scanning systems with moving objects. There are many areas for future work, including full automation and application of more advanced detection and tracking methods. There are also important microcirculation studies that can be performed, including development of a family of hemodynamic markers to investigate leukocyte behavior. Such markers could be used to quantify changes in leukocyte behavior for normal and diseased retinas. The human eye allows for a unique opportunity to directly examine the microcirculation, which has been made possible due to improvements in imaging techniques (AOSLO) combined with the image analysis algorithms presented in this chapter.

Raster scanning and eye motion contribute to significant sources of error when quantifying speed on AOSLO videos. The magnitude of this error depends on the speed of the moving object, configuration of AOSLO imaging parameters, the orientation of the vessel, and the isotropy of the eye motion, but can be as large as 37.8%. Slope modification on ST plots can correct for this error, improving the accuracy of hemodynamics using AOSLO.

Characterization of single-file flow

We demonstrate a noninvasive method to characterize single-file flow of leukocytes and plasma gaps through live retinal capillaries in the living human eye. Noninvasive methods are important to confirm previous reports of peculiarities in the microcirculation that have been observed using invasive methods. Motion contrast enhancement, combined with AOSLO, can be used to visualize and analyze the

capillary network. We confirmed and quantified the distribution of leukocytes and plasma gaps across the network, and identified two specific types of capillaries. Leukocyte-preferred-paths (LPPs), a subset of thoroughfare channels, accounted for a clear majority of leukocyte traffic, and plasma-gap capillaries (PGCs), a subset of exchange capillaries, featured continuous flow of plasma gaps with occasional changes in flow direction. LPPs may be important as a protective mechanism to prevent leukocytes from entering non-LPP capillaries, where they can potentially become lodged, resulting in plugged capillaries. PGCs may be important for serving as relief valves for when a leukocyte enters a nearby LPP. Disruption of normal flow dynamics by neighboring leukocytes may be one of the factors that cause changes in the flow direction; spontaneous changes in flow direction have been previously reported (Kleinfeld, Mitra et al. 1998). Thus, bidirectionality in PGCs may serve as an adaptive mechanism to minimize flow disruptions.

We also showed that both leukocytes and plasma gaps exhibit pulsatility. We report a pulsatility index of 0.54 and 0.61 for leukocytes and plasma gaps, which compares well to a previously published result using AOSLO data, which found a leukocyte pulsatility index of 0.45 +/- 0.09 (Martin 2009). A blue-field entoptic study reported a slightly higher pulsatility index of 0.98 in retinal capillaries, varying between 0.80 and 1.17 across 5 subjects (Riva and Petrig 1980). These measurements may have been taken from larger capillaries, since the pulsatility index increases from small capillaries to large capillaries to small arterioles, and our measurements were taken at the level of the smallest capillaries. Noninvasive measurements of velocity waveforms in human retinal arterioles showed pulsatility indices of 1.13 for first order arterioles

(those originating from the optic disc) and 0.93 for second order arterioles (those after the first branch point) (Nagaoka and Yoshida 2006).

Interestingly, leukocyte speeds appear to be significantly higher than plasma gap speeds when comparing the leukocytes found in LPPs to the plasma gaps found across all capillaries ($p < 0.05$). However, since leukocytes could not be reliably identified in non-LPPs, this difference is likely skewed, since thoroughfare channels should have a higher flow speed than exchange capillaries. Indeed, there is no significant difference between leukocyte and plasma gap speeds when considering only the LPPs. Still, previous studies have reported that erythrocytes travel at a faster speed than leukocytes in the microcirculation. This suggests that either plasma gap speed is not a good proxy for erythrocyte speed, or leukocytes and erythrocytes do travel at similar speeds when restricted to only single-file capillaries. Inclusion of either pre-capillary arterioles or post-capillary venules would decrease measured leukocyte speeds, due to initial deformations needed to enter a narrow capillary, and leukocyte-vessel wall interactions, respectively. One study reported that the frequent attachments between leukocytes and the endothelium are disrupted by plasma fluid stresses upon entering single-file capillaries (Schmid-Schonbein, Usami et al. 1980). When examining the videos, no leukocytes were observed to pause at the level of single-file flow.

As was the case for vessel perfusion mapping, it was important to select an appropriate plane of defocus. All methods described in this chapter were developed for a focus level posterior to the capillaries. When focused at the level of the capillaries, the appearance of the capillary is very different. Although it was sometimes possible to see individual objects moving through capillaries when focused at the level of the

capillaries (**Figure 2.19**), such details were typically difficult to see due to the presence of a strongly reflective vessel reflex. The vessel reflex is likely due to scattering from moving erythrocytes. Interestingly, when the plane of focus was set to the level of the large vessels, a vessel reflex could also be seen, suggesting that the dark appearance of the larger vessels in the videos focused at the photoreceptor level is not due to the fact that they are optically opaque, but rather, due to the fact that they are too far out of the plane of focus, similar to the phenomenon as the smaller vessels. That said, there is some optical opacity associated with a larger-sized column of blood cells (any light transmitted by a leukocyte or plasma gap is likely to be obscured by an erythrocyte along the optical path when considering the larger vessels). This explanation is consistent with the anatomy of larger vessels. Anatomically, larger vessels reside in an anterior plane compared to the capillary beds in the inner retina (Snodderly, Weinhaus et al. 1992). In the future, it may be possible to investigate erythrocyte dynamics in both capillaries and larger vessels, simply by changing the plane of focus. However, further studies are needed.

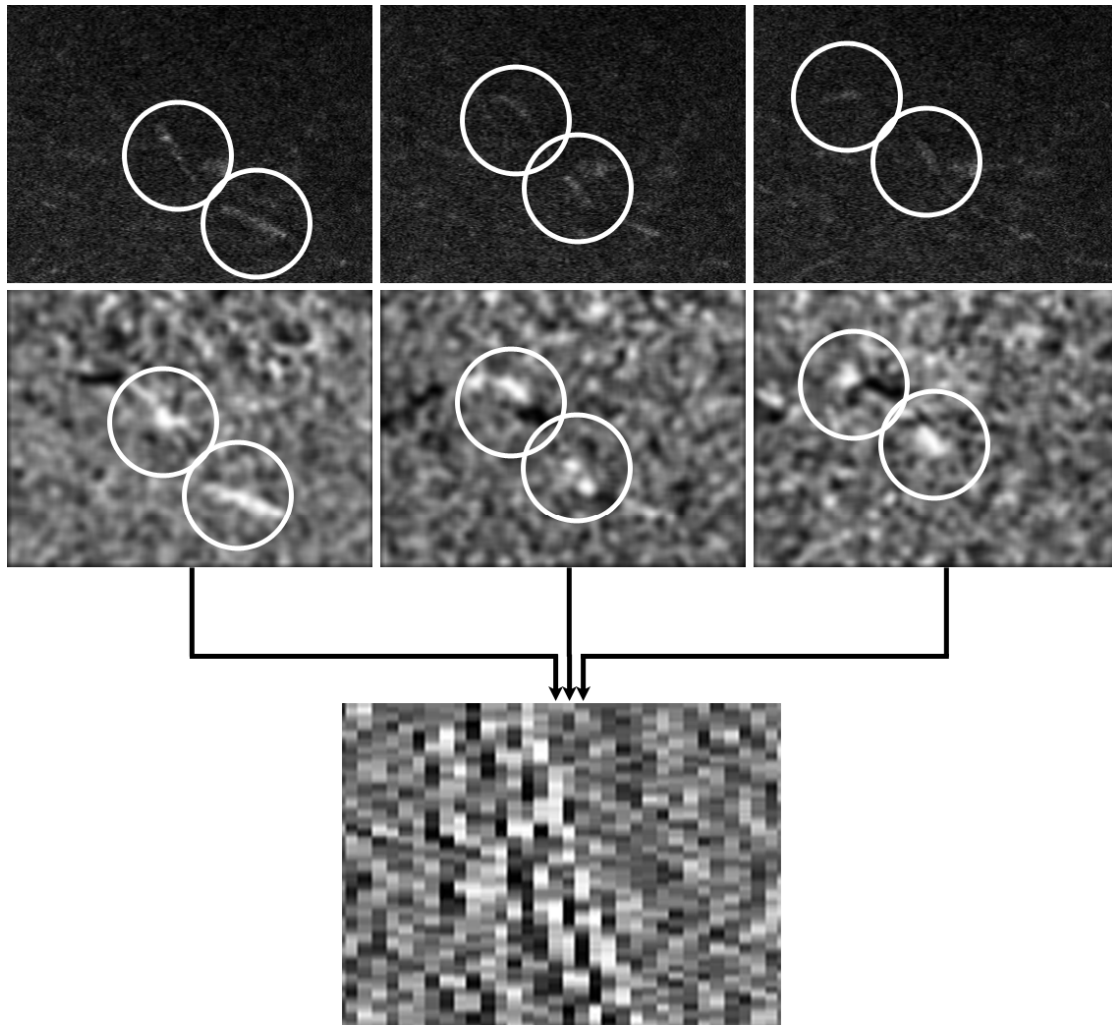


Figure 2.19: Defocus and ST Plots. The ascending slope of the M shaped vessel from the Type 1 video shown in **Figure 2.3** was imaged using an 840 nm wavelength light source with a focus level set at the level of the capillaries. Although the vessel reflex dominates the signal, it is sometimes possible to see large moving objects, as shown here. These are likely the same objects that are seen when setting the focus near the photoreceptors. A short segment from the ST plot that shows two distinct traces after motion contrast enhancement is shown. At this magnification, individual frames can be seen on the ST plot. The three corresponding frames are labeled.

A clear limitation to using a noninvasive approach is that it is not possible to directly verify the types of cells that are being analyzed. This limitation is partly due to issues of low contrast. When imaging in humans, safety is a key consideration that limits the methods that can be applied. Thus, we needed to apply new methods to better visualize signals from plasma gaps and leukocytes. Due to noise and errors in frame-to-frame registration, the process of spatiotemporal analysis is subjective. We used a conservative approach by extracting only those elements that were clearly visible on the spatiotemporal plots. This results in under-extraction, but minimizes false extractions. Therefore, reported frequencies should not be interpreted as absolute measurements, but rather as relative measurements. Since the same criteria were applied across all spatiotemporal plots, comparisons can be made between vessels. To insure repeatability, we repeated the leukocyte extraction two times, and compared the percentages of leukocytes found in each vessel. Two months elapsed between analysis sessions to minimize memory effects for the analysis sessions, which require user interaction. The average absolute difference in leukocyte percentages was 1.2%, and the same LPPs were identified in both analysis sessions. Finally, to minimize bias, pulse blips were not displayed on spatiotemporal plots during extraction.

There are other important limitations. First, the imaging and data analysis procedures are time consuming, as they have not been fully optimized. Although vascular perfusion imaging can be performed using as few as 300 frames, the leukocyte analysis requires longer imaging times in order to collect sufficient data for speed and pulsatility quantification. In this chapter, to characterize flow dynamics in the third patient, we collected 2400 frames at 60 fps, which enabled us to apply a very

conservative approach for identifying leukocyte traces. However, with a more aggressive approach, fewer frames could be used. Second, it is difficult to apply the methods to larger vessels, since larger vessels (i) tend to be out of the plane of focus, which decreases the visibility of flow through the vessel, and (ii) the spatial and temporal resolution requirements are higher for larger vessels compared to single-file flow in smaller capillaries. However, it may be possible to characterize larger vessels by setting the focus level to the vessel reflex; vessel reflexes can be seen even in larger vessels. Third, the analysis method is difficult in regions of high capillary density, since it is difficult to identify sufficiently long capillary segments for generation of spatiotemporal plots. Fourth, it is possible that the analysis method detects aliased traces on the spatiotemporal plot, particularly when interpreting regions where flow reverses direction. Finally, it is difficult to analyze motion due to individual erythrocytes, since the spatial density is high, which is disadvantageous for spatiotemporal plot analysis.

In this chapter, we examined leukocytes and plasma gaps in single-file flow through retinal parafoveal capillaries, using a noninvasive approach that we developed and validated for the AOSLO. The major advantage of a noninvasive approach is that there is no potential disruption of the natural flow and cell distribution, which can be caused by spontaneous activation of normally inactivated leukocytes; the tradeoff is that direct verification of specific cell types is difficult. We identified two distinct categories of capillaries, one which accounted for the majority of leukocyte traffic (LPPs), and the other which primarily featured plasma gap flow (PGCs). LPPs may serve as a protective mechanism to prevent inactivated leukocytes from entering exchange capillaries, and PGCs may serve as relief valves to minimize flow disruption due to the presence of a

leukocyte in a neighboring LPP. The noninvasive method presented in this chapter may be useful for imaging fine vascular details such as microaneurysms and other capillary defects that manifest in retinal diseases, and for studying leukocytes in live human capillaries.

2.6 Acknowledgments

Portions of this chapter are published in the *Journal of Biomedical Optics*, *Biomedical Optics Express*, and *IEEE Proceedings of the International Symposium for Biomedical Imaging (ISBI) 2010*. The dissertation author is the primary investigator and thanks co-authors, Pavan Tiruveedhula and Austin Roorda, for their contributions. The authors thank Mark Campanelli for developing the initial implementation of the virtual AOSLO, Scott Stevenson for his valuable insights regarding ST plots, Qiang Yang for his help with video stabilization and desinusoiding, and Brandon Lujan for assistance with interpretation of the red-free fundus photo. This work was supported, in part, by the NSF Center for Adaptive Optics (AST-9876783); the NIH Bioengineering Research Partnership (EY014375); the National Defense Science and Engineering Graduate Fellowship, sponsored by the Department of Defense; and the National Science Foundation Graduate Research Fellowship.

CHAPTER 3

CAPILLARIES IN EARLY-STAGE DIABETIC RETINOPATHY

3.1 Abstract

Vascular remodeling has long been implicated as a key factor in diabetic retinopathy. We used motion contrast enhancement methods and an adaptive optics scanning laser ophthalmoscope (AOSLO) to investigate the appearance of the parafoveal capillary network in adult subjects with diabetes. We performed a longitudinal study and a cross sectional study. For the longitudinal study, we recruited one adult subject with type 1 diabetes and severe non-proliferative diabetic retinopathy, and acquired AOSLO videos on four separate visits spaced over a 16 month time period. The goal of the longitudinal study was to identify subclinical capillary changes in a patient with diabetic retinopathy, in relation to the surrounding photoreceptors, capillaries, and leukocytes. Retinal features were tracked longitudinally. Although the majority of capillary segments were stable over a period of 16 months, one capillary segment dropped out, leading to a small, but significant increase in FAZ size. There were also signs of microaneurysm formation and disappearance, as well as the formation of tiny capillary bends. The leukocytes in the capillary network were found to preferentially travel through the same routes in all four visits. For the cross-sectional study, we compared 12 adult subjects with type 2 diabetes and no diabetic retinopathy to 11 control subjects with no diabetes. The goal of the cross-sectional study was to establish that the retinal parafoveal

capillary network is altered prior to the onset of diabetic retinopathy in adult patients with type 2 diabetes. Arterio-venous (AV) channels were identified on AOSLO images as the least tortuous capillary channels connecting terminal arterioles to postcapillary venules. We found that the average tortuosity of AV channels was 26% higher in patients with type 2 diabetes when compared to controls, even though there were no signs of diabetic retinopathy in any of the eyes that were assessed ($p < 0.05$). Additionally, metrics of capillary dropout showed small changes (between 3 to 7%), leukocyte speed was 14% lower, and pulsatility was 25% higher, but none of these differences were statistically significant. Although it is often difficult to find consistent changes in the microvasculature due to large intersubject variability, we demonstrate that motion contrast enhanced AOSLO imaging can be used to noninvasively visualize parafoveal capillaries and identify AV channels, which appear to be altered in type 2 diabetes even before onset of diabetic retinopathy.

3.2 Introduction

Diabetes is a disease that produces gradual changes in many different systems throughout the body, including the retinal parafoveal capillary network, one of the most vulnerable capillary beds in the body due to the metabolic demands imposed by the surrounding retinal tissue. In the eye, diabetes can cause diabetic retinopathy (DR). The prevalence of DR has been reported to be 35% in patients who have had diabetes for 12 years (Wong, Cheung et al. 2008). The first stage of DR, non-proliferative DR (NPDR), is marked by gradual capillary dropout. Associated with NPDR are a set of clinically-

observable changes in the microcirculation. The earliest clinical signs are microaneurysms (MAs), small outpouchings of the capillaries, and dot intraretinal hemorrhages; other clinical signs include intraretinal microvascular abnormalities (IRMAs), which are focal disruptions of the capillary topology.

Although the natural progression of DR from these signs into the late stages has been well-characterized, the early microvascular changes that precede DR are not well established, since it is very difficult to assess live human retinal capillaries, due to their small size and low optical contrast. These clinically-observable changes are noticeable mainly because they are larger in size than the surrounding capillaries. For example, fundus photography is a noninvasive method to detect MAs, visible as small dots. New dots appear and existing dots disappear over time (Hellstedt and Immonen 1996), presumably due to formation of new outpouchings and non-perfusion of existing outpouchings. However, using fundus photography, it is not possible to investigate the relationship of MAs to the surrounding capillaries. This is because it is difficult to image capillaries, due to their small size and low contrast. The gold standard for investigating human retinal capillaries is fluorescein angiography (FA). There are clear advantages for using FA to evaluate DR. These include the improved ability to detect MAs, as well as the ability to assess regions of capillary dropout or capillary remodeling. Typically, FA is performed by injecting a bolus of fluorescein dye into a peripheral vein, and then imaging the passage of the dye using a fundus camera. However, FA is not performed under normal situations on patients with type 2 diabetes and no DR, since there is little clinical justification for performing an FA at this stage; also, as with any invasive procedure, there is a small risk of adverse side effects (Kwan

2006). Moreover, there are very few animal models that investigate the capillary network before the onset of DR (Alder, Su et al. 1997), and even fewer that investigate both type 2 diabetes and DR (Kim, Johnson et al. 2004). Thus, there have been many efforts to develop instruments to noninvasively image the capillaries, in order to assess the early stages of DR, and to investigate other retinal diseases.

Capillary networks are complex. In a terminal capillary bed, there are arterioles, capillaries, and venules. In general, capillaries can be classified into two categories: thoroughfare channels, and exchange capillaries. Thoroughfare channels can be identified as those capillaries which, under normal conditions, provide the most direct path for blood cells from terminal arterioles to postcapillary venules (Chambers and Zweifach 1944; Hasegawa, Ravens et al. 1967; Tam, Tiruveedhula et al. 2011); all remaining neighboring capillaries are exchange capillaries. Assessment of capillary hemodynamics without consideration of the type of capillary or the proximity of the capillary to a thoroughfare channel can lead to misinterpretation of results. Although there have been previous studies which have investigated capillary hemodynamics in live human retinal capillaries (Arend, Wolf et al. 1994; Ludovico, Bernardes et al. 2003), the measurements were performed on isolated capillary segments without taking into consideration the relationship of the capillary to the surrounding network.

Assessment of the human parafoveal capillary network is commonly quantified using a macroscopic metric such as foveal avascular zone (FAZ) size and shape (Bresnick, Condit et al. 1984; Mansour, Schachat et al. 1993; Sander, Larsen et al. 1994; Hilmantel, Applegate et al. 1999; Conrath, Giorgi et al. 2005), or perifoveal intercapillary area (Sander, Larsen et al. 1994). Although there is a relationship between

FAZ size and DR severity, there is large intersubject variability; the average FAZ area of non-diseased eyes has been reported by three different studies as 0.152 ± 0.086 (Conrath, Giorgi et al. 2005), 0.367 ± 0.090 (Sander, Larsen et al. 1994), and 0.405 ± 0.559 (Mansour, Schachat et al. 1993) (mean \pm standard deviation, in mm^2 , as measured using FA). Thus, the large intersubject variability makes it difficult to detect changes, especially in the early stages of the disease. Moreover, these metrics mask several unique topological features of the parafoveal capillary network. First, vessels are oriented in a specific manner. Capillaries are preferentially oriented circumferentially, while arterioles and venules are preferentially oriented radially; arterioles and venules are also arranged in an interdigitating manner (i.e. as one moves circumferentially around the FAZ, one encounters an arteriole, then a venule, followed by an arteriole, and another venule, etc.) (Snodderly, Weinhaus et al. 1992; Yu, Balaratnasingam et al. 2010). There are on average 2.9 terminal arterioles that directly supply the capillaries at the edge of the FAZ (Snodderly, Weinhaus et al. 1992). Second, there is a variation in capillary density in the circumferential direction. The capillary density is slightly increased near venules and slightly decreased near arterioles (Michaelson and Campbell 1940; Snodderly, Weinhaus et al. 1992; Yu, Balaratnasingam et al. 2010), due to a small capillary free zone that surrounds arterioles. However, this effect is diminished as one approaches the edge of the FAZ (Yu, Balaratnasingam et al. 2010). Finally, there is also a variation in capillary density in the radial direction. The capillaries form a planar, single-layered structure immediately outside of the FAZ; as one moves radially outwards, a deeper capillary layer begins, although this deeper layer is more sparse than the superficial layer (Yu,

Balaratnasingam et al. 2010). Consequently, in the parafoveal capillary network, capillary density is more dependent on proximity from the edge of the FAZ than on eccentricity. Any of these topological features could become affected in DR with little consequence on a macroscopic metric of capillary density. Thus, there is a need for more sensitive imaging biomarkers to characterize DR.

DR is a heterogeneous disease. Although it is often assumed that capillary dropout is a gradual process that occurs in NPDR, existing evidence is based on images of large areas of dropout; it is unclear whether the dropout occurs at the level of individual capillary segments. This is largely due to technical limitations preventing the ability to track individual capillary segments over time. In the early stages, most vascular lesions are focal, affecting only a small subset of capillaries. This is not surprising, given that the topography of the capillary network is highly heterogeneous. However, it makes it difficult to define quantitative metrics when assessing early signs of capillary disruption and blood flow, since normal regions of the microvasculature will likely dominate focal abnormal regions when quantifying any given metric. We hypothesize that there exist specific capillary channels within the parafoveal capillary network which are affected in DR. Disruption of such channels would lead to a change in the distribution of blood flow through the network, which could lead to the development of clinical signs of DR.

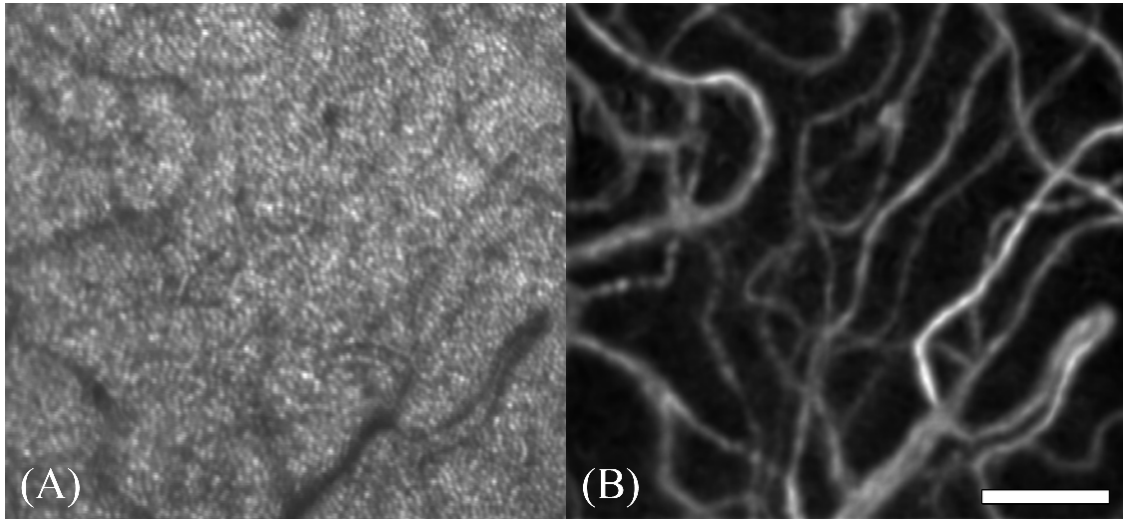


Figure 3.1: High resolution images of a live human retina, generated using an adaptive optics scanning laser ophthalmoscope (AOSLO). Both images were generated noninvasively, from the same AOSLO video. (A) This image was generated by averaging frames across the video. Small circular dots are cone photoreceptors. Dark, fuzzy lines generally correspond to capillaries; however, in many areas, the spatial contrast is low, making it difficult to determine the location of the capillaries. (B) Image of capillaries generated using intrinsic motion contrast signals, without the use of injected contrast agents. Scale bar, 100 μm .

Recently, we have developed noninvasive methods to visualize and assess the human parafoveal capillary network (Tam, Martin et al. 2010; Tam and Roorda 2011), with the ability to assess hemodynamics of specific capillaries in relation to the surrounding capillary network (Tam, Tiruveedhula et al. 2011), using an adaptive optics scanning laser ophthalmoscope (AOSLO) (Roorda, Romero-Borja et al. 2002; Zhang, Poonja et al. 2006) (**Figure 3.1**). In this chapter, we use a novel application of the AOSLO to determine the relationship between capillary channels, capillary network topology, and capillary hemodynamics in patients with type 2 diabetes and no DR. The detailed images generated using the AOSLO may enable us to detect changes in individual capillaries that were previously undetectable.

3.3 Materials and Methods

Research procedures adhered to the tenets of the Declaration of Helsinki. After a detailed explanation of procedures, written informed consent was obtained from all participants. The research protocols were approved by the University of California, Berkeley Committee for Protection of Human Subjects.

Subjects

For the longitudinal study, we invited one 26-year-old human male subject with type 1 diabetes and severe non-proliferative DR (NPDR) to participate in a series of imaging

and assessment visits to determine whether we could detect any capillary changes as well as any signs of capillary dropout.

For the cross-sectional study, we recruited 30 human subjects: 15 adult patients diagnosed with type 2 diabetes for at least five years, with no diabetic retinopathy in at least one eye (T2DM_NoDR), and 15 adult age-matched control subjects with no history of diabetes (control).

Longitudinal Study Design

Detection of capillary dropout is most likely during severe NPDR, because the next stage of the disease, proliferative DR, is marked by neovascularization. In addition, it is important to perform all assessments in the same eye, in order to make meaningful and detailed comparisons. To assess the capillaries, we utilized a method based on AOSLO imaging that enables the generation of highly detailed capillary images. In addition, we also performed conventional clinical tests to characterize the patient. There were a total of 8 visits spaced over a time-period of 16 months, with 4 visits corresponding to AOSLO imaging, 3 visits corresponding to screening tests consisting of conventional clinical measures, and 1 visit corresponding to a routine FA. A summary of the visit dates is shown in **Table 3.1**. For all visits, the subject's left eye was selected.

Table 3.1. Longitudinal Study Visit Information

	Visit 1	Visit 2	Visit 3	Visit 4
AOSLO Date	10/21/2009	11/24/2009	7/6/2010	2/6/2011
Screening Date	9/30/2009	-	4/27/2010 ^a	1/30/2011
Screening Result	Severe NPDR ^b	-	Severe NPDR	Severe NPDR ^c
HbA1c	9.8%	-	9.8%	10.8%
Visual Acuity ^d	20/20	-	20/20	20/20
log CS ^e	1.50	-	1.50	1.50
Blood Pressure ^f	125/74	-	116/74	126/62

^a Fluorescein angiogram was performed on 5/28/2010.

^b Severe non-proliferative diabetic retinopathy.

^c Contralateral eye developed clinically-significant macular edema (CSME).

^d Snellen visual acuity.

^e Contrast sensitivity.

^f Blood pressure, left arm standing.

Screening Visits

Prior to three of the AOSLO visits, the subject was invited for additional screening to monitor the clinical progression of the patient's retinal health. Each screening visit was paired to one of AOSLO visits. For the screening visits, the procedures listed in **Table 3.1** were performed, as well as a medical history, spectral domain optical coherence tomography (SDOCT) (Cirrus HD-OCT Model 4000, Carl Zeiss Meditec, Inc, Dublin, CA), and color fundus photography (Zeiss Visucam Pro NM, Carl Zeiss Meditec, Inc., Dublin, CA). A 20° x 20° macular cube was acquired using the SDOCT. The fundus photograph was examined by a retina specialist to assess the grade of DR. The assessment was performed offsite with no information about the patient or disease history.

Between AOSLO visits 2 and 3, the patient developed clinically-significant macular edema (CSME) in the contralateral eye, and was subsequently referred for a FA study. The FA was acquired using a digital fundus camera (Zeiss Visucam NM/FA, Carl Zeiss Meditec, Inc., Jena, Germany). Photos were acquired using standard protocols. The photo that most clearly showed the parafoveal capillaries in the left eye was selected for comparison to AOSLO imaging. The goal of the comparison was to verify that capillaries and clinical features such as MAs could be properly identified.

AOSLO Visits

For the AOSLO visits, a series of overlapping videos were acquired near the foveal region of the retina. Individual photoreceptors could be resolved in the videos; the flow of individual leukocytes through retinal capillaries could also be seen. Videos were

processed to generate high contrast images of photoreceptors and capillaries. On the first visit, a short series of exploratory videos were taken in 15 overlapping regions on the retina, resulting in an image of the foveal avascular zone (FAZ), but not of the surrounding capillary network. The FAZ is a large capillary-free area; the severity of DR is associated with the size of the FAZ, with a larger size corresponding to a greater severity (Mansour, Schachat et al. 1993). On subsequent visits, videos were taken in additional regions (up to 43 locations per visit), and used to generate images of both the FAZ as well as the surrounding capillaries. AOSLO imaging was performed using parameters optimized for capillary imaging (40 second videos, 60 fps) (Tam, Tiruveedhula et al. 2011). During video acquisition, the subject's pulse was simultaneously recorded.

We analyzed photoreceptors, capillaries, and leukocytes using the AOSLO videos. To analyze the photoreceptors, locations of individual cones were labeled, and cone spacing was quantified (Rodieck 1991; Duncan, Zhang et al. 2007). To assess the capillaries, the FAZ was extracted using a semi-automated procedure (Tam, Martin et al. 2010), and the diameter quantified to determine the precision with which FAZ size could be quantified. We analyzed the distribution and measured the speed of leukocytes across visits using spatiotemporal plot analysis (Tam and Roorda 2011; Tam, Tiruveedhula et al. 2011). Previously, we showed that a small subset of capillary channels called leukocyte-preferred paths (LPPs) account for a clear majority of leukocyte traffic (Tam, Tiruveedhula et al. 2011). However, it was uncertain whether the same LPPs would be identified on different visits, particularly in the presence of DR.

AOSLO images were compared across visits to detect structural changes in the capillary network, including any formation of new MAs or disappearance of existing MAs, as well as dropout of capillaries. The FAZ was also assessed to determine whether there were any changes.

Cross Sectional Study Design

Exclusion criteria were prior ocular surgery (including refractive surgeries), cataract or media opacities, and ocular diseases not associated with diabetes (including any retinopathy); patients who were pregnant or nursing (lactating) were also excluded.

AOSLO Imaging

One eye from each subject was selected for imaging. In a few subjects, only one eye satisfied all inclusion criteria. If both eyes satisfied all inclusion criteria, then the eye with the lower spherical equivalent refractive error was selected for imaging. The selected eye was dilated (2.5% phenylephrine hydrochloride, 1% tropicamide).

Images of the parafoveal capillary network were generated noninvasively, without the injection of contrast agent, as described previously (Tam, Martin et al. 2010; Tam, Tiruveedhula et al. 2011). Briefly, overlapping AOSLO videos were acquired in the parafoveal region (1.8 deg field size, 40 seconds, 60 Hz). The subject's pulse was measured using a photoplethysmograph (MED Associates Inc., St. Albans, VT, USA), and simultaneously recorded in a data file during acquisition of all videos. Custom motion-contrast enhancement algorithms were applied offline to generate capillary perfusion images from each of the acquired AOSLO videos, and the resulting

capillary perfusion images were assembled to generate a montage of the parafoveal capillary network, showing the foveal avascular zone (FAZ) and surrounding parafoveal capillaries (**Figure 3.2**).

AOSLO images of the parafoveal capillary network were successfully generated in 12 out of 15 T2DM_NoDR subjects and 12 out of 15 control subjects. The overall success rate for AOSLO imaging was 24 out of 30 subjects (80%). The proportion of subjects undergoing conventional FA who had images of sufficient quality for the delineation of individual parafoveal capillaries was 13 out of 17 in a prior study (76%) (Sander, Larsen et al. 1994). The success rate of delineating the FAZ using oral FA combined with confocal scanning laser ophthalmoscopy was 16 out of 34 (47%) (Garcia, Rivero et al. 1999). Notably, AOSLO images are generated with minimal risk considering the noninvasive nature of the method. Images of perfused capillaries were used to compare the two groups for qualitative differences. Specifically, we examined AOSLO images for subclinical capillary peculiarities, such as capillary bends and possible precursors to microaneurysms, as well as possible breakdown of the topological organization of the capillary network.

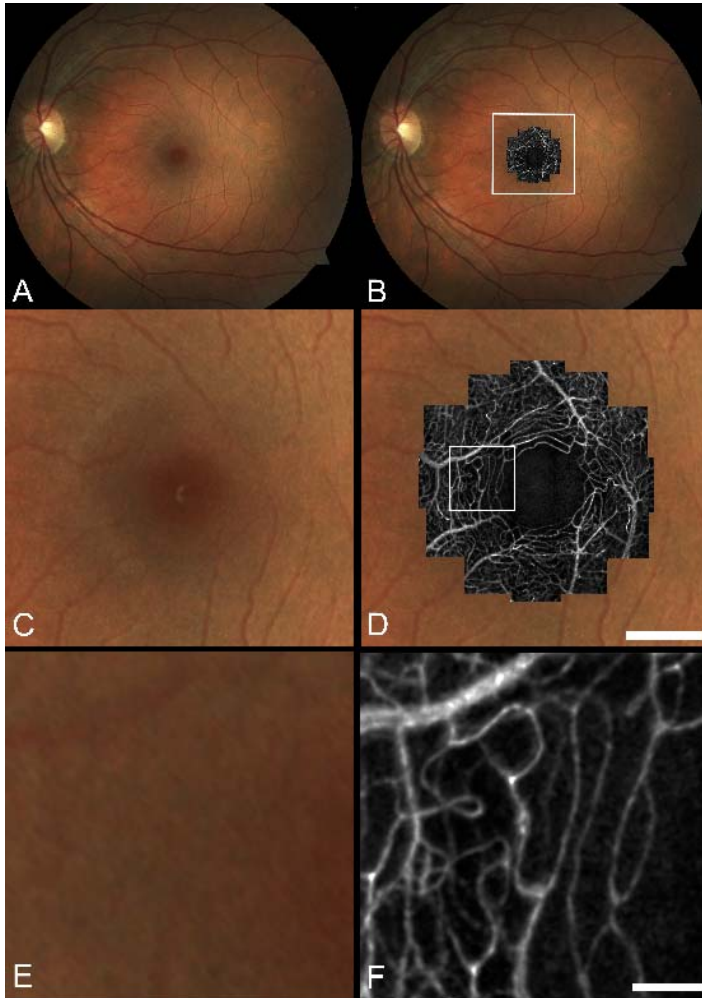


Figure 3.2: Example of AOSLO imaging for one control subject. In this example, overlapping videos were taken in 21 different locations on the retina, processed to generate capillary images, and then compiled to generate a montage of the parafoveal capillary network. (A, B) 45 degree fundus photograph, with and without AOSLO images. (C,D) Zoom of white box from (B), showing portion of the fundus photograph, with and without AOSLO images. Scale bar, 500 μm . (E,F) Zoom of white box from (D), showing fundus photograph, with and without one AOSLO image generated from a single video. Scale bar, 100 μm .

Medical history

All subjects underwent a medical history to verify inclusion and exclusion criteria as outlined above. One control subject was excluded due to a diagnosis of age-related macular degeneration (AMD). For the T2DM_NoDR subjects, hemoglobin A1c (HbA1c) levels were measured, and a slit-lamp examination was performed to verify the absence of cataract prior to AOSLO Imaging.

Biometry Measurements

Axial length, anterior chamber depth, and corneal curvature were measured and used to make accurate conversions from visual angle to distance, as described previously (Li, Tiruveedhula et al. 2010) (IOL Master, Carl Zeiss Meditec Inc., Dublin, CA, USA).

Fundus Photography and Grading

A digital fundus camera was used to acquire 45 deg fundus photographs near the posterior pole for all subjects (Zeiss Visucam Pro NM, Carl Zeiss Meditec Inc., Dublin, CA, USA). For the T2DM_NoDR subjects, two additional photographs were taken (nasal and temporal to the fovea), and the three overlapping color fundus photographs were evaluated by a retina specialist to determine whether there were signs of any retinopathy. Photographs were evaluated off-site with no subject-identifying information and no information about the subject's medical history. They were assigned a grading of no retinopathy, mild non-proliferative diabetic retinopathy (NPDR), moderate NPDR, severe NPDR, or proliferative diabetic retinopathy (PDR); in addition,

macular edema and any other signs of retinopathy not related to diabetes were also noted.

The retina specialist assigned a grading of “no retinopathy” to all T2DM_NoDR eyes that were selected for AOSLO imaging. Three of the T2DM_NoDR subjects were assigned a grading of “mild NPDR” in the contralateral eye. After excluding the one subject from the control group who presented with AMD (as described above), AOSLO images of the parafoveal capillary network from 12 T2DM_NoDR subjects and 11 control subjects were generated and used for comparison. The mean and standard deviation of the ages were 55.5 ± 7.6 years for the T2DM_NoDR subjects and 52.2 ± 10.6 years for the control subjects. Detailed information about these subjects is presented in **Table 3.2**. There was a difference in the composition of the ethnicities between the two groups (ethnicity was neither an inclusion criteria nor an exclusion criteria, and thus no attempt was made to select for ethnicity during subject recruitment). Although the prevalence of diabetes is higher in the Mexican-American population, the prevalence of DR is similar when compared to a Caucasian population (West, Klein et al. 2001). Thus far there have been no major studies that have shown any ethnic differences in the parafoveal capillary network near the FAZ.

Table 3.2. Subject characteristics

Subject ¹	Sex	Age	Eye	Ethnicity	Duration [years]	HbA1c
C2	F	33	OS	Caucasian	N/A	N/A
C3	M	37	OD	Caucasian	N/A	N/A
C4	F	59	OS	Caucasian	N/A	N/A
C5	F	53	OD	Caucasian	N/A	N/A
C6	F	52	OD	Caucasian	N/A	N/A
C7	M	51	OD	Caucasian	N/A	N/A
C9	M	63	OS	Black	N/A	N/A
C11	M	55	OD	Caucasian	N/A	N/A
C12	M	70	OD	Caucasian	N/A	N/A
C14	M	47	OS	Caucasian	N/A	N/A
C15	M	54	OS	Caucasian	N/A	N/A
D1	M	38	OD ²	Asian	14	6.1
D3	M	56	OD	Native American	6	13.1
D6	F	45	OD ²	Hispanic	12	7.2
D7	M	57	OD	Caucasian	8	7.5
D8	F	53	OS	Hispanic	10	7.4
D9	F	63	OS	Hispanic	10	6.8
D10	M	57	OD	Caucasian	8	6.6
D11	M	64	OS	Caucasian	8	7.3
D12	F	53	OS	Hispanic	5	7.8
D13	F	63	OS	Caucasian	12	6.5
D14	F	63	OD ²	Hispanic	10	7.3
D15	F	54	OS	Hispanic	14	7.8

¹ C2 to C15 are control subjects; D1 to D15 are T2DM_NoDR subjects.

² Subject presented with mild NPDR in the contralateral eye.

Identification of Arterio-Venous Channels

We identified AV channels (defined here as the simplest, most direct capillary paths connecting arteries to veins), and calculated tortuosity. The concept of AV channels is based on thoroughfare channels (Chambers and Zweifach 1944; Hasegawa, Ravens et al. 1967). In the absence of anastomoses (bypass vessels between macular arterioles or venules), as has been shown in the human retina (Yu, Balaratnasingam et al. 2010), thoroughfare channels can be identified as the simplest, most direct paths connecting arterioles to venules. We used the following steps to identify AV channels (**Figure 3.3**):

First, we identify the locations of arterioles and venules. The largest vessels in the AOSLO images were matched to the smallest vessels in the color fundus photographs. By following arteries and veins directly into the AOSLO images, locations of arterioles and venules could be identified. Second, we draw paths to represent candidate AV channels, starting at an arteriole and ending at a venule, applying a simple rule at each branch point. At each branch point, we select the branch with the smallest branch angle, where branch angle is defined as the angle between the centerline of the vessel upstream of the branch point, and the centerline of the branch. If both branch angles are similar, then both paths were selected. By proceeding in this manner for all arterioles and branch points, a set of candidate AV channels is generated. Finally, we identify the three least tortuous AV channels. There are on average about three terminal arterioles that feed the capillaries immediately outside of the FAZ (Yu, Balaratnasingam et al. 2010); thus, we expect on average about three AV channels.

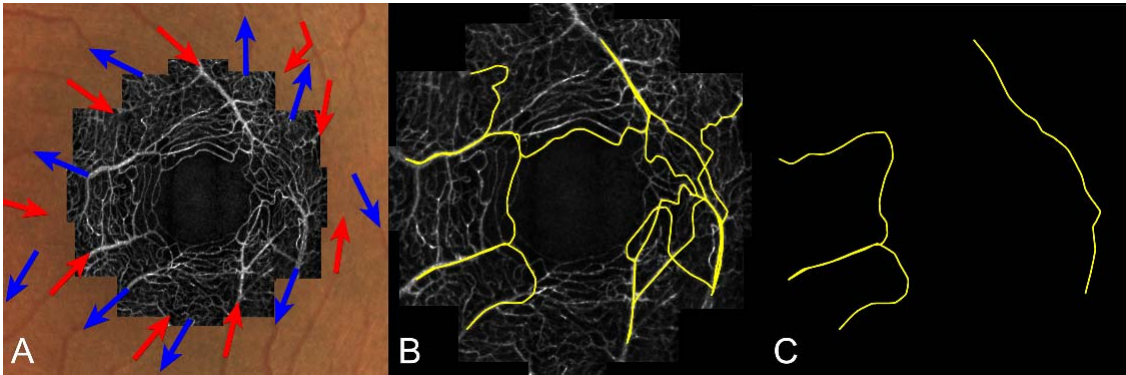


Figure 3.3: Identification of AV channels on AOSLO Images. The steps are: (A) identify locations of arterioles (red) and venules (blue), (B) identify candidate AV channels satisfying the branch selection rule, and (C) select the three least tortuous AV channels

To quantify tortuosity, we selected a metric that emphasizes areas of high curvature and de-emphasizes areas of low curvature, noting that the curvature of smaller vessels is greater than larger vessels (Hart, Goldbaum et al. 1997). This definition of tortuosity is fairly consistent with the clinical notion of tortuosity (Hart, Goldbaum et al. 1997):

$$\text{tortuosity} = \frac{\text{total squared curvature of line}}{\text{length of line}} = \frac{TSC}{L} \quad (1)$$

To minimize the effect of the discrete nature of pixel representation, we used a sliding least squares polynomial fitting scheme to calculate the curvature. To calculate the curvature at each point along the channel, we extracted a 20 μm segment centered around the point, and calculated the least squares cubic polynomial fit for that segment. We used the polynomial fit to calculate the curvature, based on taking the first and second derivatives of the polynomial, as described previously (Hart, Goldbaum et al. 1997).

We identified the three least tortuous AV channels and calculated the average tortuosity of these three channels. Not all AOSLO images could be analyzed for AV channel tortuosity, due to variations in data quality both within and across subjects. We attempted to quantify AV channel tortuosity only in the subjects whose FAZs could be delineated using the AOSLO. Thus, the quality of the AOSLO images was sufficient to enable AV channel tortuosity measurements in 11 out of 11 control subjects and 11 out of 12 T2DM_NoDR subjects.

Macroscopic Measures of Capillary Dropout

We calculated three measures of capillary dropout: FAZ size, FAZ shape, and capillary density. We attempted to quantify measures only in those subjects whose FAZs could be delineated using the AOSLO. Due to variations in the appearance of the FAZ, the number of overlapping AOSLO videos required to fully visualize the FAZ ranged from 9 to 21 videos. Since there were variations in the quality of videos both within and across subjects, sometimes it was not possible to quantify a specific metric across all subjects. However, in all cases, metrics were quantified in as many subjects as possible.

FAZ Size: The borders of the FAZs were extracted using a semi-automated algorithm, as described previously (Tam, Martin et al. 2010). We identified the FAZ as the largest avascular zone near the fovea. The area of the extracted region was quantified in pixels² and then converted to mm² using a model eye parameterized by the biometry measurements from each subject. The effective diameter of the FAZ was calculated as the diameter of the circle with equal area:

$$effective\ diameter = 2\sqrt{\frac{Area}{\pi}} \quad (2)$$

The quality of the AOSLO images was sufficient to enable quantification of the FAZ Size in 11 out of 11 control subjects and 12 out of 12 T2DM_NoDR subjects.

FAZ Shape: We measured the shape of the FAZ using the following acircularity metric:

$$acircularity = \frac{perimeter\ of\ the\ FAZ}{perimeter\ of\ the\ circle\ with\ equal\ area} \quad (3)$$

A perfectly circular FAZ has an acircularity equal to 1. Deviations from a circular shape increase the value of this acircularity metric.

The quality of the combined AOSLO images was sufficient to enable FAZ shape measurements in 11 out of 11 control subjects and 9 out of 12 T2DM_NoDR subjects.

Capillary density: The centerlines of all vessels in a region of interest (ROI) within 0.15 degrees of the edge of the FAZ were extracted using a semi-automated extraction process, as described previously (Tam, Martin et al. 2010). The inner border of the ROI was defined as the edge of the FAZ, and the outer border was defined as the contour spaced 0.15 degrees from the edge of the FAZ. In the parafovea, capillary density increases in a discontinuous manner, from zero inside to FAZ, to an intermediate value in the region of single-layered capillaries, with subsequent increases corresponding to the introduction of additional capillary layers. The eccentricities at which the additional capillary layers begin depend largely on the size of the FAZ; moreover, with an irregularly-shaped FAZ, the transition may occur at different eccentricities depending on the direction (e.g. superior vs. inferior). Therefore, to minimize confounding factors, we elected to use the ROI defined by the actual shape of the FAZ in order to capture the approximate zone where the capillary network is single-layered. We defined the capillary density metric as:

$$\text{capillary density} = \frac{\text{total length of all extracted capillaries}}{\text{area of the ROI}} = \frac{L}{A} \quad (4)$$

The quality of the AOSLO images was sufficient to enable capillary density measurements in 8 out of 11 control subjects and 9 out of 12 T2DM_NoDR subjects.

Capillary Hemodynamics

We calculated two measures of capillary hemodynamics: leukocyte speed and pulsatility index. As for the previous metrics, we attempted to quantify hemodynamics only on those subjects whose FAZs could be delineated using the AOSLO.

Leukocyte speed: We quantified the speed of leukocytes through selected AV channels. Under normal physiological conditions, there is considerable variation in the distribution of leukocytes across the parafoveal capillary network (Tam, Tiruveedhula et al. 2011). Some AV channels contained many leukocytes, while others did not. We identified the least tortuous AV channel that also contained many leukocytes, and measured the speed of all leukocytes that could be clearly identified in the corresponding 40 second AOSLO video. The speed of each leukocyte was quantified directly, incorporating corrections for raster scanning and eye motion, as described previously (Tam and Roorda 2011). We then calculated the average leukocyte speed by plotting leukocyte speed vs. relative cardiac cycle, dividing the cardiac cycle into 5 bins, calculating the average speed of each bin, and then taking the average speed of the 5 bins. Relative cardiac cycle was determined from the subject's pulse data, which was simultaneously recorded during video acquisition. Thus, leukocyte speeds were normalized for variations due to the cardiac cycle.

The quality of the AOSLO videos was sufficient to enable leukocyte speed measurements in 8 out of 11 control subjects and 7 out of 12 T2DM_NoDR subjects.

Pulsatility index: We calculated the pulsatility index (PI) for leukocytes using a method described previously (Tam, Tiruveedhula et al. 2011). Briefly, leukocyte speeds were plotted vs. relative cardiac cycle, and divided into 5 bins. We defined V_{\max} as the bin with highest average speed, V_{\min} as the bin with the lowest speed, and V_{mean} as the average speed of all 5 bins. PI was calculated as:

$$PI = \frac{V_{\max} - V_{\min}}{V_{\text{mean}}} \quad (5)$$

We calculated PI only when there were at least two leukocytes identified in each bin. Applying this criteria, we calculated PI in 7 out of 11 control subjects and 5 out of 12 T2DM_NoDR subjects.

Statistical analysis

We compared the two groups using two-tailed unpaired t-tests with a significance level of 0.05.

3.4 Results

Longitudinal Study

The patient was diagnosed with type 1 diabetes 20 years prior to his first visit, with no history of hypertension or hyperlipidemia. The SDOCT showed no clinically significant changes across visits: macular thickness was within normal limits, and the IS/OS

junction was intact (an abnormal junction would be indicative of photoreceptor disruption). For all visits, the retina specialist determined that the patient had severe non-proliferative diabetic retinopathy (NPDR). The retina specialist also assessed the FA study and determined that the patient had severe NPDR. The HbA1c, visual acuity, contrast sensitivity, and blood pressure were also similar across the visits (**Table 3.1**). These tests show that the patient was stable as assessed by conventional clinical tests over all visits.

Detailed images of the vasculature were successfully generated using noninvasive AOSLO methods. The AOSLO images of capillaries, arteries, and veins were in good agreement with images generated by conventional clinical methods (**Figures 3.4, 3.5**).

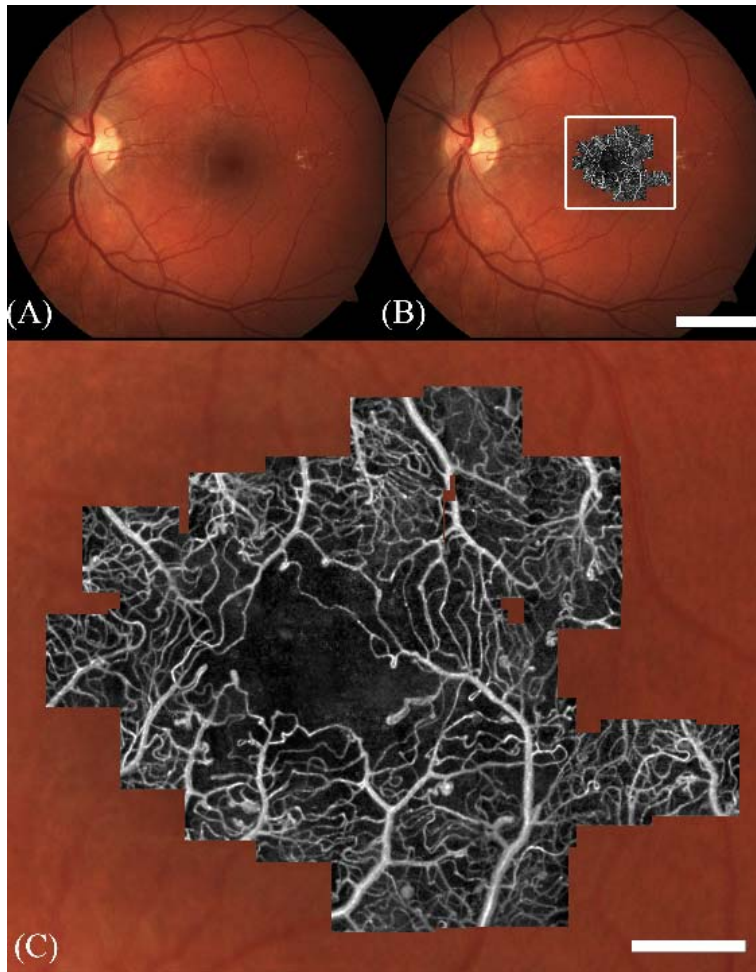


Figure 3.4: Comparison of AOSLO imaging to color fundus photography. (A,B) Color fundus photo, with and without the AOSLO image from visit 4. Scale bar, 2.5 mm. (C) Zoom of box from (B). A total of 43 overlapping AOSLO videos were combined to generate this image. In the center of the capillary network is a region free of capillaries, called the foveal avascular zone (FAZ). Near the FAZ, microaneurysms and capillary bends can be seen. It is important to identify and monitor microaneurysms in patients with diabetes. Scale bar, 500 μm .

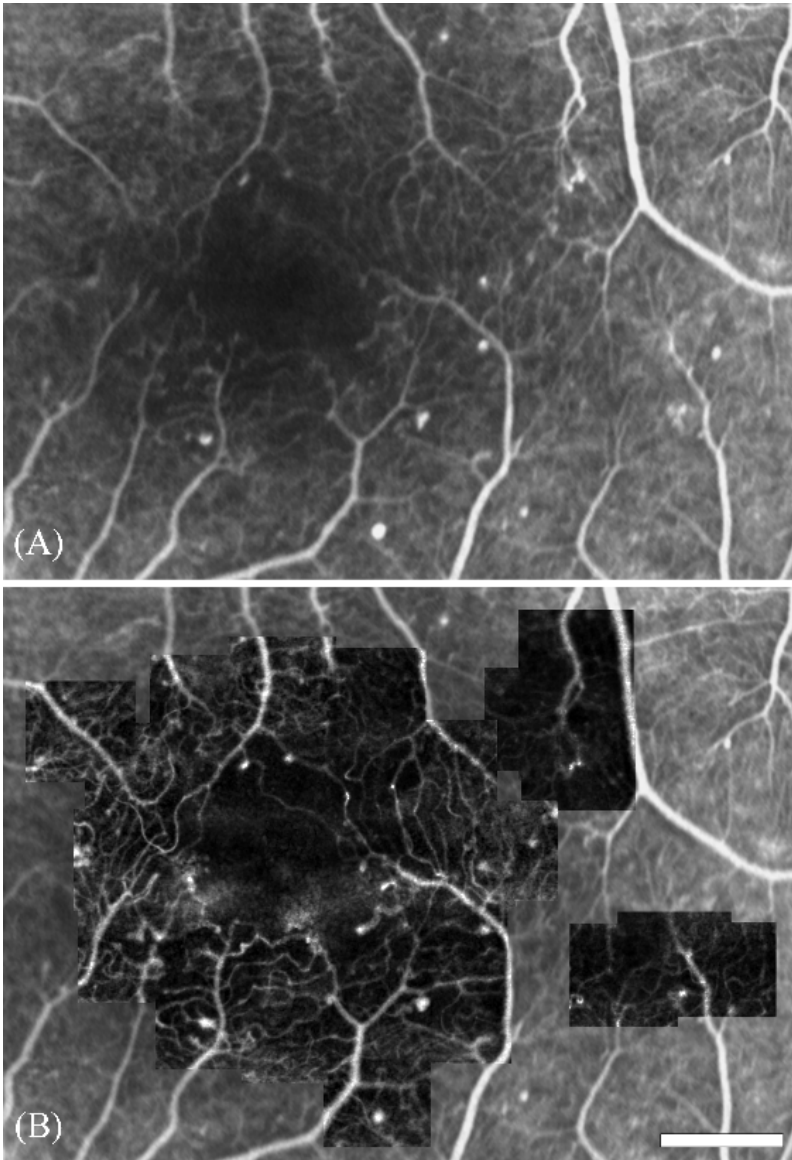


Figure 3.5: Comparison of AOSLO imaging to fluorescein angiography (FA). (A) Capillaries and MAs as visualized using FA. A portion of the FA near the fovea is shown. (B) AOSLO image from visit 3, with the FA in the background, showing good agreement between the AOSLO and the FA. Scale bar, 500 μm .

Repeatability of AOSLO imaging

Qualitatively, the same general structure of the capillary network was identified in each of the visits, with the exception of the fourth visit, where a single capillary segment dropped out, leading to a small increase in FAZ size (**Figure 3.6**).

To quantify repeatability, the FAZ was extracted and the diameter quantified for all visits (**Figure 3.7**). The diameter was calculated as the diameter of the circle with equal area. Assuming that there was no change in the FAZ for the first three visits, the FAZ diameter based on the first three visits was between 749 and 759 μm (99% confidence interval). The FAZ diameter on the fourth visit was 763 μm , a significant increase in size due to the dropout of a single capillary segment ($p < 0.01$). This suggests that AOSLO imaging can be used to quantify FAZ diameter to a precision of $\pm 5 \mu\text{m}$.

Microaneurysms and intra-retinal microvascular abnormalities

In general, there was good agreement between the MAs identified on the FA and on the AOSLO images. All MAs identified on the FA could be identified in the AOSLO image from visit 3 (taken approximately one month later); there were some changes that could be identified when comparing these images with the other visits, which included development of a new MA and disappearance of an existing MA. There was also an object that appeared to be a multi-lobed MA (**Figure 3.8**) and microaneurysm-like object with two lobes (**Figure 3.8C**), from visit 4, 300 out of 2400 frames shown in real time). One intraretinal microvascular abnormality (IRMA) was imaged in visits 3 and 4. There were several areas that were similar in appearance to the IRMA, but may have

been too small to be detected by FA. One of these micro-IRMAs developed a new capillary protrusion between visits 2 and 3, suggesting that these micro-IRMAs may be precursors to larger, clinically significant IRMAs.

Capillary bends

A large number of capillary bends were observed using the AOSLO; such bends were not resolved by the FA (**Figure 3.9**).

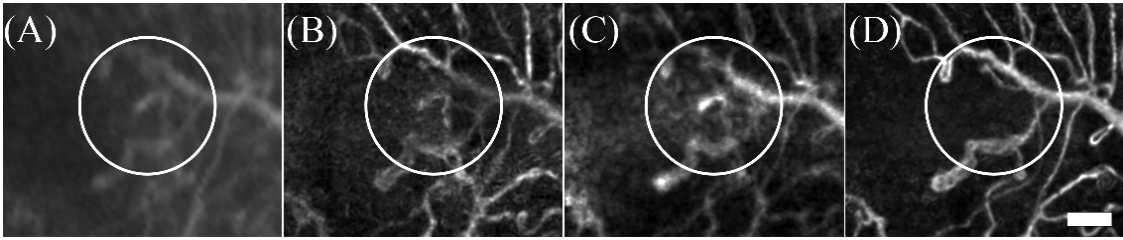


Figure 3.6: Capillary dropout at the right edge of the FAZ. The same region on the retina is shown from the (A) fluorescein angiogram (FA), (B) visit 2, (C) visit 3, and (D) visit 4. Note that the FA was taken between visits 2 and 3. Scale bar, 100 μm .

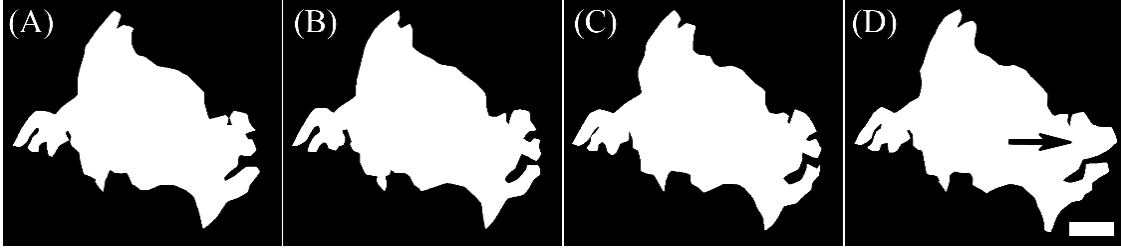


Figure 3.7: Extracted FAZs for size quantification for (A) visit 1, (B) visit 2, (C) visit 3, and (D) visit 4. Note the increase in FAZ size at the right edge of visit 4 (arrow). Scale bar, 200 μm .

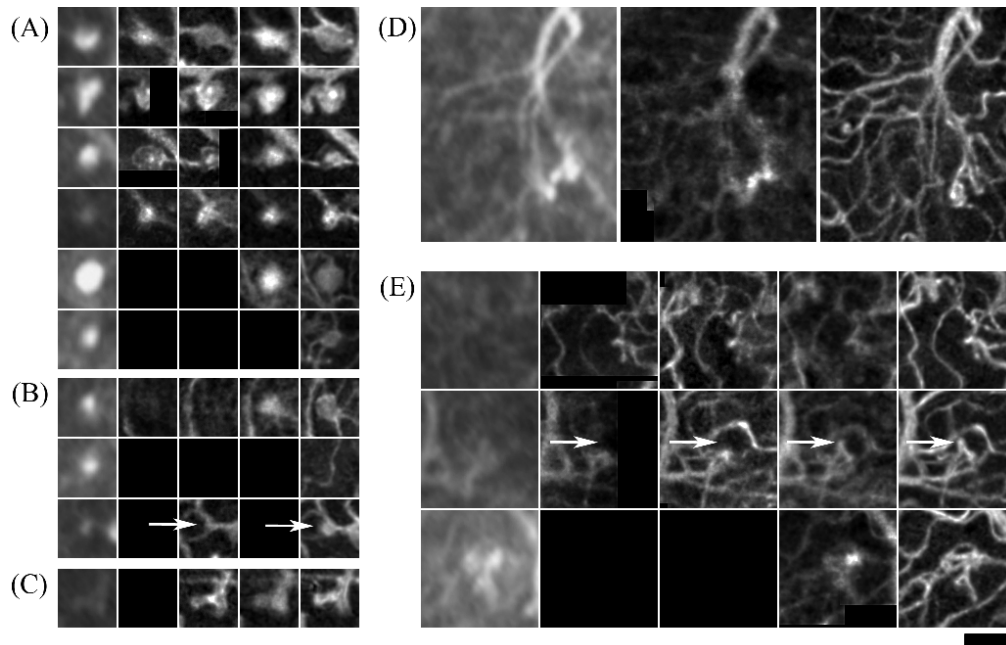


Figure 3.8: Microaneurysms (MAs) and intraretinal microvascular abnormalities (IRMAs). (A,B,C) From left to right, the columns are images from fluorescein angiography (FA), visit 1, visit 2, visit 3, and visit 4. Black regions are areas that were not imaged by the AOSLO on that visit. The FA was performed between visits 2 and 3. (A) The same MAs could be seen across multiple visits. (B) There was one new MA which developed after visit 2 (top row) and one MA which disappeared between the FA and visit 4 (middle row). One small MA appeared to grow in size between visits 2 and 4 (arrow in bottom row). (C) MA-like object with two lobes. (D) One IRMA was identified. From left to right, the IRMA as seen by FA, visit 3, and visit 4. (E) Possible micro-IRMAs that were too small to be detected by FA. In one of the micro-IRMAs, a small capillary protrusion developed between visit 2 and the FA (arrow). Scale bar, 100 μm .

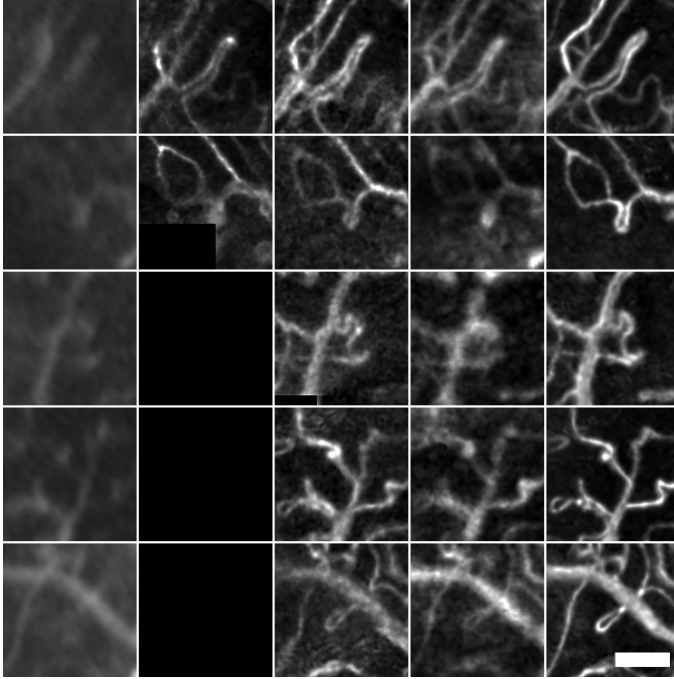


Figure 3.9: Examples of capillary bends. The columns from left to right indicate images from fluorescein angiography (FA), visit 1, visit 2, visit 3, and visit 4. The FA was performed between visits 2 and 3. Scale bar, 100 μm .

Capillary dropout

Aside from the dropout of the capillary segment at the edge of the FAZ, there were also other areas of potential subclinical capillary dropout. In normal eyes, there are several capillary-free zones in the human retina that must be taken into consideration when identifying regions of capillary dropout. The largest capillary-free zone is the FAZ (in this patient, the FAZ had an area of 0.46 mm^2). Near the FAZ, the capillary network is single-layered. Because capillaries are arranged in a circumferential manner around the FAZ, there are several rings of capillary-free zones called peri-foveal intercapillary areas, which correspond to this region of single-layered capillaries; the average area of these regions is approximately 0.001 mm^2 , based on a previous study (Sander, Larsen et al. 1994). At larger eccentricities one would not expect to find capillary-free zones of this size, except around arteries. There is a small capillary-free zone that surrounds arteries, but not veins (Michaelson and Campbell 1940).

There were two regions of capillary dropout (**Figure 3.10**). The first region was classified as a region of capillary dropout because of the size of the capillary-free zone. This region was located at an eccentricity too large to be a perifoveal inter-capillary area, and the zone extended too far away from an artery to be a capillary-free zone from an artery (the areas of the regions of capillary dropout shown were between 0.020 and 0.022 mm^2). Interestingly, this region was also a region where a MA disappeared. A second region of capillary dropout surrounded a vein, again at an eccentricity where there should have been multiple layers of capillaries.

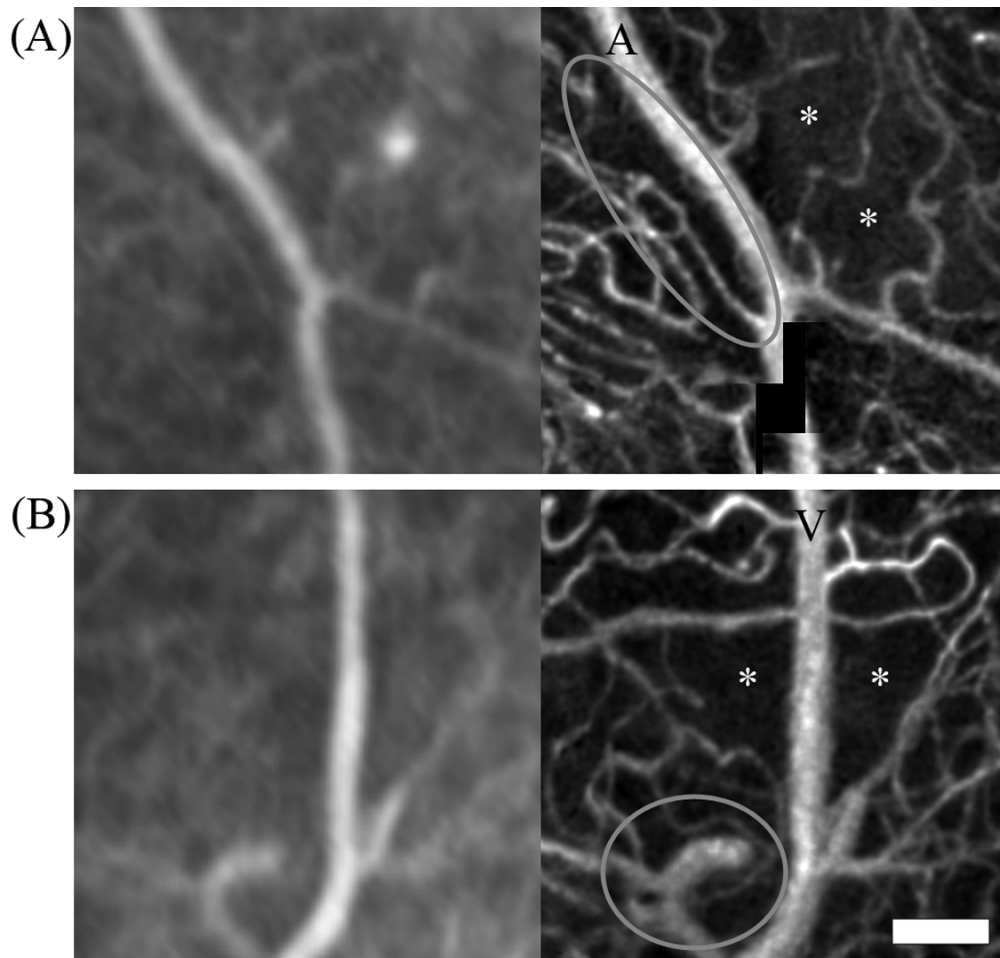


Figure 3.10: Subclinical capillary dropout. Regions of capillary dropout are marked with an asterisk (*). Images are taken from the fluorescein angiogram (left) and the AOSLO on visit 4 (right). (A) Two regions of capillary dropout next to an artery (A). The circled region is not considered to be capillary dropout since it is part of the capillary-free zone surrounding the artery. Note the disappearance of a microaneurysm at the area of capillary dropout. (B) Two regions of capillary dropout next to a vein (V). A venous bend is circled. Scale bar, 100 μm .

Distribution and speed of leukocytes

Leukocytes were analyzed on visits 2, 3, and 4. For each visit, 10 capillary segments near the FAZ were identified, and analyzed for leukocyte speed and frequency. In total, 295 leukocytes were identified across all three visits. A histogram of leukocyte frequency was used to determine the set of capillaries that accounted for a clear majority of leukocyte traffic. These capillaries were called leukocyte-preferred paths (LPPs) (Tam, Tiruveedhula et al. 2011) (**Figure 3.11**). In all three visits, the same four LPPs were identified; collectively, these LPPs accounted for 67%, 62%, and 68% of all leukocytes identified for visits 2, 3, and 4, respectively.

The speed of the leukocytes in each of the LPPs varied across visits, ranging from 1.24 to 1.97 mm/s (**Figure 3.12**). Leukocyte speeds were averaged across the cardiac cycle and then normalized for heart rate using the subject's pulse data recorded during video acquisition.

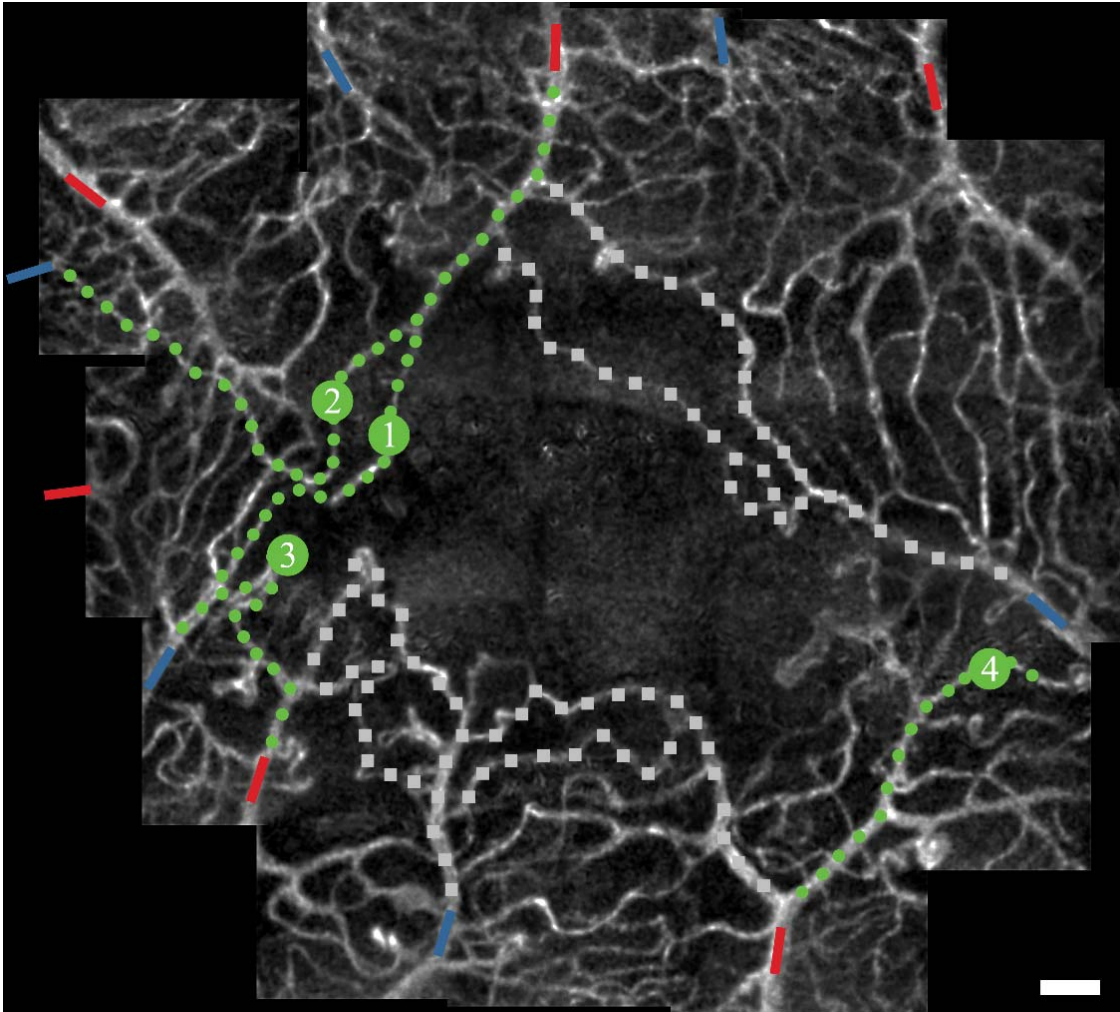


Figure 3.11: Leukocyte-preferred paths (LPP) shown on the AOSLO image from visit 2. The same four LPPs were identified in visits 2, 3, and 4. Shown are capillaries identified as LPPs (green) as well as capillaries which were assessed but not identified as LPPs (gray). Arterioles (red) and venules (blue) are shown for reference. Scale bar, 100 μm .

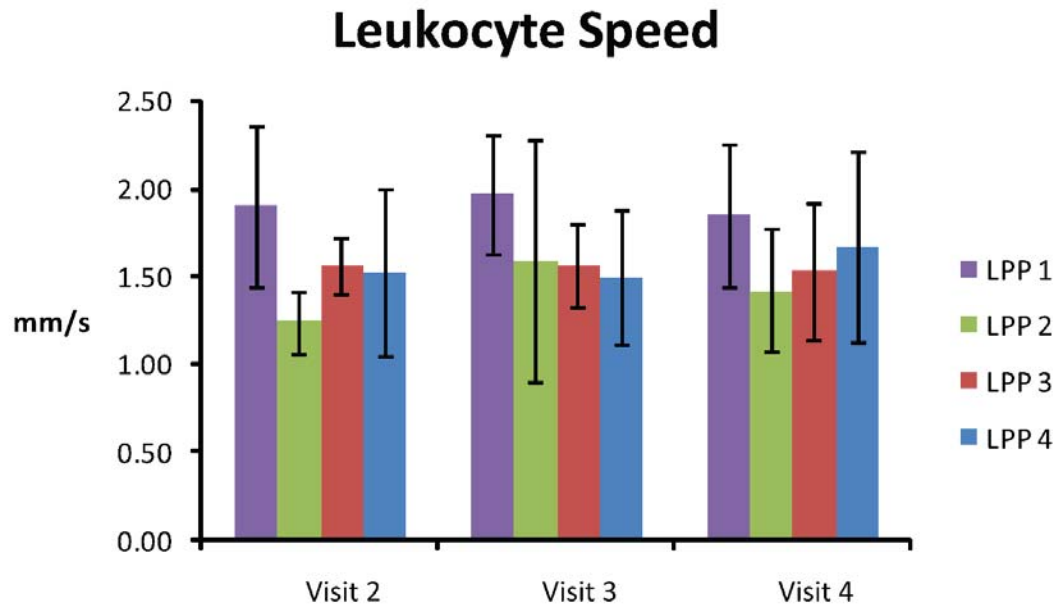


Figure 3.12: Leukocyte speed. LPP 1, 2, 3, and 4 refer to the channels as labeled on **Figure 3.11**. Speeds were averaged across the cardiac cycle and then normalized for heart rate. Error bars represent the standard deviation of the leukocyte speeds measured in the specified LPP and visit.

Assessment of cone photoreceptors

The same videos that were used to generate perfusion images were used to generate high resolution images and montages of the cone mosaic. Cone spacing was assessed in various locations within the montage for each visit. Spacing was estimated by manually selecting cone centers in contiguous unambiguous patches of cones and inferring the spacing from a histogram of all intercone distances within that set. Details on how cone spacing was estimated are reported elsewhere (Rodieck 1991; Duncan, Zhang et al. 2007). Cone spacing for each respective location was compared with expected spacing from a database of 27 normal eyes. Deviations from normal were quantified as z-scores, or the number of standard deviations from the normal mean at that location. In this particular patient, it was determined that cone spacing was normal (z-scores within +/- 2), except at the foveal center, where cone spacing was higher than expected (i.e. cone density was lower than expected) (**Figure 3.13**). The cone spacing measures were consistent between visits and there were no signs of any progression over the four visits.

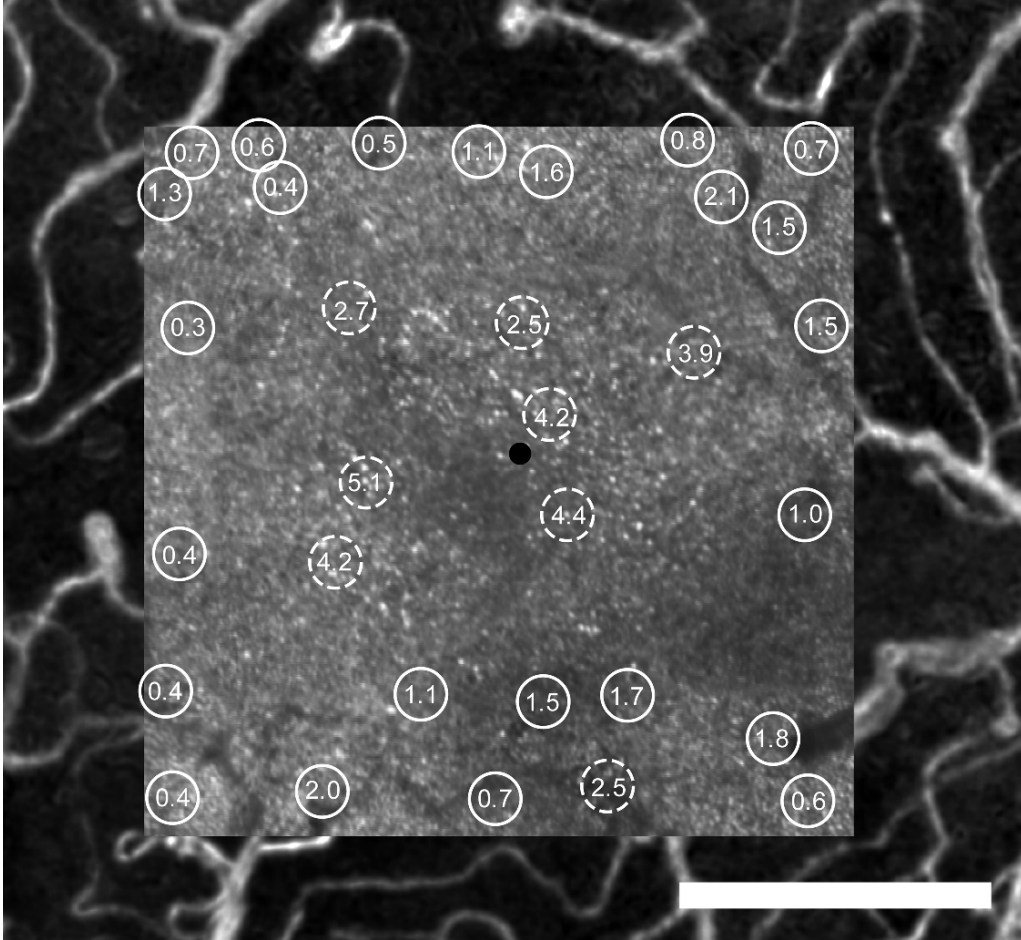


Figure 3.13: AOSLO photoreceptor montage of the foveal region superimposed on top of the corresponding AOSLO perfusion image, from visit 4. The black circle indicates the patient's preferred retinal locus for fixation. Cone spacing results are plotted as z-scores (# of standard deviations from the normal mean) at all locations where cone spacing was measured. Locations with z-scores greater than 2 are indicated with dashed circles. Near fixation, cone density is decreased; further away from fixation, cone density returns to normal. Scale bar, 300 μ m.

Cross-sectional Study

In general, there were no obvious homogeneous differences that could be observed between the T2DM_NoDR and control groups (**Figure 3.14**). The interdigitating arteriole and venule organization was maintained in all images. It appeared that there were areas of focal capillary disruption, notably around areas of capillary bend formation. Interestingly, capillary bends were present in both groups, suggesting that some aspects of capillary disruption may be present even in healthy subjects (**Figure 3.15**). There were also objects which might be precursors to microaneurysms present in both groups; such objects were not clinically identified as microaneurysms based on fundus photography. When identifying such objects, it should be noted that interpretation of AOSLO images is different than interpretation of FA images, as sources of hyper- and hypo- intensity are different; in FA, intensity is a measure of fluorescein dye accumulation, and may be indicative of leakage; in AOSLO images, intensity is a measure of high relative flow, with no information about leakage.

AV channels were identified, extracted, and quantified for tortuosity (**Figure 3.16**). Extracted FAZs and capillaries are shown (**Figures 3.17, 3.18**).

Statistical Analysis

The average AV channel tortuosity was 26% higher in T2DM_NoDR subjects compared to controls ($p < 0.05$). There were no statistically significant differences in capillary dropout or capillary hemodynamics (**Figure 3.19**). Comparing T2DM_NoDR to controls, the average FAZ size was 7.4% higher, FAZ shape 3.4% higher, capillary density 3.7% lower, leukocyte speed 14.4% lower, and pulsatility index 25% higher. It

was difficult to assess whether all variables followed a normal distribution, particularly in the case of FAZ shape, where there was one outlier. Therefore, we also performed Wilcoxon rank sum tests, which confirmed that AV channel tortuosity was significantly higher ($p < 0.05$), with none of the other metrics testing as significantly different.

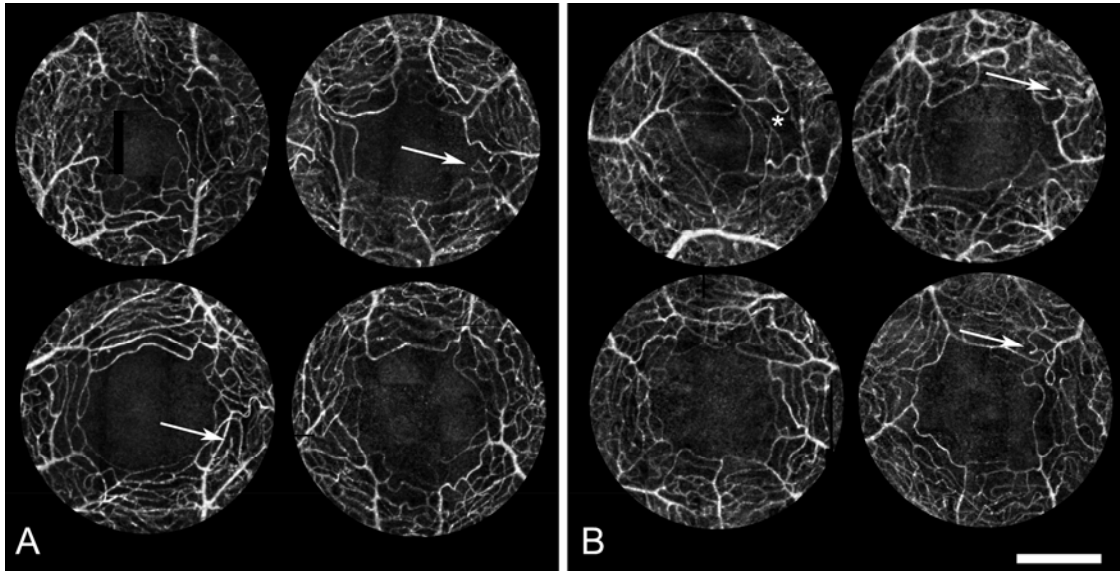


Figure 3.14: Examples of parafoveal capillary montages generated using custom motion contrast enhancement algorithms. Higher intensities denote areas of greater intensity fluctuations due to blood flow as seen on unprocessed AOSLO videos. Subtle variations in intensity in non-capillary areas are artifacts due to the use of multiple overlapping videos. There were no obvious qualitative differences in appearance between the two groups. Shown are examples: (A) four control subjects and (B) four T2DM_NoDR subjects. Arrows denote examples of peculiar capillary bends (shown in more detail in Figure 3.4). The asterisk in (B) denotes a rather large avascular region outside of the FAZ, which may be indicative of early capillary dropout. Scale bar, 500 μm .

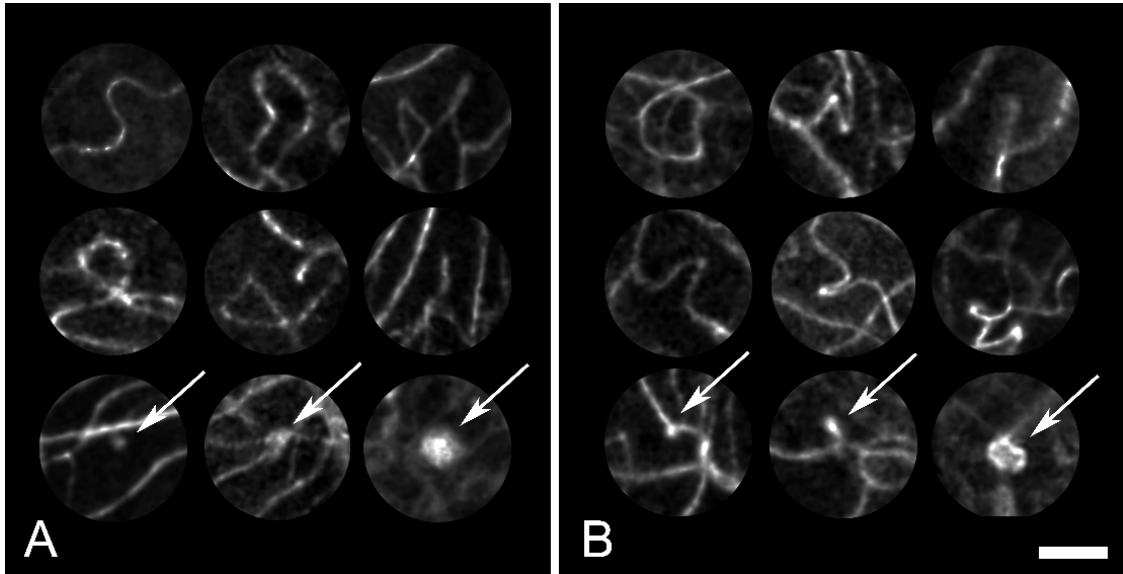


Figure 3.15: Examples of capillary abnormalities, in (A) control and (B) T2DM_NoDR subjects. There were capillary bends and dead-end capillaries present in both groups (top two rows), as well as objects of various sizes that were similar in appearance to microaneurysms (arrows in bottom row), despite the absence of microaneurysms on color fundus photographs. Scale bar, 100 μm .

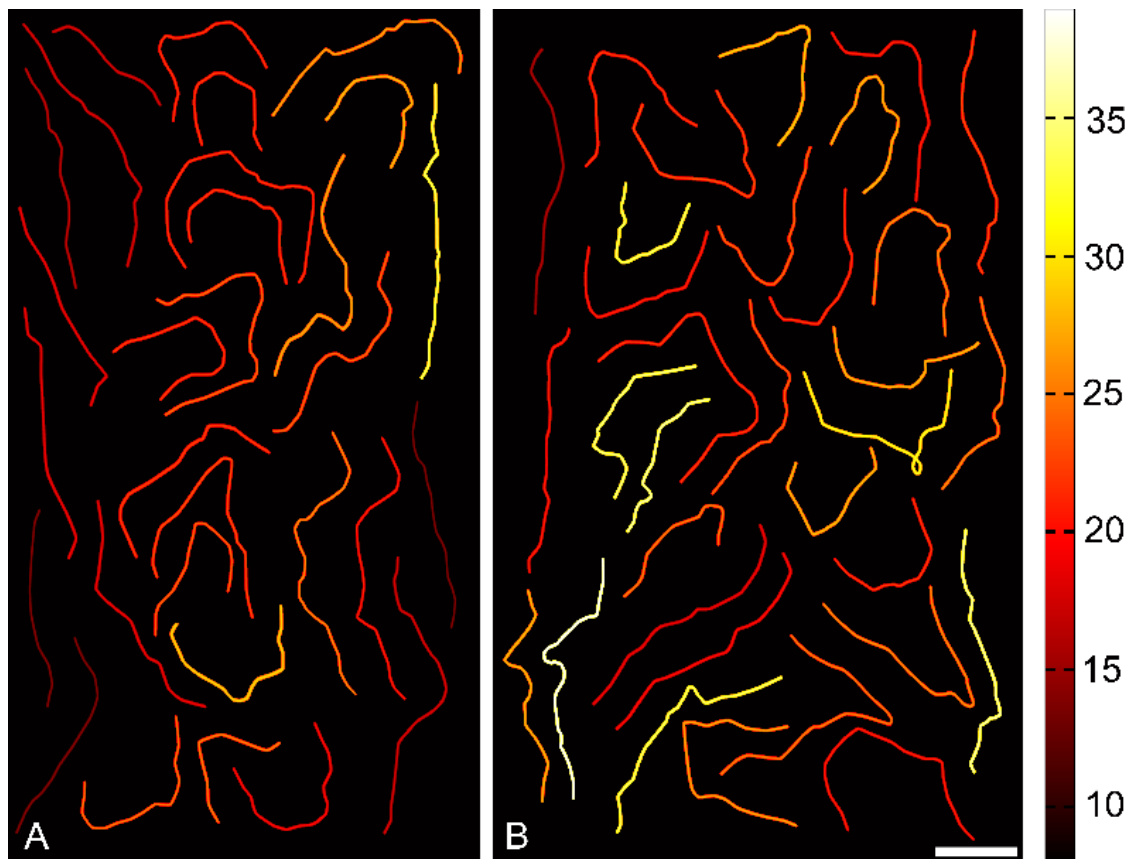


Figure 3.16: The 3 least tortuous AV channels from the (A) control and (B) T2DM_NoDR subjects. The capillary segments are arranged to best fill the space in each panel of the figure. The color map shows the range of tortuosities (Arbitrary Units, generated by calculating $TSC/L * 10^5$). Scale bar, 500 μm.

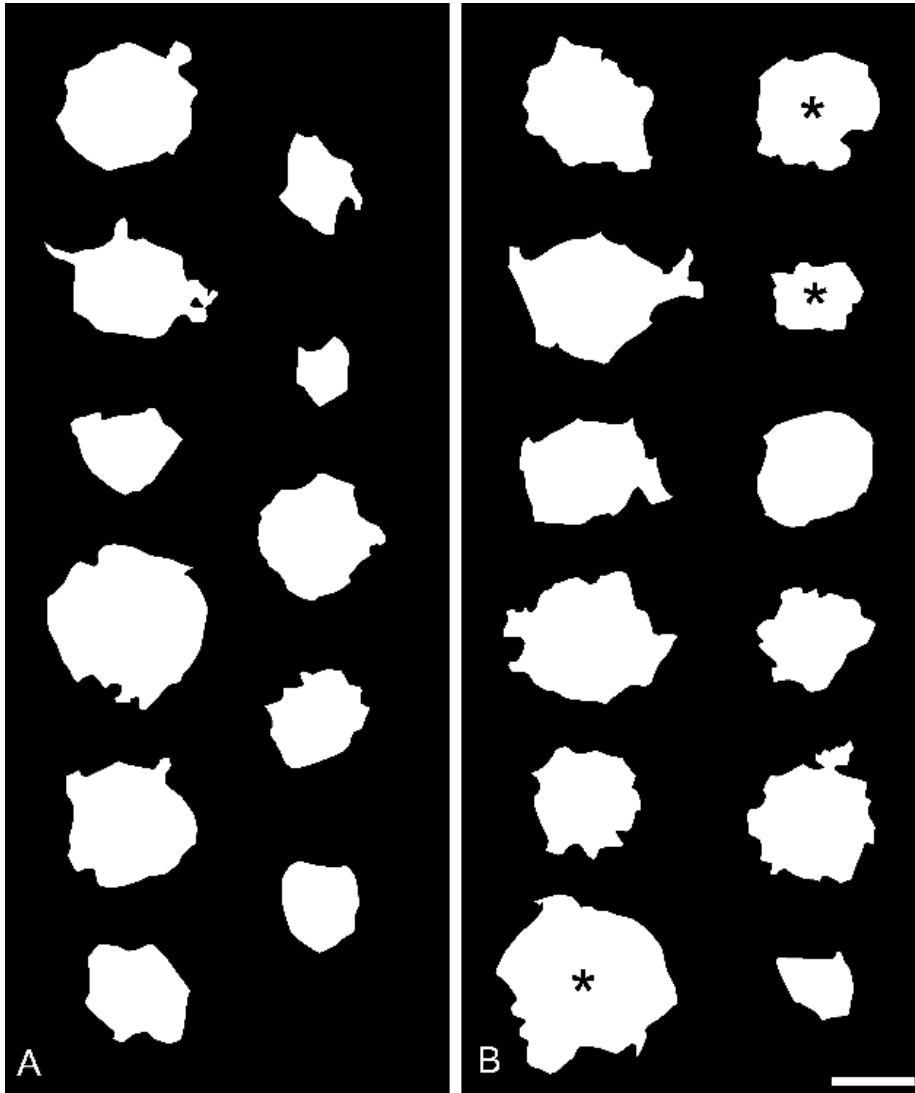


Figure 3.17: Extracted FAZs for (A) control and (B) T2DM_NoDR subjects. Three FAZs could not be extracted due to poor data quality, as described in the text. Of the extracted FAZs, three FAZs were not used for quantification of FAZ shape, due to poor quality data in one or more videos showing the edge of the FAZ (asterisk). For these FAZs, the extracted FAZ was estimated from the AOSLO image and quantified for size but not shape. Scale bar, 500 μm .

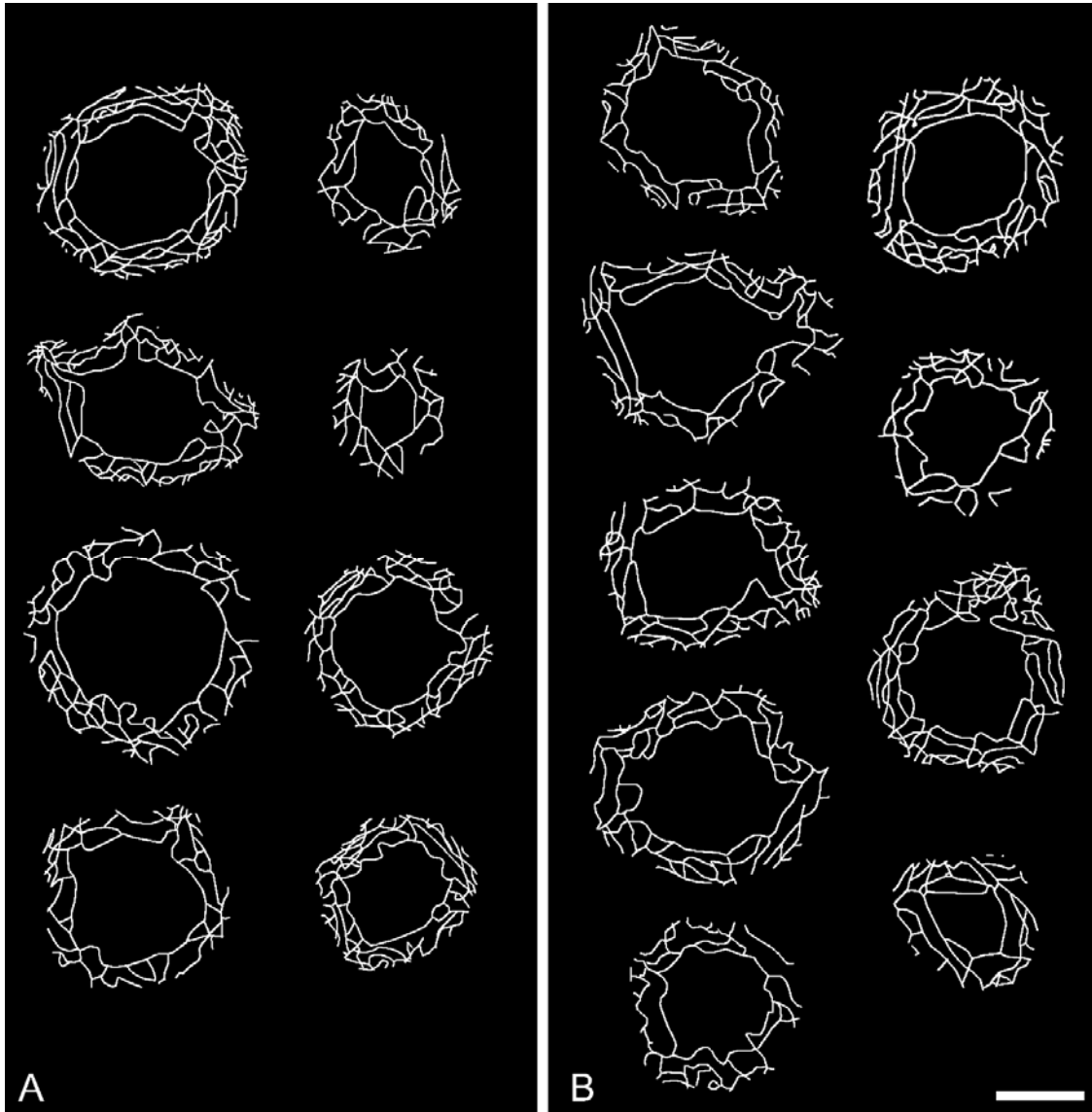


Figure 3.18: Extracted capillaries for (A) control and (B) T2DM_NoDR subjects. Some subjects could not be analyzed due to poor data quality in one or more portions within the ROI, as described in the text. Scale bar, 500 μm .

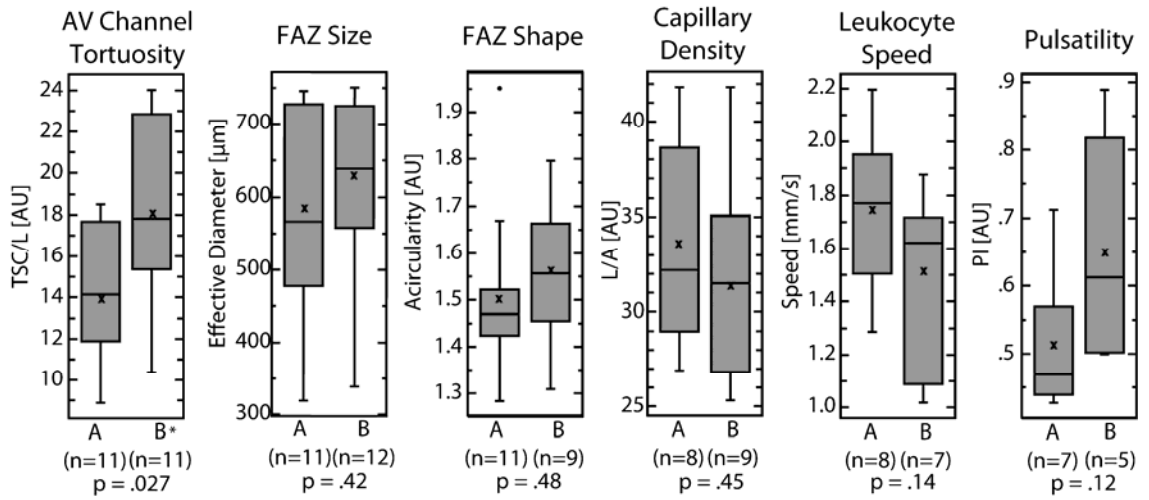


Figure 3.19: Results from statistical analyses, for control (A) and T2DM_NoDR (B) groups. AV channel tortuosity was significantly higher in the T2DM_NoDR group compared to the control group ($p < 0.05$). For FAZ shape, which had one outlier, a Wilcoxon rank sum test confirmed that the difference between groups was not statistically significant ($p = 0.26$).

3.5 Discussion

In the longitudinal study, we show that AOSLO imaging can reliably image capillaries and capillary defects in NPDR, on the basis of repeated application of AOSLO imaging alongside comparison to FA, the gold standard for visualizing human retinal capillaries.

In the cross-sectional study, we show, without fluorescein angiography, that AV channels in the human retinal parafoveal capillary network are disrupted in the early stages of type 2 diabetes, even before any signs of DR. Since most capillaries are exchange capillaries, with only a select few comprising the AV channels, it is relatively difficult to detect this change when using macroscopic metrics to assess the parafoveal capillary network.

Longitudinal study

Both clinical and subclinical features can be identified using the AOSLO. Clinical features, including MAs and IRMAs, tended to be larger in size, while subclinical features, such as capillary bends, micro-IRMAs, and the flow of individual leukocytes, tended to be smaller, similar in size to the smallest capillaries. The relationship between subclinical and clinical features can potentially be investigated using the methods presented in this chapter, since the assessment of clinical features using the AOSLO was consistent with the assessment by conventional clinical measures. Moreover, we show that subtle vascular changes occur even when the patient appears stable when assessed by conventional clinical measures.

MAAs are dynamic capillary defects, spontaneously forming and disappearing with a half life of about 2 years for patients with type 1 diabetes and mild DR (Hellstedt and Immonen 1996). The mechanism of MA formation is not completely established, but generally there is a weakening of the capillary wall due to pericyte loss (Hammes, Lin et al. 2002) or basement membrane disruption (Ashton 1963; Cunha-Vaz, Faria de Abreu et al. 1975), leading to focal endothelial cell proliferation. We found evidence of one MA increasing in size (**Figure 3.8B**), which may suggest that MAAs increase in size before disappearing. There was also one MA which disappeared (**Figures 3.8B and 3.10A**). The region near the MA disappearance is also one of capillary dropout, consistent with prior observations that MAAs disappearances are associated with capillary closure (Cunha-Vaz and Bernardes 2004). Disappearance of a MA is most likely due to thrombogenesis (Boeri, Maiello et al. 2001). It has been suggested that thrombotic phenomenon in MA is facilitated by changes in erythrocyte and leukocyte flow through the capillaries (Cunha-Vaz and Bernardes 2004). In this eye, there are no LPPs in the supero-temporal region of the parafovea (**Figures 3.4 and 3.11**). The absence of LPPs in this region could lead to a disruption of erythrocyte and leukocyte flow near that region; the location of the MA disappearance is in the supero-nasal region, although at a greater retinal eccentricity (**Figures 3.4C and 3.10A**).

The large number of capillary bends may be indicative of endothelial cell proliferation. Significantly, MAAs were not observed at the tips of capillary bends, suggesting that bends and MAAs are the result of endothelial cell proliferation occurring under different conditions. Unfortunately, it was difficult to determine whether any of these bends increased in size over the four visits. In one of the microIRMAs, a new

capillary bend developed (**Figure 3.8E**), suggesting that capillary bends may also evolve over time. In FA, small capillary bends are typically not resolved, and can potentially be mistaken as MAs. The detail with which retinal features can be resolved may enable the AOSLO to detect precursors to MAs and IRMAs.

FAZ size is often used as a proxy for capillary dropout, with larger FAZs indicative of more serious levels of retinopathy (Mansour, Schachat et al. 1993). It is often assumed that increases in FAZ size are the direct consequence of capillary dropout; in this chapter, we show direct evidence of capillary dropout leading to an increase in FAZ size. Although the sensitivity of FAZ size as an imaging biomarker is limited due to large intersubject variability, noninvasive assessment of the FAZ may be important for longitudinal comparisons within the same patient (that is, changes to the size of the FAZ in an individual may be more significant than the absolute size of the FAZ compared to a population; at the end of this chapter, we estimate that 160 subjects would be needed to achieve a significance for a change in FAZ diameter). The AOSLO can be used to identify subtle events that cause the FAZ to increase in size. In this subject, we also show some areas of subclinical capillary dropout; such areas are likely too small in size to be captured by FA.

Leukocytes are involved in the development of DR (Chibber, Ben-Mahmud et al. 2007). However, the direct relationship between leukocytes and clinical signs of DR has not been shown in humans, due to the difficulty of assessing leukocytes in vivo. In this study, we showed that the distribution of leukocytes in the capillaries near the FAZ are stable over a period of 15 months, even in the presence of small changes in the neighboring capillaries (**Figure 3.11**). At the venous end of the LPP at the right of the

FAZ, there is a MA. Interestingly, the presence of this MA does not appear to affect the upstream flow of the leukocytes into the LPP. There were no MAs or IRMAs along the path of the other LPPs. Whether the dropout of such a MA would result in a redistribution of leukocytes remains to be seen. Leukocyte speed through LPP1 was consistently higher when compared to the other LPPs. Thus, an important consideration for the interpretation of capillary speed measurements in other studies is that the speed is dependent on the specific capillary that is being measured.

The state of cone photoreceptor spacing in DR is unknown. Although there is an increase in foveal cone spacing for this patient, it is uncertain whether this result is due to diabetes or another unknown variable. Photoreceptors are not clinically assessed, since the ability to image them in live human subjects has only been enabled with recent advances in imaging technology. There is evidence of neural damage in DR(Barber 2003), suggesting that the photoreceptors may also be affected. In this patient, there was no evidence of photoreceptor disruption across visits as assessed by SDOCT; the increase in cone spacing as observed by the AOSLO may have subclinical significance. However, further studies are needed to answer this question, and to further investigate the results presented in this chapter.

The main limitation of this study is that one subject was assessed. However, it is important to consider that there is a large amount of data that can be quantified from the AOSLO videos, each consisting of 2400 video frames, enabling both static histological comparisons as well as dynamic blood flow assessments (as an example, we quantified the speed of 295 leukocytes over 3 visits). Although no conclusions can be made about the natural progression of DR, there are several important clinical implications. First,

we show that subtle capillary changes exist even when the patient appears to be stable. Such changes include the enlargement of an existing MA, development of IRMA-like capillary bends, and the dropout of a single capillary segment leading to the FAZ enlargement. Second, we show that the distribution of leukocytes traveling through the parafoveal capillary network is maintained over time, even in the presence of subtle changes in the neighboring capillaries. Moreover, we demonstrate the importance of specifying the capillary through which speed measurements are performed, since certain capillaries consistently feature faster flow rates than other capillaries. Finally, we show that areas of subclinical capillary dropout exist, even when accounting for natural capillary-free zones in the parafoveal capillary network. These isolated areas may lead to the more widespread capillary dropout that is seen in the later stages of DR.

Simultaneous assessment of photoreceptors, capillaries, and leukocytes can potentially give rise to novel imaging biomarkers, which could be used to monitor the progression of DR. Future work includes establishing a procedure for clinical interpretation of AOSLO images, since the sources of hyper- and hypo- intensity are different than what is conventionally expected. The quality of the AOSLO images increased over the visits due to continual modifications that were made to the AOSLO, which is a custom-built research instrument. Standardization of the technology will help ensure that the data quality is consistent across visits. Despite these limitations, reproducible, detailed images of capillary features were successfully generated. Our results show that additional AOSLO studies involving patients with diabetes are warranted.

In conclusion, AOSLO imaging may give insights into how DR affects the photoreceptors, capillaries, and leukocytes. AOSLO imaging is repeatable, and sensitive enough to detect changes such as the dropout of MAs and individual capillary segments, as well as the development of new MAs and IRMAs. The distribution of leukocytes seems to be unaffected by neighboring microvascular changes in the time course of 15 months. However, the relationships among the different vascular changes in DR are complex. Our results show that subclinical changes to the capillaries may exist even when conventional clinical measures detect no change.

Cross-sectional study

Based on the results of this study, we propose a novel hypothesis for the development of clinical microvascular changes (**Figure 3.20**). Unlike prior studies, this model links microvascular changes and hemodynamics to account for clinical signs.

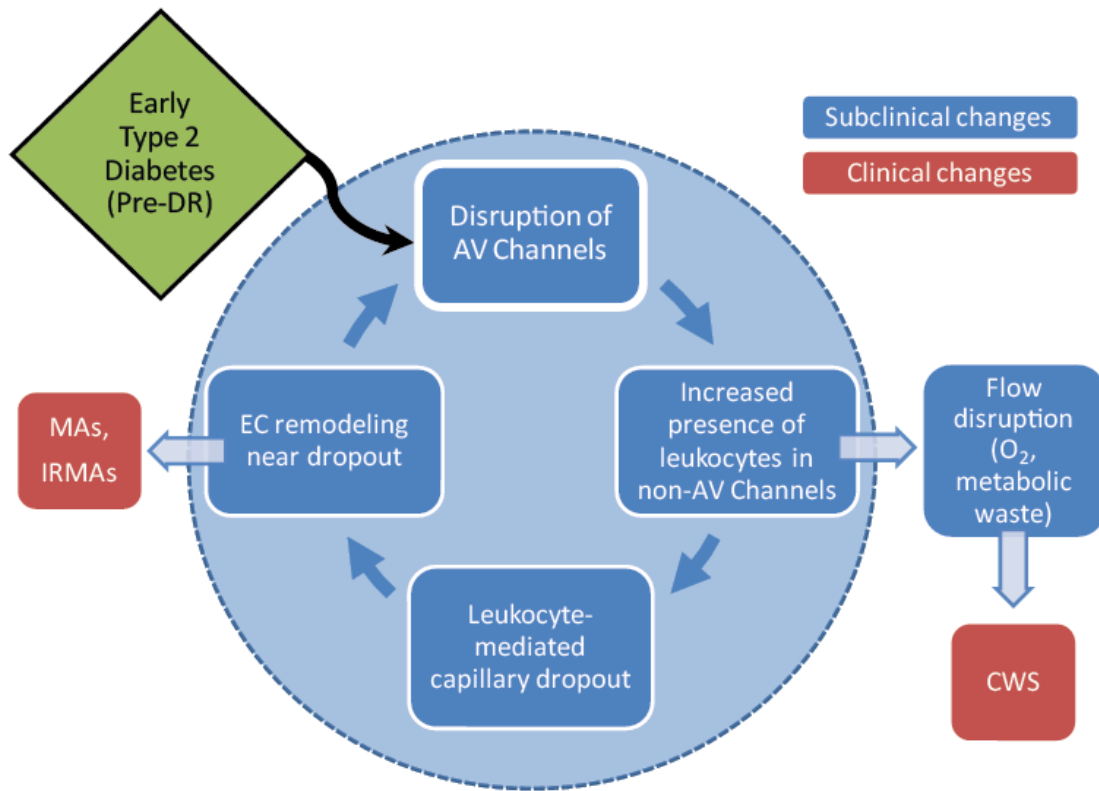


Figure 3.20: Flow chart showing the proposed mechanism for progression from AV channel disruption to NPDR. EC, endothelial cells; MAs, microaneurysms; IRMAs, intraretinal microvascular abnormalities; CWS, cotton wool spots.

We hypothesize that there is an ongoing cycle of AV channel disruption, which propagates with a redistribution of leukocytes out of AV channels and into exchange capillaries. A redistribution of blood flow prior to the onset of DR has been previously reported in a streptozotocin rat model for diabetes (Alder, Su et al. 1997). Initially, with incremental changes in tortuosity, existing AV channels are likely to be replaced by new AV channels, which would be the next least tortuous path connecting arterioles to venules. However, replacement AV channels would likely include some exchange capillaries, which may not be suitable for increased leukocyte traffic. Specifically, the passage time for leukocytes through exchange capillaries is likely to be much higher than for leukocytes through AV channels. This would lead to an overall accumulation of leukocytes in the network, consistent with previous findings (Kim, Johnson et al. 2005). These leukocytes inside exchange capillaries may lead to focal capillary dropout, for which many leukocyte-based mechanisms have been proposed (Chibber, Ben-Mahmud et al. 2007), which may be triggered by a decrease in the deformability and increase in activation of diabetic polymorphonuclear leukocytes (Braun, Fisher et al. 1996; Miyamoto and Ogura 1999). As the cycle of AV channel disruption continues, one can imagine that there could be two points of no return: first, when all AV channels have been replaced by exchange capillaries, and second, due to progressive disruption, when there are finally no longer any more viable replacement AV channels.

This cycle could lead to clinical signs of DR, with endothelial cell remodeling resulting in the formation of microaneurysms and intra-retinal microvascular abnormalities. If leukocytes were to accumulate inside microaneurysms, as has been

qualitatively observed (Ashton 1963; Kim, Johnson et al. 2005), then this could lead to the subsequent disappearance of the affected microaneurysm. This accumulation of leukocytes inside microaneurysms would be aided by any redistribution of leukocytes resulting from AV channel disruption. Simultaneously, since leukocytes have such a dominant role in determining the flow mechanics in capillaries, disruption of the tissue homeostasis may lead to neural damage or formation of cotton wool spots. Therefore, disruption of AV channels could lead to the formation of clinically observed changes.

There are several potential explanations for why AV channel tortuosity is higher in the T2DM_NoDR group. First, it is possible that the increase is due to endothelial cell proliferation. However, given that our results occur prior to the formation of clinically-identifiable microaneurysms (a sign of endothelial cell proliferation), it is unlikely that the increase in tortuosity can be attributed to endothelial cell proliferation alone. Second, it is possible that a flow parameter such as increased intramural pressure could contribute to an increase in tortuosity, as has been modeled using 7.9 mm diameter latex tubing (Kylstra, Wierzbicki et al. 1986). However, it is unclear whether the mechanisms for increased tortuosity of larger vessels can be applied to capillaries, since capillaries are by nature more tortuous than larger vessels. Although it is tempting to apply existing mechanisms for increases in vessel tortuosity, it is important to keep in mind that our definition of AV channel tortuosity is based on finding the least tortuous paths. Hence, a higher AV channel tortuosity implies that the set of least tortuous paths is higher, but does not necessarily imply that the tortuosity of any one capillary segment has increased. Given these considerations, along with our hypothesis (**Figure 3.20**), a

higher AV channel tortuosity in patients without retinopathy may simply be the result of the progressive loss of key capillary segments.

Our results are consistent with previous studies that have investigated capillary dropout, which is a hallmark of NPDR. There are several methods to quantitatively assess capillary dropout. The most intuitive method is to quantify the size of the FAZ, with a larger FAZ corresponding to capillary dropout in the parafovea. While some studies have found statistically significant increases in FAZ size in NPDR (Mansour, Schachat et al. 1993; Conrath, Giorgi et al. 2005), data from other studies show increases only in the later stages (Hilmantel, Applegate et al. 1999); this is likely due to the large intersubject variability in FAZ size. There is also some evidence that the FAZ becomes more acircular in DR, with greater effects on the perimeter than on the size (Bresnick, Condit et al. 1984; Conrath, Giorgi et al. 2005). Our measurements of FAZ size and shape are consistent with the numbers reported in these studies, falling between the numbers reported for normal and diabetic FAZs. Finally, our capillary density metric is similar to perifoveal intercapillary area, which has been found to increase in NPDR (Arend, Wolf et al. 1994; Sander, Larsen et al. 1994), with the change likely to occur between mild NPDR and moderate NPDR (Sander, Larsen et al. 1994). These studies and the data from our study suggest that macroscopic capillary dropout is a gradual process that likely occurs only after the manifestation of clinical signs of DR.

There have been many studies of blood flow in DR. However, results are potentially confounded by differences in measurement location (e.g. arteriole, venule, or capillary; papillary, macular; retina, choroid), disease severity (e.g. NPDR, PDR), disease type (e.g. type 1, type 2), object of measurement (e.g. erythrocyte, leukocyte,

plasma bolus), or even disease model (e.g. rat, monkey, human). Considering only results from human subjects, it appears that blood flow in arteries and veins are decreased prior to the onset of DR (Feke, Buzney et al. 1994; Bursell, Clermont et al. 1996; Konno, Feke et al. 1996) and increased during NPDR (Kohner, Hamilton et al. 1975; Cunha-Vaz, Fonseca et al. 1978; Patel, Rassam et al. 1992; Konno, Feke et al. 1996). Perifoveal capillary velocity was found to be decreased in patients with diabetes (Arend, Wolf et al. 1994), consistent with the data in this study; however, papillomacular capillary blood flow was found to be increased in patients with type 2 diabetes but no DR (Ludovico, Bernardes et al. 2003), suggesting that changes to the blood flow are heterogeneous in nature. Finally, studies investigating the pulsatility of blood in choroidal vessels have found increases in pulsatility in the later stages of DR (severe NPDR, PDR) (Geyer, Neudorfer et al. 1999; Savage, Hendrix et al. 2004), but the results are inconsistent in the earlier stages, with decreases (Geyer, Neudorfer et al. 1999), no change (Savage, Hendrix et al. 2004), and increases (MacKinnon, O'Brien et al. 2009) shown. In our study, leukocyte speed was 14% lower, and pulsatility index 25% higher. We identified capillary segments using AV channels in order to perform leukocyte speed measurements in the same corresponding location of the parafoveal capillary network in all subjects; furthermore, measured speeds were normalized for the cardiac cycle. The average heart rate, which was simultaneously recorded during the acquisition of every AOSLO video, was similar in both groups (66.4 ± 11.7 for T2DM_NoDR and 64.7 ± 9.4 for controls, reported as mean \pm standard deviation, in beats per minute). Increased AV channel tortuosity is consistent with decreased leukocyte speed, since leukocytes must deform to travel through small capillaries in single-file

(Schmid-Schonbein, Usami et al. 1980), and any increase in tortuosity is likely to require additional deformations for leukocyte passage. In addition, the decreased leukocyte speed is consistent with the increased rigidity of diabetic leukocytes (Pécsvarády, Fisher et al. 1994). Although the results of statistical testing for these hemodynamic measures were not significant (i.e. inconclusive), such metrics may still be of clinical importance.

There are several limitations to this study.

First, the sample sizes of the control and T2DM_NoDR groups are small. Due to the small sample size, it was not meaningful to examine correlations with variables such as HbA1c, disease duration, or age. The age range in this study was narrow, as it was pre-determined mostly by the inclusion criteria of type 2 diabetes with no DR, and at least 5 years disease duration; by 15 years duration, nearly 80% of type 2 diabetes patients have signs of DR (Klein, Klein et al. 1984). Despite the small sample size, AV channel tortuosity was significantly different when comparing patients with type 2 diabetes and controls, suggesting that this metric is highly sensitive. In this study, we selected the three least tortuous channels. To explore the robustness of this metric, we also compared the least tortuous channel, as well as the average of the two least, four least, and five least tortuous channels, and found statistically significant differences in all cases. However, larger studies should be undertaken to validate our findings.

Second, the ethnicity is markedly different between the two groups. While there are no studies to suggest that the parafoveal capillaries are different with respect to ethnicity, it is possible that changes may be due to ethnicity. We did not find changes in

the macroscopic measures of capillary dropout, which supports our assumption that there are no significant ethnic differences.

Finally, the process of AOSLO imaging combined with video and image analysis is time consuming, and requires specialized equipment that is not yet commercially available. In this study, AOSLO imaging for one eye from each subject required about 2.5 hours, followed by about 20 hours of offline processing per eye to generate images of parafoveal capillaries and to quantify the metrics described in this study. However, these methods are not yet optimized, as nearly every step utilizes custom hardware and software. Future optimization and automation of imaging and processing will certainly result in significant improvements in speed.

In the future, studies should be performed to validate the AV channel tortuosity metric, perhaps by examining high-quality FAs to evaluate AV channel tortuosity in NPDR and PDR. Results from this study are important for planning future studies. As examples, our results suggest that about 180 subjects would be needed to achieve significance for a change in FAZ shape (when including the outlier), 160 subjects for a change in FAZ diameter, 120 subjects for capillary density, and about 30 subjects for leukocyte speed or pulsatility index (assuming a two-sided t-test, significance level 0.05, and power level 0.80).

In conclusion, we demonstrate a unique method to noninvasively assess retinal capillaries and leukocytes in patients with type 2 diabetes and no DR. Although there are now several methods to noninvasively visualize capillaries in humans (Nelson, Krupsky et al. 2005; Kim, Fingler et al. 2011; Schmolz, Singh et al. 2011), the system of imaging and analysis described in this chapter is unique in that capillaries and

leukocytes can be analyzed from the same dataset. Furthermore, we offer a “causative” model that links microvascular changes and blood flow to clinical signs of DR (**Figure 3.20**).

These new methods may be useful for assessing the microcirculation in other diseases, particularly as advances in technology reduce the time commitment for analysis and allow for larger study populations. This application may find the most use in cases when FA is not performed (for whatever clinical reason), or for establishing a normal database of parafoveal capillaries, since our data suggests that subclinical capillary peculiarities may exist even before the onset of disease (**Figure 3.14**).

Although it is often difficult to find changes in the microvasculature due to large intersubject variability, AV channels in the parafoveal capillary network are disrupted even before the presence of any clinical signs ($p < 0.05$), and this change appears to precede measurable levels of capillary dropout as well as alterations to leukocyte flow. As such, AV channel tortuosity is the most promising candidate as an imaging biomarker for evaluating the efficacy of a therapeutic agent, or as a tool to assess the onset and progression of DR.

3.6 Acknowledgments

Portions of this chapter are published in *Investigative Ophthalmology and Visual Science*. The dissertation author is the primary investigator and thanks co-authors, Kavita Dhamdhere, Pavan Tiruveedhula, Silvestre Manzanera, Shirin Barez, Marcus Barse, Anthony Adams, and Austin Roorda. The author would also like to thank David

Merino for his assistance with the AOSLO; Brandon Lujan for his valuable insights regarding clinical aspects of diabetic retinopathy; Shirin Barez, for clinical assistance; Brian Wolff, Maria Cardenas, Wendy Harrison, Glen Ozawa, and Michal Laron, for assistance with patient recruitment; Nicholas Jewel and Winston Li for assistance with statistical planning and analysis. These studies was funded by the NIH Bioengineering Research Partnership EY014375, JDRF Grant 8-2008-823, NIH Grant EY02271, an NSF Graduate Research Fellowship under Grant DGE-0648991, and a National Defense Science and Engineering Graduate (NDSEG) Fellowship, under and awarded by DoD, Air Force Office of Scientific Research, 32 CFR 168a.

CHAPTER 4

CONCLUSIONS

4.1 Summary of Findings

The objective of this work was to develop a better understanding of capillaries and moving blood cells seen by adaptive optics scanning laser ophthalmoscopy, in order to extend the applicability of the overall imaging system for studying normal and diseased retinas. To address this objective, novel approaches were taken. In summary, the novel methodologies were:

- (A) Development of custom motion contrast enhancement algorithms in order to noninvasively generate detailed images of the retinal vasculature, without the use of injected contrast agents (Chapter 1).
- (B) Development of a system of video and image analysis based on motion contrast enhanced spatiotemporal plots for accurate tracking and speed quantification of moving objects in a raster scanning system that acquires images in the presence of eye motion (Chapter 2).
- (C) Development of image analysis tools to quantify metrics about the parafoveal capillary network, including measurement of the foveal avascular zone, parafoveal capillary density, pulsatility of moving objects, and tortuosity of arterio-venous capillary channels (Chapters 1,2,3).

The major scientific findings were:

1. Parafoveal capillary density in the single-layered region is uniform in the superior, inferior, nasal, and temporal directions.
2. Leukocytes and plasma gaps are distributed in a heterogeneous manner around the parafoveal capillary network, with certain capillaries accounting for a clear majority of leukocyte traffic (leukocyte preferred paths), and others primarily featuring plasma gap flow (plasma gap capillaries).
 - a. Leukocyte preferred paths may serve as a protective mechanism to prevent inactivated leukocytes from entering exchange capillaries.
 - b. Plasma gap capillaries may serve as relief valves to minimize flow disruption due to the presence of a leukocyte in a neighboring capillary.
3. Arterio-venous capillary channels are disrupted in type 2 diabetes even before the onset of diabetic retinopathy.
 - a. Disruption of arterio-venous channels would result in a redistribution of leukocytes out of thoroughfare channels and into exchange capillaries.
 - b. This redistribution could lead to clinically observed signs of diabetic retinopathy, such as microaneurysms, intra-retinal microvascular abnormalities, and cotton wool spots.
 - c. Arterio-venous channel tortuosity is a promising candidate as an imaging biomarker for evaluating the efficacy of a therapeutic agent, or as a tool to assess the onset and progression of diabetic retinopathy.

4.2 Future Directions

There are many areas for future work. We describe four potential directions: (i) further investigation of diabetic retinopathy, (ii) application of motion contrast imaging to other retinal diseases, (iii) development of an engineering model for microhemodynamics of retinal capillaries, and (iv) optimization and automation of video and image processing algorithms. For each area, we describe the scientific questions of interest, key technical problems that need to be solved, and proposed approaches.

4.2.1 Diabetic Retinopathy

There are many questions that remain to be answered, in patients with no diabetic retinopathy, non-proliferative diabetic retinopathy (NPDR), or proliferative diabetic retinopathy (PDR).

Leukocyte studies

The system of AOSLO imaging combined with video and image processing allows for the noninvasive investigation of leukocytes in live human capillaries. In Chapter 3, we hypothesized that a redistribution of leukocytes out of AV channels and into surrounding capillaries could lead to the formation of clinical signs seen in NPDR. If this were true, then we would expect a decrease in leukocyte frequency through AV channels. For the 7 T2DM_NoDR and 8 control subjects on which leukocyte speed quantification was performed, the frequency at which leukocytes flowed through

selected AV channels was 30.0 ± 21.6 leukocytes/minute for the T2DM_NoDR group, and 54.8 ± 32.8 leukocytes/minute for the Control group (mean \pm standard deviation, two sided unpooled t-test, $p = 0.11$). Although these numbers are in agreement with the hypothesis, there are several important considerations. First, it should be noted that leukocyte frequency measurements are highly dependent on the quality of the videos, and as such, these results could simply reflect a lower video quality in the T2DM_NoDR group. Second, identification of leukocyte traces is based on a user-defined criteria for evaluation of spatiotemporal plots, as described in Chapter 2. The key assumption is that the traces identified on spatiotemporal plots are due to leukocytes. Finally, there are many factors that can lead to changes in leukocyte frequency, both systemically, and locally within a tissue. Although our hypothesis is based on local factors, differences in systemic white blood cell counts could also have an impact. It has been shown that white blood cell counts are increased in patients prior the onset of type 2 diabetes (Vozarova, Weyer et al. 2001), and also in smokers (Nakanishi, Yoshida et al. 2002). However, the fact that we observed a decrease in leukocyte frequency despite any increase in systemic white blood cell count suggests that AV channel leukocyte frequency probably is in fact diminished. To be certain, before reporting absolute measures of leukocyte frequency, a method for normalizing frequencies, along with a series of validation experiments, need to be performed.

As with any imaging system, validation of the objects being imaged using experimental conditions is important. Direct verification of leukocyte imaging can be performed using fluorescent labeling and a nonhuman primate. An AOSLO equipped

with fluorescent imaging capabilities is needed (Gray, Merigan et al. 2006). Leukocytes can either be labeled *in vivo* or *ex vivo*. A popular dye for *in vivo* (*intravital*) labeling of leukocytes is Acridine Orange (AcOr), a DNA-staining probe that spares erythrocytes due to their lack of a nucleus; the dye is not fluorescent until it diffuses across the cell membrane and binds to the DNA, and has similar absorption and emission spectra as fluorescein, making it a convenient choice for retinal imaging systems. Other candidate dyes for leukocyte imaging that have similar absorption and emission spectra include fluorescein isothiocyanate (FITC), calcein-AM, and carboxyfluorescein diacetate (CFDA) (Tsuji-kawa and Ogura 2011). The AcOr dye can be injected systemically, as has been done in monkeys (Nishiwaki, Ogura et al. 1995), rats (Komatsu, Koo et al. 1990; Nishiwaki, Ogura et al. 1996; Miyamoto, Hiroshiba et al. 1998; Tsujikawa, Kiryu et al. 2000), and snake (Zwick, Elliott et al. 1999). In the case of retinal imaging, the choroidal circulation is largely blocked due to staining of the RPE nuclei (relevant for widefield imaging techniques). The main limitation of using AcOr is its low quantum yield (0.20); it may be possible to find a different probe with a higher quantum yield. Additionally, all types of leukocytes are equally likely to be labeled by the dye. The second possibility based on *ex vivo* labeling is to extract whole blood, isolate leukocytes, stain with a fluorescent dye, and reinject the leukocytes into the circulation. This strategy has been done using fluorescein dye in humans (Paques, Boval et al. 2000). Although the number of labeled objects is likely to be small, a potential advantage of this method is that it would be possible to specify the type of leukocyte that is being measured. Incorporation of flow cytometry after isolation of leukocytes and before staining would enable selective staining of specific classes of leukocytes,

which would be useful for studying the different types of leukocytes. As examples, monocytes and granulocytes are more likely to cause injury to the capillaries, since their activation releases proteases and O₂-derived free radicals (Fantone and Ward 1982). As additional evidence, an increase in post-mortem granulocyte density (also known as polymorphonuclear leukocytes) was found in diabetic monkeys in the parafoveal region ($p < 0.01$) (Kim, Johnson et al. 2004).

Finally, peculiarities in leukocyte flow are currently uncharacterized. As examples, leukocyte flow retardation along the walls of microaneurysms, leukocyte flow through sharp capillary bends, and spontaneous reversals in flow direction can be observed in select patients and controls. Temporary occlusion of a capillary segment by a plugged leukocyte may not be visible unless there are changes that can be observed on the time scale of imaging (40 seconds in this dissertation). Although it may be difficult to observe leukocyte dwelling, we did observe an example of a leukocyte changing speeds in one of the AV channels from one of the T2DM_NoDR patients (**Figure 4.1**). Irregularities in flow could lead to the formation or evolution of focal capillary defects, such as the formation of a new capillary bend or the enlargement of an existing microaneurysm. However, it is challenging to identify these regions of abnormal flow and to characterize them in normal and pathological conditions, and further work is needed.

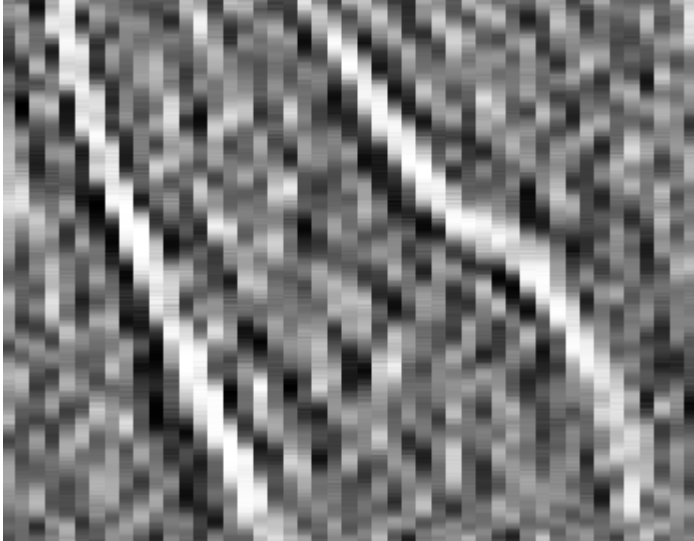


Figure 4.1: Two leukocyte traces from an AV channel of a subject from the T2DM_NoDR group. The start of the vessel is at the top of the spatiotemporal plot. The trace on the left is a typical trace that shows no appreciable variation in speed. The trace on the right shows that the speed slowed down in the center of the capillary segment, before speeding up again.

Neuro-vascular relationships

Broadly, the abnormalities in DR can be classified as neural or vascular. Using AOSLO imaging, we can assess capillary structure, hemodynamics, and the structural integrity of photoreceptors. Studies investigating cone photoreceptor spacing in the T2DM_NoDR patients are currently in progress.

Neural function can also be examined using a multifocal electroretinogram (mfERG). Recently, a method to identify local regions of abnormalities in neural function has been developed using mfERG implicit time measurements (Bears, Adams et al. 2006). A stimulus array comprised of 103 hexagons spanning 20 radial degrees from the foveal center is used to measure implicit time, a marker of neural function. Implicit time is an important metric in early diabetic retinopathy, because delays in implicit time have been shown to predict sites of new retinopathy (Han, Bears et al. 2004). In order to match up AOSLO data with mfERG data, we acquired AOSLO videos in locations corresponding to the central 7 hexagons of the mfERG stimulus grid (**Figure 4.2**).

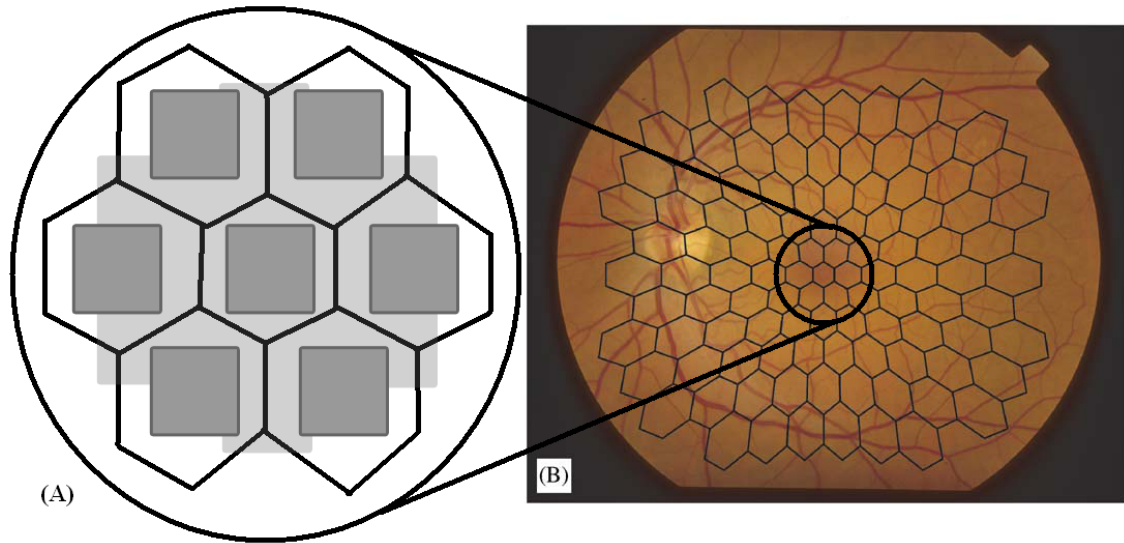


Figure 4.2: Diagram showing the locations at which AOSLO videos were taken. (A) Videos were taken in 21 locations (combined area of light and dark gray shading. These are the same 21 locations that were selected for imaging in the cross-sectional study of Chapter 3). 7 of these locations were centered in one of the central 7 hexagons of the mfERG stimulus grid (dark gray squares). (B) Overlay of mfERG grid on a fundus photograph.

Unfortunately, we were unable to reliably quantify capillary density within the outer 6 hexagons, due to the presence of multiple capillary layers, and large variations in data quality. Moreover, the high capillary density made it difficult to delineate clear capillary paths for hemodynamic analysis. Thus, it was difficult to derive AOSLO-based metrics for the videos inside the outer 6 hexagons (the central hexagon has little or no capillaries due to the presence of the FAZ). In the future, with further technical development, it may be interesting to explore neural-vascular relationships in the outer hexagons.

Instead, to investigate whether neural and vascular abnormalities are related, we compared AV channel tortuosity to implicit time. AV channel tortuosity was defined as the average tortuosity of the 3 least tortuous capillary channels, consistent with the methods described in Chapter 3. We converted AV channel tortuosity values in the T2DM_NoDR group to z-scores by using the group of age-matched controls. Implicit time was measured using the mfERG in each of the T2DM_NoDR patients within one month of the AOSLO imaging session, and converted to z-scores using a database of normal subjects. AV channel tortuosity z-scores were then plotted against implicit time z-scores in order to determine whether there was a correlation between the two metrics. We found that there was no apparent correlation between the two metrics ($R^2 = 0.007$) (Figure 4.3).

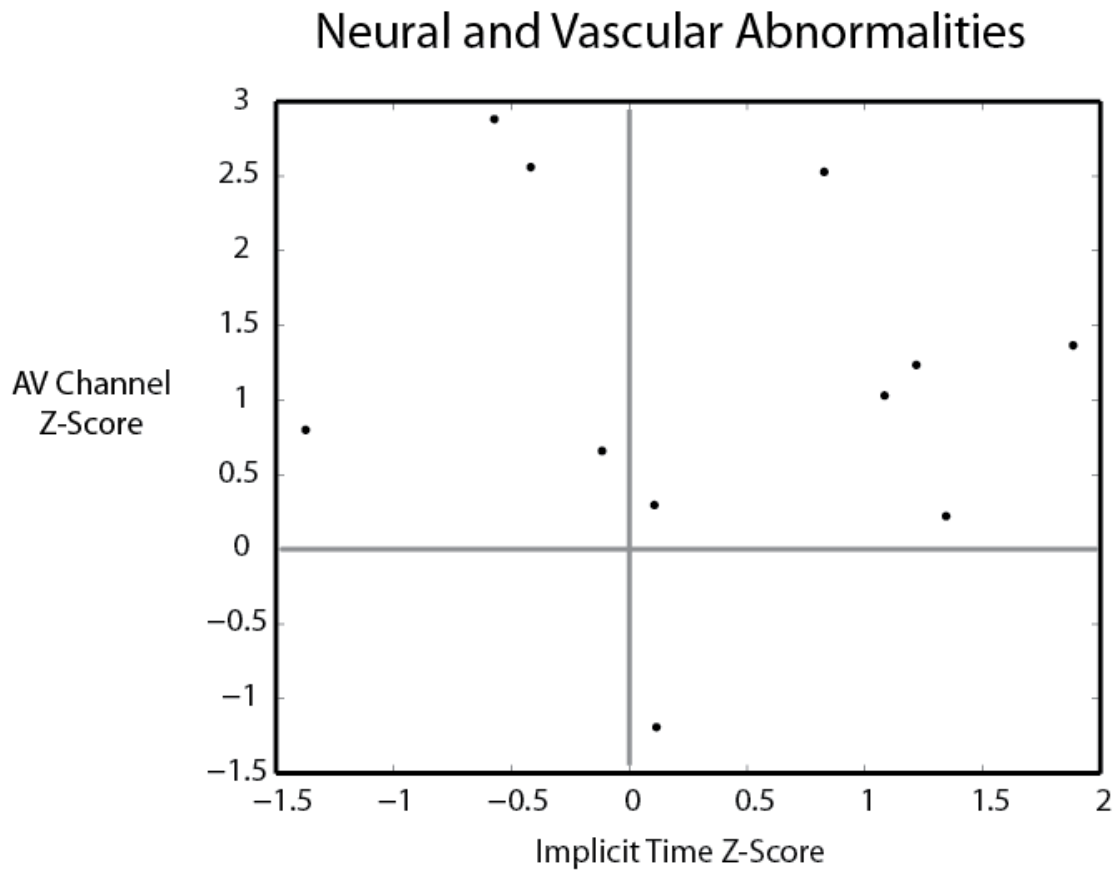


Figure 4.3: Comparison of neural and vascular abnormalities for 11 T2DM_NoDR subjects. The metric for vascular abnormality is average AV channel tortuosity z-score, generated from the AOSLO data, which is plotted against implicit time z-score, generated from mfERG data.

The early changes in type 2 diabetes are complex. Although there are local regions of retinal damage that manifest even prior to the onset of DR, with respect to both neural function measured by the mfERG (Bears, Adams et al. 2006) and capillary channel disruption measured by the AOSLO (Tam, Dhamdhere et al. 2011), it appears that the two are not correlated. The fact that we do not observe a correlation suggests that diabetes can affect different components of the retina through different mechanisms. Specifically, the mechanisms for capillary channel disruption appear to be different from the mechanisms that damage the cell bodies of bipolar cells, the location from which mfERG implicit time is derived (Hood, Frishman et al. 2002). Thus, different strategies may be necessary for the therapeutic treatment of damage to neural and vascular components of the retina.

Evaluation in NPDR and PDR

It is unclear whether AV channels are further disrupted in NPDR and PDR. In Chapter 3, we suggested that there is a “point of no return” when all viable AV channels have been lost, which may mark the transition in PDR. Careful delineation of capillary channels in patients with NPDR and PDR would be needed to determine whether this is the case.

We quantified AV channel tortuosity in the patient with type 1 diabetes and severe NPDR described in Chapter 3 (**Figure 4.4**). This patient had an average AV channel tortuosity of 0.32, compared to 0.18 ± 0.04 for the T2DM_NoDR group, and 0.14 ± 0.03 for the control group (arbitrary units, all numbers average \pm standard

deviation), consistent with our hypothesis. Detailed comparison of the metrics for capillary dropout and hemodynamics quantified in Chapter 3 are presented in **Table 4.1**. Except for leukocyte speed, the metrics measured in the patient with NPDR were in the same general direction as the T2DM_NoDR group (i.e. increased or decreased relative to controls). However, as described in the discussion of Chapter 3, blood flow is decreased prior to the onset of DR, and increased during NPDR. Thus, our data is still consistent with expected changes reported in prior studies. To further explore relationships in NPDR and PDR, additional patients are needed.

Conclusions

There are several promising areas that should be further explored. These areas include leukocyte redistribution, relationships between neural and vascular abnormalities, and capillary abnormalities in NPDR and PDR.

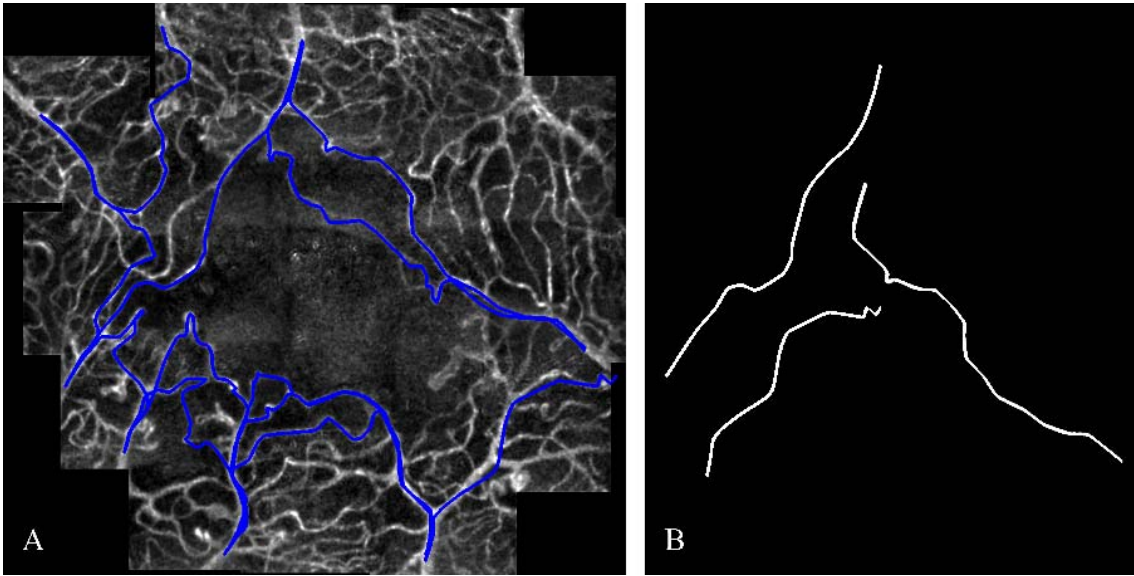


Figure 4.4: Identification of AV channels in the patient with NPDR. (A) AOSLO montage from visit 2, along with all candidate AV channels. (B) The three least tortuous AV channels.

Table 4.1. Evaluation of study metrics in NPDR

Metric	NPDR ¹	T2DM_NoDR	Control
AV Channel Tortuosity	0.32	0.18 ± 0.04	0.14 ± 0.03
FAZ Size [μm]	780	627 ± 118	584 ± 136
FAZ Shape	2.57	1.56 ± 0.15	1.51 ± 0.17
Capillary Density	31.30	31.43 ± 5.52	33.45 ± 5.23
Leukocyte Speed ² [mm/s]	1.90 ± 0.46	1.50 ± 0.32	1.75 ± 0.29
Pulsatility Index	0.50	0.52 ± 0.10	0.65 ± 0.17

¹Numbers from visit 2 are shown for the patient with type 1 diabetes and severe NPDR.

²For the patient with type 1 diabetes and severe NPDR, LPP 1 was identified as the least tortuous AV channel that also exhibited leukocyte traffic.

4.2.2 Capillaries in Other Retinal Diseases

There are many diseases affecting the retinal capillaries. Motion contrast imaging using the AOSLO would be most useful for situations where fluorescein angiography is not routinely performed, or where subclinical changes are suspected to occur. Examples include (i) establishing a normal database of the retinal capillaries, (ii) investigating the early stages of diseases (in cases where fluorescein angiography is not performed until the later stages), (iii) longitudinal investigation of diseases where the subclinical time course of disease progression is suspected to be rapid. In the long term, motion contrast-based metrics might be useful as endpoint measures for assessing the efficacy of novel therapeutic agents. In this section, we show brief case examples of images acquired in patients with diseases other than diabetic retinopathy; further work is needed to develop an understanding of the capillary pathologies that are being imaged.

Case 1: Macular Telangiectasia

Macular Telangiectasia (MacTel) is a disease affecting the vasculature near the fovea. Example capillary images are shown from two patients with MacTel. One feature of this disease is a disruption of the planar orientation of vessel planes, leading to vessels oriented in unexpected directions (**Figure 4.5**). The unexpected orientation of these vessels would make it difficult to accurately quantify hemodynamics, since a key assumption in Chapter 2 is that capillaries are planar. There are also new sources of artifacts that need to be taken into consideration when interpreting images (**Figure 4.6**).

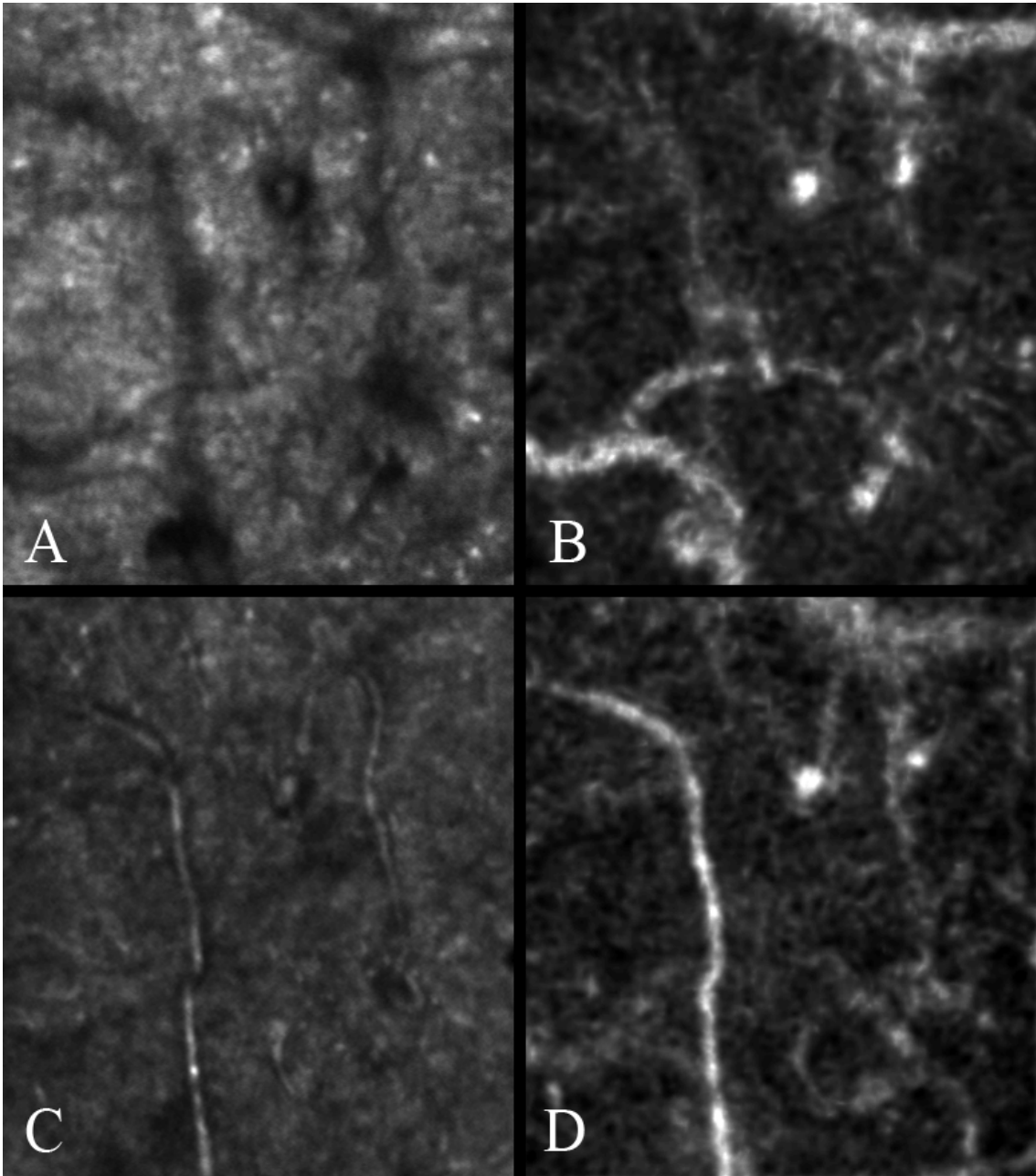


Figure 4.5: Example of vessels in different planes at the same retinal location, in MacTel. Averaged images and motion contrast enhanced images taken at two different planes of focus, (A,B) near the photoreceptors, and (C,D) anterior to the photoreceptors. Out of focus vessels can be seen in both images.

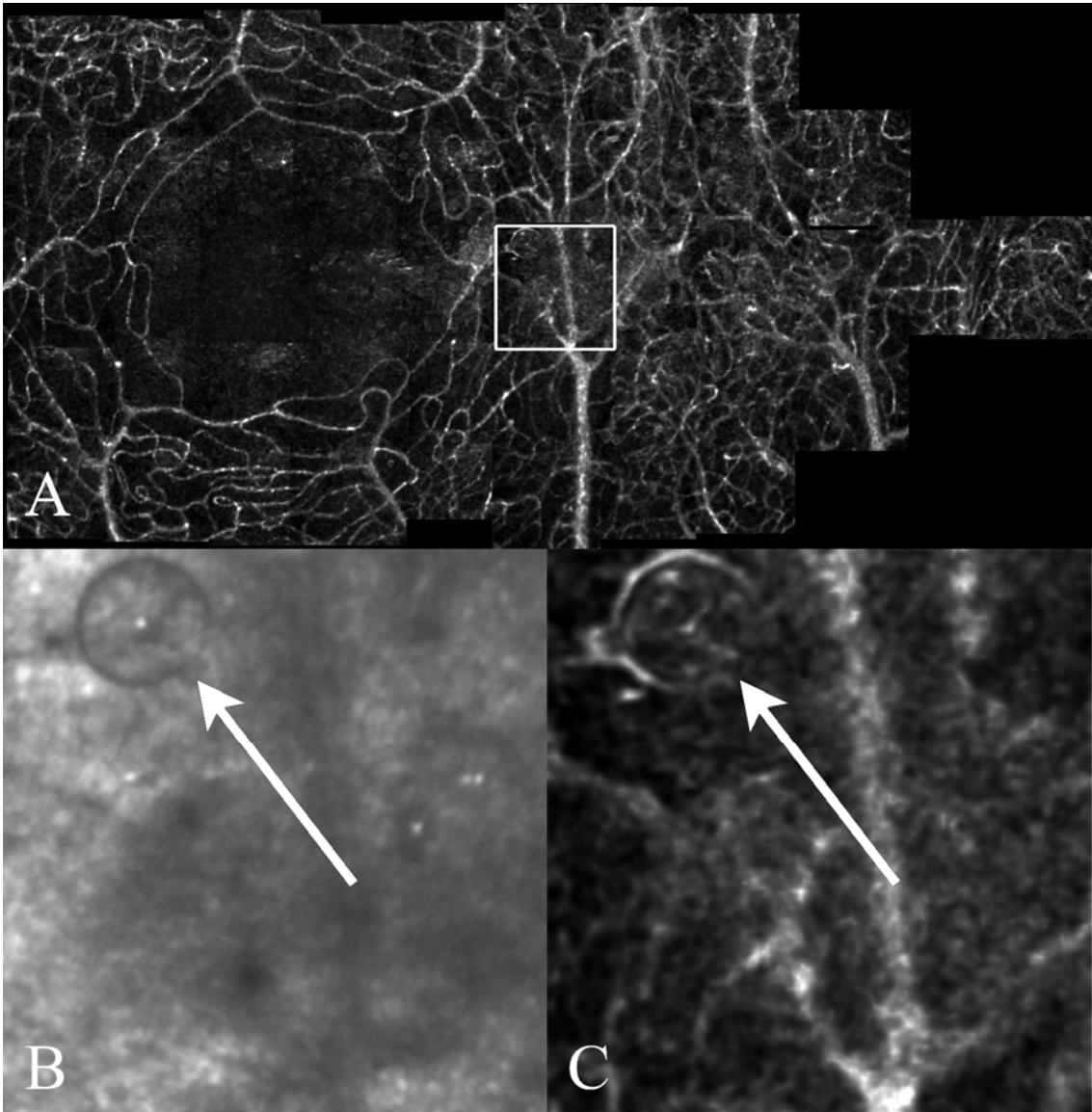


Figure 4.6: Parafoveal capillaries in a patient with MacTel. (A) Montage showing parafoveal capillaries. (B) Close-up of box in (A), showing a circular “bubble” that appears on the image of photoreceptors. (C) The bubble from (B) generates an artifact after motion contrast enhancement.

Case 2: Retinal Vein Occlusion

Retinal vein occlusion (RVO) is an obstruction of the retinal vein. We present images from a 48-year-old male patient. During a routine eye examination by the referring physician, it was discovered that the patient had previously had a RVO in the right eye. Subsequently, a fluorescein angiogram was performed. Two months later, we acquired AOSLO images of the patient and used motion contrast enhancement to generate images of the capillary network. Images of the FAZ are shown, along with what appears to be a large microaneurysm and two vessel abnormalities (**Figure 4.7**).

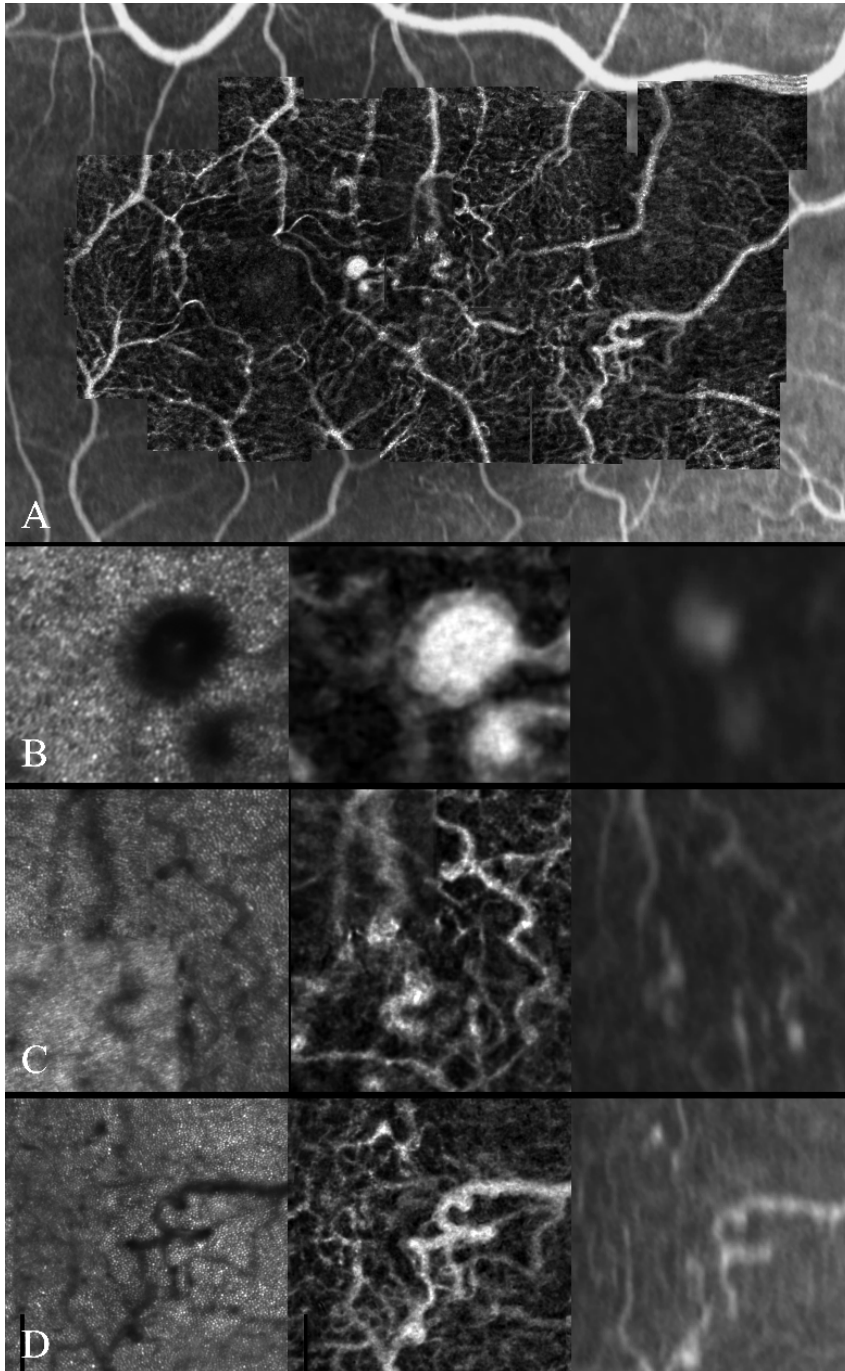


Figure 4.7: Example images from a patient who was previously diagnosed with a retinal vein occlusion. (A) Montage of capillaries overlaid on a FA. (B, C, D) Close up of various regions, showing the photoreceptor image, capillary image, and FA.

Case 3: Age-Related Macular Degeneration

Age-related macular degeneration (AMD) is a disease that causes gradual deterioration of central vision. AMD can occur with or without the new formation of abnormal vessels (wet-AMD and dry-AMD, respectively). In the cross-sectional study in Chapter 3, we excluded one control subject who presented with dry-AMD. Motion-contrast-enhanced AOSLO images from this patient are shown below (**Figure 4.8**). Since there are no new vessels that form in dry-AMD, it is especially relevant to consider motion contrast artifacts that result from the breakdown of the assumption that intensity fluctuations are due only to blood flow. These artifacts need to be carefully considered when using motion contrast enhancement to evaluate any retinal disease. Motion contrast enhancement may be of interest for evaluating wet-AMD.

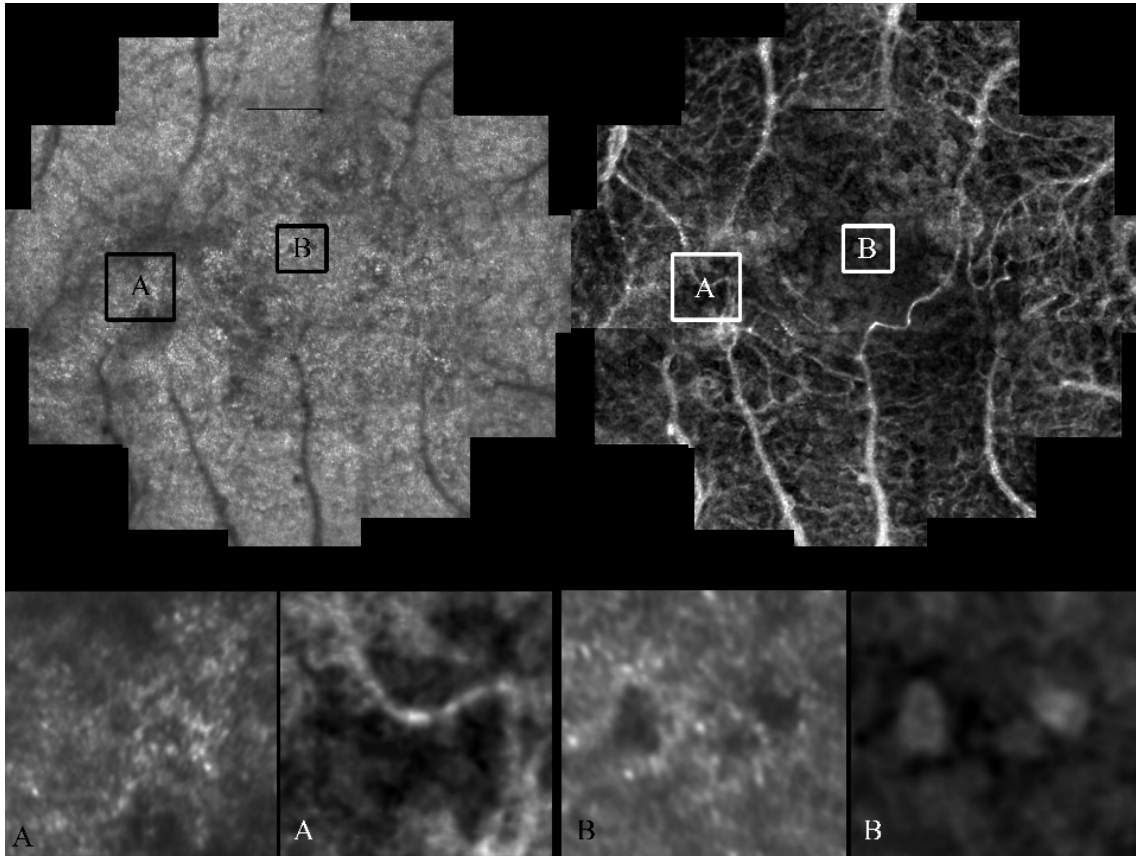


Figure 4.8: AOSLO images of a patient with dry-AMD. (A) An example of a capillary that appears after motion contrast enhancement. (B) Dark areas on the retina in the foveal avascular zone generate non-vascular artifacts that need to be taken into consideration.

Areas for further technical development

The unique features of certain retinal diseases can potentially violate the motion contrast assumption that all intensity fluctuations are due to blood flow. Development of a clinical interpretation of sources of hyper- and hypointensity in motion contrast enhancement would be needed prior to evaluating new diseases. Based on the definition of high relative motion (i.e. the standard deviation of intensity ratios), there are two mechanisms for contrast generation: high intensity fluctuation or low background intensity. It is instructive to consider the case of small vessels and large vessels separately. For small vessels, the object intensity is typically high. This is due to two reasons: first, the capillaries are smaller and therefore more optically transparent, and second, the capillaries are near the plane of focus, and are therefore either bright, transparent, or slightly dark. Hence, the mechanism for contrast generation in capillaries is mostly due to high intensity fluctuation. For larger vessels, the object intensity is typically low, for the opposite reasons: not only is the vessel larger and more optically opaque, but the vessel is typically further away from the plane of focus, which would cause it to appear darker. The nonlinearity of division results in a high value when the denominator approaches zero. It is likely that this effect would be reduced if one were to use subtraction instead of division, since subtraction is a linear operation. In our case, the mechanism for contrast generation in larger vessels is mostly due to low background intensity. The artifacts which appear due to dark objects on the retina typically follow this second principle.

A second area for future development is the ability to differentiate multiple capillary beds. This would expand the analysis of capillaries and hemodynamics beyond the region of interest immediately near the FAZ (further away from this region, there are multiple layers of capillary beds, and it is currently difficult to distinguish whether neighboring capillary segments belong to the same capillary layer). Specifically, it would be useful to develop methods to separate capillary beds in order to separate the superficial and deep capillary beds in the para- and peri-foveal regions of the retina, and to separate the four layers of retinal peripapillary capillaries. These capillaries surround the fovea and the optic disc, respectively, two regions of particular importance in many retinal diseases.

An important first step is to develop a method to distinguish, at the capillary level, whether two vessels are branching or crossing. A simple, but tedious method to accomplish this is to examine the spatiotemporal plots. On the one hand, if two vessels are crossing each other, then there should be no change in the appearance of the cell traces in the spatiotemporal plots at the site of the crossing; on the other hand, if two vessels are connected and branching, then the cell traces would have change in appearance representing the fact that the flow is disrupted by the presence of a branch. We illustrate an example of this strategy below (**Figure 4.9**).

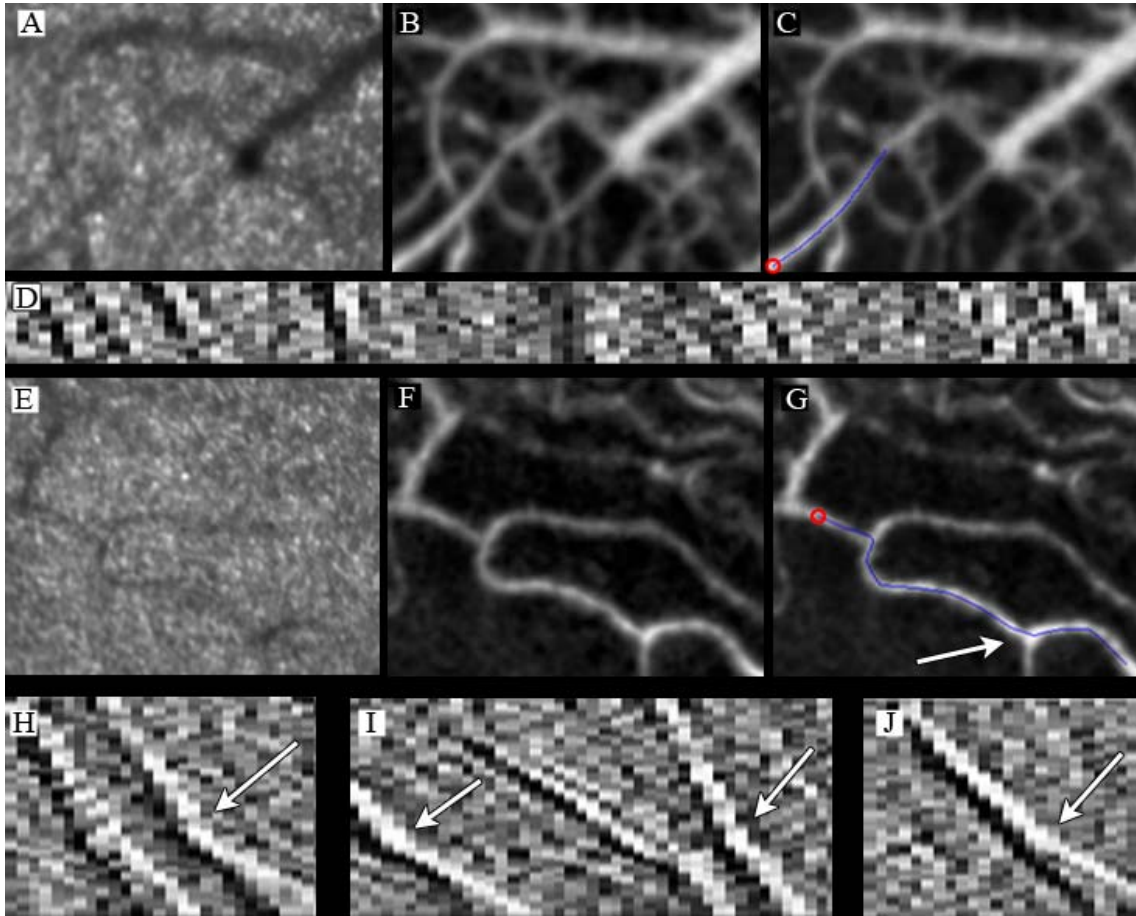


Figure 4.9: Strategy for distinguishing a vessel crossing from a vessel branching. The normal subject that was imaged in **Figure 1.18** is shown. (A) Capillaries feeding into a venule at the edge of the FAZ. This venule is at a plane anterior to the capillaries. (B,C) A clearly distinguishable vessel crossing was identified and extracted (beginning of segment marked with red circle). (D) Portion of spatiotemporal plot corresponding to the capillary in (C). Traces extend the entire length of the spatiotemporal plot without sharp deviations. (E, F, G) Example of capillary branching from the same subject. (H, I, J) Example traces showing sharp deviations (arrows). Downstream of the branch point, the “trace thickening” phenomenon illustrated in **Figure 4.10** can be seen.

Flow disruption at a branch point is often subtle, but may be useful for studying erythrocyte dynamics. As a special case, two consecutive leukocytes were identified flowing through a capillary in a single-file manner (**Figure 4.10**). At first glance, it appears that the trace has thickened (“trace thickening”). In this case, the thickening is due to the presence of a branch point midway through the capillary segment. The speed of the leukocyte is 2.23 mm/s before the branch point, and 1.62 mm/s after the branch point. If the diameter of the capillaries are the same, then by flow conservation, this suggests that the velocity of the erythrocytes in the branch point is 0.61 mm/s. One might be able to use this concept of trace thickening to study erythrocyte trains in the absence of a branch point, as described in the microhemodynamics section below.

Potential methods for differentiation of capillary beds include the use of defocus cues or the incorporation of multi-modal information. To use defocus cues, one can take advantage of the fact that the intensity of a vessel centerline is brightest when the plane of focus is set at the level of the capillary, and darker above and below the capillary. Hence, capillary beds can be optically separated by generating “fly-through” videos of varying defocus. By carefully controlling the defocus parameter (e.g. by simultaneously recording the defocus parameter during video acquisition), one can begin to determine the relative z-locations of neighboring capillary segments. Incorporation of optical coherence tomography (OCT) might also be useful for differentiation multiple capillary beds, and for introduction of a speed correction for sloping vessels (since we assume that the capillary bed is planar to perform the speed quantification in Chapter 2).

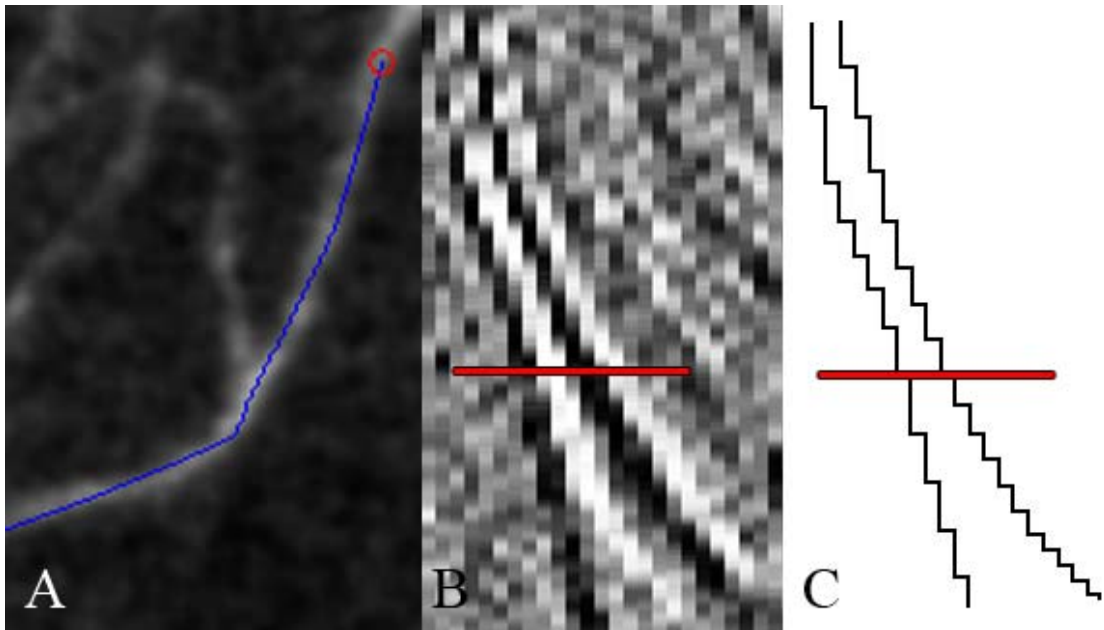


Figure 4.10: Special case of two leukocyte flowing by a branch point. (A) A capillary segment is extracted (start of segment marked by red circle). (B) Two leukocyte traces are disrupted at the site of the branch point (marked by red line). (C) The extracted leukocyte traces show that the speed of the second leukocyte has decreased from 2.23 mm/s to 1.62 mm/s. Since flow is necessarily single-file, this decrease in speed can be attributed to the branch point.

The imaging of patients also poses unique challenges, since a small but significant level of cooperation is needed from each patient for successful imaging. The series of cases presented in this section, along with the images in Chapter 3, demonstrate that the AOSLO technology is at a mature enough stage to enable clinical imaging. However, future advances in imaging technology can help to ensure that AOSLO imaging is successful in a larger pool of patients.

Conclusions

Motion contrast imaging can give new insights into many other retinal diseases. Unique aspects of retinal diseases, such as drusen, may give rise to imaging artifacts, which need to be interpreted in light of the motion contrast enhancement method. These methods may also be useful for studying diseases that affect specific blood cells, such as sickle cell anemia, which would likely result in the formation of large plasma gaps due to inefficient erythrocyte deformation, and leukemia, which would result in altered leukocyte flow. In addition, development of new techniques for imaging different capillary beds would enable delineation of capillary paths outside of the parafoveal region, and allow for a more comprehensive picture of microhemodynamics.

4.2.3 Microhemodynamics

Quantitative models based on solid and fluid mechanics are useful for characterizing diseases affecting the vasculature. Although there are many such models that have been developed in the past few decades, one notable example is the discovery that there is a relationship between wall shear stress and atherosclerotic plaques (Ku, Giddens et al. 1985). This has led to the use of noninvasive imaging methods to assess hemodynamics in patients with specific conditions, such as the use of magnetic resonance angiography to assess the relationship between wall shear stress and intracranial aneurysm growth (Jou, Wong et al. 2005). Ultimately, quantitative models of hemodynamics could be useful for generating noninvasive, imaging-based biomarkers for disease. As there are many retinal diseases affecting the microvasculature, it would be useful to develop a quantitative model for retinal microhemodynamics. However, there are many complications that need to be addressed, which arise due to heterogeneities in cell distribution, cell-cell and cell-vessel interactions. These complications challenge common modeling assumptions such as fluid homogeneity and the constancy of fluid material properties.

In the retinal capillaries, a relationship between shear stress and pathology may exist. A recent *in vitro* study found that laminar shear stress affected the expression of endothelial nitric oxide synthase, endothelin-1, and thrombomodulin in cultured human retinal microvascular endothelial cells (Ishibazawa, Nagaoka et al. 2011). *In vivo* assessment of shear stress may give new insights into the natural progression of disease at the capillary level. Shear stress could potentially be assessed using noninvasive

optical imaging combined with an engineering model for microhemodynamics. This model could test the hypothesis that there is a relationship between shear stress and capillary defects, such as microaneurysms or intraretinal microvascular abnormalities.

In this section, we discuss the considerations needed to formulate an engineering-based model, and then propose a new approach to model the single-file flow of leukocytes through retinal capillaries. With further work, such a model could potentially be used to characterize the flow seen in AOSLO videos.

Background

There are many features of the microcirculation which affect hemodynamics. To begin, hemodynamics in the microcirculation can be complicated by factors such as irregularities in vessel cross sections, retardation of the plasma layer, asymmetry of erythrocytes, and leukocyte plugging (Pries, Secomb et al. 1990). We will focus on the leukocytes, which play an important role in the flow dynamics through capillary systems. The equivalent resistance of a non-activated leukocyte through a capillary has been estimated to be that of 750 erythrocytes (Sutton and Schmid-Schonbein 1992). The behavior of leukocytes in the microcirculation is also dependent on the organ system; for example, dramatic leukocyte sequestration occurs in the pulmonary capillaries (Kuebler, Kuhnle et al. 1994; Hogg and Doerschuk 1995). There are also many different types of leukocytes, including lymphocytes, which have a diameter of about 5.75 μm , and neutrophils, monocytes, and eosinophils, which have diameters of about 7.25 μm (Schmid-Schonbein, Skalak et al. 1980). Hemodynamics also depend on the size scale of the microcirculation, which can range from cell-free flow in capillaries that are

extremely small ($\sim 3 \mu\text{m}$), to single-file flow in small capillaries ($\sim 5\text{-}6 \mu\text{m}$), to multi-file flow in larger capillaries and small arterioles and venules ($\sim 15 \mu\text{m}$). To further complicate things, leukocytes can spontaneously activate, resulting in changes in mechanical properties (Schmid-Schonbein, Sung et al. 1981). Finally, leukocyte distribution through capillaries is not homogeneous, with respect to both space (Schmid-Schonbein, Skalak et al. 1980) and time (Kleinfeld, Mitra et al. 1998). To summarize, the mechanics of leukocyte flow through capillaries set up a unique and interesting regime for analysis. In this section, we will examine the problem of leukocyte deformation in single-file flow through retinal capillaries, and suggest novel application of the AOSLO to develop a quantitative engineering model.

To the best of the author's knowledge, modeling of single-file flow of leukocytes through small capillaries using in vivo leukocyte data has not been done before. This is probably due to the difficulty in measuring leukocyte deformation and transit in vivo (Zhou, Yue et al. 2007). However, there are many related problems that have been studied in the microcirculation, including mechanics of the vessel wall, cell cytoplasm, cell membrane, and plasma. Clearly, a complete model that takes into consideration all of the nonlinearities presented by these problems will be extremely difficult. Zhou, et. al., assumed a rigid vessel wall to model neutrophil entrance and transit in single-file flow (Zhou, Yue et al. 2007). Using Newtonian and viscoelastic drop models for a neutrophil cytoplasm, they found that the entrance time of neutrophils from a reservoir into a fixed, small capillary is dependent on both the size and geometry of the capillary and the viscosity and viscoelasticity of the cytoplasm. In particular, entrance times increased with cell viscosity according to a power law with coefficient

1/7, and viscoelasticity in the cytoplasm helped to facilitate cell deformation and shorten entrance times. An obvious shortcoming of this model is the simplification of the cytoplasm to a viscoelastic or Newtonian drop; in fact, leukocyte nuclei are probably a major contributor to leukocyte mechanical properties (Schmid-Schonbein, Sung et al. 1981). To address this concern, a number of two-layered models of leukocytes including the drop-rigid-particle model and the compound-drop model have been proposed (Jin, Verdier et al. 2007). The area of cellular fluid mechanics is rich and complicated, and reader is referred to a review (Kamm 2002).

One shortcoming of the model is that friction between the leukocyte and vessel wall is ignored. For example, it is known that the endothelium possesses a glycocalyx consisting of proteoglycans, glycoproteins, glycosaminoglycans, and adherent plasma proteins (Damiano and Stace 2005). The glycocalyx is transiently stripped down when a leukocyte traverses a capillary, subsequently recovering within a few seconds (Popel and Johnson 2005). To investigate this phenomenon, a model of the flow and deformation of the glycocalyx on the vessel wall in the wake of a leukocyte was developed to estimate bulk material properties of the glycocalyx (Damiano and Stace 2005). In this model of single-file flow, they assumed that leukocytes press on the glycocalyx, resulting in a transient wake. Erythrocytes, which are smaller and more easily deformed, were ignored. For a 5 μm diameter capillary with a leukocyte traveling at 50 $\mu\text{m/s}$, they found a glycocalyx recovery time on the order of 1 s, with a recovery length of $\sim 50 \mu\text{m}$. This interaction would be important in modeling leukocyte rolling, a well-known phenomenon observed in post-capillary venules (caused by transient

leukocyte adhesion to the vessel wall). The glycocalyx is usually neglected in most models.

It is instructive to consider the Reynolds (Re) and Womersley (α) numbers. For a capillary of diameter $6 \mu\text{m}$, with speed 1 mm/s , viscosity 2 cP , density 1 g/cm^3 , and heart rate 1 Hz , the Reynolds number is $\sim .003$ and the Womersley number is $\sim .002$. Based on these parameters, common assumptions are to assume that viscous forces dominate ($Re \ll 1$), and that transient, convective acceleration is negligible ($\alpha \ll 1$). By further assuming Newtonian fluid properties, Stokes flow has been previously used as a preliminary model for microcirculatory blood flow (Fung 1997; Schmid-Schonbein 1999). Using this model, the fluid shear stress distribution on the leukocyte membrane in the microcirculation was found to be inhomogeneous with sharp increases at locations of membrane attachments to the vessel wall (Sugihara-Seki and Schmid-Schonbein 2003). Thus, there may be high temporal stress gradients on the leukocyte membrane. It should be noted that they used a capillary of diameter $10 \mu\text{m}$, which is not single-file flow. An earlier model investigated the leukocyte adhesion to the endothelium by deriving an equilibrium between hydrodynamic and adhesive forces (Dong, Cao et al. 1999). The model was based on an elastic ring adhered to a surface under fluid shear stresses - again, a model of flow through larger capillaries. Leukocytes were modeled with a leading edge, at which new adherent bonds were formed, and a trailing edge, at which the leukocyte membrane peeled away from the endothelium; the extent of the peeling zone was found to be less than 5% of the total contact interface.

Thus far, the discussion has been regarding only leukocytes. In fact, most of the work in microvascular hemodynamics ignores leukocytes in favor of erythrocytes,

which we have shown should not be the case at the level of single-file flow. For completeness, we present a brief survey of a few relevant concepts. Perhaps the most famous of these is the Fahraeus effect, which states that tube hematocrit decreases in flow through small bore tubes, resulting in a lower than expected value for tube viscosity (Lipowsky 2005). As a side note, a further differentiation between erythrocytes and leukocytes (Lichtman, Gregory et al. 1973) introduces the question of whether these concepts apply to leukocytes as well - particularly in disease states such as leukemia. As a result of the Fahraeus effect, there has been much work in the area of viscosity and effective viscosity estimation in vessels, due to this effect of variations in blood constituents, and hence viscosities, at different vessel diameters. One important consequence of this effect is phase separation (Lee and Smith 2008), where uneven erythrocyte distributions at branch points result in non-uniform viscosity distributions in vessels, which is observed in the microcirculation. Another consequence is the shear-thinning property of blood, which is observed experimentally when erythrocyte-erythrocyte interactions are inhibited. When in their natural setting in vivo, erythrocytes can form spontaneous trains and clusters, the behavior of which is not well understood. Single erythrocytes also spontaneously deform into characteristic shapes that have been colorfully described as bullets, slippers, parachutes, and tanks. There is a model for some of these deformations based on a boundary-integral method for axisymmetric Stokes flow (Pozrikidis 2005).

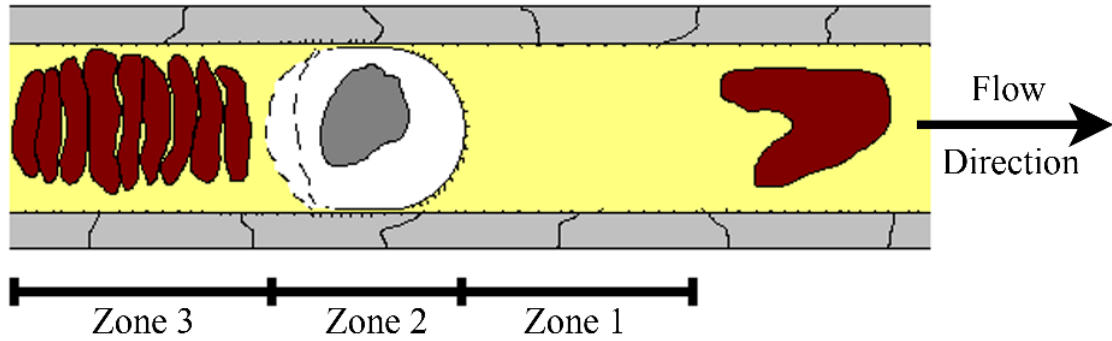


Figure 4.11: Illustrated schematic showing author’s interpretation of problem, showing erythrocytes (red), a single leukocyte (white and gray), membrane folds in the leukocyte (protrusions on leukocyte), plasma (yellow), endothelial cells (gray), and glycocalyx (protrusions on endothelial cells). Due to differences in cells speeds, we propose that there is an erythrocyte-free area (Zone 1) in front of the leukocyte, glycocalyx compression at the leukocyte (Zone 2), and an erythrocyte train behind the leukocyte (Zone 3). Note that the leukocyte geometry is unknown. We assume a spherical endcap on the leading edge and an unstable endcap on the trailing edge in the spirit of bubble mechanics. The erythrocyte in front of Zone 1 is shown in a classic parachute formation.

Proposed Model

To simplify the problem, we make a few remarks based on the idealized situation presented in **Figure 4.11**:

1. Existence of an erythrocyte-free zone (Zone 1). It is well established that leukocytes travel slower than erythrocytes through small capillaries. We hypothesize that there is a significant erythrocyte-free zone in front of the leukocyte. If we ignore effects due to platelets and plasma proteins, then we can model plasma as a Newtonian fluid. Moreover, we can take the viscosity of plasma as constant (and don't need to worry about hematocrit distributions, in particular). With these considerations, the Navier-Stokes equations can be written as:

$$\begin{aligned}\frac{\partial u}{\partial t} + u \frac{\partial u}{\partial x} + v \frac{\partial u}{\partial y} + w \frac{\partial u}{\partial z} &= X - \frac{1}{\rho} \frac{\partial p}{\partial x} + \frac{\mu}{\rho} \nabla^2 u \\ \frac{\partial v}{\partial t} + u \frac{\partial v}{\partial x} + v \frac{\partial v}{\partial y} + w \frac{\partial v}{\partial z} &= Y - \frac{1}{\rho} \frac{\partial p}{\partial y} + \frac{\mu}{\rho} \nabla^2 v \\ \frac{\partial w}{\partial t} + u \frac{\partial w}{\partial x} + v \frac{\partial w}{\partial y} + w \frac{\partial w}{\partial z} &= Z - \frac{1}{\rho} \frac{\partial p}{\partial z} + \frac{\mu}{\rho} \nabla^2 w \\ \frac{\partial u}{\partial x} + \frac{\partial v}{\partial y} + \frac{\partial w}{\partial z} &= 0\end{aligned}\tag{1}$$

where u , v , and w denote the Cartesian components of velocity, ρ denotes density, μ viscosity, and X , Y , and Z the body forces acting on the object. Since $Re \ll 1$ (viscous forces dominate) and $\alpha \ll 1$ (transient forces and convective

acceleration are negligible), we can simplify the equations for Zone 1, and write the governing equations in the form of Stokes flow:

$$\begin{aligned} \mu \nabla^2 u &= \frac{\partial p}{\partial x}, & \mu \nabla^2 v &= \frac{\partial p}{\partial y}, & \mu \nabla^2 w &= \frac{\partial p}{\partial z} \\ \frac{\partial u}{\partial x} + \frac{\partial v}{\partial y} + \frac{\partial w}{\partial z} &= 0 \end{aligned} \tag{2}$$

Because the membrane of a leukocyte is wrinkled due to an abundance of folding, we can model the leading edge as a rough endcap on the leading edge. If we use a spherical endcap, then we suggest a modification of Stokes solution for a falling sphere (by adding friction and/or a gravity-like term to account for the force of the erythrocyte train, plus additional boundary conditions), or some sort of bolus flow (Prothero and Burton 1961; Fitz-Gerald 1972).

2. Negligible normal flow component. Normally, there is flow in the direction normal to the vessel centerline due to capillary permeability. However, in the inner retinal vasculature, a blood-retinal-barrier is established by tight junctions. Therefore, we ignore flow in the normal direction.
3. Glycocalyx compression in Zone 2, followed by restoration in Zone 3. In Zone 2, lubrication theory would be most valuable, in a similar manner that has been developed for erythrocytes through very narrow capillaries (Secomb, Skalak et al. 1986). However, the exact location of the transition from Zone 1 to Zone 2 will depend on the distance between the leukocyte and the endothelial cell wall – near the spherical endcap, the distance will quickly become too large for the regime of lubrication theory.

4. Zone 3 is the most complicated, and it may be most worthwhile to define bulk fluid properties using an apparent viscosity. In particular, viscosity may be modeled as a Newtonian part plus a non-Newtonian part, as described previously (Sirs 1991). It may also be worthwhile to consider combining the erythrocyte train with the trailing edge of the leukocyte in order to derive a bulk flow condition, for use as a boundary condition for Zone 2. A more complex simulation will be needed to identify the characteristics of the flow in this zone.
5. Appropriate boundary conditions need to be defined for each of the interfaces. At the interface between the leukocyte and the fluid, a solid mechanics model for the leukocyte may need to be matched with the fluid mechanics model. Possible approaches that have been previously adopted were described in the background section, which include the leukocyte drop models; further modeling may consider the fact that there are multiple types of leukocytes, with varying sizes and configurations of the nucleus body. Since the nucleus tends to be the stiffest portion of the cell, it would be important to incorporate this into the model. A second interface occurs between the vessel wall and the fluid. Although irregular cross sections likely exist, due to bulges of the endothelial cells at the locations of the nuclei, currently most models do not take this into consideration. A more significant irregularity could be due to a pathological condition, such as the presence of a microaneurysm or the development of some other capillary defect.

Further work is needed to develop solutions to the proposed model.

In vivo data acquisition

Ultimately, it would be meaningful to pair any proposed model with in vivo data. Using an AOSLO, we can noninvasively acquire videos in the parafoveal region of the retina on human subjects and visualize individual leukocytes traveling through small capillaries. We provide an example of an isolated retinal capillary that could be used for quantitative measurements.

As a proof of concept, an example of a capillary segment that could be used for investigating microhemodynamics is shown in **Figures 4.12 and 4.13**. We identified a straight segment away from branching and approximately free of axial curvature at the top of the capillary segment shown in **Figure 4.12**. At this location, the capillary network forms a single, planar layer, providing a good location for analysis. Briefly, we applied image processing algorithms to enhance the vessel contrast using dynamic analysis from multiple frames in the video. The idea is to use in vivo measurements to better account for the complexities due to the cell environment and cell-cell interactions (Zharov, Galanzha et al. 2006). These considerations, in particular, are typically ignored in current models of leukocyte flow through capillaries.

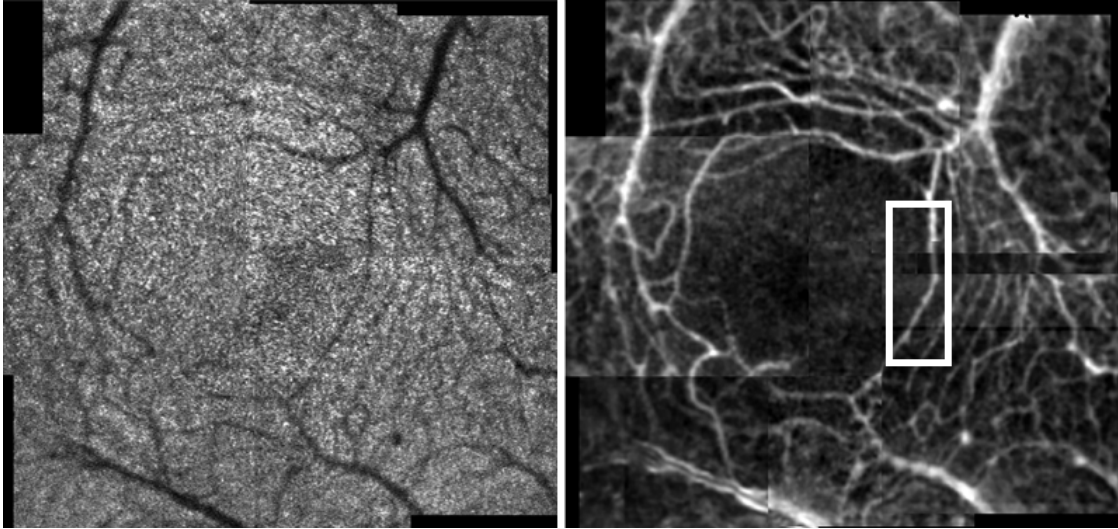


Figure 4.12: Selection of a capillary for microhemodynamics modeling. A montage of the parafoveal capillary network generated from unprocessed AOSLO images (left) is converted into a montage that shows the capillary network (right) using image processing algorithms. A straight capillary segment free of branching is selected near the FAZ (shown again in **Figure 4.13**).

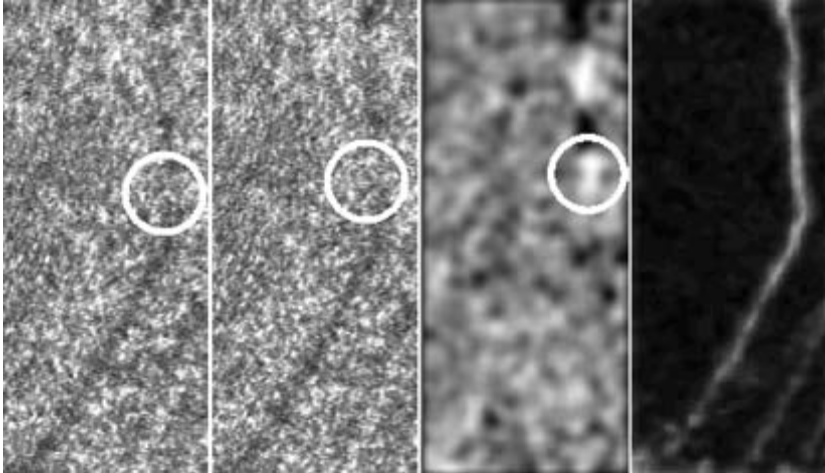


Figure 4.13: Example of capillary segment for microhemodynamics modeling. Two consecutive frames of a parafoveal capillary showing leukocytes moving through the capillary (left), one frame showing highlighted leukocyte (middle right), and a view of the capillary network (right), generated using image analysis algorithms. This region is marked with a white rectangle in **Figure 4.12**.

When analyzing the in vivo data, measurement of vessel diameter is important for development of a flow model. However, as shown in **Figure 1.8**, the apparent diameter of the vessel changes as a function of defocus. One method to standardize measurement of vessel diameter would be to set the plane of focus to the level of the vessel, in order to measure the diameter of the blood column. In any given video, it is unclear how far from the plane of defocus any given vessel is. Thus, by focusing at the level of the vessel, diameter measurements can be standardized.

Other potential metrics that would be useful to quantify for the microhemodynamics model include: plasma gap and leukocyte lengths, deformability index (length / width), and acceleration. Measurement of variations in speed are important for deriving measures of wall shear.

Conclusions

Clearly, there are many areas that need further investigation. Future work includes development of better theoretical models, coupled with in vivo data on leukocyte morphometry and deformation, and determination of shear or pressure distributions based on the model presented. Ultimately, calculation of the wall shear stress could be useful for investigation of retinal disease.

4.2.4 Computer Vision

Although we have developed a set of algorithms for motion contrast enhancement, there are still many areas for future work, particularly in the areas of automation and optimization. We demonstrate a potential method for the automated extraction of cell traces on ST plots, and then describe additional areas for further optimization or automation.

Extraction of Cell Traces on Spatiotemporal Plots

We describe a method to extract high-contrast leukocyte traces from ST plots. First, we enhance the cell paths on the ST plot by suppressing the background. We assume that (i) cell paths are one dimensional and monotonic, (ii) cell paths do not cross each other, and (iii) cell paths are sparse. These assumptions are valid for the smaller retinal capillaries under consideration. The steps are: (i) background suppression, (ii) thresholding, (iii) morphological opening, and (iv) least squares fitting.

Background Supression

We use an approach based on Frangi “vesselness” (Frangi, Niessen et al. 1998), which detects tubular structures. Motion contrast enhanced cell paths satisfy “vesselness” due to their appearance (white lines with black borders). Locally, the elements of the Hessian matrix are given by

$$H_{ij} = \frac{\partial^2 L}{\partial x_i \partial x_j} \quad (3)$$

where L is a local image region. The eigenvalues of H , λ_1 and λ_2 , are ordered such that $|\lambda_1| \leq |\lambda_2|$. Regions of “vesselness” are identified where $|\lambda_1| \approx 0$ and $|\lambda_1| \ll |\lambda_2|$.

Thresholding

Three-step thresholding is used to segment the cell paths, an extension of a previously proposed two-step thresholding method (Sato, Chen et al. 1995). The goal of the thresholding step is to identify the brightest cell paths (i.e. the cells that are most visible on the raw video). Selection of the threshold parameter presents a tradeoff. On the one hand, a high threshold value will exclude undesired image regions, but may also exclude portions of desired image regions (clipping), resulting in false negatives. On the other hand, a low threshold value will include desired image regions, but may also include undesired image regions, resulting in false positives. Multi-step thresholding addresses this tradeoff. High, medium, and low threshold values are applied to the ST plot image, and stored as ST_h , ST_m , and ST_l , respectively. ST_l contains both desired and undesired image regions that are not present in ST_h . The idea is to include the desired image regions of ST_l and exclude the undesired regions of ST_l , using both ST_m and ST_h . First, ST_m is compared against ST_h . Image points $(x,y) \in ST_m$ are kept if they are connected to an identified region of ST_h , and deleted if they are not connected to any identified regions of ST_h . The result is compared against ST_l , and the procedure is repeated. Thus, three-step thresholding minimizes the number of false positives while reducing clipping of desired image regions.

Morphological Opening

Morphological opening is performed to connect pieces of the cell paths together. This step is important for low SNR ST plots, since cell paths are not well connected. A line structural element oriented vertically is used, because the orientations of cell paths are approximately vertical in pixel space when viewed locally (note that cell paths do not appear to be vertical due to rescaling for display purposes; the aspect ratio for display purposes is 1:20).

Least Squares Fitting

Least-squares polynomial fits are used for extraction of segmented cell paths. Prior to extraction, the following conditions must be met: first, the length of the cell path must be sufficiently long; second, the slope of the cell path must be sufficiently different from horizontal. We also require that the fit results be monotonic.

Results

We tested the algorithms on retinal videos, which were collected on separate days from two subjects with no systemic or ocular disease, using an AOSLO. For the first data set, 40-second videos were acquired at 30 Hz using a 532 nm wavelength laser; for the alternate data set, 40 second videos were acquired at 60 Hz using an 840 nm wavelength laser. Videos were preprocessed offline. The steps in preprocessing were (i) correction for frame distortions (Vogel 2006), (ii) registration of frames to a single reference frame (Vogel 2006), (iii) cropping registered videos to eliminate inconsistent boundaries, and (iv) a median filter to reduce the effects of noise. We used the first dataset to calibrate

the analysis parameters, and repeated the analysis on the alternate dataset using the same parameters. Results of the proposed algorithms using the first data set are shown in **Figure 4.14**.

For the multi-frame division videos, instabilities in division were handled by trimming responses to lie within the bit depth of the images: $[0, 255]$. An example of division instability can be seen as black and white horizontal lines on the ST plots, which were due to the subject blinking during the imaging session, resulting in frames with near-zero intensity.

We performed manual cell path extraction for comparison with the automatic method. Manual extraction was performed using a graphical user interface, asking the user to select points along each cell path. The extracted cell paths were assumed to be ground truth. For the first dataset, the automatic approach correctly identified 42 out of 50 cell paths (**Figures 4.14, 4.15**). The false negatives were all cell paths that were not distinct enough, possibly due to (i) proximity to a neighboring cell path, violating the assumption of sparseness, or (ii) lack of connectivity among segmented image regions. For the alternate dataset, the automatic approach correctly identified 26 out of 29 cell paths, and incorrectly identified 1 cell path. The incorrectly identified cell path was due to a cell path that was too close to an imaging artifact. The alternate dataset had more noise compared to the first dataset, and also more imaging artifacts (**Figure 4.16**). Overall, the automatic method correctly identified 86% of all the cell paths in low SNR datasets cluttered with imaging artifacts.

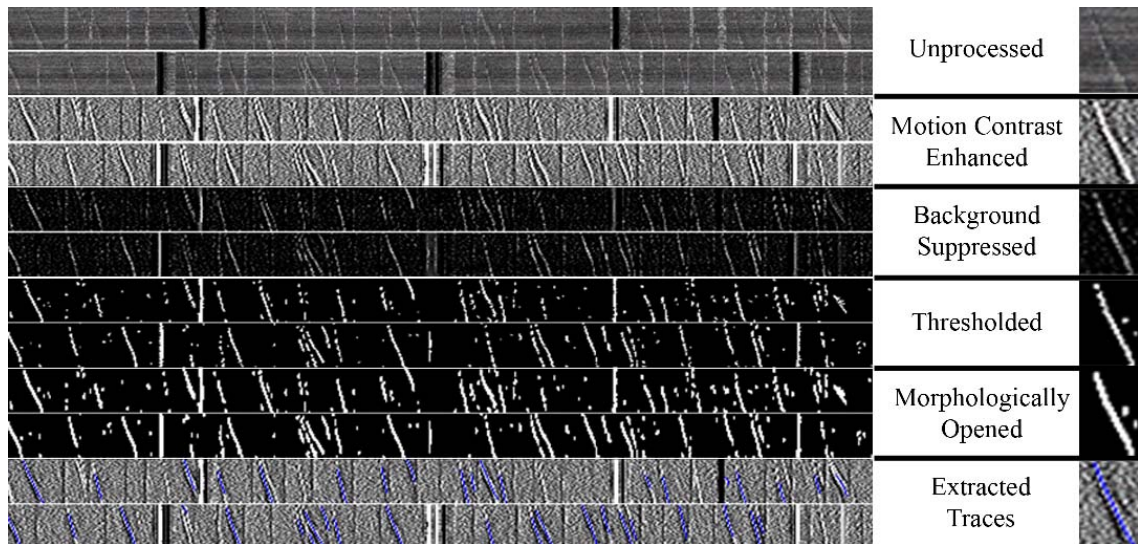


Figure 4.14: ST plots are shown after each of the intermediate steps proposed for automated cell path extraction. Each pair of two rows is one continuous ST plot, split into two rows for display purposes. To the right of the labels is a close up of the first trace from the first row of the ST plots. The effect of each step of processing is as follows: increase the contrast of the trace; suppress the background; eliminate the background; connect the traces together; extract the objects that satisfy the extraction criterion.

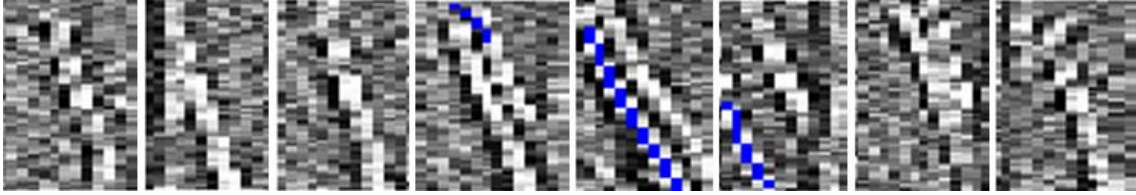


Figure 4.15. Errors of automated extraction. For each of these errors, either the assumption of sparseness or of connectedness was violated.

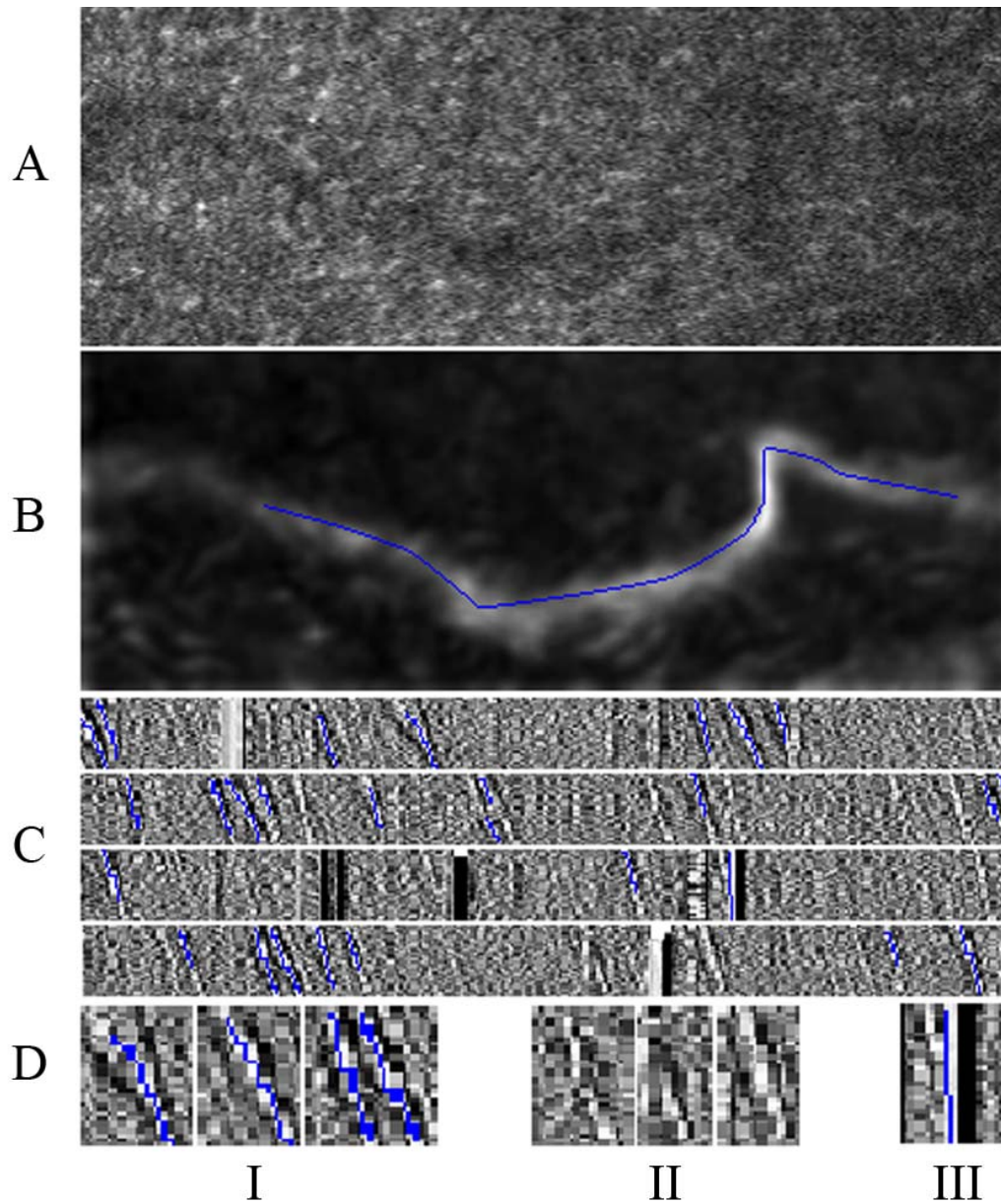


Figure 4.16: Automated extraction results on the alternate data set. (A,B) Capillary segment before and after motion contrast enhancement, with extracted vessel centerline shown in blue. (C) ST plot split into 4 rows for display purposes. (D) Close-ups. I, three correctly extracted cell paths (aspect ratio set to 1:20), II, three false negatives due to lack of connectedness, and III, one false positive due to a blink.

Areas for further technical development

Improvements in the motion contrast enhancement processing software can lead to both improved results as well as faster processing times. The key areas are described chronologically, starting with preprocessing, and followed by motion contrast enhancement and analysis of videos.

Weaving and Drift

To image at 60 Hz, the forward and backward sweeps of the raster scan are recorded on one continuous line, with a configuration such as 256 lines acquired in the vertical direction, while 1128 pixels are acquired in the horizontal direction. To reconstruct a 60 Hz video that has the same pixel sampling in the horizontal and vertical directions, raw videos are “woven” by interleaving lines from the forward and backward sweeps of the raster scan (**Figure 4.17**). In order to achieve this, the pixels from the backward sweep need to be reversed in order, and then registered to the neighboring lines. Currently, this is achieved by manually displacing lines until a “properly-woven” image is generated. Due to hardware drift, the amount of displacement varies across the imaging session, typically on the order of 3-4 pixels per hour. However, this also depends on how long the scanning components have been turned on prior to the start of the imaging session. Thus, the amount of displacement is determined for each video in the imaging session. Automation of the weaving procedure along with a method to account for the drift can streamline the process of generating 60 Hz videos.

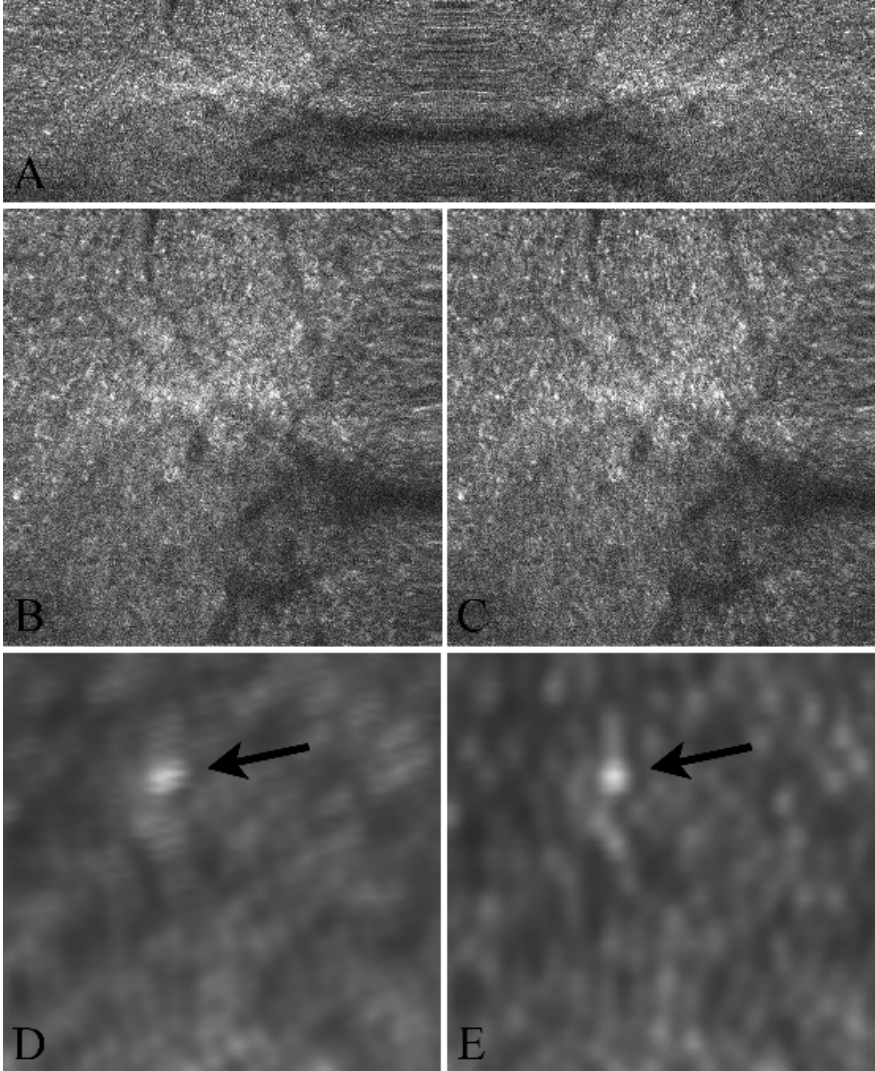


Figure 4.17: Demonstration of proper weaving used to generate 60 Hz videos. (A) Unprocessed AOSLO video acquired at 60 Hz using 256 vertical lines and 1128 horizontal pixels. (B) Improperly woven video frame. (C) Properly woven video frame. (D,E) Averaged image of photoreceptors generated from (D) improperly and (E) properly woven videos. Consider the sheared appearance of the photoreceptor marked by the arrow, as well as a general distortion over the entire image. Subtle differences between (B) and (C) lead to larger differences in the averaged images of photoreceptors.

One possible method to improve the process of weaving and drift correction is to implement a cross-correlation scheme to register lines from the forward and backward sweep to each other. Since the amount of displacement is relatively stable, it would only need to be calculated every 5-10 minutes during imaging to maintain proper weaving, for the current AOSLO system. As a further refinement, one could also allow for sub-pixel displacements, using an interpolation scheme that maps the sub-pixel displaced lines back into the pixel space.

Cropping the video

During preprocessing, due to eye motion, the borders of stabilized videos is variable. A simple method to crop the video is to calculate the standard deviation image of the stabilized video (**Figure 4.18**).

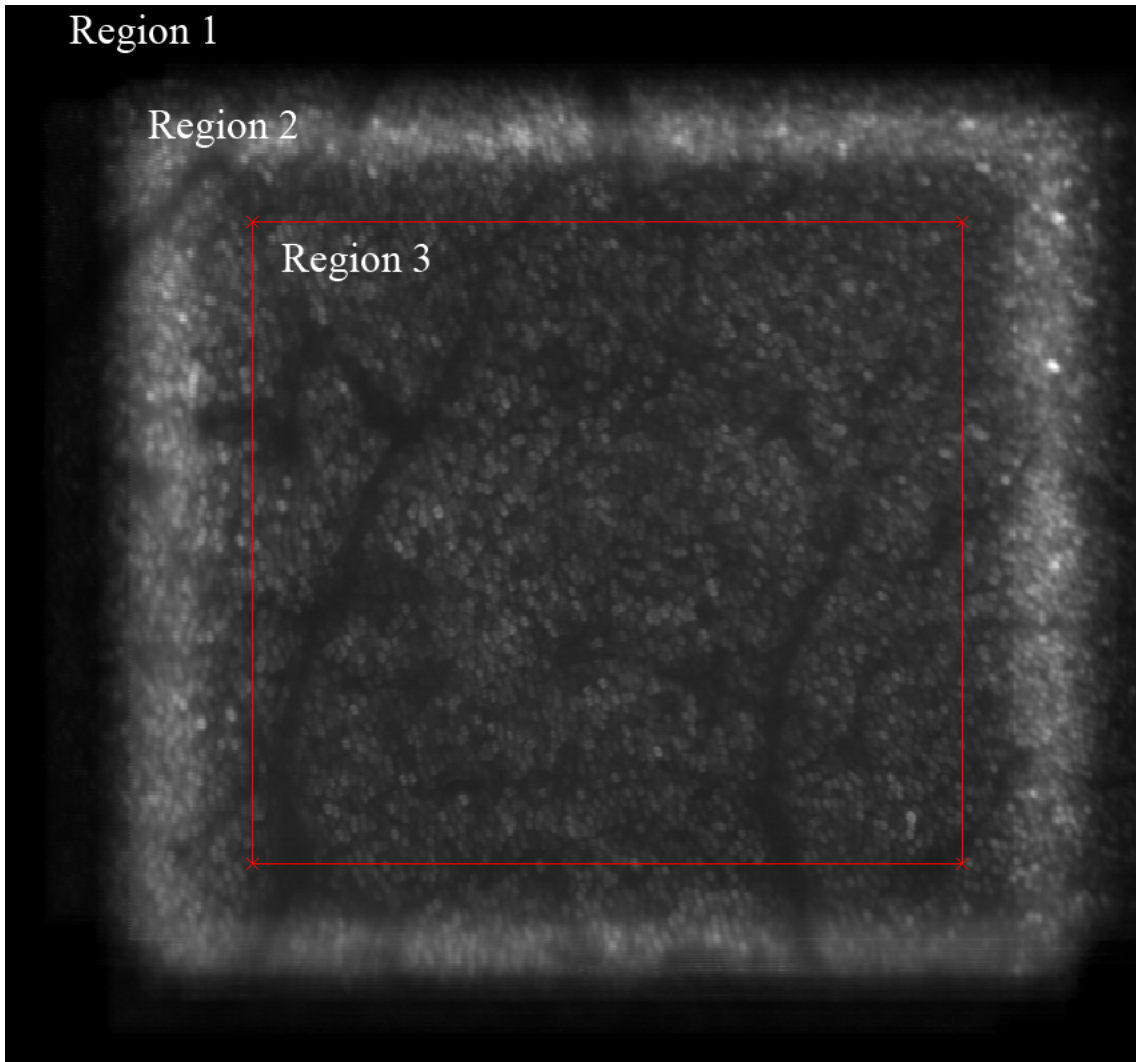


Figure 4.18: Video cropping strategy. A simple method to remove the variable black border from the stabilized video is to calculate the standard deviation of the stabilized video. The resulting image shows three distinct regions. Region 1 is an area where no portion of the video was present; region 2 marks the area where the video was sometimes present, and sometimes absent; and region 3 marks the area where the video was present in the majority of frames. A red rectangle marks the area that was selected for cropping.

Although it is simple to crop videos for motion contrast processing, future versions of motion contrast enhancement may consider eliminating the need for cropping. For each pixel, the frame numbers corresponding to non-black pixels can be determined, and division and standard deviation calculations can be performed on the subset of non-black pixels. As an example, in **Figure 4.18**, since there are only black pixels in region1, no motion contrast enhanced image would be generated. In region 2, using a subset of frames, a motion contrast image with reduced SNR could be generated. Finally, in region 3, the conventional motion contrast image can be generated. The main problem that needs to be addressed is a strategy for efficient indexing of data, since there are 512x512 pixels in each of 1200 frames that need to be organized. The key advantage would be more efficient retinal coverage of the AOSLO videos (i.e. fewer videos would be needed to acquire capillary images of the same region on the retina).

Deletion of Poorly-Stabilized Frames

Although there will be continual improvements in the accuracy and robustness of stabilization algorithms to correct for intra-frame eye motion artifacts, the fact remains that there will be frames or portions of frames which were poorly stabilized. Identification and removal of these frames is perhaps the easiest strategy for improving the quality of motion contrast images of vessels. In Chapter 3, in order to generate videos of near-perfect stabilization, approximately 40-60% of all frames were removed. Manual deletion of frames is time-consuming, given that 40 seconds of video at 60 Hz

results in 2400 frames; 21 video locations in one imaging session would result in 50,400 frames, out of which 25,200 need to be deleted. Thus, to streamline the process, automated frame deletion methods were developed and used. Improvement of these methods can significantly reduce the processing time needed to generate motion contrast perfusion images, while improving the overall quality of the image.

The most obvious method to identify poorly-stabilized frames is to access the stabilization data of the software that was used to stabilize the video. Most conventional algorithms for stabilization will have some sort of “goodness of fit” parameter that marks how successful the stabilization was for any given portion of the video or frame. In Chapter 2, we generated a look-up table for eye motion that was used in the speed quantification. Embedded in the lookup table was data from the stabilization software that marked questionable frames, due to poor cross-correlation scores. Approximately 15-30% of poorly-stabilized frames fit in this category. Thus, the first step in automated frame deletion was to remove the frames marked by the stabilization software.

The next step was to remove all frames that deviated too far from a reference image. A reference image was generated by calculating the averaged image of the video, using the video with the software-identified frames removed. Individual frames were compared to this reference image, and removed if they were too dissimilar in appearance. To implement this strategy, we performed the following steps: (i) for each frame, divide the frame by the reference image, and calculate the average value of the resulting division image (thus generating a single number for each frame that represents the deviation of that frame from the reference image; this single number can be plotted

against frame number to generate a trace); (ii) calculate the first derivative of the trace from (i) and delete all frames that deviate from the mean by more than 0.3 times the standard deviation of the trace. This second step removed approximately 50-70% of the remaining poorly-stabilized frames. The remaining frames were deleted manually.

The remaining poorly-stabilized frames, which were not identified by either of the two methods above, were primarily “twitch” frames. At large field sizes, approximately every 12 seconds, for 1 second at a time, the left and right edges of the frame contract and expand (**Figure 4.19**). Although subtle, if one does not remove these “twitch” frames from the video, subtle blurring and distortions at the edges of frames can be noticed in both the motion contrast enhanced image of vessels as well as the averaged image of photoreceptors. Although twitching is very noticeable in the calibration videos of grids, it is difficult to identify during imaging due to the confounding eye motion. An automated method to identify and remove twitching can be useful when very high quality images are needed.

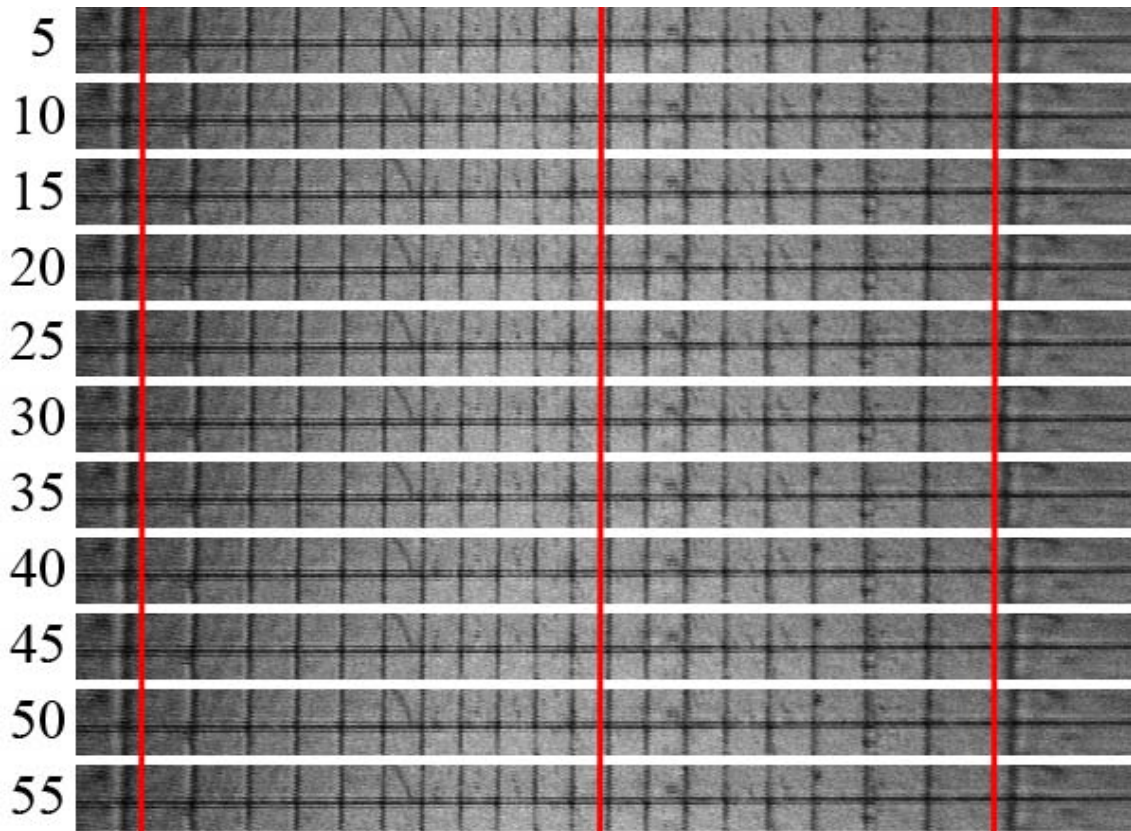


Figure 4.19: Demonstration of twitching. A calibration grid was imaged using the AOSLO and a video was acquired during a twitch. Shown are horizontal strips from the calibration grid at frame numbers 5, 10, 15, ... , 55. Red lines are vertical reference lines. Notice that the location of the grid lines at the left and right edges of the frame change during the twitch, while the center of the frame remains constant.

Post-processing

Additional strategies for post-processing can also be applied to improve image quality. Potential areas for exploration include the use of the Frangi Vesselness filter (Frangi, Niessen et al. 1998), incorporation of additional spatial or frequency-domain filtering, or application of histogram stretching techniques.

In addition, there are many methods for contrast enhancement, which can be applied after motion contrast enhancement has been applied. A simple example is to compute the image raised to an exponential power. Consider an image, $I(x,y)$, which is the motion contrast enhanced image. By computing $I^n(x,y)$, where n is an integer greater than 1, the contrast of the resulting image can be further enhanced. Application of additional contrast enhancement techniques could potentially result in further improvements in image quality.

Conclusions

Motion contrast enhancement is an effective tool for detection of cell paths in ST plots, and an important precursor to automated analysis. We demonstrate that ST plot analysis can be successfully applied to high resolution retinal videos of the microcirculation, despite challenges such as low SNR, and similarities in texture between moving cells and the background tissue. The method is most promising for noninvasive, in vivo assessment of hemodynamics through small capillaries, where contrast and noise issues are prevalent. Further optimization of key algorithms can lead to significant improvements in processing time.

4.3 Acknowledgments

Portions of this chapter are published in the *IEEE Proceedings of the International Symposium for Biomedical Imaging (ISBI) 2010*. The dissertation author is the primary investigator and thanks co-author Austin Roorda, for his contributions. The author would also like to thank Jacque Duncan, Brandon Lujan, and Pavan Tiruveedhula for assistance with perfusion imaging; Vincent Liu for processing data in several patients with retinal diseases not related to diabetes; Jitendra Malik and Ruzena Bajcsy, for insightful discussions about computer vision and medical image analysis; and Stanley Berger, Dorian Liepmann, and Omer Savaş for insightful discussions about microhemodynamics.

REFERENCES

- Alder, V. A., E. N. Su, et al. (1997). "Diabetic Retinopathy: Early Functional Changes." Clinical and Experimental Pharmacology and Physiology **24**: 785-788.
- ANSI (2007). American National Standard for the Safe Use of Lasers. ANSI Z136.1-2007. New York, American National Standard Institute.
- Applegate, R. A., A. Bradley, et al. (1997). "Entoptic Evaluation of Diabetic Retinopathy." 1997 **38**(5): 783-791.
- Arathorn, D. W., Q. Yang, et al. (2007). "Retinally stabilized cone-targeted stimulus delivery." Optics Express **15**: 13731-13744.
- Arend, O., A. Harris, et al. (1995). "Macular capillary particle velocities: a blue field and scanning laser comparison." Graef's Arch. Clin. Exp. Ophthalmol. **233**: 244-249.
- Arend, O., S. Wolf, et al. (1991). "Retinal microcirculation in patients with diabetes mellitus: dynamic and morphological analysis of perifoveal capillary network." Br. J. Ophthalmol **75**: 514-518.
- Arend, O., S. Wolf, et al. (1994). "Perifoveal microcirculation with non-insulin-dependent diabetes mellitus." Graefe's Arch Clin Exp Ophthalmol **232**: 225-231.
- Ashton, N. (1963). "Studies of retinal capillaries in relation to diabetic and other retinopathies." Br. J. Ophthalmol **47**: 521-538.
- Barber, A. J. (2003). "A new view of diabetic retinopathy: a neurodegenerative disease of the eye." Progress in Neuro-Psychopharmacology & Biological Psychiatry **27**: 283-290.

- Bearse, M. A., A. J. Adams, et al. (2006). "A multifocal electroretinogram model predicting the development of diabetic retinopathy." Prog in Retinal and Eye Res **25**: 425-448.
- Becker, H. M., M. Chen, et al. (2004). "Tracking of leukocyte recruitment into tissues of mice by in situ labeling of blood cells with the fluorescent dye." J. Immunological Methods **286**: 69-78.
- Bennett, A. G. (1990). Clinical visual optics. Oxford, Butterworth-Heinemann.
- Ben-nun, J. (1996). "Comparative Flow Velocity of Erythrocytes and Leukocytes in Feline Retinal Capillaries." Invest. Ophthalmol. Visual Sci. **37**: 1854-1859.
- Bird, A. C. and R. A. Weale (1974). "On the Retinal Vasculature of the Human Fovea." Exp Eye Res. **19**: 409-417.
- Blum, H. (1967). A transformation for extraction new descriptors of shape. Proc. Symposium on Models for the Perception of Speech and Visual Form. W. Whaters-Dunn. Cambridge, Mass, MIT Press: 362-380.
- Boeri, D., M. Maiello, et al. (2001). "Increased Prevalence of Microthromboses in Retinal Capillaries of Diabetic Individuals." Diabetes **50**: 1432-1439.
- Bradley, A., H. Zhang, et al. (1998). "Entoptic image quality of the retinal vasculature." Vision Research **38**: 2685-2696.
- Braun, R. D., T. C. Fisher, et al. (1996). "Decreased Deformability of Polymorphonuclear Leukocytes in Diabetic Cats." Microcirculation **3(3)**: 271-278.
- Bresnick, G. H., R. Condit, et al. (1984). "Abnormalities of the Foveal Avascular Zone in Diabetic Retinopathy." Arch Ophthalmol **102**: 1286-1293.

- Bursell, S. E., A. C. Clermont, et al. (1996). "Retinal Blood Flow Changes in Patients With Insulin-Dependent Diabetes Mellitus and No Diabetic Retinopathy." Invest. Ophthalmol. Visual Sci. **37**(5): 886-897.
- Buttery, R. G., C. F. L. Hinrichsen, et al. (1991). "How thick should a retina be? A comparative study of mammalian species with and without intraretinal vasculature." Vision Research **31**(2): 169-187.
- Campanelli, M., C. Vogel, et al. (2003). "Dewarping Scanned Retinal Images." Unpublished Report.
- Chambers, R. and B. W. Zweifach (1944). "Topography and function of the mesenteric capillary circulation." Am J of Anatomy **75**(2): 173-205.
- Chibber, R., B. M. Ben-Mahmud, et al. (2007). "Leukocytes in Diabetic Retinopathy." Current Diabetes Reviews **3**: 3-14.
- Conrath, J., R. Giorgi, et al. (2005). "Foveal avascular zone in diabetic retinopathy: quantitative vs qualitative assessment." Eye **19**: 322-326.
- Cunha-Vaz, J. and R. Bernardes (2004). "Nonproliferative retinopathy in diabetes type 2. Initial stages and characterization of phenotypes." Progress in Retinal and Eye Research **24**: 355-377.
- Cunha-Vaz, J., J. R. Faria de Abreu, et al. (1975). "Early breakdown of the blood-retinal barrier in diabetes." Br. J. Ophthalmol **59**: 649-656.
- Cunha-Vaz, J., J. R. Fonseca, et al. (1978). "Studies on Retinal Blood Flow. II. Diabetic Retinopathy." Arch Ophthalmol **96**: 809-811.
- Damiano, E. R. and T. M. Stace (2005). "Flow and deformation of the capillary glycocalyx in the wake of a leukocyte." Physics Fluids **17**: 031509-1-17.

- Ditchburn, R. W. (1987). "What is psychophysically perfect image stabilization? Do perfectly stabilized images always disappear?: comment." JOSA A **4**(2): 405-406.
- Dong, C., J. Cao, et al. (1999). "Mechanics of Leukocyte Deformation and Adhesion to Endothelium in Shear Flow." Annals Biomed. Eng. **27**: 298-312.
- Duncan, J. L., Y. Zhang, et al. (2007). "High-resolution imaging with adaptive optics in patients with inherited retinal degeneration." Invest. Ophthalmol. Visual Sci. **48**(7): 3283-3291.
- Ellis, C. G., M. L. Ellsworth, et al. (1992). "Application of Image Analysis for the Evaluation of Red Blood Cell Dynamics in Capillaries." Microvascular Res **44**: 214-225.
- Evans, E. and Y. C. Fung (1972). "Improved Measurements of the Erythrocyte Geometry." Microvascular Res **4**: 335-347.
- Fantone, J. C. and P. A. Ward (1982). "Role of oxygen-derived free radicals and metabolites in leukocyte-dependent inflammatory reactions." Am J Pathol **107**(3): 397-418.
- Feke, G. T., S. M. Buzney, et al. (1994). "Retinal circulatory abnormalities in type 1 diabetes." Invest. Ophthalmol. Visual Sci. **35**: 2968-2975.
- Fitz-Gerald, J. M. (1972). "Plasma motions in narrow capillary flow." J. Fluid Mech **51**: 463-476.
- Flower, R., E. Peiretti, et al. (2008). "Observation of Erythrocyte Dynamics in the Retinal Capillaries and Choriocapillaris using ICG-loaded Erythrocyte Ghost Cells." Invest. Ophthalmol. Visual Sci. **49**(5510-5516).

- Frangi, A. F., W. J. Niessen, et al. (1998). "Multiscale vessel enhancement filtering." MICCAI: 130-137.
- Friedman, E., T. R. Smith, et al. (1964). "Retinal Microcirculation in vivo." Invest. Ophthalmol. Visual Sci. **3**: 217-226.
- Fung, Y. C. (1997). Biomechanics: Circulation, 2nd ed. USA, Springer.
- Garcia, C. R., M. E. Rivero, et al. (1999). "Oral fluorescein angiography with the confocal scanning laser ophthalmoscope." Ophthalmol. **106**(6): 1114-1118.
- Geyer, O., M. Neudorfer, et al. (1999). "Pulsatile ocular blood flow in diabetic retinopathy." Acta Ophthalmologica Scandinavica **77**: 522-525.
- Glantz, S. A. (2002). Primer of Biostatistics, 5th ed. New York, McGraw Hill.
- Gray, D. C., W. Merigan, et al. (2006). "In vivo fluorescence imaging of primate retinal ganglion cells and retinal pigment epithelial cells." Optics Express **14**(16): 7144-7158.
- Hammes, H.-P., J. Lin, et al. (2002). "Pericytes and the Pathogenesis of Diabetic Retinopathy." Diabetes **51**: 3107-3112.
- Han, Y., M. A. Barse, et al. (2004). "Multifocal electroretinogram delays predict sites of subsequent diabetic retinopathy." Invest. Ophthalmol. Visual Sci. **45**(3): 948-954.
- Hart, W. E., M. Goldbaum, et al. (1997). "Automated measurement of retinal vascular tortuosity." Proc. AMIA Annual Fall Symposium: 459.
- Hasegawa, T., J. R. Ravens, et al. (1967). "Precapillary arteriovenous anastomoses. "Throughfare channels" in the brain." Arch Neurol **16**: 217-224.

- Hellstedt, T. and I. Immonen (1996). "Disappearance and formation rates of microaneurysms in diabetic retinopathy." Br J Ophthalmol **80**: 135-139.
- Henkind, P., R. W. Bellhorn, et al. (1975). "Development of macular vessels in monkey and cat." Br J Ophthalmol **59**: 703-708.
- Hilmantel, G., R. A. Applegate, et al. (1999). "Entoptic Foveal Avascular Zone Measurement and Diabetic Retinopathy." Optometry and Visual Science **76**(12): 826-831.
- Hogg, J. C. and C. M. Doerschuk (1995). "Leukocyte Traffic in the Lung." Annu. Rev. Physiol. **57**: 97-114.
- Hood, D. C., I. J. Frishman, et al. (2002). "Retinal origins of the primate multifocal ERG: implications for the human response." Invest. Ophthalmol. Visual Sci. **43**: 1673-1685.
- Hudetz, A. G. (1997). "Blood Flow in the Cerebral Capillary Network: A Review Emphasizing Observations with Intravital Microscopy." Microcirculation **4**: 233-252.
- Ishibazawa, A., T. Nagaoka, et al. (2011). "Effects of Shear Stress on the Gene Expressions of Endothelial Nitric Oxide Synthase, Endothelin-1, and Thrombomodulin in Human Retinal Microvascular Endothelial Cells." Invest. Ophthalmol. Visual Sci. **52**(11): 8496-8504.
- Iwasaki, M. and H. Inomata (1986). "Relation Between Superficial Capillaries and Foveal Structures in the Human Retina." Invest. Ophthalmol. Visual Sci. **27**(12): 1698-1705.

- Japee, S. A., C. G. Ellis, et al. (2004). "Flow Visualization tools for Image Analysis of Capillary Network." Microcirculation **11**: 39-54.
- Jensen, P. S. and M. R. Glucksberg (1997). "Regional Variation in Capillary Hemodynamics in the Cat Retina." Invest. Ophthalmol. Visual Sci. **39**: 407-415.
- Jin, Q., C. Verdier, et al. (2007). "Migration and deformation of leukocytes in pressure drive flows." Mechanics Res. Commun. **34**(411-422).
- Jonnal, R. S., J. Rha, et al. (2007). "In vivo functional imaging of human cone photoreceptors [Abstract]." Optics Express **15**: 16141-16160.
- Jou, L. D., G. Wong, et al. (2005). "Correlation between luminal geometry changes and hemodynamics in fusiform intracranial aneurysms." AJNR Am J Neuroradiol **26**(9): 2357-2363.
- Kamm, R. D. (2002). "Cellular Fluid Mechanics." Annu. Rev. Fluid Mech. **34**: 211-232.
- Kim, D. Y., J. Fingler, et al. (2011). "Visualization of human retinal micro-capillaries with phase contrast high-speed optical coherence tomography." Proc. of SPIE **7889**: 78890H-1-6.
- Kim, S. Y., M. A. Johnson, et al. (2005). "Neutrophils Are Associated With Capillary Closure in Spontaneously Diabetic Monkey Retinas." Diabetes **54**: 1534-1542.
- Kim, S. Y., M. A. Johnson, et al. (2004). "Retinopathy in Monkeys with Spontaneous Type 2 Diabetes." Invest. Ophthalmol. Visual Sci. **45**(12): 4543-4553.
- Klein, R., B. E. K. Klein, et al. (1984). "The Wisconsin Epidemiologic Study of Diabetic Retinopathy. III. Prevalence and Risk of Diabetic Retinopathy When Age at Diagnosis is 30 or More Years." Arch Ophthalmol **102**(4): 527-532.

- Kleinfeld, D., P. P. Mitra, et al. (1998). "Fluctuations and stimulus induced changes in blood flow observed in individual capillaries in layers 2 through 4 of rat neocortex." Proc. Natl. Acad. Sci. USA **95**: 15741-15746.
- Kohner, E. M., A. M. P. Hamilton, et al. (1975). "The retinal blood flow in diabetes." Diabetologia **11**: 27-33.
- Komatsu, H., A. Koo, et al. (1990). "Leukocyte Flow Dynamics in the Rat Liver Microcirculation." Microvascular Res **40**: 1-13.
- Konno, S., G. T. Feke, et al. (1996). "Retinal blood flow changes in type I diabetes. A long-term follow-up study." Invest. Ophthalmol. Visual Sci. **37**(6): 1140-1148.
- Ku, D. N., D. P. Giddens, et al. (1985). "Pulsatile flow and atherosclerosis in the human carotid bifurcation. Positive correlation between plaque location and low oscillating shear stress." Arteriosclerosis **5**(3): 293-302.
- Kuebler, W. M., G. E. H. Kuhnle, et al. (1994). "Leukocyte kinetics in pulmonary microcirculation: intravital fluorescence microscopic study." J. Applied Physiol. **76**: 65-71.
- Kwan, A. S., Barry, C., McAllister, I.L., Constable, I. (2006). "Fluorescein angiography and adverse drug reactions revisited: the Lions Eye experience." Clin and Exp Ophthalmol **34**: 33-38.
- Kylstra, J. A., T. Wierzbicki, et al. (1986). "The relationship between retinal vessel tortuosity, diameter, and transmural pressure." Graefe's Arch Clin Exp Ophthalmol **224**: 477-480.
- Laatikainen, L. and J. Larinkari (1977). "Capillary-free area of the fovea with advancing age." Invest. Ophthalmol. Visual Sci. **16**: 1154-1157.

- Lee, J. and N. P. Smith (2008). "Theoretical Modeling in Hemodynamics of Microcirculation." Microcirculation **15**(8): 699-714.
- Li, K. Y., P. Tiruveedhula, et al. (2010). "Inter-subject variability of foveal cone photoreceptor density in relation to eye length." Invest. Ophthalmol. Visual Sci. **51**: 6858-6867.
- Liang, J., Williams, D.R., Miller, D.T. (1997). "Supernormal vision and high-resolution retinal imaging through adaptive optics." J. Opt. Soc. Am. A **14**: 2884-2892.
- Lichtman, M. A., A. Gregory, et al. (1973). "Rheology of Leukocytes, Leukocyte Suspensions, and Blood in Leukemia." J. Clin. Invest. **52**: 350-358.
- Lipowsky, H. H. (2005). "Microvascular Rheology and Hemodynamics." Microcirculation **12**: 5-15.
- Loebl, M. and C. E. Riva (1978). "Macular circulation and the flying corpuscles phenomenon." Ophthalmol.: 911-917.
- Ludovico, J., R. Bernardes, et al. (2003). "Alterations of retinal capillary blood flow in preclinical retinopathy in subjects with type 2 diabetes." Graefe's Arch Clin Exp Ophthalmol **241**: 181-186.
- Lutty, G. A., J. Cao, et al. (1997). "Relationship of Polymorphonuclear Leukocytes to Capillary Dropout in the Human Diabetic Choroid." Am J of Pathology **151**: 707-714.
- MacKinnon, J. R., C. O'Brien, et al. (2009). "Pulsatile ocular blood flow in untreated diabetic retinopathy." Acta Ophthalmologica Scandinavica **75**(6): 661-664.
- Mansour, A. M., A. Schachat, et al. (1993). "Foveal Avascular Zone in Diabetes Mellitus." Retina **13**(2): 125-128.

- Martin, J. A., Roorda, A. (2005). "Direct and Non-Invasive Assessment of Parafoveal Capillary Leukocyte Velocity." Ophthalmol. **12**: 2219-2224.
- Martin, J. A., Roorda, A. (2009). "Pulsatility of parafoveal capillary leukocytes." Exp. Eye Res. **88**: 356-360.
- Martinez-Conde, S., S. L. Macknik, et al. (2004). "The role of fixational eye movements in visual perception." Nat. Rev. Neurosci. **5**: 229-240.
- Meinke, M., G. Muller, et al. (2007). "Optical properties of platelets and blood plasma and their influence on the optical behavior of whole blood in the visible to near infrared wavelength range." J Biomed Optics **12**: 014024.
- Michaelson, I. C. (1954). Retinal Circulation in Man and Animals. Springfield, Illinois, USA, Charles C Thomas.
- Michaelson, I. C. and A. C. P. Campbell (1940). "The anatomy of the finer retinal vessels." Tr. Ophth. Soc. U. Kingdom **60**: 71-112.
- Mintz-Hittner, H. A., D. M. Knight-Nanan, et al. (1999). "A small foveal avascular zone may be an historic mark of prematurity." Ophthalmology **106**(7): 1409-1413.
- Miyamoto, K., N. Hiroshiba, et al. (1998). "In Vivo Demonstration of Increased Leukocyte Entrapment in Retinal Microcirculation of Diabetic Rats." Invest. Ophthalmol. Visual Sci. **39**(11): 2190-2194.
- Miyamoto, K. and Y. Ogura (1999). "Pathogenic Potential of Leukocytes in Diabetic Retinopathy." Seminars in Ophthalmology **14**(4): 233-239.
- Nagaoka, T. and A. Yoshida (2006). "Noninvasive Evaluation of Wall Shear Stress on Retinal Microcirculation in Humans." Invest. Ophthalmol. Visual Sci. **47**: 1113-1119.

- Nakanishi, C., A. Yoshida, et al. (2002). "White blood-cell count and the risk of impaired fasting glucose or Type II diabetes in middle-aged Japanese men." Diabetologia **45**: 42-48.
- Nelson, D. A., S. Krupsky, et al. (2005). "Special report: Noninvasive multi-parameter functional optical imaging of the eye." Ophthalmic Surg Lasers Imaging **36**: 57-66.
- Nishiwaki, H., Y. Ogura, et al. (1995). "Quantitative Evaluation of Leukocyte Dynamics in Retinal Microcirculation." Invest. Ophthalmol. Visual Sci. **36**(1): 123-130.
- Nishiwaki, H., Y. Ogura, et al. (1996). "Visualization and Quantitative Analysis of Leukocyte Dynamics in Retinal Microcirculation of Rats." Invest. Ophthalmol. Visual Sci. **37**: 1341-1347.
- Pallikaris, A., D. R. Williams, et al. (2003). "The reflectance of single cones in the living human eye." Invest. Ophthalmol. Visual Sci. **44**: 4580-4592.
- Paques, M., B. Boval, et al. (2000). "Evaluation of fluorescein-labeled autologous leukocytes for examination of retinal circulation in humans." Current Eye Research **37**: 165-170.
- Parodi, M. B., F. Visintin, et al. (1995). "Foveal avascular zone in macular branch retinal vein occlusion." International Ophthalmology **19**(1): 25-28.
- Patel, V., S. Rassam, et al. (1992). "Retinal blood flow in diabetic retinopathy." British Medical Journal **305**: 678-683.
- Pécsvarády, Z., T. C. Fisher, et al. (1994). "Decreased polymorphonuclear leukocyte deformability in NIDDM." Diabetes Care **17**(1): 57-63.

- Polyak, S. L. (1957). The vertebrate visual system; its origin, structure, and function and its manifestations in disease with an analysis of its role in the life of animals and in the origin of man, preceded by a historical review of investigations of the eye, and of the visual pathways and centers of the brain, University of Chicago Press.
- Popel, A. S. and P. C. Johnson (2005). "Microcirculation and Hemorheology." Annu. Rev. Fluid Mech. **37**: 43-69.
- Pozrikidis, C. (2005). "Axisymmetric motion of a file of red blood cells through capillaries." Physics Fluids **17**: 031503-1-14.
- Pries, A. R., T. W. Secomb, et al. (1990). "Blood flow in microvascular networks. Experiments and simulation." Circ. Res. **67**: 826-834.
- Prothero, J. and A. C. Burton (1961). "The physics of blood flow in capillaries, I. The nature of the motion." Biophysical Journal **1**: 565-579.
- Provis, J. and A. E. Hendrickson (2008). "The Foveal Avascular Region of Developing Human Retina." Arch Ophthalmol **126**(4): 507-511.
- Provis, J. M., P. L. Penfold, et al. (2005). "Anatomy and development of the macula: specialisation and the vulnerability to macular degeneration." Clinical and Experimental Optometry **88**(5): 269-281.
- Putnam, N. M., D. X. Hammer, et al. (2010). "Modeling the foveal cone mosaic imaged with adaptive optics scanning laser ophthalmoscopy." Optics Express **18**: 24902-24916.

- Racine, V., M. Saschse, et al. (2007). "Visualization and quantification of vesicle trafficking on a three-dimensional cytoskeleton network in living cells." J Microscopy **225**: 214-228.
- Reinholz, F., R. A. Ashman, et al. (1999). "Simultaneous three wavelength imaging with a scanning laser ophthalmoscope." Cytometry A **37**: 165-170.
- Riva, C. E. and B. Petrig (1980). "Blue field entoptic phenomenon and blood velocity in the retinal capillaries." J. Opt. Soc. Am. **70**: 1234-1238.
- Rodieck, R. W. (1991). "The density recovery profile: a method for the analysis of points in the plane applicable to retinal studies." Vis Neurosci **6**: 95-111.
- Roorda, A., F. Romero-Borja, et al. (2002). "Adaptive optics scanning laser ophthalmoscopy." Optics Express **10**: 405-412.
- Sander, B., M. Larsen, et al. (1994). "Early changes in diabetic retinopathy: Capillary loss and blood-retina barrier permeability in relation to metabolic control." Acta Ophthalmologica **72**: 553-559.
- Sanders, R. J., G. C. Brown, et al. (1991). "Foveal avascular zone diameter and sickle cell disease." Arch Ophthalmol **109**(6): 812-815.
- Sato, Y., J. Chen, et al. (1995). "Measuring Microcirculation Using Spatiotemporal Image Analysis." MICCAI.
- Sato, Y., Chen, J., Zoroofi, R.A., Harada, N., Tamura, S., Shiga, T. (1997). "Automatic Extraction and Measurement of Leukocyte Motion in Microvessels using Spatiotemporal Image Analysis." IEEE Trans. Biomed. Eng. **44**: 225-236.

- Savage, H. I., J. W. Hendrix, et al. (2004). "Differences in Pulsatile Ocular Blood Flow among Three Classifications of Diabetic Retinopathy." Invest. Ophthalmol. Visual Sci. **45**(12): 4504-4509.
- Schmid-Schonbein, G. W. (1980). "Morphometry of Human Leukocytes." Blood **56**: 866-875.
- Schmid-Schonbein, G. W. (1999). "Biomechanics of Microcirculatory Blood Perfusion." Annu. Rev. Biomed. Eng. **1**: 73-102.
- Schmid-Schonbein, G. W., R. Skalak, et al. (1980). "Cell Distribution in Capillary Networks." Microvascular Res **19**: 18-44.
- Schmid-Schonbein, G. W., K. P. Sung, et al. (1981). "Passive Mechanical Properties of Human Leukocytes." J Biophys. **36**: 405-423.
- Schmid-Schonbein, G. W., S. Usami, et al. (1980). "The Interaction of Leukocytes and Erythrocytes in Capillary and Postcapillary Vessels." Microvascular Res **19**: 45-70.
- Schmoll, T., A. S. G. Singh, et al. (2011). "Imaging of the parafoveal capillary network and its integrity analysis using fractal dimension." Biomed. Opt. Express **2**(5): 1159-1168.
- Secomb, T. W., R. Skalak, et al. (1986). "Flow of axisymmetric red blood cells in narrow capillaries." J. Fluid Mech. **163**: 405-423.
- Sinclair, S. H., M. Azar-Cavanagh, et al. (1989). "Investigation of the source of the blue field entoptic phenomenon." Invest. Ophthalmol. Visual Sci. **30**(4): 668-673.
- Sirs, J. A. (1991). "The flow of human blood through capillary tubes." J. Physiol. **442**: 569-583.

- Smal, I., I. Grigoriev, et al. (2009). "Accurate estimation of microtubule dynamics using kymographs and variable-rate particle filters." Conf Proc IEEE Eng Med Biol Soc 1: 1012-1015.
- Snodderly, D. M., R. S. Weinhaus, et al. (1992). "Neural-Vascular Relationships in Central Retina of Macaque Monkeys (*Macaca fascicularis*)." J. Neurosci. **12**: 1169-1193.
- Stevenson, S., A. Roorda, et al. (2010). "Eye Tracking with the Adaptive Optics Scanning Laser Ophthalmoscope." Proc. Eye Tracking and Research Applications (ETRA) Meeting.
- Sugihara-Seki, M. and G. W. Schmid-Schonbein (2003). "The Fluid Shear Stress Distribution on the Membrane of Leukocytes in the Microcirculation." J Biomech Eng. **125**: 628-638.
- Sutton, D. W. and G. W. Schmid-Schonbein (1992). "Elevation of organ resistance due to leukocyte perfusion." Heart and Circ. Physiol. **262**: 1646-1650.
- Tam, J., K. P. Dhamdhere, et al. (2011). "Disruption of the Retinal Parafoveal Capillary Network in Type 2 Diabetes Prior to the Onset of Diabetic Retinopathy." Invest. Ophthalmol. Visual Sci.: (to be published).
- Tam, J., J. A. Martin, et al. (2010). "Non-invasive visualization and analysis of parafoveal capillaries in humans." Invest. Ophthalmol. Visual Sci. **51**: 1691-1698.
- Tam, J. and A. Roorda (2010). "Enhanced detection of cell paths in spatiotemporal plots for noninvasive microscopy of the human retina." 2010 IEEE International Symposium on Biomedical Imaging: From Nano to Macro: 584-587.

- Tam, J. and A. Roorda (2011). "Speed quantification and tracking of moving objects in adaptive optics scanning laser ophthalmoscopy." J Biomed Optics **16**(3): 036022.
- Tam, J., P. Tiruveedhula, et al. (2011). "Characterization of single-file flow through human retinal parafoveal capillaries using an adaptive optics scanning laser ophthalmoscope." Biomed. Opt. Express **2**(4): 781-793.
- Tsujikawa, A., J. Kiryu, et al. (2000). "Leukocyte-endothelial cell interactions in diabetic retina after transient retinal ischemia." Am J Physiol Regul Integr Comp Physiol **279**(3): R980-9.
- Tsujikawa, A. and Y. Ogura (2011). "Evaluation of Leukocyte-Endothelial Interactions in Retinal Diseases." Ophthalmologica: Epub ahead of print.
- Vogel, C. R., Arathorn, D.W., Roorda, A., Parker, A. (2006). "Retinal motion estimation in adaptive optics scanning laser ophthalmoscopy." Optics Express **14**: 487-497.
- Vojarova, B., C. Weyer, et al. (2001). "High White Blood Cell Count Is Associated With a Worsening of Insulin Sensitivity and Predicts the Development of Type 2 Diabetes." Diabetes **51**: 455-461.
- Weinhaus, R. S., J. M. Burke, et al. (1995). "Comparison of fluorescein angiography with microvascular anatomy of macaque retinas." Exp Eye Res. **61**: 1-16.
- West, S. K., R. Klein, et al. (2001). "Diabetes and diabetic retinopathy in a Mexican-American population." Diabetes Care **24**(7): 1204-1209.

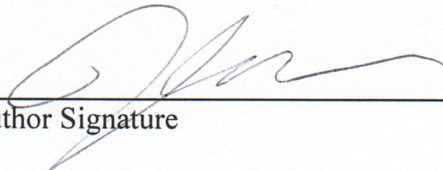
- Wong, T. Y., N. Cheung, et al. (2008). "Prevalence and Risk Factors for Diabetic Retinopathy: The Singapore Malay Eye Study." Ophthalmology **115**(11): 1869-1875.
- Xu, H., A. Manivannan, et al. (2002). "Improved Leukocyte Tracking in Mouse Retinal and Choroidal Circulation." Exp Eye Res. **74**: 403-410.
- Yang, Q., D. W. Arathorn, et al. (2007). "Retinally stabilized cone-targeted stimulus delivery." Optics Express **15**: 13731-13744.
- Yu, P. K., C. Balaratnasingam, et al. (2010). "Microstructure and network organisation of the microvasculature in the human macula." Invest. Ophthalmol. Visual Sci. **51**(12): 6735-6743.
- Zhang, Y., S. Poonja, et al. (2006). "MEMS-based Adaptive Optics Scanning Laser Ophthalmoscopy." Optics Letters **31**: 1268-1270.
- Zharov, V. P., E. I. Galanzha, et al. (2006). "In vivo high-speed imaging of individual cells in fast blood flow." J Biomed Optics **11**(054034-1-5).
- Zheng, D., A.-S. LaMantia, et al. (1991). "Specialized Vascularization of the Primate Visual Cortex." J of Neurosci **11**: 2622-2629.
- Zhong, Z., B. L. Petrig, et al. (2008). "In vivo measurement of erythrocyte velocity and retinal blood flow using adaptive optics scanning laser ophthalmoscopy." Optical Society of America **16**: 12746-12756.
- Zhou, C., P. Yue, et al. (2007). "Simulation of Neutrophil Deformation and Transport in Capillaries using Newtonian and Viscoelastic Drop Models." Annals Biomed. Eng. **35**: 766-780.

- Zweifach, B. W. (1961). Functional Behavior of the Microcirculation. Springfield, Illinois, Charles C Thomas.
- Zweifach, B. W. (1974). "Quantitative Studies of Microcirculatory Structure and Function I. Analysis of pressure distribution in the terminal vascular bed." Circ. Res. **34**: 843-857.
- Zweifach, B. W. (1974). "Quantitative Studies of Microcirculatory Structure and Function II. Direct measurement of capillary pressure in splanchnic mesenteries." Circ. Res. **34**: 858-868.
- Zweifach, B. W. and D. B. Metz (1955). "Selective Distribution of Blood Through the Terminal Vascular Bed of Mesenteric Structures and Skeletal Muscle." Angiology **6**: 282-289.
- Zwick, H., R. Elliott, et al. (1999). "In-vivo Imaging of Photoreceptor Structure and Laser Injury Pathophysiology in the Snake Eye." Proc. SPIE Conference on Laser and Noncoherence Light Ocular Effects: Epidemiology, Prevention, and Treatment III **3591**: 368-374.

Publishing Agreement

It is the policy of the University to encourage the distribution of all theses, dissertations, and manuscripts. Copies of all UCSF theses, dissertations, and manuscripts will be routed to the library via the Graduate Division. The library will make all theses, dissertations, and manuscripts accessible to the public and will preserve these to the best of their abilities, in perpetuity.

I hereby grant permission to the Graduate Division of the University of California, San Francisco to release copies of my thesis, dissertation, or manuscript to the Campus Library to provide access and preservation, in whole or in part, in perpetuity.



Author Signature

12/7/11

Date